Optical Set-Up for Automatised SiPM Characterisation

Von der
Fakultät für Mathematik, Informatik und Naturwissenschaften
der
RWTH Aachen University
zur Erlangung des akademischen Grades eines Doktors der Naturwissenschaften
genehmigte Dissertation
vorgelegt von
Diplom-Physiker

Carsten Andreas Heidemann

aus Mettmann

Berichter:

Univ.-Prof. Dr. rer. nat. Thomas Hebbeker

Priv.-Doz. Dr. rer. nat. Oliver Pooth

Tag der mündlichen Prüfung: 25.08.2016

Zusammenfassung

In dieser Arbeit wird der Aufbau und die Inbetriebnahme eines automatisierten Teststandes zur elektrischen und optischen Charakterisierung von Silizium-Photomultipliern (SiPMs) beschrieben. Eine umfassende Charakterisierung von SiPMs ist erforderlich, um ihr Potential in Detektoren voll ausschöpfen zu können. Ziel dieser Arbeit war es, einen Aufbau zu erstellen, der zur Messung der Eigenschaften von SiPMs in einem 4D-Parameterraum (Temperatur, Betriebsspannung, Lichtwellenlänge und Lichtintensität) verwendet werden kann. Die erfolgreiche Umsetzung des Ziels wird gezeigt. Der Teststand besteht aus der Lichtquelle, dem optischen Aufbau zur Lichtverteilung, der Temperaturstabilisierung, den Messgeräten und einer dazu passende Kontroll- und Datenerfassungssoftware, welche alle in dieser Arbeit beschrieben werden. Im Weiteren werden die Messmethoden für die verschiedenen Eigenschaften von SiPMs vorgestellt und deren Ergebnisse gezeigt.

Abstract

In this work the construction and the initial operation of an automatised test set-up for the electrical and optical characterisation of Silicon Photomultipliers (SiPMs) is described. A characterisation of SiPMs is required to exploit their full potential in detectors. The aim of this work was the construction of a test set-up with the capability to measure the SiPM properties in a 4D parameter space (temperature, operating voltage, wavelength of the light and light intensity). The successful implementation of the goal is shown. The test set-up consists of the light source, the optical set-up for light distribution, the temperature stabilisation, the measuring instruments, and a custom-made control and data acquisition software which are all presented in this thesis. The measuring methods for the different SiPM properties are explained and the results are shown.

Contents

List of Figures

List of Tables

1. Introduction

Cutting edge technologies require a new generation of detectors which are based on the measurement of smallest light fluxes. Silicon Photomultipliers (SiPMs) are light detectors with properties that make them attractive for many use cases. They are small and thin compared to classical Photomultiplier Tubes (PMTs) which allows for a more compact detector design. The avalanche mechanism generating the signal uses a high electric field strength, which is obtained by minimising the distance between the potentials in order to allow for a low operating voltage ($< 100\,\mathrm{V}$). The high electric field combined with the small distance renders theses devices insensitive even to high magnetic fields [1], a feature essential for many detectors. The Geiger mode operation[1] of each cell makes them sensitive to very low or even single photon signals. By optimising the entrance window and the absorption layer SiPMs can be tuned to accept photons with wavelengths from ultraviolet (UV) to infrared (IR) range. Thanks to their versatility they have found a widespread use in many particle physic experiments and industrial applications.

All these properties make SiPMs interesting for particle physics detectors (e.g. CMS [2], LHCb [3], T2K [4], (future) ILD [5]), astroparticle physics (e.g. Auger [6], IceCube [7], FACT [8], CTA [9]), dark matter searches (e.g. XENON [10]), medical physics (e.g. proton therapy) and medical imaging (e.g. PET scanners). These use cases differ in the way that light is coupled to the SiPMs: direct coupling, fibre (wavelength shifting or clear) coupling, and optic system coupling. The chosen coupling has a great effect on the expected photon count.

In the CMS Hadron Outer Calorimeter, the tail catcher of the hadronic calorimeter placed outside the magnet, the hybrid photodiodes were replaced by SiPMs [11] which are coupled with wavelength shifting and clear fibres to the scintillator tiles. In LHCb, the scintillating fibre tracker is directly read out with SiPM arrays [12].

The CALICE AHCAL [13] is a calorimeter prototype for the ILD. This is a highly granular calorimeter with active detection volumes down to $30\,\mathrm{mm} \cdot 30\,\mathrm{mm} \cdot 3\,\mathrm{mm}$ and direct readout. A prototype with 7608 channels was successfully tested at CERN[2].

[1] See Section 2.4.3 for more details.

[2] Conseil Européen pour la Recherche Nucléaire

The near detector ND280 of the T2K experiment uses scintillator bars and wavelength shifting fibres with SiPM readout [14]. The FACT experiment is a Cherenkov telescope based on mirrors and a camera built with SiPMs for long-term monitoring of astrophysical sources [15]. At least one camera type in the telescopes planned for the CTA will be SiPM-based [16]. A small prototype telescope for the fluorescence detection of ultra-high-energy cosmic rays [17] was build the physics institute IIIA of the RWTH Aachen University, which uses SiPMs as very sensitive photon detectors for the camera. For XENON, a liquid xenon dark matter search experiment, SiPMs were tested at the liquid xenon temperature of 175 K for the detection of scintillation light in xenon in the deep UV range ($\lambda_{Xe} = (175 \pm 5)\,\mathrm{nm}$) [18].
In the medical imaging sector, SiPMs are used to build a new generation of hybrid scanner [19], combining PET (positron electron tomography) with MRI (magnetic resonance imaging). The combination of thin LYSO[3] crystal blocks with SiPMs for direct readout lead to a PET scanner which can operate in high magnetic fields. This allows for a simultaneous operation with an MRI scanner. Since PET and MRI are displaying different things, the resulting picture is a combination of soft tissue and anatomy from the MRI and the metabolic image of the PET.
Since the first prototypes of SiPMs, which evolved from the single photon avalanche diode (SPAD) around the year 2005, many new generations have been placed on the market. With each generation at least one key feature has been improved. SiPMs are getting more and more involved as modern detectors require both larger number of read out channels and lower photon counts from a single channel. At the same time, stringent space limitations prevent PMTs from being used as an alternative. Many concepts are now practicable, since SiPMs are suited for a very wide range of operating conditions: not influenced by magnetic field, varying ambient temperature can be compensated by adjusting the supply voltage, and high sensitivity for the chosen wavelength. The spectral sensitivity of the SiPM should match the main wavelength of the used scintillator material (e.g. air, plastic, crystal). The expected light flux determines the optimal cell count. Since modern detectors are designed for increasingly small photon counts, the series parameter spread of the SiPMs has to be verified.
Each detector has different requirements for the light detection. To find the optimally suited SiPM one can do simulations of the designed detector with different SiPMs. To obtain the parameters needed for a correct simulation and operation, many characterisation measurements of possible SiPM types are required.
Several test set-ups for the characterisation of the SiPMs were published [20–22] with

[3] Lutetium-yttrium oxyorthosilicate, an inorganic scintillator material

individual set-ups for different measurements, which require a change of the SiPM for the different measurements. Furthermore there are detailed measurements [23] with a non-published test set-up.
For the complex characterisation process a single test set-up was built. It allows for the measurement of the intrinsic SiPM parameters in a 4D operational parameter space. The test set-up can control the temperature, the operating voltage, the wavelength and the flux of the incident light. The dedicated test environment allows for high statistics to be accumulated in short time. Combining these functionalities in a single device, the test set-up allows for a full characterisation of an SiPM without manual changes. The key goals of this work are the determination of the breakdown voltage, the relative and absolute photon detection efficiency and the noise effects of optical crosstalk, afterpulsing, and thermally induced dark count rate.
During the building process many existing characterisation measurements using specialised hardware, like flash ADC[4] or QDC[5], have been adapted to the used universal hardware, a high-speed oscilloscope. This involved in-depth studies of the measuring methods which may allow other users to implement improved and/or simplified versions to be run with the detector readout.
This thesis is structured as follows: After an introduction of the underlying principles of SiPMs in Chapter 2, the hardware set-up is described in chapter 3. The implemented software for the set-up is described in Chapter 4, followed by the description of the characterisation in Chapter 5. The raw data analysis is described in Chapter 6 and the measuring methods in Chapter 7. Finally a summary with conclusions is given in Chapter 8, followed by an outlook in Chapter 9.

[4] A fast analogue-to-digital converter
[5] A charge-to-digital converter

2. Theory

In this chapter, a brief overview of the working principle of semiconductors and how semiconductors can be used in different operating modes to detect photons is given. More details can be found in e.g. [24]. Formulae in this chapter are taken from [24], if not stated explicitly.

2.1. Semiconductors

Materials are classified as conductors, semiconductors or non-conductors (isolators) depending on the width of the band gap between valence band and conduction band (see Figure 2.1). The valence band is the band with the highest energy level filled with electrons at a temperature of 0 K. The conduction band is the band with the lowest energy level without electrons at a temperature of 0 K. Unlike in conductors, the valence and conduction bands of semiconductors do not overlap. However, their band gap is small compared to non-conductors. The band gaps in semiconductors have values that allow them to work as non-conductors at very low temperatures and as conductors at high temperatures. At low temperatures no electron is in the conduction band and hence there are no holes in the valence band either. Without free charge carriers no current can flow. At higher temperatures some electrons may have enough kinetic/thermal energy to jump to the conduction band and leave a hole in the valence band. This hole and the electron in the conduction band are able to move around in their respective bands and can be used for charge transportation (current). There are two different kinds of transitions from one band to the other: the direct and the indirect.
To understand the difference one has to regard the band scheme as a function of the wave vector. The wave vector is used to describe the movement of charge carriers as a material wave in crystals. The band gap depends on the direction of the wave vector relative to the reciprocal lattice. The direct lattice structure of the most important semiconductor materials is shown in Figure 2.2. In the case of Si it is a diamond structure and for GaAs it is zincblende structure. Both have similar Brillouin zones,

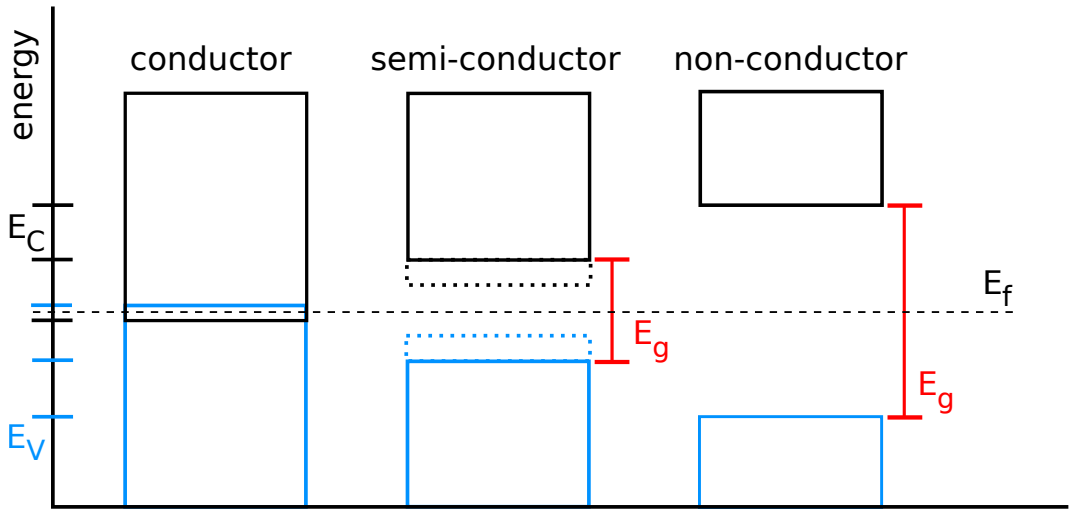

Figure 2.1.: Simplified band scheme for conductor, semiconductor, and non-conductor. The shown bands are the valence band (E_V) and the conduction band (E_C). The band gap (E_G) is indicated in red. The Fermi level (E_F) is indicated by the black dashed line. The dotted lines represent the modified energy levels for doped semiconductors, blue n-doped, black p-doped, respectively. The difference between the modified energy level and the nearest band can be from a few meV up to hundreds of meV. Common dopants for silicon are boron (p-dopant), and phosphor and arsenic (both n-dopants), which result in a small difference between the acceptor/donator level and the nearest band of about 44, 46, and 54 meV, respectively.

shown in Figure 2.3, which are constructed with the reciprocal lattice. In the reciprocal lattice three points/directions are of interest for the description of the bandgap: L, Γ, and X. Γ is the centre of the elementary cell. X is in the direction of Cartesian base vectors of the direct lattice and L is pointing to $[1, 1, 1]$.

If the minimum energy of the conduction band and the maximum energy of the valence band are at the same quasi momentum the electron only needs the energy E_g to jump to the conduction band. This energy could be gained, for example, by absorbing a photon. If the minimum and the maximum are at different quasi momenta then an additional momentum change of the electron, by absorbing a much larger energy amount, is required. Due to the low momentum of optical photons this momentum change of the electron can not be achieved by absorbing an optical photon with an energy of a few (1-5) electron volts (eV). However, the momentum change can be achieved through lattice vibration (phonons).

Typically, intrinsic semiconductors are made from elements in the 4th group of the periodic system. These intrinsic semiconductors can be improved by doping. Doped

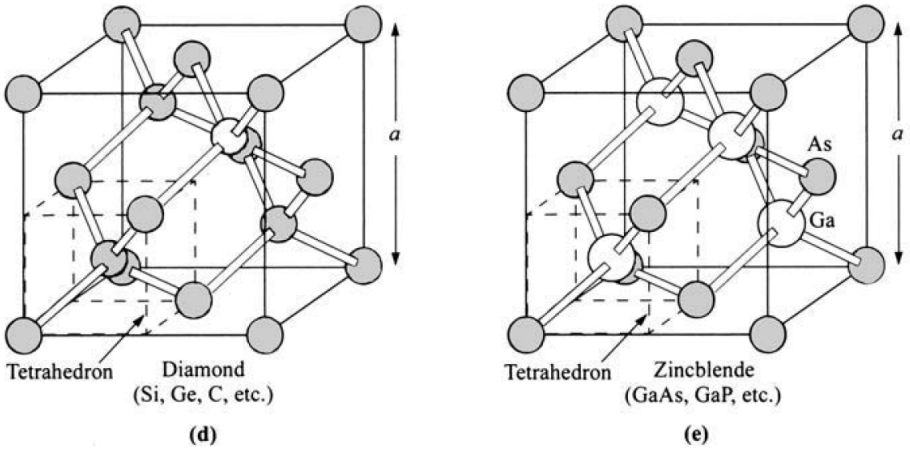

Figure 2.2.: Direct lattice for Si (d), diamond lattice, and GaAs (e), zincblende lattice. Taken from [24].

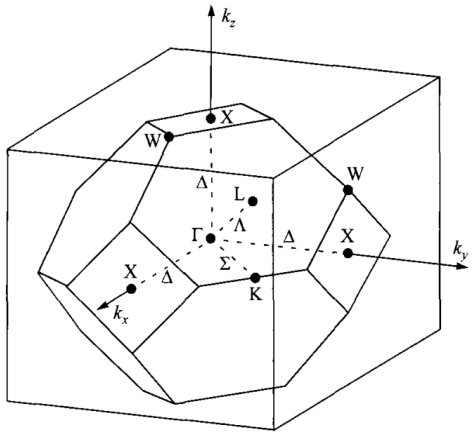

Figure 2.3.: Brillouin zone for Si and GaAs. Taken from [24].

semiconductors contain an additional element to increase the number of charge carriers in one of the bands. If the additional element is from the 5th group of the periodic system, an additional electron with lower required energy for jumping to the conduction band (E_C) is placed in the lattice, creating a donator level. This is called donator doped (n-doped). If the dopant is from the 3rd group, it is called acceptor doped (p-doped). The acceptor is basically a hole with an energy level closer to the valence band (E_V), creating an acceptor level, to which an electron can jump with lower required energy as shown in Figure 2.1.

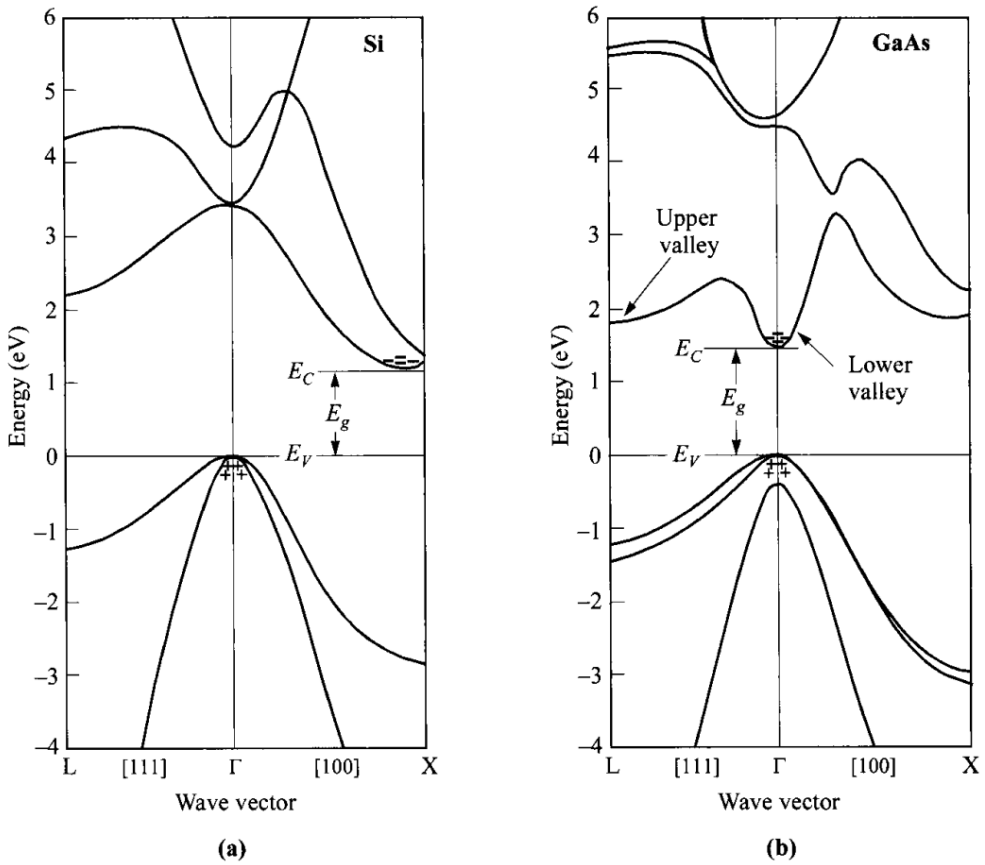

Figure 2.4.: Energy bands for a material (GaAs) with a direct band gap (right plot). The minimum and maximum are at the same wave vector. The left plot shows the energy bands for an indirect band gap model (Si). The minimum and maximum are not at the same wave vector. The interaction of a phonon or additional external energy is required. Taken from [24].

2.2. Important properties of semiconductors

In this section the most important properties with regard to the working principle of SiPMs are described.

2.2.1. Charge carrier concentrations

The charge carrier concentration n is strongly temperature dependent. For an intrinsic semiconductor it can be calculated from the total number of states $N(E)$ and the occupancy $F(E)$ by integrating over the energy levels in the conduction band:

$$n = \int_{E_C}^{\infty} N(E)F(E)dE. \tag{2.1}$$

While $N(E)$ is only dependent on E for intrinsic semiconductors, $F(E)$ is the Fermi-Dirac distribution, a function strongly dependent on temperature T and energy E:

$$F(E) = \frac{1}{1+\exp\left(\frac{E-E_F}{kT}\right)}, \tag{2.2}$$

where E_F is the Fermi level, which can be thought of as a hypothetical energy level which has a 50% probability of being occupied all the time at thermodynamic equilibrium. If a dopant is added, the function of n gets some more temperature dependent features as can be seen from Figure 2.5. In the intrinsic case the strong temperature dependency can be used for thermal sensors. For the normal operation of a semiconductor device a broader temperature range with stable properties is preferable, which can be achieved by doping. The Fermi level for intrinsic semiconductors is given by:

$$E_F = \frac{E_C + E_V}{2} + \frac{kT}{2} \cdot \ln\left(\frac{N_V}{N_C}\right), \tag{2.3}$$

where N_V and N_C are the effective densities of states in valence and conduction band, respectively. The Fermi level for intrinsic states lies nearly in the middle of the band gap. This is not the case for doped states. With known n-dopant concentration N_D, dopant energy level E_D, N_C and temperature T, the Fermi level E_F can be approximated by solving:

$$N_C \cdot \exp\left(-\frac{E_C - E_F}{kT}\right) \approx \frac{N_D}{1+2\cdot\exp\left(\frac{E_F-E_D}{kT}\right)}. \tag{2.4}$$

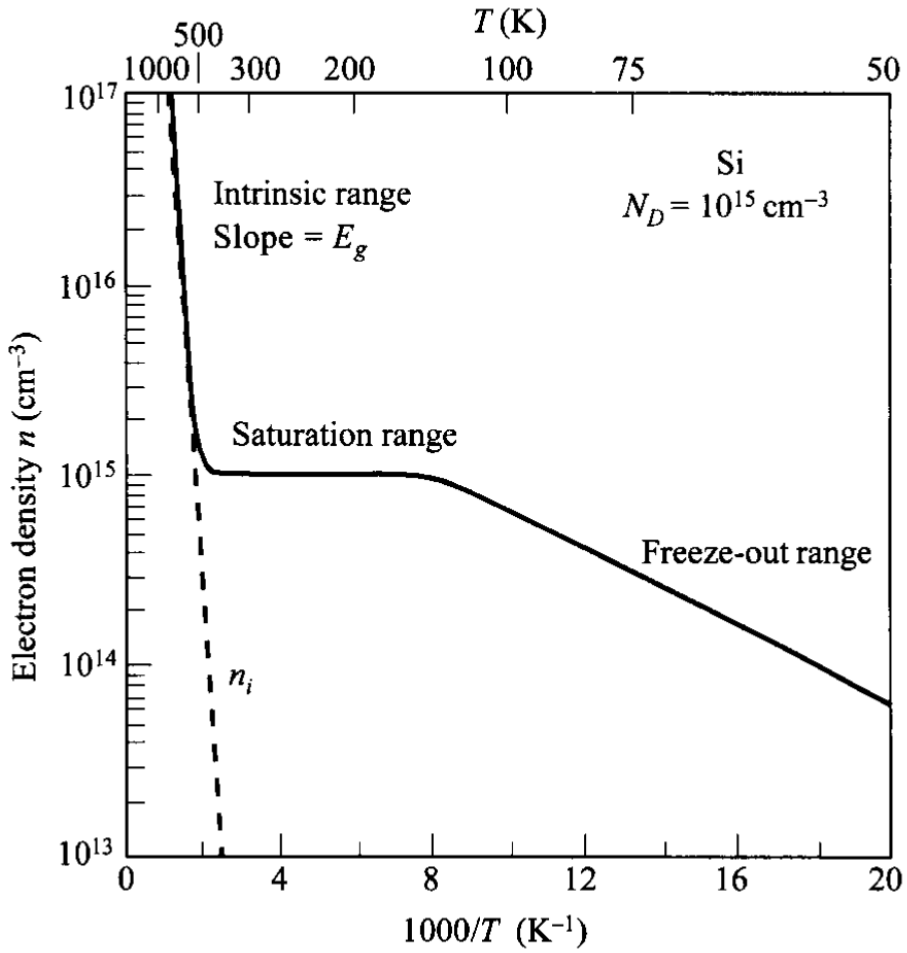

Figure 2.5.: Electron density of doped ($N_D = 10^{15}\,\mathrm{cm}^{-3}$) silicon as a function of the temperature. Three ranges are visible. On the left the intrinsic range where thermally enabled electrons from silicon dominate over the donor ones. In the middle the saturation range where donor electrons dominate. On the right the freeze out range where the temperature is so low, that even the donor electrons are no longer able to move around freely. The dashed line represents the behaviour of intrinsic silicon. Taken from [24].

In n-doped silicon E_C is shifted towards the Fermi level, for p-doped silicon E_V is shifted towards the Fermi level.

2.2.2. Charge carrier transport phenomena

In this section, the focus is set on the mobility and drift of charge carriers, as well as high field effects for charge transport in semiconductors. The high field effects

are used for signal generation in SiPMs. The low field effects are used in SiPMs and photodiodes in the drift regions.

2.2.2.1. Mobility and drift

At low electric fields E the average movement of charges in a silicon semiconductor can be described by

$$v_{drift} = \mu \cdot E, \tag{2.5}$$

considering the effects of interactions with phonons from the lattice (μ_l) and with ionized impurities (μ_i) for the mobility μ:

$$\mu_l \propto \frac{1}{(m_c^*)^{5/2} \cdot T^{3/2}} \tag{2.6}$$

$$\mu_i \propto \frac{T^{3/2}}{N_I \cdot (m_c^*)^{1/2}}, \tag{2.7}$$

with m_c^* for the conductive effective mass. The mobility component related to scattering off phonons from the lattice, μ_l, decreases with temperature T and effective mass. The mobility μ_i, influenced by ionized impurities with a concentration of N_I increases with temperature and decreases with effective mass. This behaviour is expected, as faster electrons are less deflected by the Coulomb scattering. Both mobilities can be combined into one mobility by the Matthiessen rule:

$$\frac{1}{\mu} = \frac{1}{\mu_l} + \frac{1}{\mu_i}. \tag{2.8}$$

The combined mobilities for n-type and p-type silicon are shown in Figure 2.6.

2.2.2.2. High field effects

For medium and high fields the linear relation between field strength and drift velocity is no longer valid. SiPMs work with internal electric field strength greater

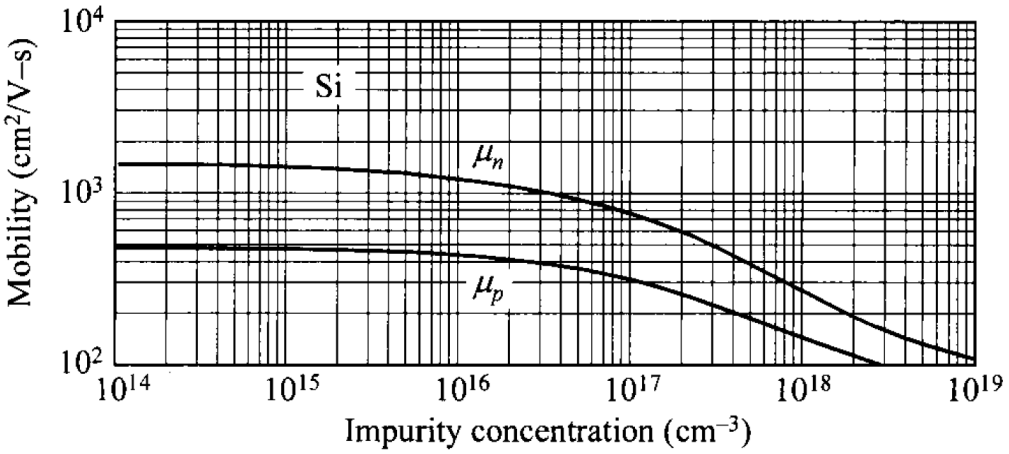

Figure 2.6.: Charge carrier mobility as a function of impurity concentration at 300 K for n-type and p-type silicon. Taken from [24].

then 10^5 V/cm. For medium field strength a term with an effective temperature T_e is introduced:

$$v_{drift} = \mu_0 \cdot E \cdot \sqrt{\frac{T}{T_e}} \tag{2.9}$$

$$\frac{T}{T_e} = \frac{1}{2} \cdot \left[1 + \sqrt{1 + \frac{3\pi}{8} \cdot \left(\frac{\mu_0 \cdot E}{c_s} \right)^2} \right], \tag{2.10}$$

where μ_0 is the mobility at low fields, E the electric field strength, c_s the speed of sound in the semiconductor material, and T the temperature. At high fields the drift velocity of charge carriers (see Figure 2.7) in silicon saturates at

$$v_s = \sqrt{\frac{8 \cdot E_p}{3 \cdot \pi \cdot m_0}} \approx 10^7 \,\text{cm/s} \tag{2.11}$$

and is only dependent on the optical phonon energy E_P and the mass m_0 of the charge carrier.

At high fields, charge carriers gain enough energy to create electron-hole (e-h) pairs through impact-ionisation, resulting in charge avalanches. The ionisation rate α, shown in Figure 2.8, which is strongly dependent on the electric field E, is given as:

$$\alpha(E) = \frac{q \cdot E}{E_c} \cdot \exp\left(-\frac{E_I}{E \cdot [1 + (E/E_P)] + E_T} \right). \tag{2.12}$$

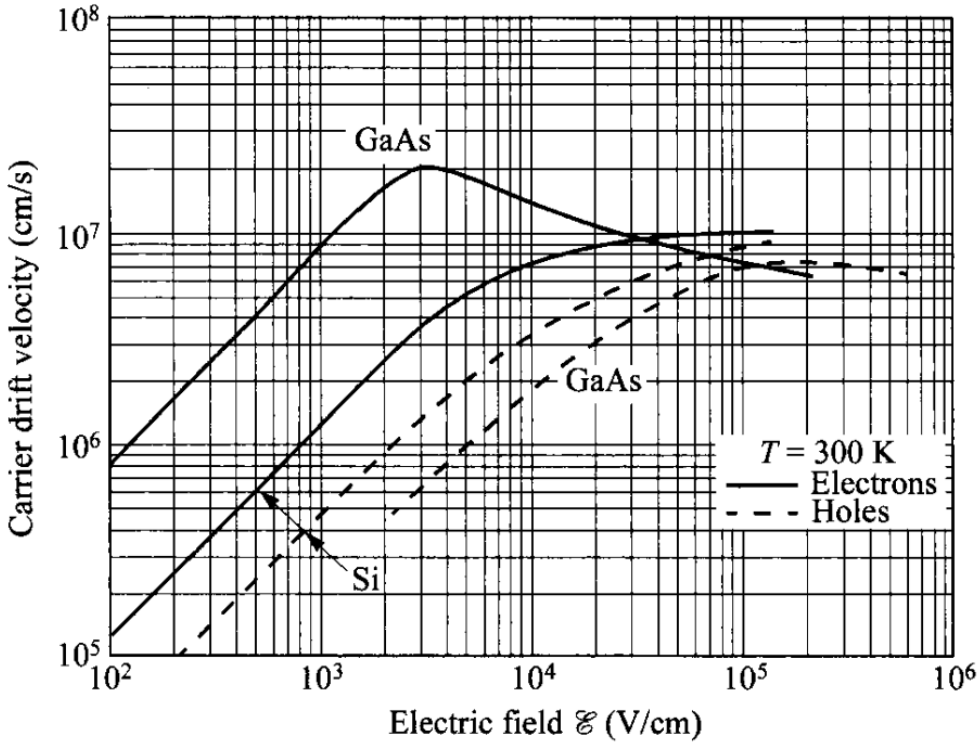

Figure 2.7.: Charge carrier drift velocities for high-purity Si and GaAs as a function of electric field strength at 300 K. In the high-field region the velocity is nearly independent of the dopant concentration. SiPMs are normally operated at field strengths, where the velocity saturates. Taken from [24].

For limited field range this yields

$$\alpha(E) = \frac{q \cdot E}{E_c} \cdot \exp\left(\frac{E_I}{E}\right) \quad \text{for} \quad E_P > E > E_T \tag{2.13}$$

$$\alpha(E) = \frac{q \cdot E}{E_c} \cdot \exp\left(\frac{E_I \cdot E_P}{E^2}\right) \quad \text{for} \quad E > E_P \text{ and } E > \sqrt{E_P \cdot E_T}, \tag{2.14}$$

where E_T, E_P and E_I are the field strengths to overcome the decelerating effects of thermal, optical phonon, and ionisation scattering, respectively. The high-field effective ionisation threshold energy E_c is found to be around 3.6 eV for electrons and around 5.0 eV for holes in silicon.

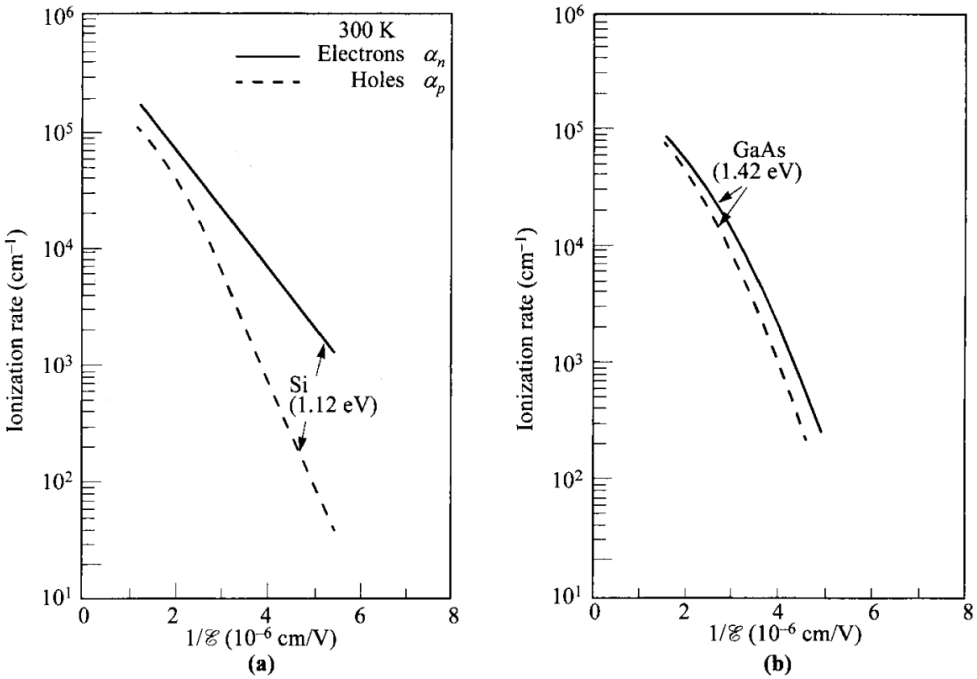

Figure 2.8.: Ionisation rates in Si and GaAs. Taken from [24] and modified.

2.2.3. Optical properties

The optical properties of semiconductors are described by the complex refractive index:

$$\bar{n} = n_r - i \cdot k_e \tag{2.15}$$

with the refractive index n_r:

$$n_r = \frac{c}{v} = \frac{\lambda_0}{\lambda} \tag{2.16}$$

and extinction coefficient k_e:

$$k_e = \frac{\alpha \cdot \lambda}{4 \cdot \pi}. \tag{2.17}$$

The equation is valid under the assumption that the ambience is vacuum and the incoming wavelength is λ_0. The refractive index n_r describes the propagation in the medium. In combination with the refractive index of the ambience the intensities of the reflected and transmitted parts of the incoming light can be calculated. The wavelength in the medium (semiconductor) is λ. The extinction coefficient k_e describes

the energy loss in the material. The absorption coefficient α of semiconductors is a strong function of λ (and thus the energy) of the photons. For photon energies near the absorption edge (band gap), the relation

$$\alpha \quad \propto \quad (h\nu - E_g)^{\gamma} \tag{2.18}$$

can be used for direct band gap semiconductors with $\gamma = 1/2$ for allowed and $\gamma = 3/2$ for forbidden transitions. Forbidden transitions can only occur for $k \neq 0$. For indirect band gaps the formula has to be modified to account for the emitted or absorbed phonon energy E_p:

$$\alpha \quad \propto \quad (h\nu - E_g \pm E_p)^{\gamma}. \tag{2.19}$$

In this case, the parameter γ is 2 for allowed, and 3 for forbidden transitions. A graphic representation of the transitions can be found in Figure 2.9. Measuring the

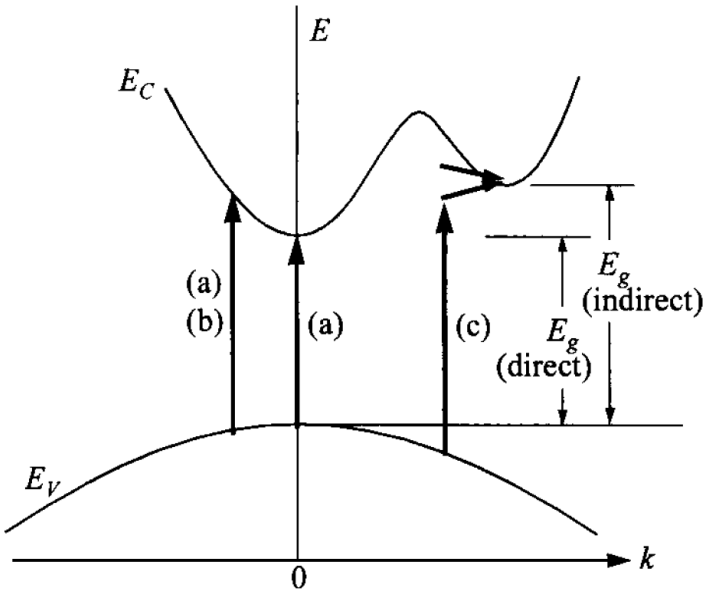

Figure 2.9.: Different transitions: (a) allowed and (b) forbidden for direct transitions, (c) indirect transition. The left transition can be allowed or forbidden because it is at $k \neq 0$. Shown transition (c) can also be allowed or forbidden ($k \neq 0$). Taken from [24].

absorption coefficient as shown in Figure 2.10, the expected behaviour near the band gap energy can be confirmed. For higher energies the measured values deviate from the simple model, as it does not take into account the higher energy bands.

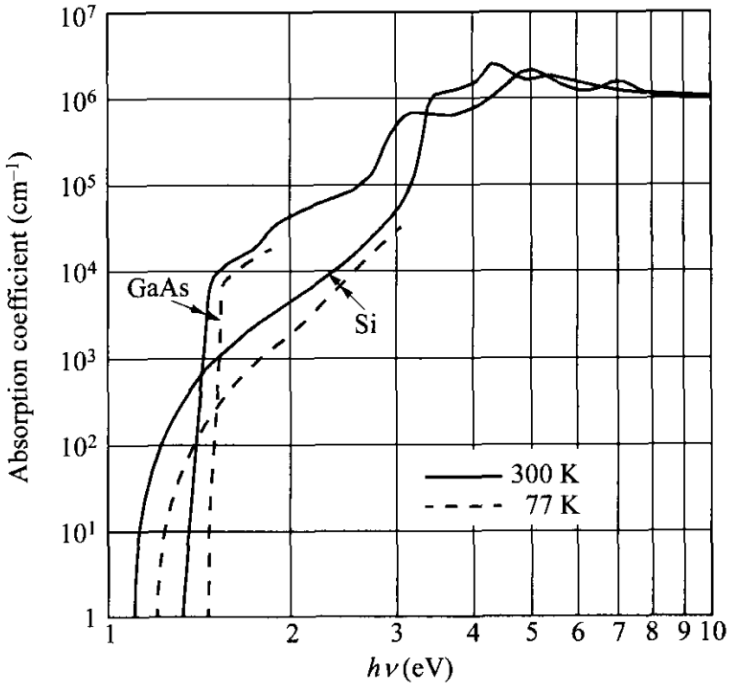

Figure 2.10.: Photon absorption coefficients for Si and GaAs near the band gap. Taken from [24].

2.3. pn-junction

The combination of p-doped and n-doped semiconductor material creates a pn-junction. At the contact surface between p-doped and n-doped material the donor electrons will drift into the p-doped material and recombine with the acceptor holes, thus creating the depletion zone with no free charge carriers. However, the depletion zone now has stationary space charges, as shown in Figure 2.11. These create an electric field across the pn-junction. Without an external voltage this will lead to a built-in potential wall of height V_{bi}. By applying a voltage in bias direction (anode at p-doped material, cathode at n-doped material) the depletion zone, and hence the potential wall is decreased. When applied in reverse bias direction the depletion zone and hence the potential wall is increased. The width d of the depletion zone as a function of the applied voltage can be described by the Shockley formula:

$$d(V) = \sqrt{\frac{2 \cdot \epsilon_r \epsilon_0}{e} \cdot \left(\frac{1}{N_A} + \frac{1}{N_D} \right) \cdot (V_{bi} - V)}, \tag{2.20}$$

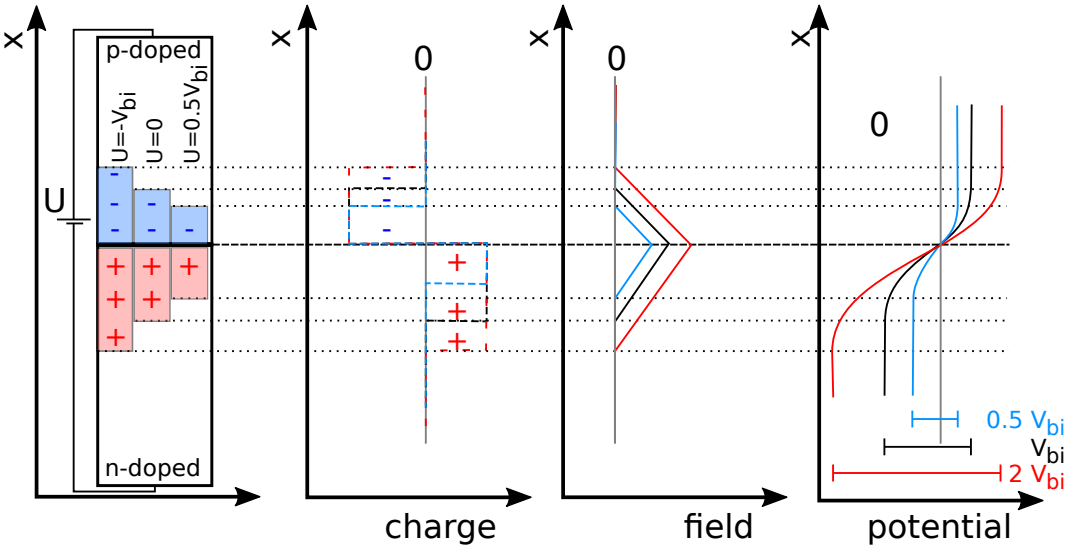

Figure 2.11.: Schematic illustration of a pn-junction, its charge distribution, electric field, and potential for different external supplied voltages. The width of the depletion zone is proportional to $\sqrt{V_{bi} - V}$.

where e stands for the electron charge, N_A and N_D are the dopant densities of acceptor and donator atoms, V_{bi} is the built-in voltage and V is the applied voltage with V smaller than or equal to V_{bi}. The constant ϵ_r is the relative electric constant of the material and ϵ_0 is the electric constant in vacuum.
This is the principle used in semiconductor diodes to create a forward (small or no depletion zone, current conducting) and reverse (large depletion zone, current blocking) direction.

2.3.1. Noise effects

A pn-junction is a source of noise in semiconductors. There are three noise effects: thermal or Johnson noise, flicker noise and shot noise.
Thermal noise is created by the thermally induced random movement of current carriers. It occurs in all types of semiconductors and has a white spectrum. The flicker noise is often called $1/f$ noise due to its frequency dependence of $1/f^{\alpha}$ where $\alpha \approx 1$. Flicker noise is mostly created by surface effects.
Shot noise results from the discreteness of the charge carriers and is independent of the frequency for low and intermediate frequencies. For higher frequencies the spectrum becomes frequency dependent. Only the thermal noise is significant for SiPMs.

2.4. Devices

In the following sections several photon sensitive devices based on pn-junctions are described. Each described device is a step towards the SiPM working principle and is an advancement of the previous device.

2.4.1. Photodiode (PiN photodiode)

A photodiode is a semiconductor diode. This diode is optimised for photon detection and not for their other electrical properties (e.g. maximal current, voltage drop, etc.). The pn-junction can be stretched by an additional intrinsic layer between the n-doped and p-doped material to increase the depletion zone ('active' volume). A typical photodiode structure, as shown in Figure 2.12, is a weakly n-doped material with a n-doped contact on the back and a thin, p-doped front contact. The front contact is thin to allow photons to reach the depletion zone. If a photon with an energy greater than the band gap is absorbed in the depletion zone it can create an electron-hole (e-h) pair. The built-in electric field in the pn-junction prevents direct recombination and separates the charges. Each of these pairs will help to build up the open circuit voltage, which is always smaller than the band gap. If the contacts are short-circuited, for example by an ampere-meter, the current is proportional to the photon flux over many magnitudes. The measured current is the sum of the intrinsic dark current and the photo current. An external bias voltage can be applied to speed up the response of the PiN photodiode but will reduce the signal to noise ratio due to the induced additional (noise) current. In this case the measured current is the sum of the increased dark current and photo current. The dark current depends on the external bias voltage (if external bias is zero, there is no contribution from it) and the temperature (thermally generated e-h pairs in the active area getting separated in the same way as e-h pairs generated by absorbing photons), while the photocurrent is linearly dependent only of the photon flux. Default operation mode in this test set-up is short-circuited with no external bias voltage. The multiplication gain M of a photodiode, defined as the number of generated e-h pairs per absorbed photon, is one ($M = 1$) and does not vary for low bias voltages.

2.4.2. Avalanche photodiode (APD)

If a multiplication gain of a photodiode ($M = 1$) is not sufficient, one may increase the external reverse bias voltage until avalanches are created due to the high electric

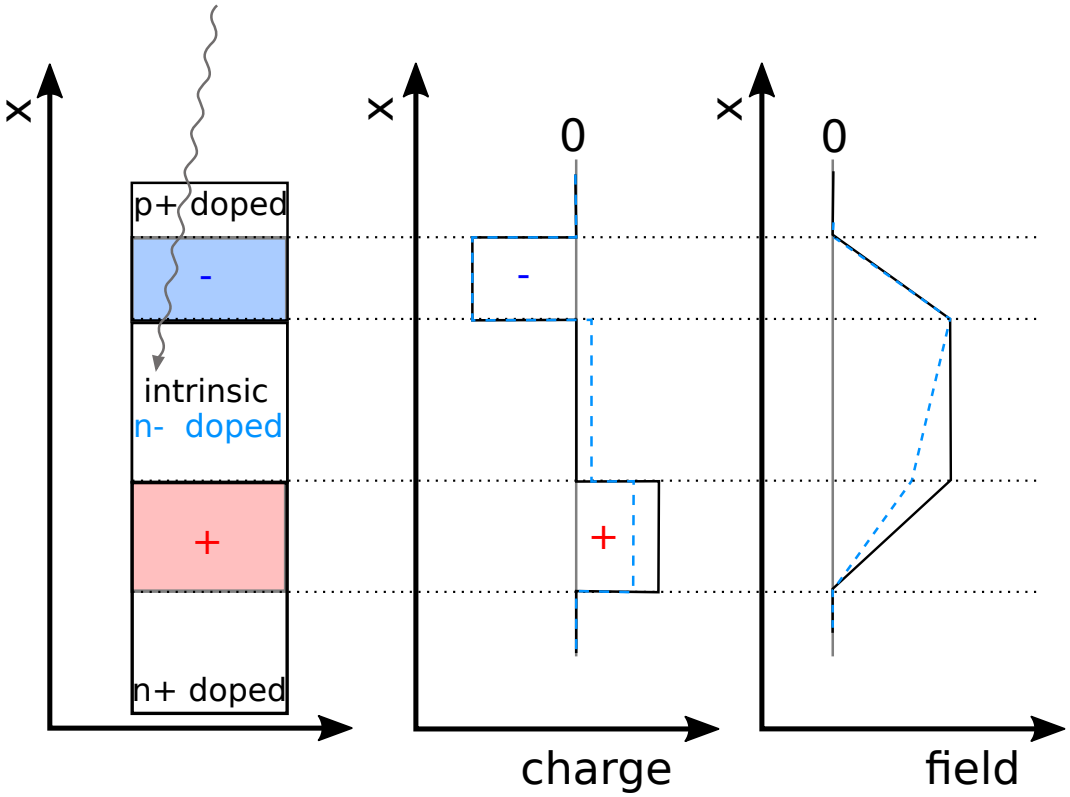

Figure 2.12.: Typical layers of a PiN photodiode and the local field strength. The thin, strongly p-doped layer is the entrance window for the photons. Photons absorbed in the depletion zone, stretched by an intrinsic (solid line)/weakly n-doped (dashed line) layer, can create an electron-hole pair, which is then separated by the built-in electric field.

field strength inside the semiconductor. A better way is to implement a different layer structure as shown in Figure 2.13 to create the required electric field strength with much lower bias voltages ($V_{op} = \mathrm{O}(100\,\mathrm{V})$). The mechanism of these avalanches is shown in the left part of Figure 2.14. In this strong field, the electron from the initial photon-generated electron-hole pair gains enough energy to create additional electron-hole pairs. These electrons, in turn, gain enough energy for further e-h generation. The gain of this avalanche is constant over the whole active area. Typical gain factors for silicon avalanche photodiodes range from 100 to 500. The multiplication gain M is a function of the reverse bias voltage V_R and can be given as:

$$M(V_R) = \frac{1}{1 - \left(\frac{V_R - I \cdot R_S}{V_{br}}\right)^n} \quad \text{with} \quad n < 1,\ V_R < V_{br}. \tag{2.21}$$

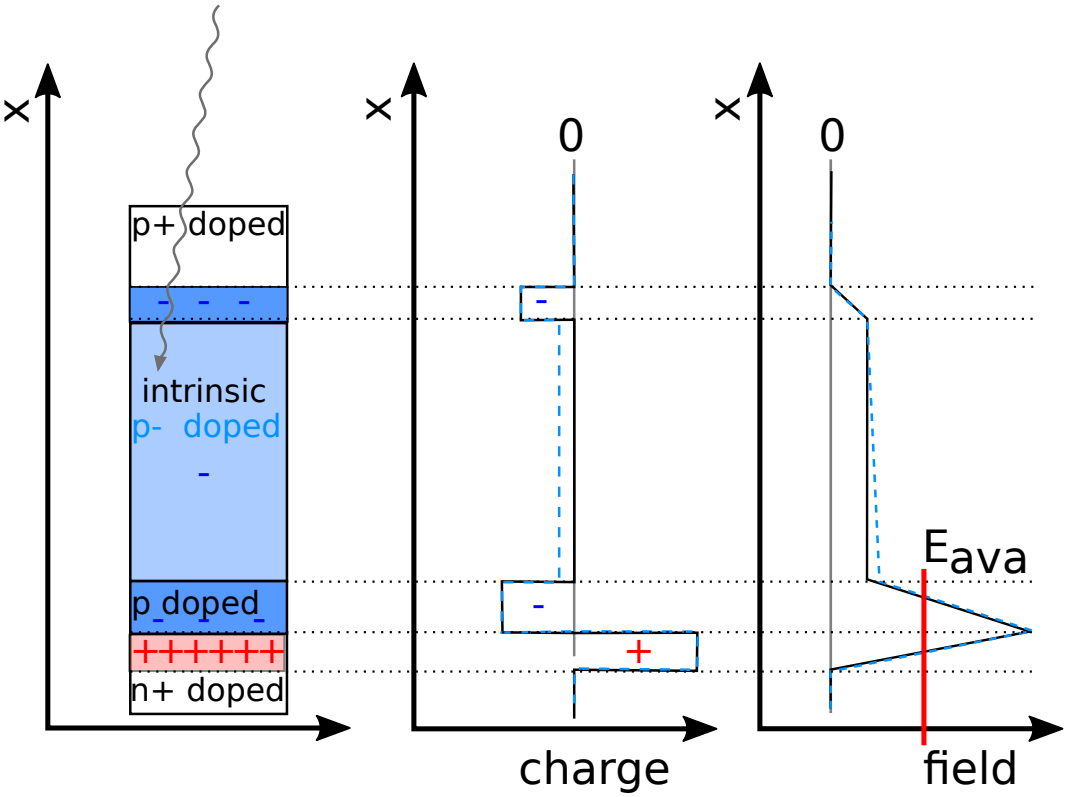

Figure 2.13.: Typical layers of a silicon-based avalanche photodiode, space charges and the local electric field strength. The relative layer thicknesses are manufacturer dependent. The two shown variants are intrinsic (solid line) and weakly doped (dashed line). The extra layer in front of the back contact creates a local high electric field strength which is higher than the required field E_{ava} and thus allows for electron avalanches. These avalanches stop naturally after all available electrons arrived at the anode.

The breakdown voltage V_{br} and n are material and design dependent. $I \cdot R_S$ is the voltage drop across the series resistance R_S of the avalanche photodiode at a current I. The breakdown voltage is the reverse bias voltage above which avalanches start to be self-sustaining and thus making the pn-junction conductive and therefore insensitive to further photons. It can be determined from the steep rise in the I-V characteristics of the APD. In silicon-based avalanche photodiodes the electrons are used for multiplication, while in photodiodes based on germanium and compound semiconductors the holes are used for multiplication. By using only one charge carrier type the avalanche propagation is spatially limited and therefore can not trigger a new avalanche. The complete avalanches rise and decay process can happen within 300 ps in high speed APDs [25].

2.4.3. Geiger-mode avalanche photodiode (GAPD)

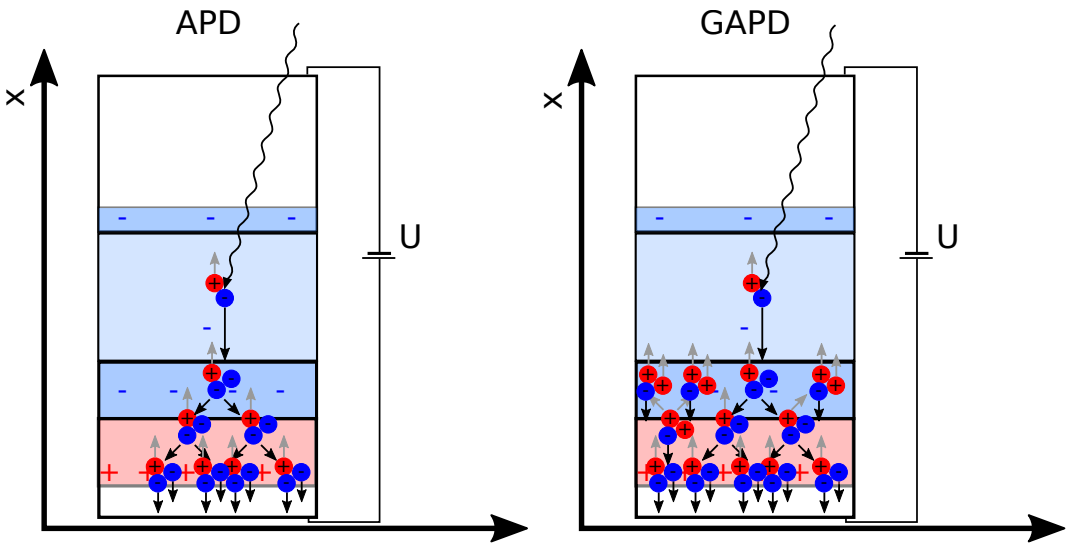

Figure 2.14.: Left plot illustrates a pure electron avalanche occurring in a Si-based APD. The initial electron-hole (e-h) pair is separated by the electric field in the absorption/drift zone. In the multiplication zone the field is so strong that the electrons gain enough energy to create new e-h pairs, while the holes just drift towards the cathode. The right plot illustrates the avalanche process in a Si-based Geiger mode APD. In the Geiger mode both charge carriers contribute to the avalanche because the field is so strong that both electron and holes gain enough energy to create additional e-h pairs. Hence avalanches are no longer spatially limited and will spread across the whole multiplication zone. The dopant structure shown is the same as in Figure 2.13. The layer thicknesses have been modified to give more room for the representation of the avalanche process.

Taking an avalanche photodiode and increasing the reverse bias voltage over the breakdown voltage enables both charge carrier types to do charge multiplication (see Figure 2.14). The voltage above the breakdown voltage is called *overvoltage* ($V_{ov} = V_{op} - V_{br}$). This leads to self-sustaining avalanches which require a quenching mechanism to stop the avalanche process. This is done by reducing the effective voltage either passively by adding a resistor in series or a pulse detection circuit with active dropping of the bias voltage. The reachable gain is up to 10^8. Quenching and restoring the depletion zone takes time of the order of 10 ns. The main advantage of GAPDs is the large signal for single photons, the downside is the extremely limited dynamic range of one, making it a binary device.

2.4.4. Silicon Photomultipliers (SiPMs)

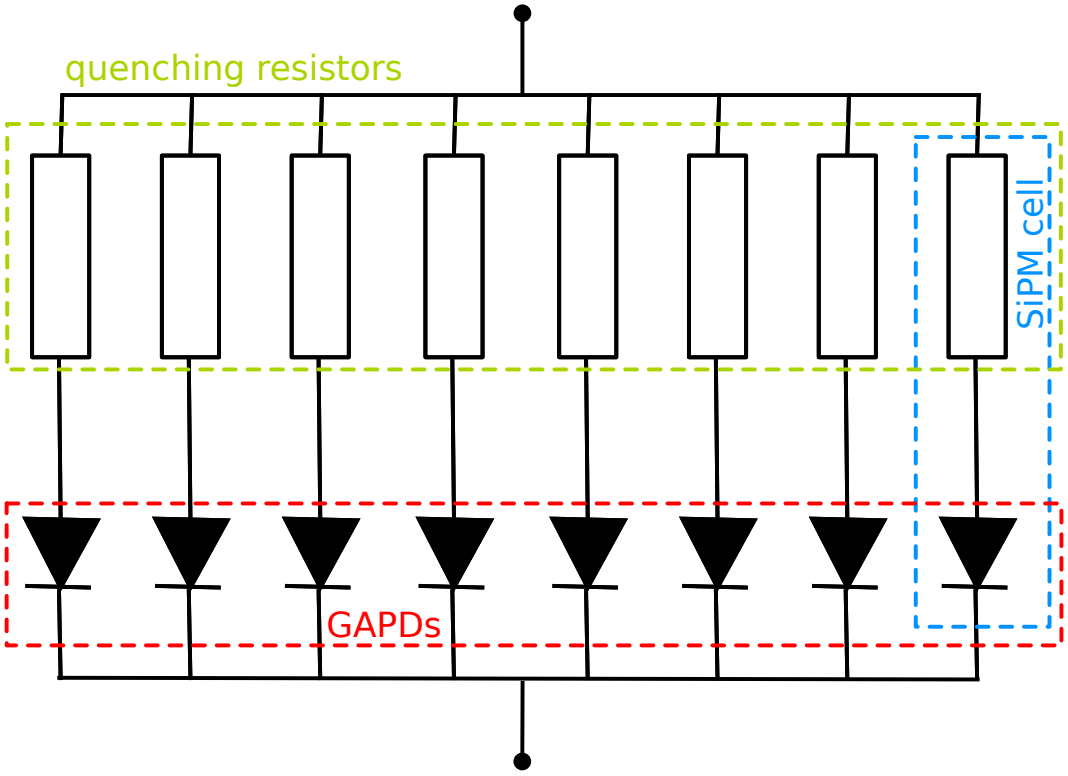

Figure 2.15.: Equivalent circuit diagram for SiPM. The diagram shows the parallel connection of eight SiPM cells. Each cell consist of an GAPD and its quenching resistor. In a real SiPM all cells are connected in parallel and not only eight as shown here.

To overcome the limited dynamic range of a GAPD in SiPMs many small GAPD cells are connected in parallel, sharing anode and cathode, as shown in Figure 2.15. For electrical simulations with SPICE[6] each cell can be represent by a combination of resistors, capacitors and an avalanche model as shown in Figure 2.16. The cell pitch typically varies from 10 μm to 100 μm, due to the required separation of the cells this has great influence on the geometric fill factor as shown in Figure 2.17. In this configuration, the dynamic range goes up to the number of GAPD cells, while having the high single photon detection efficiency of a GAPD for a single cell. The gain of the GAPD used in the cells is typically around 10^5 to 10^6. The only

[6] SPICE (Simulation Program with Integrated Circuit Emphasis) is a software for the simulation of electrical circuits.

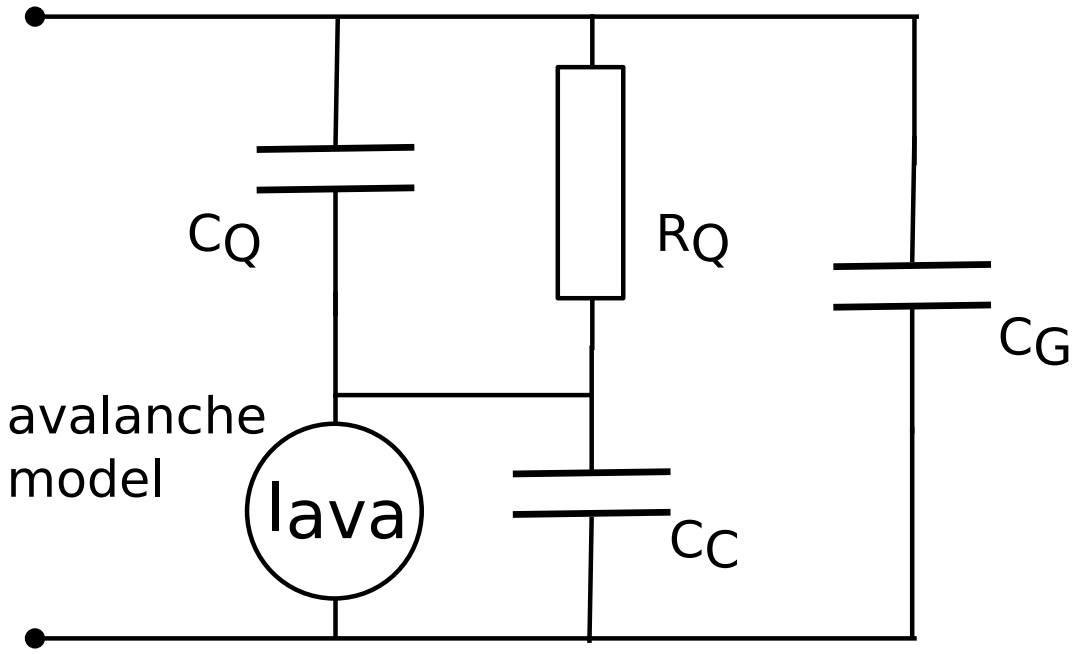

Figure 2.16.: The diagram shows the equivalent circuit for a single cell (and the parasitic grid capacitance (C_G) used for electrical simulations. The cell is represented by the quenching resistor (R_Q), the parasitic quenching resistor capacitance (C_Q), the cell capacitance (C_C) and an avalanche model (I_{ava}) for the simulation of a firing cell. The avalanche model could be a simple switch or a more sophisticated model.

directly controllable operational parameter of an SiPM is the supplied voltage V_{op}. At a certain temperature T this leads to an overvoltage V_{ov}:

$$V_{ov}(T) \quad = \quad V_{op} - V_{br}(T) \tag{2.22}$$

The regulation of the supply voltages allows to keep overvoltage constant, which is important, as most properties vary directly with the overvoltage.
SiPMs are great photon detectors as they have many advantages over the classical Photomultiplier Tubes (PMT) and the previously mentioned semicoductor devices for photon detection. The most important advantages over the PMTs are their size, their insensitivity to magnetic fields and the much lower opartion voltage. Drawbacks are the small size of the active area and the higher noise level compared to PMTs.
The generated signal (pulse height or pulse charge) for a single detected photon is in general the same, regardless of which cell has fired. Thus the generated signals have discrete level for low counts of firing cells. For larger counts of firing cells, the smearing of the signal height/charge due to slight inhomogeneities in the silicon and

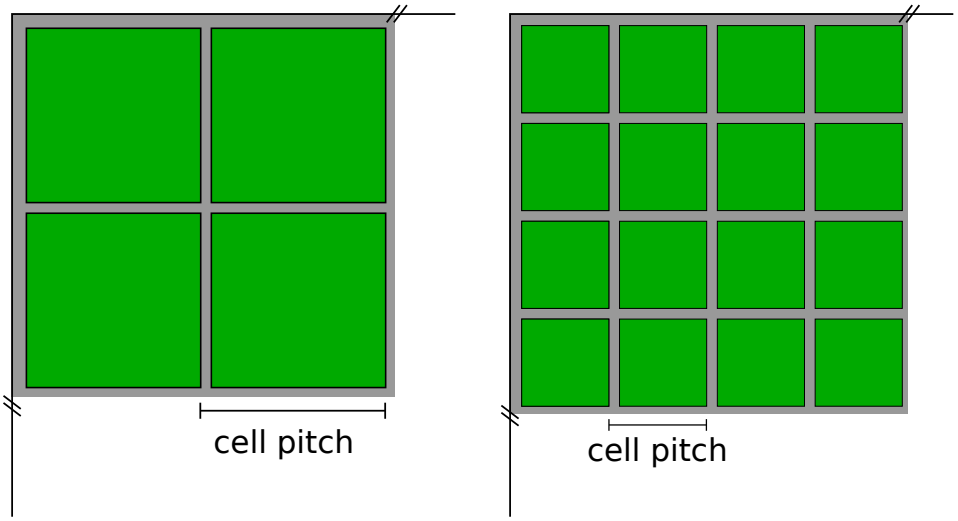

Figure 2.17.: In green the active (photo-sensitive area) of the GAPD cell, in grey the insensitive area (electrical connections, quenching resistors, cell separation). For smaller cell pitches the insensitive area takes a larger part of the surface. This results in a smaller geometric fill factor.

statistical fluctuation in the charge generation becomes so large, that it can not be regarded as discrete any more. The signal height/charge for a single photon event is called 1 p.e. (photon equivalent), for a two photon event it is called 2 p.e. and so on. For triggering on single or more photon events a trigger threshold of 0.5 p.e. is used. If at least two or more photons are required a trigger threshold of 1.5 p.e. is used.

2.4.5. Ideal SiPM

For SiPMs the semiconductor properties define an 'ideal' SiPM. It would be electron based because of higher mobility and better ionisation rate.The dopant concentration would be around 10^{15} to be in the highest regime of the mobility. The SiPM would be operated at saturated drift speed to make it independent of applied voltage. The desired optical properties would define the layer (doping) structure for optimal spectral sensitivity.

2.5. Photon detection efficiency of SiPMs

The photon detection efficiency (p.d.e.) depends on the geometric fill factor (see Figure 2.17), the quantum efficiency, the avalanche probability, and the coating. The geometric fill factor is the ratio between active (photon sensitive) area and total SiPM (photon sensitive and insensitive) area. The geometric fill factor typically varies from 0.3 to larger than 0.8. Smaller cells have in general a lower fill factor than larger cells. The quantum efficiency depends on the wavelength of the incident photon, the used material, and the concentration of the dopant as shown in Figure 2.18. The avalanche

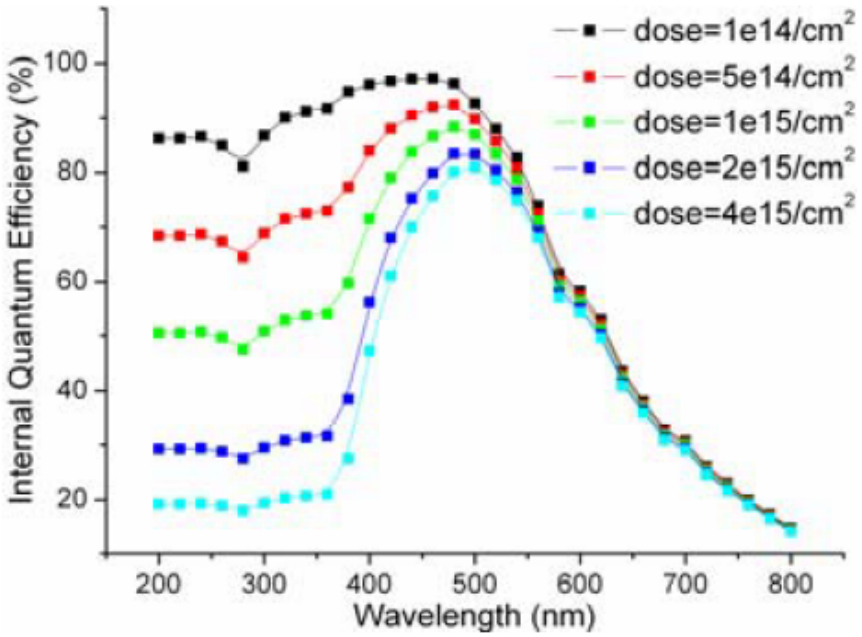

Figure 2.18.: Simulation data: "Internal quantum efficiency of QR-SiPMs with different dosages applied to define the active p+ region" from [26]. For a high UV quantum efficiency the dopant concentration (stated as dose in the picture) has to be low. This would have a bad effect on the layer structure, as a strongly doped p++ layer is used to overcome the limited penetration depth of the UV photons.

trigger probability (p_{ava}) strongly depends on the over voltage. All factors combined yield:

$$p.d.e.\ (V_{ov}, \lambda, f_{fill}) \quad = \quad QE(\lambda) \cdot p_{ava}(V_{ov}) \cdot f_{fill}. \tag{2.23}$$

For UV light, photon energies around $3 - 5\,\mathrm{eV}$, the high absorption coefficient of silicon, as shown in Figure 2.10, makes it harder to optimize SiPMs for UV light,

because the photons are absorbed before reaching the photo sensitive drift region. This problem is targeted with shallow junctions using a thin p+ layer on n substrate. The coating used to protect the SiPM surface can influence the p.d.e. by additional absorption.

2.6. Noise effects of SiPMs

Due to the nature of semiconductors there are some noise effects. Some are temperature induced, others arise from impurities in the semiconductor materials or from the geometric and mechanical design of the single cells.

2.6.1. Thermal noise

The thermal noise is the dominant source of the dark count rate (DCR). The thermal noise events are created by thermal excitation, which can occur due to the impact of randomly moving charge carriers. If the electron-hole pair production happens in the absorption or drift zone the signal (1 p.e.) is indistinguishable from real photon events.

2.6.2. Afterpulsing

Afterpulses can occur after an avalanche has been triggered, no matter whether it was triggered by a photon or noise event. During the avalanche a charge carrier may be trapped by impurities in the multiplication zone [27] and is released after some time (from a few ns to hundreds of ns). This creates an additional signal on the decaying edge of the SiPM signal. The additional signal amplitude depends on the recharge status of the cell. Long trapped charge carriers create a 1 p.e. signal. Shortly trapped ones create a much smaller signal. Both signals can trigger noise effects again.

2.6.3. Crosstalk

Another noise effect is optical crosstalk. This is caused by photons, which can be emitted during the avalanche process. An avalanche produces on average about $3 \cdot 10^{-5}$ photons per created electron-hole pair [28]. Each avalanches produces typically around 10^5 to 10^6 electron-hole pairs. The created photons can reach neighbouring cells and trigger them, creating an output signal of at least 2 p.e.. The

probability of reaching another cell is affected by the mechanical design of the SiPM. Newer designs show significantly lower crosstalk due to optical barriers between their cells.

2.7. State of the art in SiPM development

There are several manufactures of SiPMs (e.g. [29][30][31][32]). All of them have single SiPMs as well as arrays of SiPMs announced or up for order. The single SiPM active areas vary from $1\,\mathrm{mm}^2$ [33] up to $36\,\mathrm{mm}^2$ [34]. SiPMs optimised for blue light reach a p.d.e. of up to 60 % [35]. Cell pitches range from $10\,\mu\mathrm{m}$ to $100\,\mu\mathrm{m}$ and thus the cell count ranges from 100 to 90000 ($9\,\mathrm{mm}^2$, $10\,\mu\mathrm{m}$ cell pitch [36]). The geometric fill factor ranges from 0.33 [33] for $10\,\mu\mathrm{m}$ cell pitches up to 0.82 [34] for the newest generation with $75\,\mu\mathrm{m}$ cell pitch. Some SiPMs offer a much lower crosstalk due to their optical trenches between the cells. There are two types of quenching resistors used, namely poly-silicon resistors and metal film resistors, which have large influence on the temperature behaviour of the recharging process.

2.8. Implication for the test set-up

Due to the large spread of operating voltages a precise wide-range power supply is needed. The large range of the cell count, nearly four orders of magnitude, requires a light source with a large dynamic range. The chosen wavelengths should cover the spectral sensitive range of SiPMs. The temperature must be stabilised as many properties of semiconductors are overvoltage dependent and thus temperature dependent. Older SiPM types have an temperature coefficient for the breakdown voltage around $60\,\mathrm{mV/K}$. The recommended overvoltage for this models is greater $1\,\mathrm{V}$. Thus a temperature stability $\Delta T < 0.1\,\mathrm{K}$ results in a stability of the (linear dependent) properties better then 0.6%. The stability is even better for newer SiPM types with lower temperature coefficients and much higher recommended overvoltages. The available temperature range should cover most use cases.

3. Hardware of the Test Set-up

The aim of this doctoral thesis was to build an automatised single table top set-up which can measure most of the SiPM properties under stable and repeatable conditions in an automatised way, that needs as less as possible user interaction. For these measurements of the SiPM properties the operational parameters can be varied in a 4D parameter space. The operational voltage, the temperature, the photon flux, and the photon wavelength can be varied. The used components can cover a large range of each parameter. Some of the hardware components are custom-made, all others are commercially available. Besides the general characterisation of all components, large effort had been put into the calibration of the light distribution system, as it has direct impact on light flux on the SiPM. The working principle as well as the single components are described in the following sections.

3.1. Operating principle

A general overview is given by the schematic in Figure 3.1. The test set-up consists of four main functional groups: the temperature stabilisation of the SiPM holder, the light source and light distribution, the measuring instruments, and the control and data acquisition. The light is distributed via optical fibres from the source to the SiPM and the reference detectors.

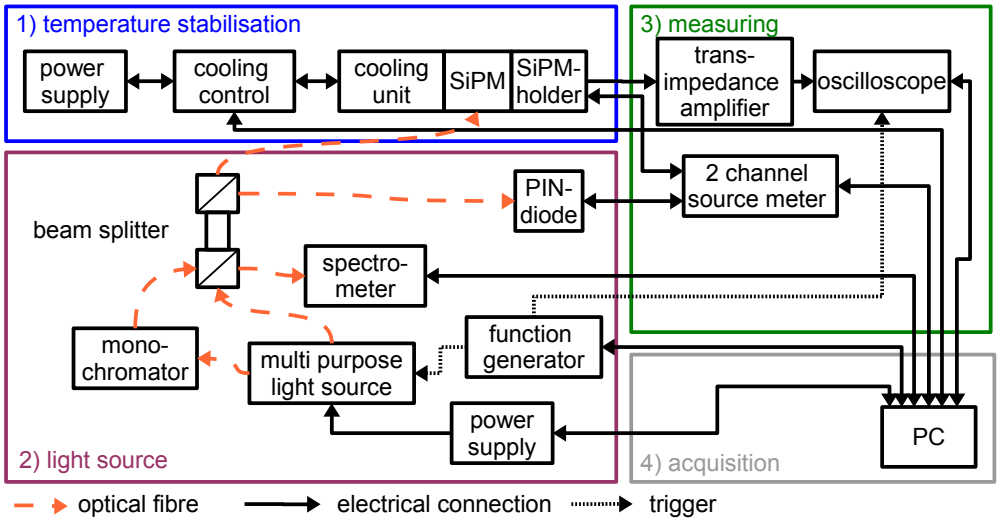

Figure 3.1.: Schematic of the test set-up. The four main functional groups are: the temperature stabilisation around the SiPM holder (No. 1), the light source and light distribution (No. 2), measuring instruments (No. 3), and control and data acquisition (No. 4).

3.2. Multi-purpose light source

The multi-purpose light source (MPLS) is a LED based custom-made light source. The first version has been built in the context of a masters' project [37] and was improved over the course of the project presented in this thesis. It can house up to 32 LED modules. There are two versions of the LED modules: a DC module and a pulser module. The DC modules only house a LED and the module type detection circuit. The DC modules offer tunable continuous light fluxes which can go up to $23\,\gamma/\mathrm{ns}$ for a $1 \times 1\,\mathrm{mm}^2$ area at the position of the SiPM. The voltage is controlled by the external direct current (DC) source (see Section 3.5). An installed series resistor is used to achieve a linear behaviour of the current as a function of the voltage instead of the exponential behaviour above the LED working voltage. The pulser modules contain a custom-built high voltage (HV) pulser capable of driving pulses up-to 130 V with pulse widths of only a few nanoseconds.

To minimise the number of required HV and DC sources, the HV and DC sources are shared among the modules. The LED operational voltage can be switched for each module with electromagnetic relays to ensure only the selected LED is powered up and the other LEDs are protected from a possibly too high current or voltage. The

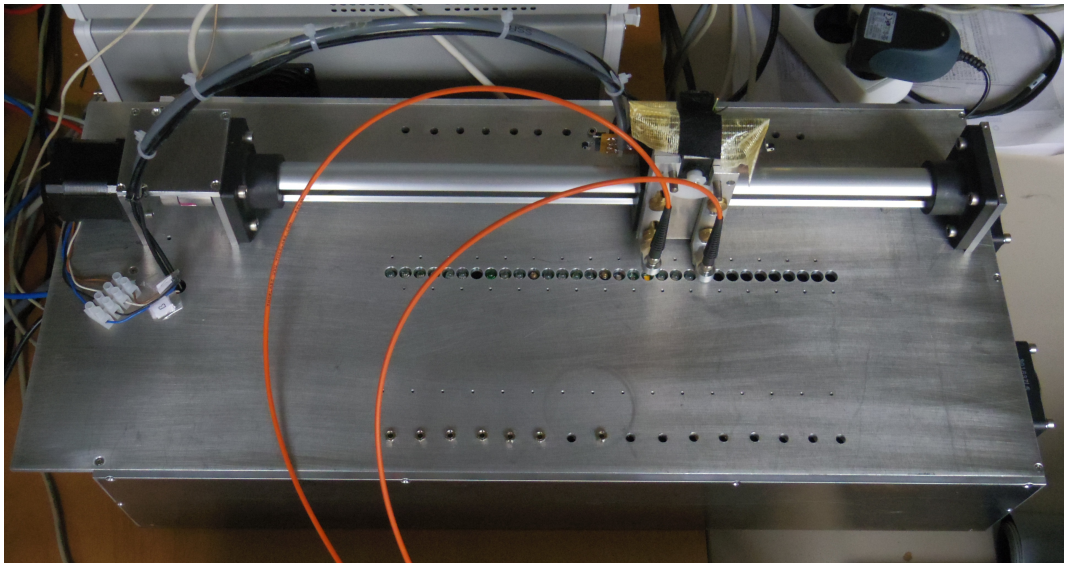

Figure 3.2.: Photo of the multi-purpose light source, clearly visible are the line of up to 32 LEDs and the moveable fibre holder with the two orange optical fibres.

geometrical design of the modules allows for the LEDs to be mounted side by side with minimised distance. The LED modules are placed in a line in such a way that the moveable fibre holder can move one of two fibres above the selected LED. The two fibres allow for coupling the light in two different ways into SiPM and reference detector (see 3.4 for more details). The currently installed LEDs are listed in Table 3.1. They cover the wavelength range from red to UV. The individual spectra are shown in Figures 5.6 and 5.7. The characterisation of the MPLS operation can be found in Section 5.2.1.

LED No.	type	mode	λ / nm	I_{typ} / mA
1	Roithner LED405-03V	pulsed	405	20
2	Roithner LED405-03V	DC	405	20
3	Roithner XSL-355-5E	pulsed	355	25
4	Roithner XSL-355-5E	DC	355	25
5	Vishay TLCY5800	pulsed	591	50
6	Vishay TLCY5800	DC	591	50
7		n.a.		
8	Avago HLMP3519	DC	558	25
9	Avago HLMP-CB14	pulsed	463	30
10	Avago HLMP-CB14	DC	463	30
11	Roithner UVTOP315-BL-TO18	pulsed	315	20
12	Avago HLMP-CE14	DC	506	30
13	Vishay TLHB580	DC	410-470	30
14	Vishay TLDR580	DC	650	30
15	Avago HLMP-CE14	pulsed	506	30
16	Roithner UVTOP335-BL-TO18	pulsed	335	20
17		n.a.		
18	Cree XP-E rot-orange	DC	621	1000
19	Cree XP-G Q2	DC	470-700	1500
20	Nichia NSPG500DS	DC	526	35
21	Nichia NSPY500S	DC	510-650	35
22	Roithner VL420-5-15	DC	420	20
23	Roithner LED440-6-30	DC	440	20

Table 3.1.: Installed LEDs with information on operation mode, peak wavelength for narrow spectra or wavelength range for wide spectra, and typical maximum current.

3.3. Monochromator

The monochromator [38, 39] is used to pick out narrow spectral ranges from the input light. To this end, incoming light from the light source is collimated to a beam of about 1 cm diameter, which is refracted by a blazed grating [40]. This grating creates a stretched spectrum with maximal intensity in the first order. From the resulting stretched spectrum a small range is picked up with a fibre, made out of the material FG400AEA [41] with a diameter of 400 μm, on a translation stage (motorised stage MTS50 [42] with controller TDC001 [43]). Depending on the picked up central wavelength the achievable width ranges from 6 nm to 10 nm full width half maximum (FWHM). Further details can be found in Section 5.2.2.

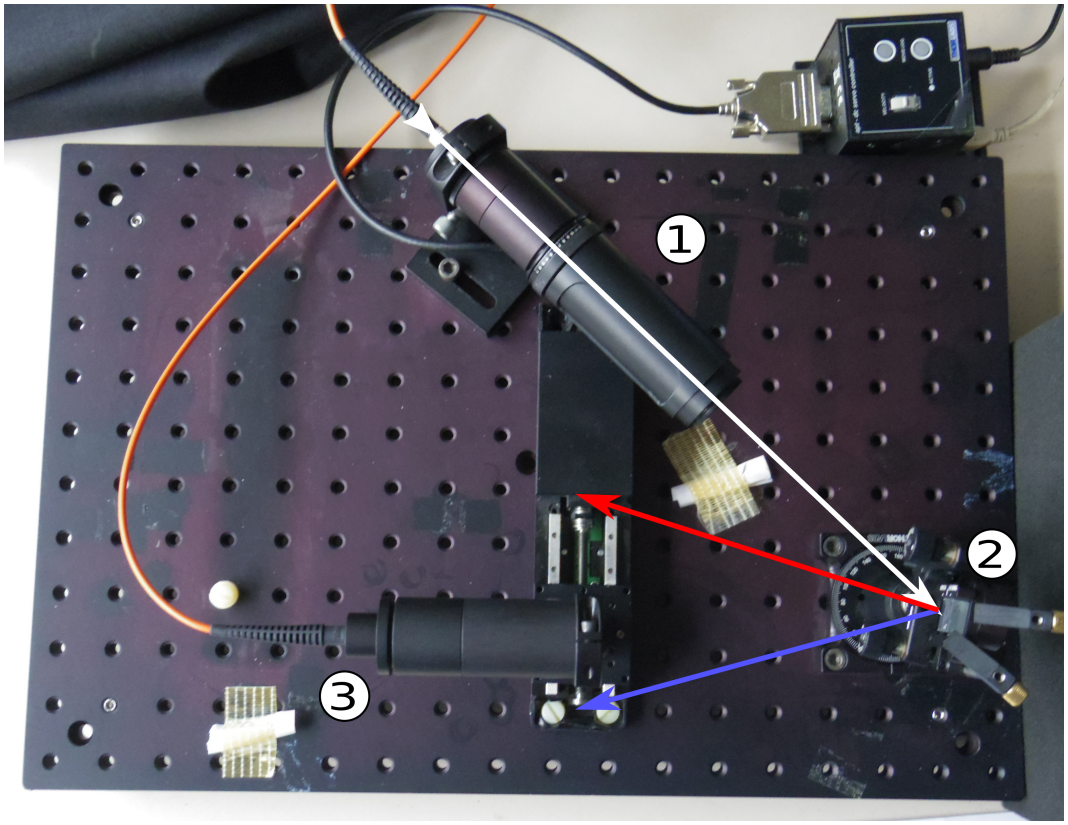

Figure 3.3.: Photo of the monochromator, clearly visible are the input collimator (No. 1), the blazed grating (No. 2) and the moveable pick up (No. 3). The incoming light beam is represented by the white line. After the blazed grating the light is separated into its spectral components. Reddish components are directed towards the red line, while blueish components are direct towards the blue line.

3.4. Light distribution system

The light distribution system (shown in Figure 3.4) is used to merge the two possible light paths (either via the monochromator (No. 1) or directly (No. 2)) and direct them to the three locations, where the light is needed: spectrometer (No. 3), SiPM (No. 4), and PiN photodiode (No. 5) which acts as a reference detector. This is done by using two Polka dot beam splitters [44]. The installed Polka dot beam splitters are silica substrates with metallic reflecting dots on the surface. The size and density of the dots determine the splitting ratio between reflected, transmitted and absorbed photons. The Polka dot beam splitters were chosen over normal beam splitting cubes due to their much better performance at UV wavelengths. For lower light losses all the fibres [41] are coupled with fibre collimators [45] to the beam splitting system.

The output ratio between SiPM port and PiN photodiode port as a function of the wavelength was measured because it is crucial to know the exact ratio for the correct calculation of the flux on the SiPM. Further details are given in Section 5.2.3.

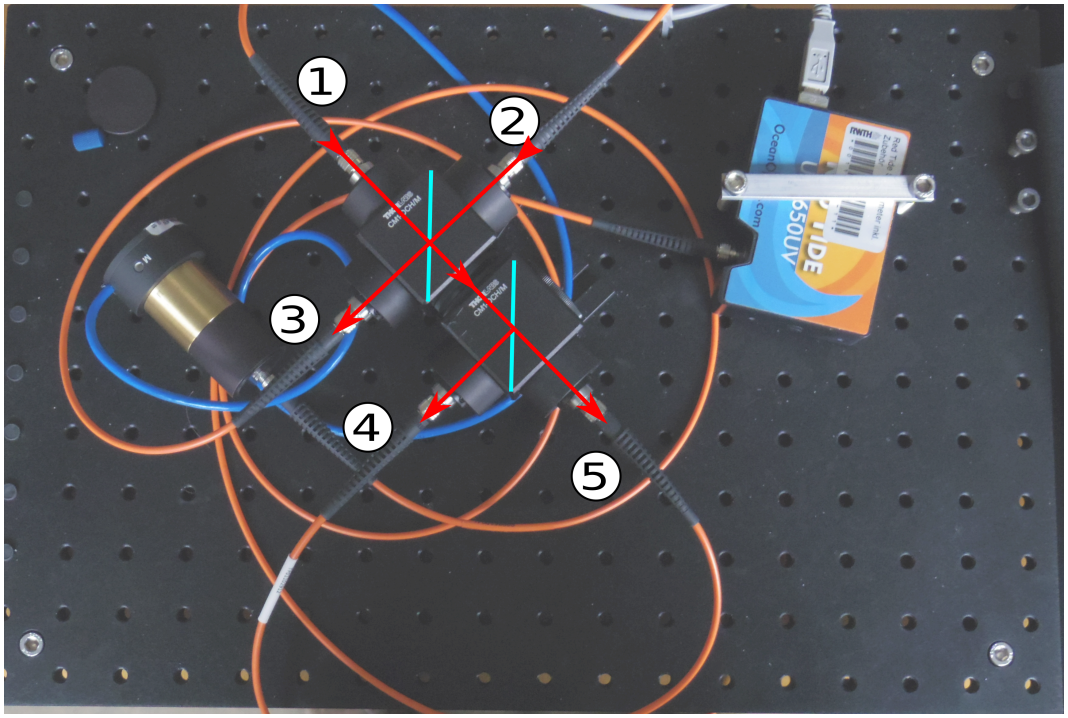

Figure 3.4.: Photo of the beam splitters, on the top left the two input fibres, from the monochromator (No. 1) and directly from the LED (No. 2). From the first beam splitter, one outlet (No. 3) is fed into the spectrometer and the other into the second beam splitter. The outlets of the second beam splitter are fed into the fibres to the reference detector (PiN photodiode) (No. 5) and the SiPM. (No. 4). The beam paths are shown in red. The orientations of the polka dot beam splitters are indicated in cyan.

3.5. Power supply and monitoring

Two four-channel HAMEG HMP4040 [46] power supplies are used for powering all low voltage DC consumers. The stability after the settling time is around 1 mV. Current measurement is possible with a resolution down to 0.1 mA. The current readback is used to obtain the LED current for the DC-mode LEDs.

3.6. Temperature stabilisation

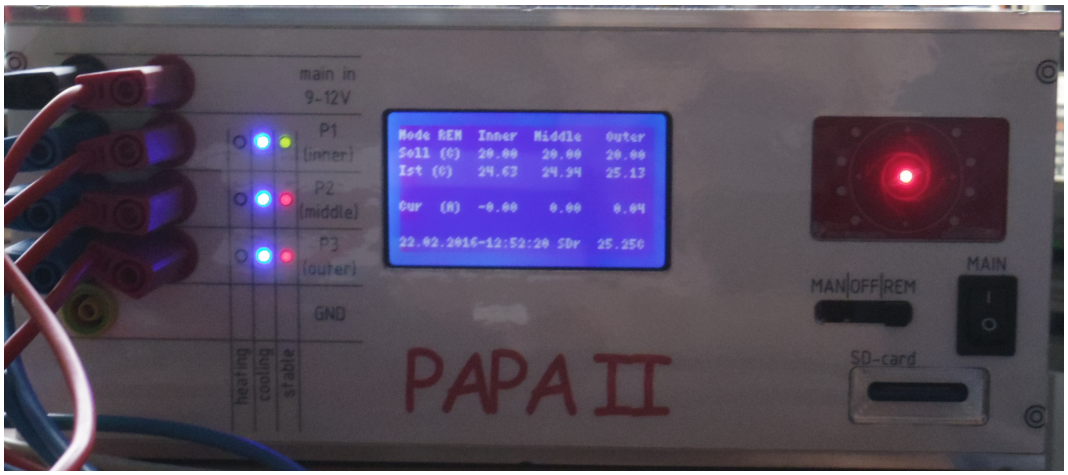

Figure 3.5.: Photo of the Peltier controller PAPA2.

The temperature stabilisation is important for precise measurements. The system called PAPA2, which was built as a part of this thesis, is a triple-stacked Peltier element system with forced airflow on the hot side of the largest Peltier element. It offers great advantages over a simple programmable current source. The controller (shown in Figure 3.5) offers 3 H-bridges[7] to allow for heating and cooling of each of the Peltier elements. The system offers a large temperature range from below $-30\,^{\circ}\mathrm{C}$ to above $60\,^{\circ}\mathrm{C}$. The temperature of the copper cold mass is kept stable to the least significant bit of the installed digital temperature sensors ($\Delta T_{stab} \leq 0.07\,^{\circ}\mathrm{C}$) with the integrated PID controller. The system utilises three out of four channels of the HMP4040 as a current source for the Peltier elements and the fourth channel as the supply for the system itself. The controller offers three main modes of operation: manual, remote, and script-based.

3.7. SiPM quick mount

The custom-made SiPM quick mount is made of copper and is placed in the cold mass (see Figure 3.6). With its spring mount and the gold spring contacts it allows for fast change of SiPMs and offers a good electrical connection to the readout without soldering. The milled enclosure with bayonet fixture offers exactly repeatable positioning and good thermal contact of the SiPM to the cold mass. The exact

[7] A four-transistor circuit, able to invert the current through the load

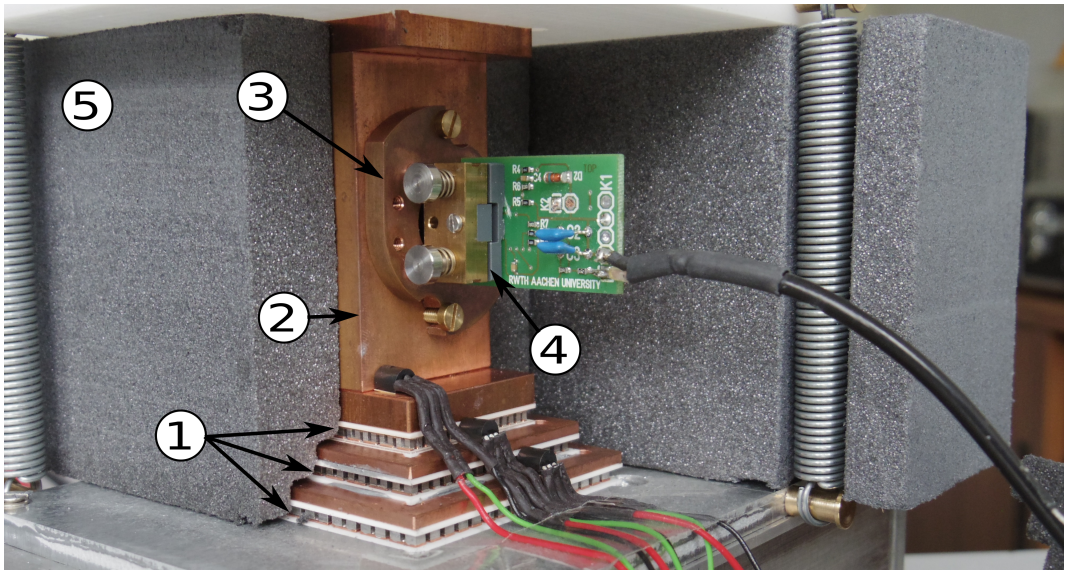

Figure 3.6.: Triple-stacked Peltier elements (No. 1), on top of these the cold mass (No. 2) with the inserted SiPM quick mount (No. 3) with the spring mount (No. 4). The thermal insulation (No. 5) is completely closed during operation.

repositioning is important to ensure the same geometric set-up for each measurement. The distance from the fibre end to the back surface of the SiPM is 59.75 mm. The effective distance is reduced by the distance of the sensitive surface to the back surface of the SiPM. This distance should be found in the technical drawing in the data sheet of the SiPM under study.

3.8. Measuring instruments

Another integral part of the test set-up are the measuring instruments for the digitisation and acquisition of the data from SiPM signals and the reference detector, and for the monitoring of the wavelength. These are described in the following sections.

3.8.1. Oscilloscope

The choice of the oscilloscope was driven by the requirement of both speed and precision, along with sufficient memory depth. Finally an Agilent DSO9204H [47] which offers a sampling rate of 10 GS/s with a hardware resolution of 10 bit and a memory depth of 41M samples was bought.

The oscilloscope is used to capture single signal events. This is done in two different ways. One way is to record long traces with a minimal length of 4.1 ms with 100 ps timestep. These traces can be analysed to obtain single signal events and their timing. However, it is not suited for the accumulation of large trigger counts, due to the fact that most of the recorded data is only baseline and (white) noise. This can be prevented by using a dedicated trigger. This can be the signal coming from the SiPM (self trigger), a copy of the trigger for the LED pulser, or a random trigger, which is implemented but not used in the measurements presented in this thesis. The first option can lead to a bias towards greater signal, thus suppressing the pedestal. The LED trigger will only capture possible signals and will have a small or no pedestal or a desired large pedestal for absolute p.d.e. measurements. The random trigger can be used to capture the pedestal. The triggered modes allow for the utilisation of the segmented memory to capture up to 8192 short traces (typically with 2048 samples each in this set-up) in a single acquisition.

3.8.2. Sourcemeter

The dual-channel sourcemeter (Keithley 2614B [48]) allows for the parallel recording of the currents from SiPM and reference detector (PiN photodiode) while supplying these with their required bias voltages. The measured current can not be used to evaluate single events but can be used as an averaged response from the SiPM and the reference detector. Due to the low current for the reference detector it can be connected with triaxial cable (ground, guard, signal) to keep the leakage current out of the measurement, if it is used with a bias voltage. Alternatively, cables with Teflon as dielectric with a very high resistivity can be used. Details on the concept of triaxial cables can be found in appendix B. Furthermore, triaxial cables offer better shielding against electromagnetic interferences.

3.8.3. Spectrometer

A spectrometer (Ocean Optics USB650 UV-VIS Red Tide) is used to monitor the wavelength of the incident light. The spectrometer uses a combination of mirrors, grating, and line CCD to analyse the incoming light and create a spectrum for the user. It is sensitive over the whole wavelength range of the installed LEDs. It is calibrated and offers a resolution of ~ 0.8 nm with custom-made readout software.

3.8.4. Arbitrary function generator

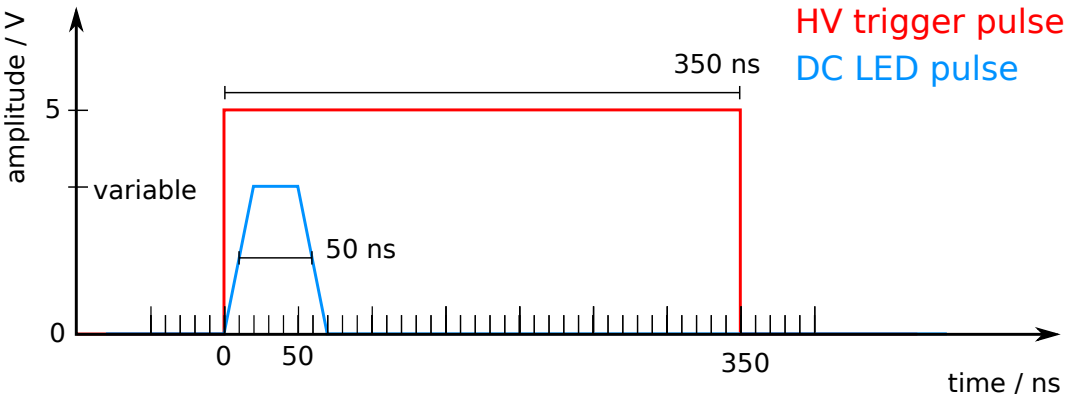

Figure 3.7.: Schematic representation of used trigger pulses. Shown in red the HV trigger pulse with a 5 V amplitude and a pulse duration of 350 ns. Shown in blue the DC LED pulse with variable amplitude, a pulse duration of 50 ns and leading and trailing edge of 20 ns.

For trigger signal generation and for the pulsed mode of DC LEDs an arbitrary function generator (AFG 3252) [49]) is used. When used for triggering the HV pulsed modules a pulse with 5 V amplitude and a width of 350 ns is generated with a repetition frequency of 10 kHz. For pulsing the DC LED modules, a pulse with adjustable amplitude (up to 5 V), 20 ns leading edge, 50 ns pulse width, and 20 ns trailing edge is generated. The typical used repetition frequency in this mode is 1 MHz.

3.9. Electromagnetic shielding

Initially, large noise signals were found in the first test measurements. These signals were analysed and found to be radio, digital television (DVB-T), mobile phone net carrier and wi-fi. Since SiPM signals have similar frequency components, these components cannot easily be filtered out after the measurement. In order to reduce the influence of the environmental electromagnetic radiation on the measurements a metal mesh cage was built around the Peltier cooling unit. A first version was made from aluminium mesh with 2 mm mesh width. An improved version was made from stainless steel mesh with a mesh width of 0.1 mm. The stainless steel version offers better conductivity (no aluminium oxide) and a finer mesh. The effect of the shielding is demonstrated in Section 5.3.3.

4. Software of the Test Set-up

In this chapter the software developed for the testing and operation of the test set-up is described. The software design also included the development of drivers for the proprietary hardware to be able to use it with Scientific Linux 6. Details on the implemented analysis algorithms can be found in Chapter 6.

4.1. Drivers

4.1.1. Motorised stage MTS50 with TDC001

The Thorlabs MTS50 is a high-precision 50 mm translation stage with a servomotor. The Thorlabs TDC001 is a servomotor controller suited for driving the MTS50. It is used in the monochromator to move the pick-up fibre across the spread spectrum. The required command codes and data structures were extracted from recorded USB traffic which was generated by the Windows Active-X software. With the command codes and the data structures a Linux driver was created, which supported all necessary commands for the use in the test set-up. At a later stage of this work, a documentation of the command set was released [50] and it was used to complement the command set implemented in the Linux driver.

4.1.2. Spectrometer USB-650 UV-VIS Red Tide

In this set-up, it is used to monitor the wavelength of the light fed into the beam splitter system. Again, recorded USB data allowed for the extraction of the required commands to operate the spectrometer without the manufacturers software. These commands enable the user to set the integration time and access the raw spectrum data. It was interesting to find the returned data to be more than the 650 enabled pixels stated in the product specifications by the manufacturer [51]. All 2048 channels of the installed CCD can be read, the limitation to 650 is not done in the hardware. Using all pixel yields a better resolution.

4.2. Firmware

The following two hardware objects designed by the author of this thesis and built in the mechanics workshop and the electronics workshop of our institute required the writing of firmware for the embedded microcontrollers.

4.2.1. Peltier controller

The Peltier controller powers the three Peltier elements with individual currents in such a way that the temperature of the cold mass around the SiPM is kept stable at the desired value. The requirements for the controller were: three independent channels, invertible current, PID controlled currents, remote/manual operation, (stand-alone) logging, and displaying the current status. The core functions are running on an Atmel ATmega2560 [52]. One of the core functions is the serial communication with the external power supply to control the currents. Other core functions include the control of the three H-bridges for inverting the current and thus switching between heating and cooling, and (stand-alone) logging to a SD card. Further core functions are the PID controllers for each channel and the status display with LEDs and the LC display. The functions for the easy manual control with a touch pad rely on a Texas Instruments MSP430G2553 [53]. It is used to convert the signals from the passive touch panel to commands and send them via a serial connection to the ATmega2560. This was achieved by modifying a demo application for the MSP430G2553 to fit the needs.
The core control has several additional functions: receive SCPI[8]-style commands from the PC and execute them or pass them to the programmable power supply connected to the PAPA2, allowing for a transparent control of the power supply from the computer if needed. In stand-alone operation mode (without a computer), it is possible to read settings and/or scripts from a SD card and write logging data to the SD card.
All parameters can be viewed in any operation mode and can be modified during manual operation with the touch panel and a menu on the display. The menu is shown, when the proximity sensor has detected an object in front of the touch panel. The menu will disappear after a short time of no activity at the touch panel. While the menu is not shown, real time values of temperatures and currents are shown as can be seen in Figure 4.1. Furthermore there are clearly visible LEDs indicating the state of the temperature regulation for each Peltier stage (heating/cooling, stable).

[8]Standard Commands for Programmable Instruments

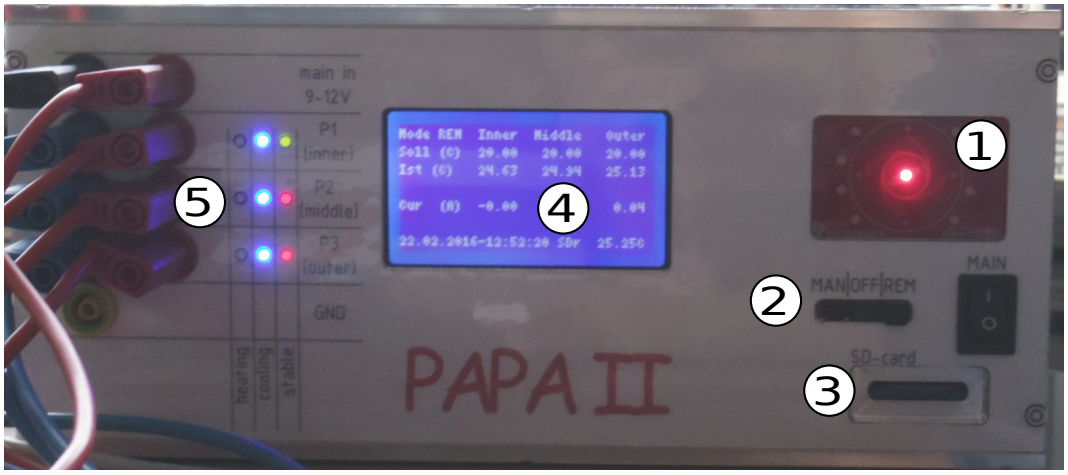

Figure 4.1.: Photo of the Peltier controller PAPA2. The red Touchpanel is used for manual operation (No. 1). The Switch (No. 2) is used for the selection of the operation mode. Next to it the main power switch. The SD card (No. 3) can be used to load scripts and store log data. The display (No. 4) is used displaying the menu as well as the real time data. The status LEDs (No. 5) indicate heating(red on/off), cooling (blue on/off), and stable temperature (green/yes and red/no) for each Peltier stage.

4.2.2. Multi-purpose light source

The controller of the MPLS needs to control the LED modules, the internal HV source, the input selection, the position of the sled, and the position of the fibres. For controlling the 32 LED module slots, the coils of 96 electromagnetic relays need to be driven, these relays are visible in Figure 4.2. These relays are used to ensure a physical disconnection of the HV voltage, the DC voltage, and the trigger for the unused LED modules to prevent any interferences and damages.[9] Due to the physical disconnection it does not matter how many LED modules are installed. Furthermore, three changeover relays are installed for the HV, DC, and trigger source selection (internal/external). To reduce the number of required I/O ports on the embedded Atmel ATmega328 [54] microcontroller, the signals for the relay control pins are buffered with output shift registers. The 32 input lanes of the read back are demultiplexed with input shift registers. Both shift register types are chained, so that only 9 I/O ports[10] are required to control all relays and read back. The read

[9] One could argue, that at least the trigger signal separation could have been done by optocoupler, but a single high speed optocoupler requires around 7.5 mA input current. Resulting in roughly up to 240 mA current required from the pulser for 32 modules. That is more than the pulser can drive.

[10] Required signals: SERIN, RCLK, RCLKEXT, OE, RES, CLK, SEROUT, READRCLK and READLOAD

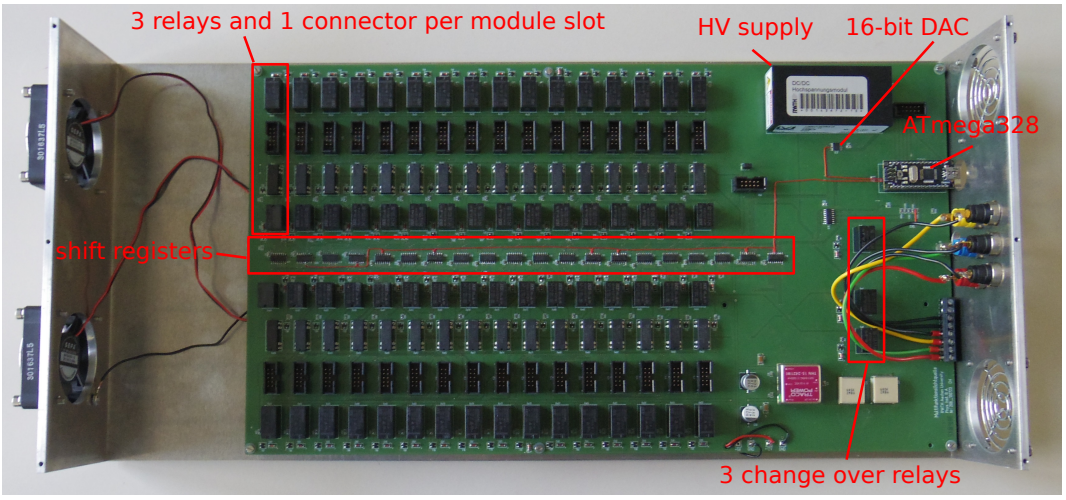

Figure 4.2.: Photo of the main printed circuit board of the multi-purpose light source. For each of the 32 available module slot one group of 3 relays and a 10-pin connector is needed. The relays are controlled by the shift registers in the middle. In the right top corner the adjustable HV supply is visible and below it, the 16-bit DAC for controlling the HV supply. On the right the main controller (ATmega328) and the three changeover relays for the source (internal/external) selection for the trigger, the DC current, and the high voltage.

back allows the user to determine whether a direct current (DC) or a pulsed LED module is installed in that slot. Furthermore an additional 16-bit DAC (digital to analog converter) is needed to control the integrated high voltage supply module with sufficient precision. The lifting and lowering of the fibres requires the microcontroller to drive the servomotor with certain pulse durations. The stepper motor requires bookkeeping of the current position and the control of step, enable and direction signal lines. To ensure a correct position, the stepper motor drives the sled until it hits the near end switch after a reset. Due to the limited port number on the microcontroller both end switches are monitored with only one analog input. To ensure the immediate reaction, namely stopping the movement, this analog port is read in digital mode. This offers fast response to the hitting of an end switch. If one of the switches was hit and the motor has been stopped, a slower analog read is performed to identify the hit end switch. Another safety feature is the check that prior to moving, any lowered fibre is pulled up. For convenience the serial interface has a SCPI[11]-like syntax.

[11] Standard Commands for Programmable Instruments

4.3. Data acquisition

The developed data acquisition system collects the requested data from all used hardware components. This raw data is stored on disk and can be analysed afterwards. Different requirements apply to each part of the test set-up. The data taking with the oscilloscope incorporates a high bandwidth Ethernet connection and fast storage or real time analysis of larger amounts of data. For the sourcemeter a precise estimation of the required measuring time is a great speed up, as it reduces the non-measuring waiting time. For the communication with the TDC001 for the motor stage used in the monochromator it was necessary to have a very close look at possible combination of the expected command confirmation message and the randomly send status message. The random status message could be added at the beginning and/or end of any return message. This then resulted in return messages much longer than expected and required separation and identification of each message. It was solved by scanning the complete incoming data blocks for the headers of each message type.

4.3.1. Typical work flow for data taking

The determination of the breakdown voltage of an SiPM as a function of the temperature is the most important measurement and must be done as one of the first measurements. All further measurements that required the overvoltage as an input parameter use the data from this measurement. The user has to call the main measurement program with the script, that should be executed via command line:

```
main_measure --script ../script/script_abs_pde.txt
```

The script typically contains only a few lines of commands:

```
# Path for output directory
SetPath( ./data/abspde_run_1/ )
# Parameters overvoltage (V), temperature (°C), name tag
MEASURE.ABSPDE( 1.5, 25.0,  t_p25_ov15_ )
# Run the analysis script to create plots
RUN( RunAnalysis.sh )
```

This script collects the raw data required for an absolute p.d.e. measurement. The called analysis script executes the signal analysis described in Chapter 6 and does

the measurement described in Chapter 7.
In the flow chart in Figure 4.3 the simplified chain of actions caused by the above program call is depicted.

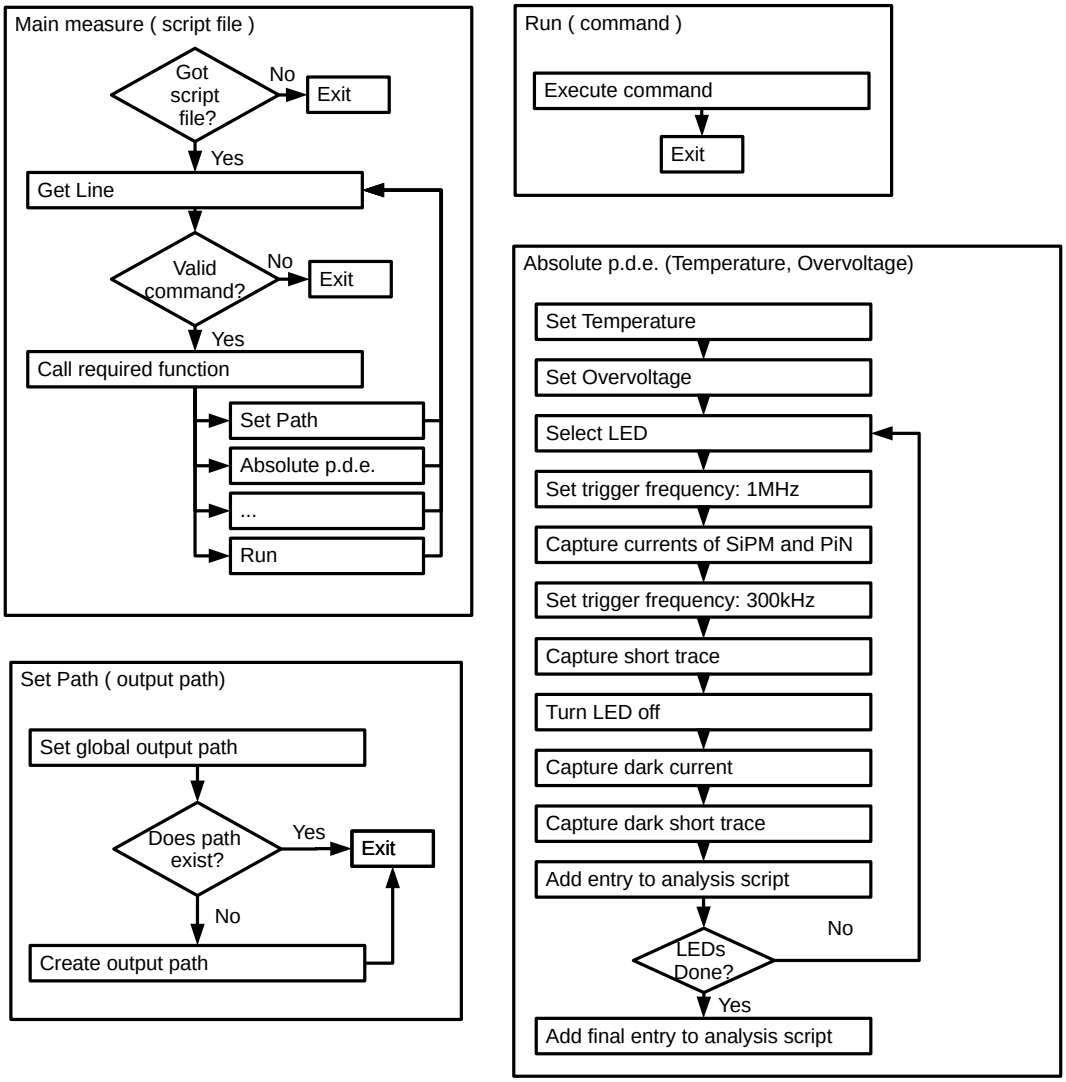

Figure 4.3.: Flow chart for one of the implemented measurements (absolute p.d.e.). The results of this measurement can be found in Section 7.2.8.2.

5. Characterisation of the Test Set-up

In this chapter the single components of the test set-up are characterised in detail. This is required to achieve the best accuracy and precision of the test set-up. Many different properties influence the main parameters of the measurement. Estimating them by manufacturer data sheets is not precise enough, since the single data sheets do not include the interplay/connection of the components. Especially the optical light path contains many places where light can be lost. For the custom-built parts of the test set-up data sheets do not exist. Hence they are all characterised in detail within this thesis. In the following sections the cooling system, the light distribution system, and the powering and signal processing are described.

5.1. Cooling system

There are three main values that describe the performance of the cooling unit: the accessible temperature range, stabilisation time, and the absolute temperature stability. For the performance measurements the ambient temperature was around 25 °C. Pre-amplifier and SiPM were turned on. The pre-amplifier has a power dissipation of around 1.5 W. The power dissipation of the SiPM (< 1 mW) is negligible. The minimum SiPM temperature reachable with the fine stainless mesh used as shield is around −34 °C as can be seen in Figure 5.1. From the same plot one can deduce that working at lowest SiPM temperatures will take some time, due to the limited cooling efficiency. Down to SiPM temperatures of approx −25 °C the required time is reasonable (see Figure 5.2).

For temperature dependency measurements, for example the determination of V_{br} of the SiPM as a function the temperature, a fast SiPM temperature change and (re-)stabilisation is key. The time from a change of the target temperature by 1 °C to a stabilised SiPM temperature is around 1 minute. A full scan from 25 °C to −25 °C and back to 25 °C is shown in Figure 5.3.

Long measurements, such as multiple absolute p.d.e. measurements at multiple wavelengths and/or overvoltages, require a stable temperature over a long time. As shown in Figure 5.4 the temperature is held stable at a value of 25 °C with a deviation of

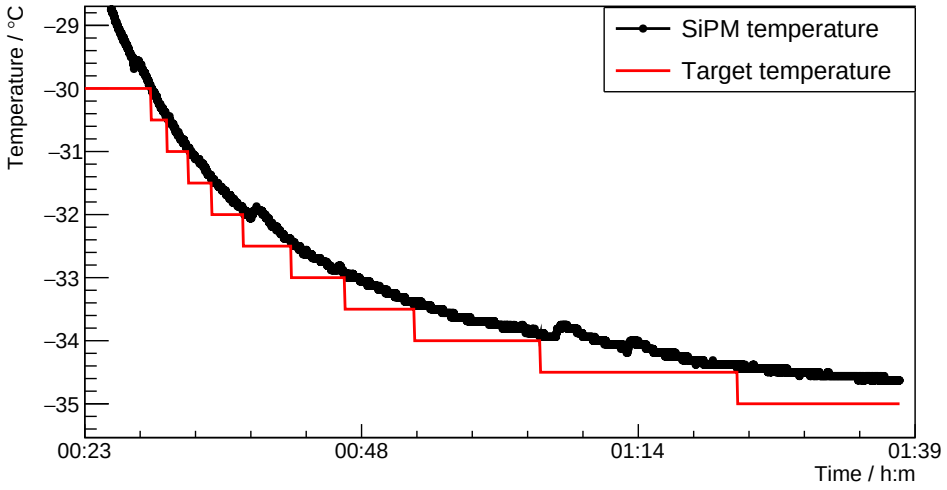

Figure 5.1.: Minimum SiPM temperature that can be reached with PAPA2 is around −34 °C. Going below approx −25 °C will take long time. The data for the first part (< 23 min) is shown in the Figure 5.2.

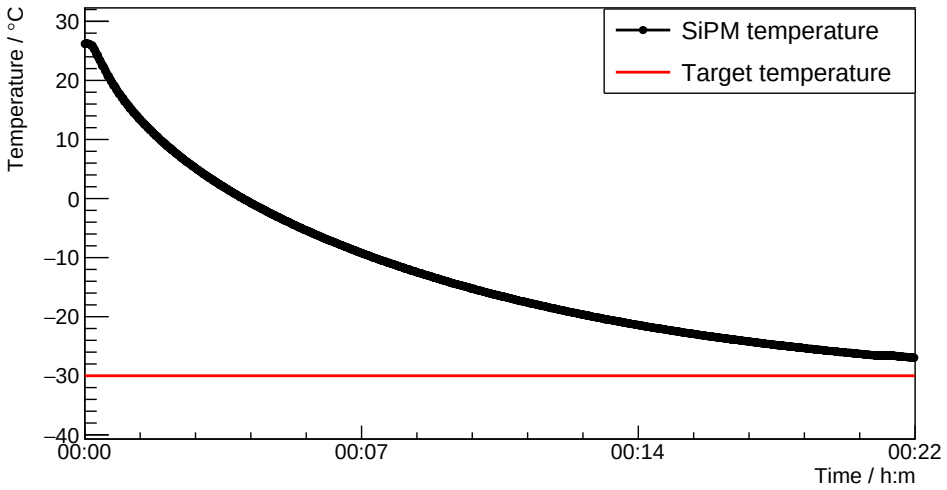

Figure 5.2.: SiPM temperatures down to −25 °C are reachable in a reasonably short time.

at most 0.07 °C, while the ambient temperature varies by approx 3 °C. Additional plots for different target temperatures can be found in appendix A.1.

The absolute stability is affected by the target temperature. At lower target tem-

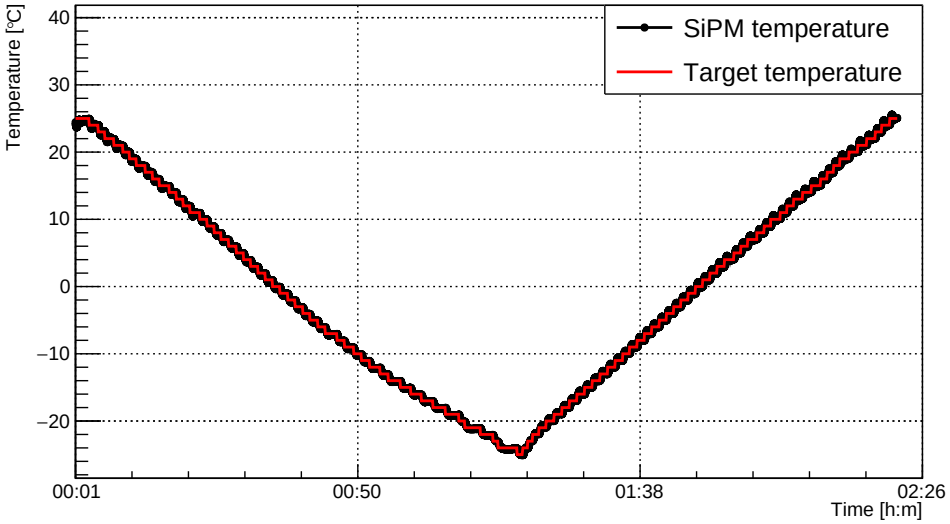

Figure 5.3.: SiPM temperature scan from 25 °C to −25 °C and back. The average time to stabilise the SiPM temperature at the new target temperature is around 1 minute. After stabilisation the next target temperature is set. The target temperature is changed in steps of 1 °C.

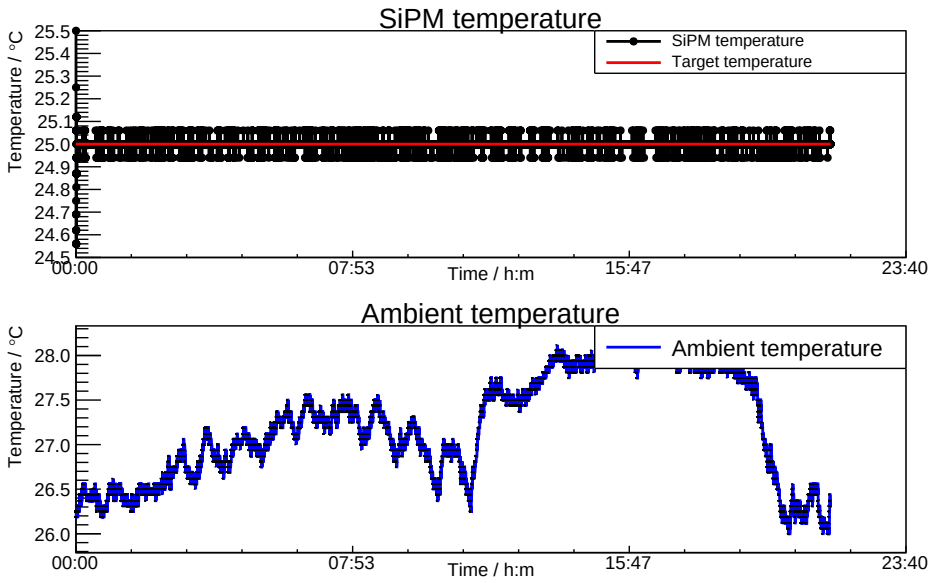

Figure 5.4.: SiPM temperature stability at 25 °C over 21 h. The absolute variation after stabilisation is smaller than 0.07 °C, while the ambient temperature varies by roughly 2 °C.

peratures the spread gets a bit wider, as shown in Figure 5.5. The distributions show

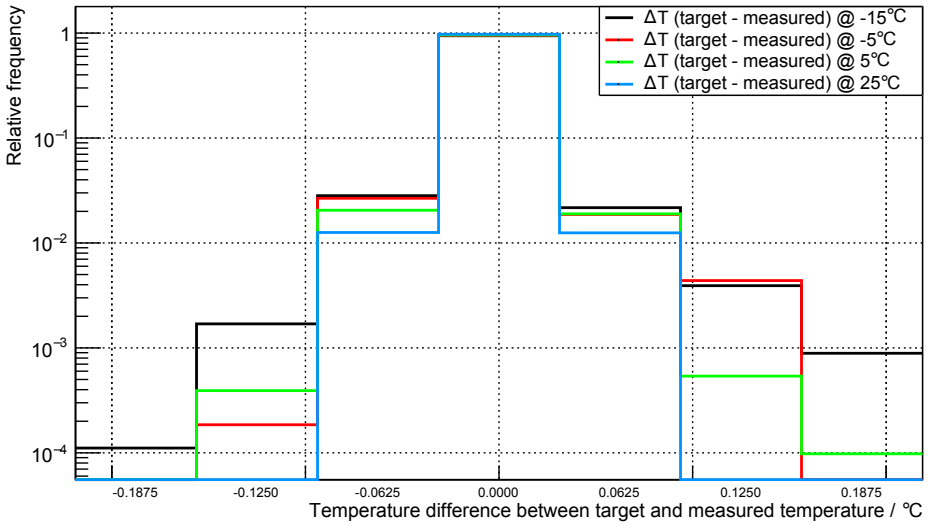

Figure 5.5.: Temperature variation for different target temperatures. The target temperature is stated after the @ in the legend. For lower temperatures the spread gets a little larger, but is still very good. There are no entries outside the shown range.

an asymmetry with more entries on the right. A positive difference (target temperature - measured SiPM temperature) means that the measured temperature is too low. This behaviour is expected, since the system is running at a rather high cooling power to maintain the low temperature. A drop below the target temperature requires a reduction in cooling power, but the heat flow for the temperature increase has to come from the outside through the thick thermal insulation material as at low temperature no active heating is available. If the measured SiPM temperature rises above the target temperature the active cooling can be increased. Hence the different times required for passive heating up and active cooling down lead to the asymmetry.

5.2. Optical system

In the following sections the characterisation of light source and light distribution are described. These component are the heart of the test set-up as an optical test set-up for photon detectors needs a reliable and well understood light source. Since the light is needed for at least two, better three, different detectors at the same time a stable and reliable light distribution system is required.

5.2.1. Multi-purpose light source

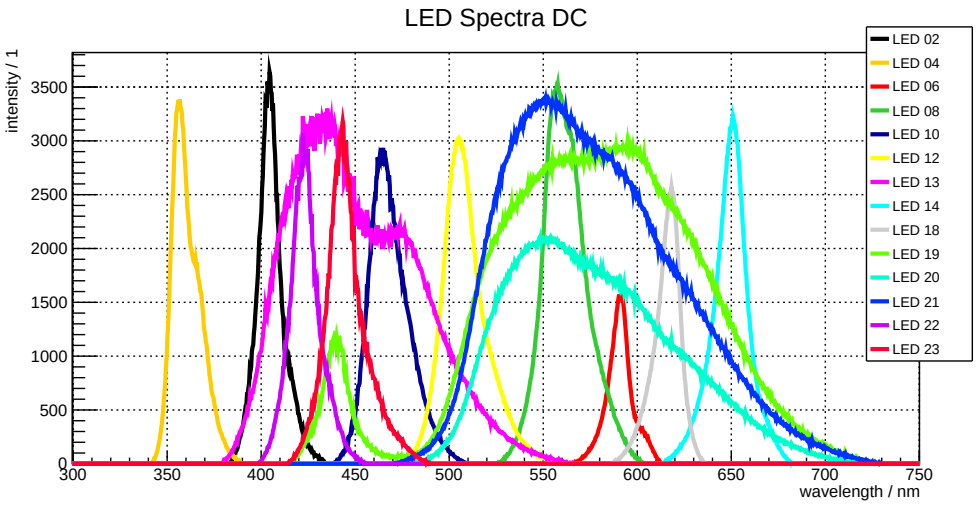

Figure 5.6.: Spectra of installed DC LED modules.

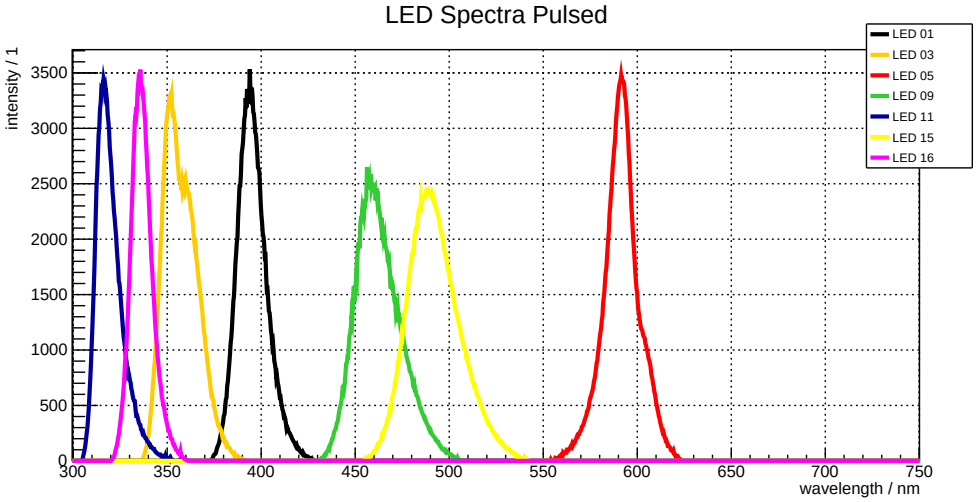

Figure 5.7.: Spectra of installed pulsed LED modules.

The selected LEDs cover a large wavelength range. The spectra of the installed LEDs are shown in Figure 5.6 for the DC LED modules and in Figure 5.7 for the pulser modules. The available light fluxes on SiPM and reference detector, created by these LEDs, are discussed in Section 5.2.6. The temperature dependency of the output of the LEDs has been seen and measured, the variation due to the internal warm up is around 2 % [37]. However, it has no effect on the light flux dependent measurements because the actual light flux (used in the analysis) is determined in each measurement with the reference detector (PiN photodiode).

5.2.2. Monochromator

The monochromator has two variables of interest. One is the dependence of the picked up (output) centre wavelength versus the position of the motorised stage and the other one is the width of the selected part of the spectrum. Both have been measured with the build in spectrometer. For this measurement spectra were recorded at many positions of the motorised stage. Two of these spectra are shown in Figures 5.8 and 5.9. The intensity after the monochromator is so low, that even with an integration time of 1000 ms, the measured intensity is only 100. That is only 1/40 of maximum of the spectrometer. In each of these spectra the position

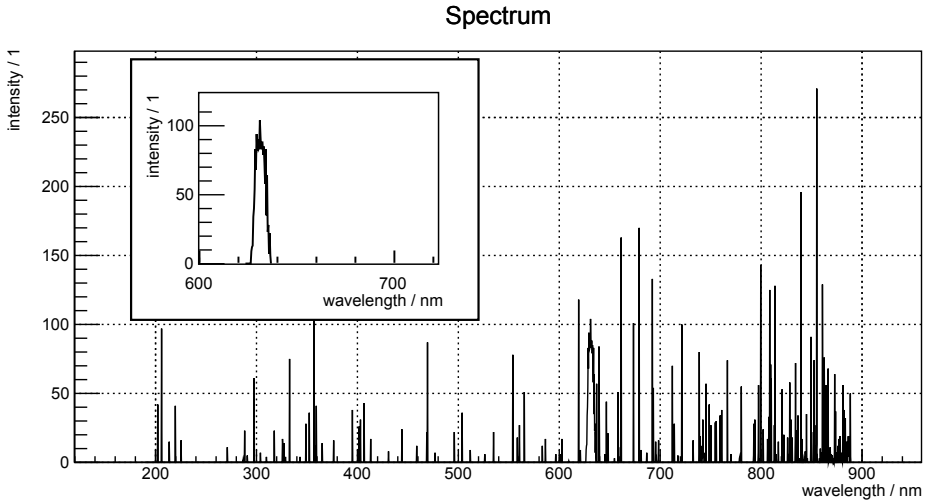

Figure 5.8.: Raw spectrum for LED 21 and monochromator position of 5.0 mm. After removing noise the signal peak in region around 630 nm is better visible. A zoom to the cleaned signal region is shown in the left upper corner. The signal in this example is a smooth peak. The two methods for the width determination yield in this case compatible values around 6.5 nm(FWHM) and 2.9 nm(fit of Gaussian function).

of the maximum intensity is determined after noise cleaning and used as the centre wavelength at the corresponding position, the final result for this is shown in Figure 5.10. Furthermore the width of the peak around the centre wavelength is determined in two ways (FWHM and fit of a Gaussian function). This results in two plots which are shown in Figure 5.11. As can be seen the results vary. This is due to the fact that the recorded signal in the spectra is not always smooth as shown in Figure 5.9. This leads to a larger variation in the blue/UV regime of the spectrum (monochromator position > 25 mm). The overall result with a maximum FWHM smaller than 10 nm

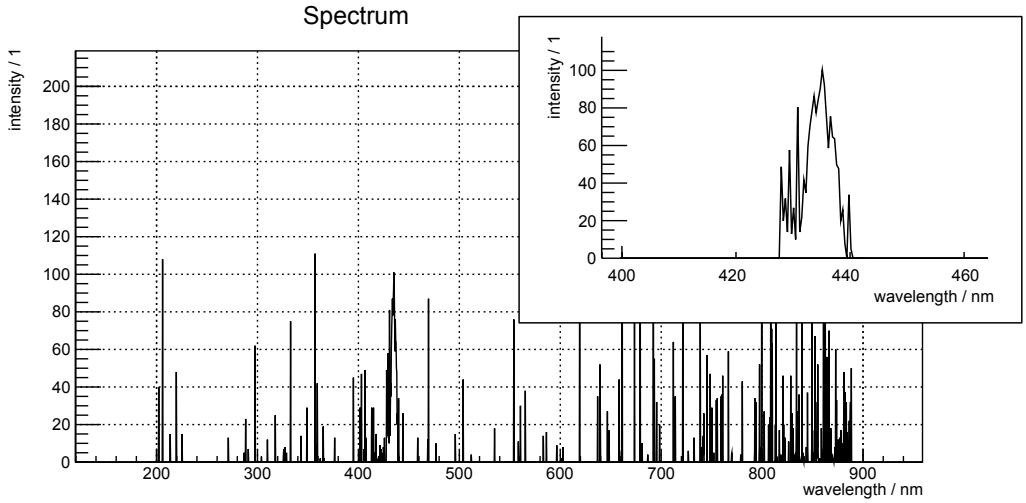

Figure 5.9.: Raw spectrum for LED 2 and monochromator position of 31.0 mm. After removing the noise the signal peak in region around 435 nm is better visible. A zoom to the cleaned signal region is shown in the right upper corner. The intensity after the monochromator is so low, that even with an integration time of 1000 ms, the measured intensity is only 100. That is only 1/40 of maximum of the spectrometer. Additional the peak in this example itself is not a smooth peak. The two methods for the width determination yield in this case values around 8.2 nm(FWHM) and 5.1 nm(fit of Gaussian function), which are not fully compatible.

is still good. That fact that the FWHM is around 6 nm for many makes it even better.

A linear fit to the data from the wavelength versus position plot obtains following result:

$$\lambda(pos) = p_{\text{offset}} + p_{\text{slope}} \cdot pos \quad \text{with} \quad 0\,\text{mm} < pos < 50\,\text{mm} \tag{5.1}$$

$$p_{\text{Offset}} = (668.40 \pm 0.10)\,\text{nm} \tag{5.2}$$

$$p_{\text{Slope}} = (-7.520 \pm 0.004)\,\frac{\text{nm}}{\text{mm}} \tag{5.3}$$

The constants p_{Offset} and p_{Slope} will change, when the monochromator is modified. Any change of the orientation of the collimator or the blazed grating (or the motorstage with the pickup) results in a shifted spectrum along the pick up axis, thus making the presented results obsolete. A recalibration is a very rare event, due to the fact that the components are screwed to the baseplate.

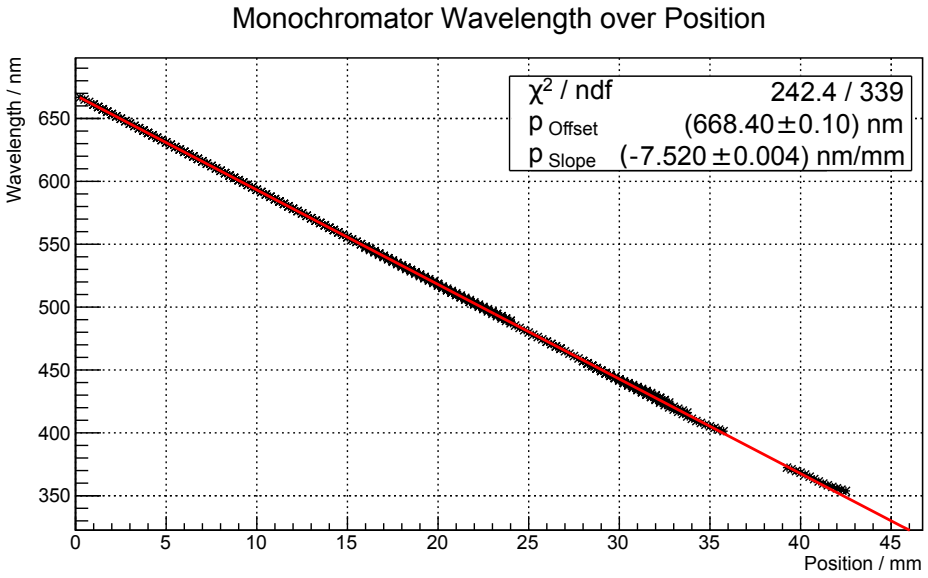

Figure 5.10.: Wavelength versus position of the moveable pick up. The parts where the black points get a little wider spread, is where the LED spectra overlap. The falling and rising edges in the LED spectra result in a very small shift of the picked up wavelength due to the different intensities across the pick up region. The gap around 37 mm is due to the low intensity behind the monochromator which prevents the recording of spectra with sufficient signal height for clean fits. The red line is a linear fit to the data.

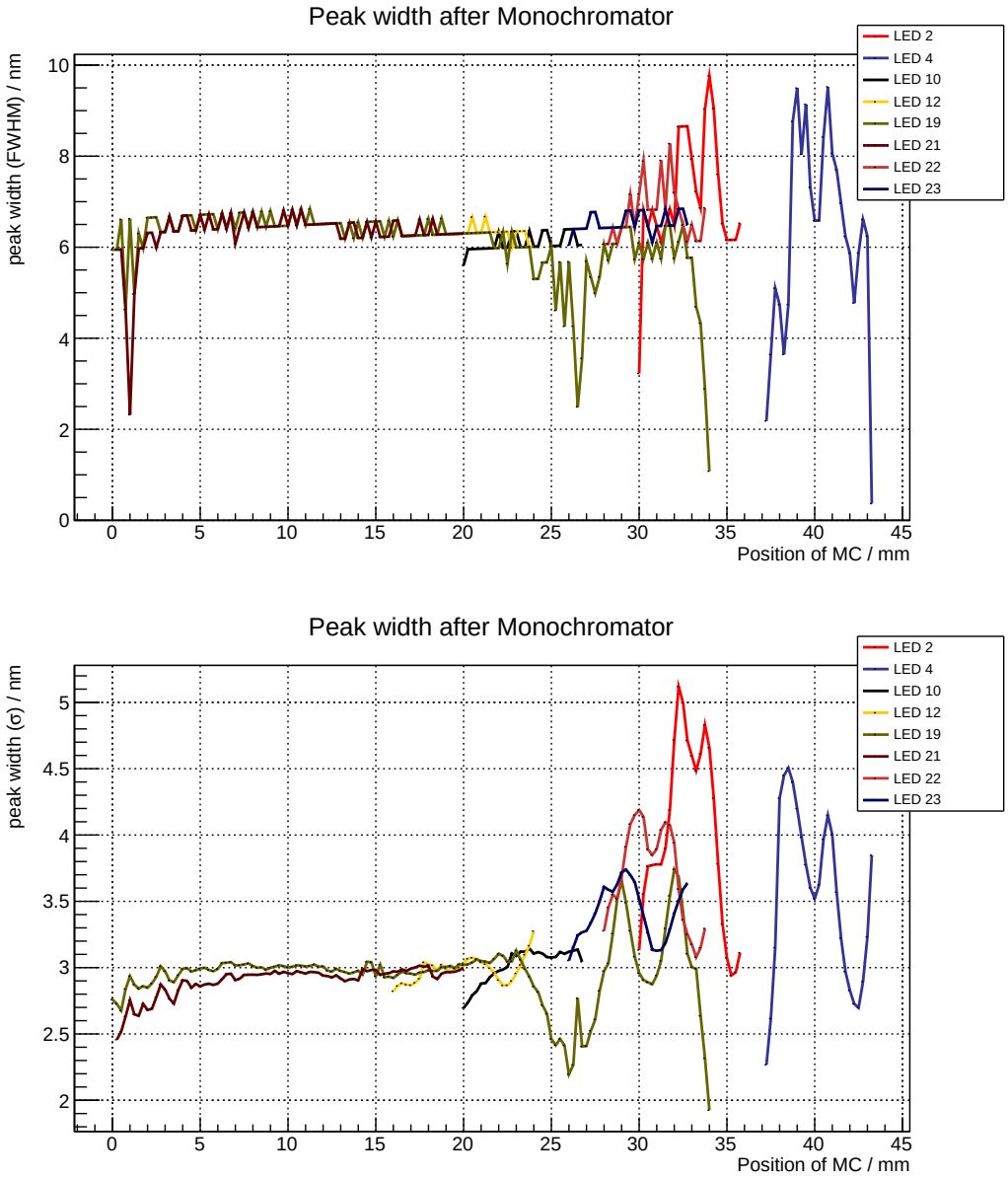

Figure 5.11.: In the upper plot the width (FWHM) of picked up spectrum versus monochromator position is shown. It is discrete due to the usage of the spectrometer CCD bins. In the lower plot the σ of a Gaussian function fitted to the peak at each monochromator position is shown. Up to a position of 25 mm the width of the picked up part of the spectrum is very good. For positions greater than 25 mm the picked up width gets slightly worse. The reason for this have been shown in Figure 5.9. An additional plot with wavelength dependence instead of monochromator position can be found in appendix A.2.

5.2.3. Beam splitters

The light distribution system consisting of two Polka dot beam splitters has been characterised for both light paths in order to calculate the light flux on the SiPM using a reference measurement with the PiN photodiode. The characterisation is necessary because the beam splitters are not ideal. They have wavelength dependent transmission/reflection/absorption ratios. In addition the beam displacement caused

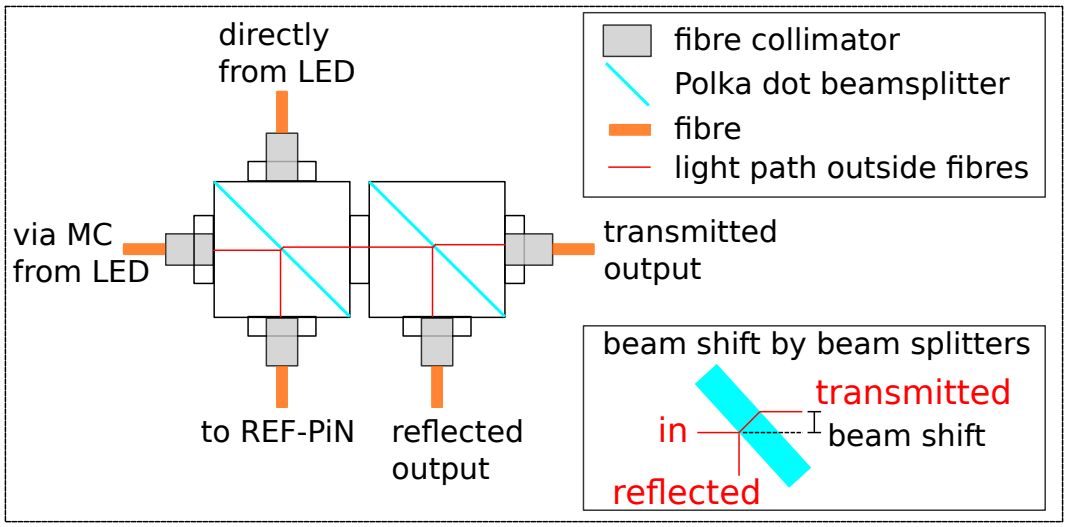

Figure 5.12.: The two inputs are connected directly to the light source or via the monochromator. The reflected output of the first beam splitter (left) is connected now to a second PiN diode, during normal use, this port is connected to the spectrometer. The transmitted port of the first is fed to a second beam splitter (right). The reflected port (normally used for the SiPM) and the transmitted port (normally used for the 818 PiN diode) are connected one at a time to the 818 PiN diode for this characterisation measurement. In the lower right box the beam shift caused by the substrate of the beam splitter is shown. The substrate thickness is around 1.5 mm.

by the silica substrates of the Polka dot beam splitters creates off-centred beams with reference to the fibre collimators. Differently off-centred beams are coupled differently to the connected fibres.

5.2.3.1. Light path via monochromator

For characterising the light path via the monochromator, the measurement was done using the monochromator and LEDs in DC mode. The measurement consists of two runs over seven LEDs and all monochromator positions where signal for the currently actively used LED is existent. Leaving out the monochromator positions with no signal reduces the required time by a factor greater than five. A dark measurement of the currents is done at every measurement point. All the fibre stays firmly connected to the beam splitters. In the first run the fibre from SiPM port (reflected port) of second beam splitter in light path is connected to the 818 PiN diode. In the second run the fibre from the PiN port (transmitted port) of second beam splitter in light path is connected to the 818 PiN diode. The reflected port of the first beam splitter in the light path is fed to a second PiN photodiode (REF-PiN) to be used as an input reference to make sure that the input light flux is the same level in both measurements. Small variations in the input light flux can be corrected for. An example for LED 12 can be found in Figure 5.13. The plots for all seven LEDs can be found in the appendix A.3.

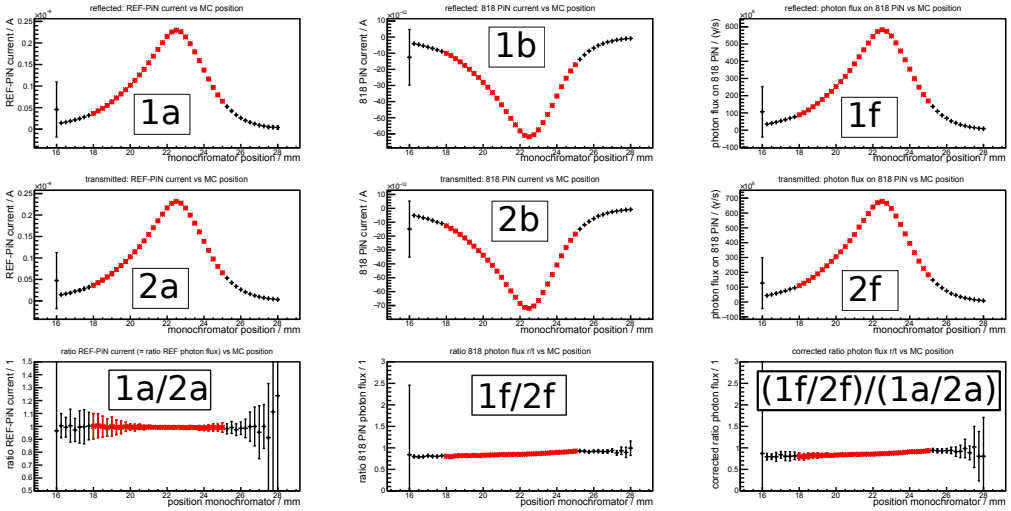

Figure 5.13.: Beam splitter characterisation measurements for LED 12. The plots marked with 1a and 1b are the measured currents of the first run. The plots marked with 2a and 2b are from the second run. With the data from plots 1b and 2b the light fluxes shown in plots 1f and 2f are calculated. The plot 1a/2a is calculated from the data in 1a and 2a. This is the ratio of the REF-PiN currents and thus the ratio of the input light flux, too. The plot 1f/2f is calculated from the data in plots 1f and 2f. This is the ratio of the fluxes at the two output ports of the second beam splitter. The last plot is the (1f/2f)/(1a/2a) plot. It is the ratio at the output ports corrected for a possible change in the input flux. This is the data later used for the calculation of the light flux in all measurements.

The combination of the red marked data points from the seven LEDs yields a smooth curve for the splitting ratio $R_{r/t}$ versus the monochromator position and is shown in Figure 5.14. The shown errors come from the four measurements which are used to calculate the values. All statistical errors from the measurements are propagated to the final error. Systematic errors are cancelled out by the subtraction of the dark measurement. The main contribution to the errors comes from the REF-PiN current measurements, which show sometimes large errors even when the neighbouring point have small errors. These fluctuations are of unknown source. There is no obviously bad (single) data point in the raw data. Furthermore it should be noted that the dark current is larger than the remaining signal current for many measurement points, thus the signal-to-noise ratio is far from optimal.

Due to the use of standard[12] fibres this measurement has to be rerun, if any fibre was loosened and/or reconnected at the beam splitters. Manual tests have shown that the

[12] Core alignment is not perfect. Rotation of the fibre results in a shift of the core.

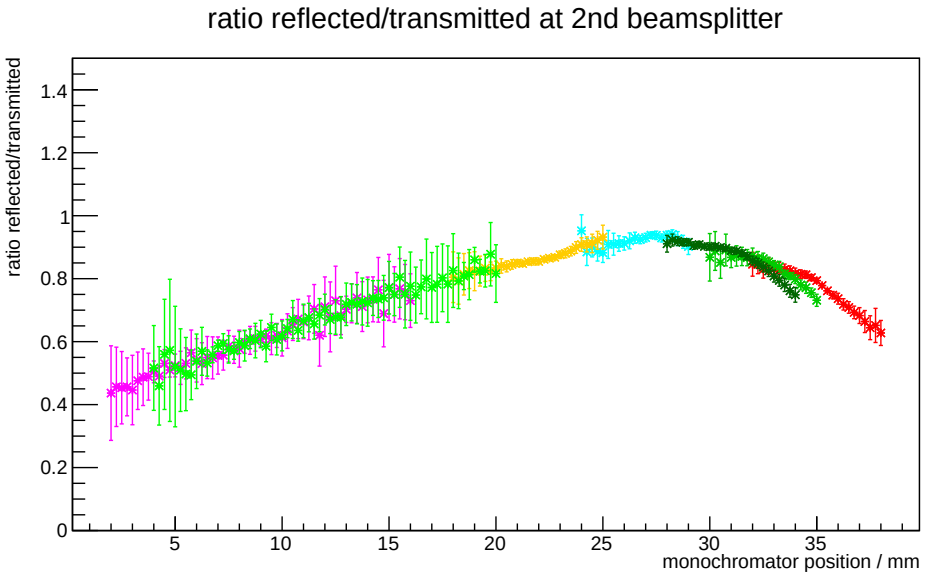

Figure 5.14.: Beam splitter characterisation by combining the seven single measurements to one curve. The errors are propagated from the initial four measurements. A version of this plot with a x-axis depicting the wavelength λ / nm is shown in Figure A.6.

orientation of the fibre has a great effect on the coupling and thus on the light flux through it. A factor between minimum and maximum larger than 4 was observed. As long as the fibres are not moved on the beam splitter side, the result of the measurement is reproducible. The data shown in the ratio curve (Figure 5.14) is used in the calculations of the photon flux on the SiPM from the PiN current measurement at the transmitted port during normal operation. The resulting systematic error for the ratio is shown and discussed in Figure 5.15.

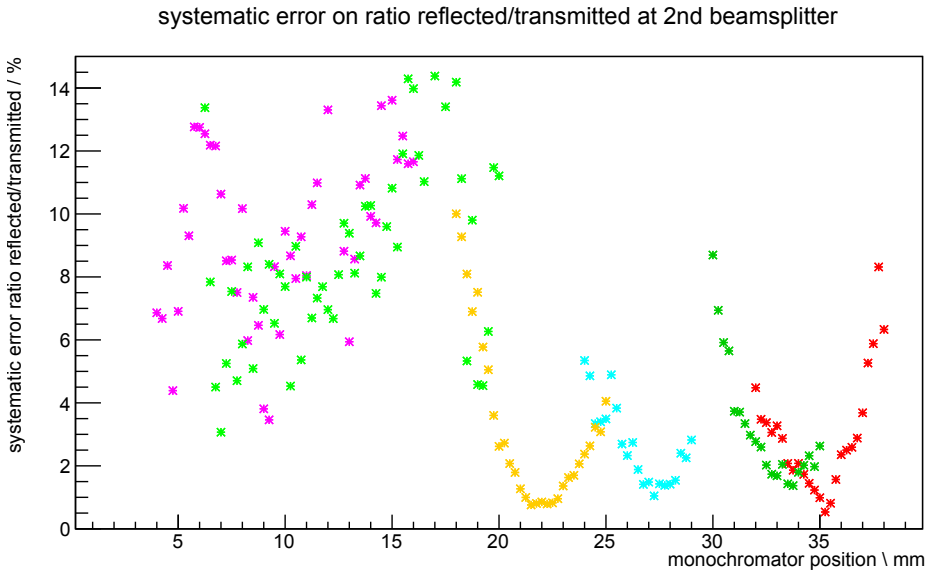

Figure 5.15.: Systematic error for the ratio $R_{r/t}$ when using the monochromator as a function of the position. At the peak wavelength of the LED with the highest intensities, the error is sufficiently low (partly even below 1 %). At the boundaries of the spectra, where the intensity drops down, the error gets quickly larger then 2 %, mainly due to the resolution limit of the sourcemeter. In the red regime, mostly covered by wide band LEDs, the error is varying from 4 % to 14 %. These errors are caused by a unknown noise source, which disturbs the REF-PiN current measurement in some points, as can be seen in Figures A.11 and A.12.

5.2.3.2. Direct light path

For characterising the direct light path, which uses the other input at the first beam splitter and thus have different beam offsets, for each LED the light flux was measured at the two output ports of the 2nd beam splitter. From these measurements the ratio for each LED was calculated and is shown in Table 5.1. The errors on these values are below 0.001, as the direct light path has a much larger light flux compared to the light flux of the monochromator and thus the sourcemeter did not have to operate a the lower resolution limit and returned measurements with much lower relative errors.

LED no.	$R_{r/t}$	LED no.	$R_{r/t}$
1	1.136	13	1.132
2	1.136	14	0.951
3	1.401	15	0.851
4	1.401	16	0.754
5	1.208	17	-
6	1.208	18	1.117
7	-	19	0.944
8	0.930	20	0.951
9	1.140	21	1.136
10	1.140	22	1.032
11	1.014	23	1.035
12	1.014		

Table 5.1.: Values of $R_{r/t}$ for the direct light path. The errors on these numbers are smaller than 0.001 and thus do not affect the quoted digits.

If rebuilding the test set-up, one could use fibre connectors with a notch, so that the orientation is maintained. A caveat of this would be the missing easy tuning option.

5.2.4. Beam intensity profile

Furthermore, the beam intensity profile has to be taken into account because PiN and SiPM do not have the same size and geometry and the distance from fibre end to sensitive surface is not exactly equal, as depicted in Figure 5.16. The beam profile from multimode fibres is Gaussian [55]. In this case a potential shift of the core is negligible. The incident angle of the light on the SiPM is 0 ° with respected to the surface normal of the active area in the centre and goes up to 2.9 ° at a distance of 3 mm from the centre. This small angle is negligible as it does not influence the optical measurements [56]. With a given numerical aperture (NA) of the fibre, the distance between fibre end and PiN surface d_{pin}, the distance between fibre end and SiPM surface d_{sipm}, the PiN active area radius R_{pin}, the edge length a of the quadratic SiPM active area, the ratio $R_{r/t}$ (Figure 5.14 and Table 5.1), and the measured photon flux on the PiN $\Phi_{pin,t}$, the total flux on the SiPM surface can be calculated. According to the definition of the beam diameter in [55] for a multimode

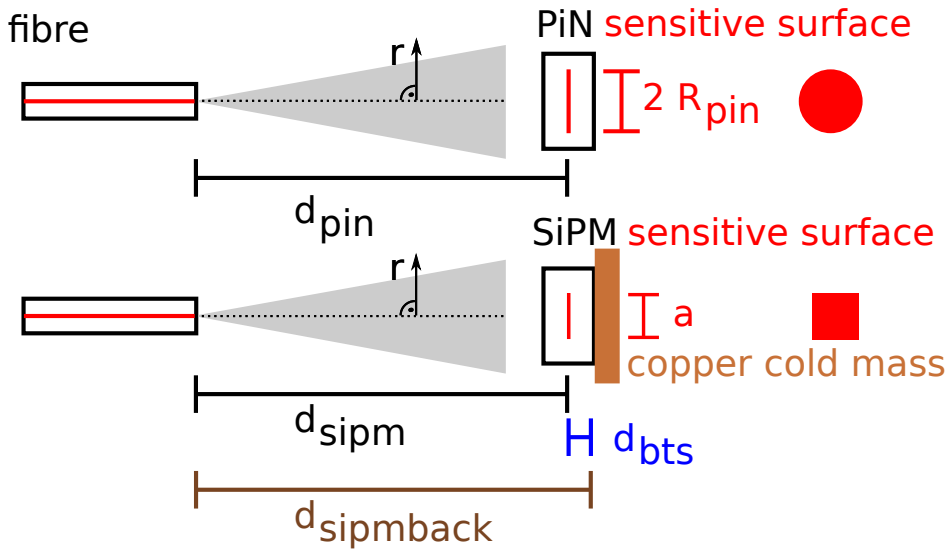

Figure 5.16.: Schematic representation of the different distances and dimension used in the beam profile calculation.

fibre, the beam radius, $r_{0.05}$, in a distance d from the fibre end at which the intensity has dropped to 5% of its maximum value can be described by

$$r_{0.05} = \frac{d \cdot \tan(\sin^{-1}(\mathrm{NA}))}{b} \quad \text{with} \tag{5.4}$$

$$b = \sqrt{-\ln(0.05)} \approx 1.730. \tag{5.5}$$

Only the value of constant b is given in [55]. The expression was found during the derivation, while using the 5% from the definition of the beam diameter. The beam intensity profile is then given by:

$$I(r,d) = I_0(d) \cdot \exp\left(\frac{-r^2}{\sigma^2}\right) \tag{5.6}$$

$$\tag{5.7}$$

where $I_0(d)$ is the maximum intensity in distance d from the fibre end and r is the orthogonal distance to the beam axis. To obtain the σ of the distribution, the following equation is solved:

$$\begin{aligned} I(r_{0.05}, d) &= 0.05 \cdot I_0(d) && (5.8)\\ \Leftrightarrow 0.05 \cdot I_0(d) &= I_0(d) \cdot \exp\left(\frac{-(r_{0.05})^2}{\sigma^2}\right) && (5.9)\\ \Leftrightarrow \ln(0.05) &= \frac{-(r_{0.05})^2}{\sigma^2} && (5.10)\\ \Leftrightarrow \sigma &= d \cdot \tan(\sin^{-1}(\mathrm{NA}))/b^2 && (5.11) \end{aligned}$$

In general the flux at a given distance d on an area A is the integral of the intensity:

$$\Phi_A(d) = \int_A I(r,d)dA = I_0 \cdot \int_A \exp\left(\frac{-r^2}{\sigma^2}\right) dA \tag{5.12}$$

For the calculations of the total flux, the flux on the PiN photodiode with radius $R_{PiN} = 5.6\,\mathrm{mm}$, and the flux on SiPM with size of $a \times a$ in a distance d from the fibre with a numerical aperture NA three integrals are needed:

$$\begin{aligned} F_{full}(d, \mathrm{NA}) &= \int_0^{2\pi}\int_0^{\infty} \exp\left(\frac{-r^2}{[d \cdot \tan(\sin^{-1}(\mathrm{NA}))/b^2]^2}\right) r\, dr\, d\phi && (5.13)\\ &= \frac{\pi \cdot d^2 \cdot \mathrm{NA}^2}{b^4 \cdot (1-\mathrm{NA}^2)} && (5.14)\\ F_{pin}(d, \mathrm{NA}) &= \int_0^{2\pi}\int_0^{R_{pin}} \exp\left(\frac{-r^2}{[d \cdot \tan(\sin^{-1}(\mathrm{NA}))/b^2]^2}\right) r\, dr\, d\phi && (5.15)\\ &= \frac{\pi \cdot d^2 \cdot \mathrm{NA}^2}{b^4 \cdot (1-\mathrm{NA}^2) \cdot \left(1 - \exp\left(\frac{b^4(\mathrm{NA}^2-1)\cdot R_{pin}^2}{d^2 \cdot \mathrm{NA}^2}\right)\right)} && (5.16)\\ F_{sipm}(d, \mathrm{NA}, a) &= \int_{-a/2}^{a/2}\int_{-a/2}^{a/2} \exp\left(\frac{-\sqrt{x^2+y^2}^2}{[d \cdot \tan(\sin^{-1}(\mathrm{NA}))/b^2]^2}\right) dx\, dy && (5.17)\\ &= \frac{\pi \cdot d^2 \cdot \mathrm{NA}^2}{b^4 \cdot (1-\mathrm{NA}^2)} \cdot \mathrm{erf}\left(\frac{\frac{a}{2} \cdot b^2 \cdot \sqrt{1-\mathrm{NA}^2}}{d \cdot \mathrm{NA}}\right)^2 && (5.18) \end{aligned}$$

During the calibration the light fluxes on the PiN photodiode at the reflected port ($\Phi_{pin,r}$) and the transmitted port ($\Phi_{pin,t}$) have been measured to calculate the ratio $R_{r/t}$. It should be noted that the factor $R_{r/t}$ is wavelength dependent. During nor-

mal measurements only $\Phi_{pin,t}$ can be measured and used to calculate the maximum intensity at the reflected port $I_{0,r}(d)$:

$$\begin{aligned}
\Phi_{pin,r} &= \Phi_{pin,t} \cdot R_{r/t}(\lambda) && (5.19)\\
\Phi_{pin,r} &= I_{0,r}(d_{pin}) \cdot F_{pin}(d_{pin}, \mathrm{NA}) && (5.20)\\
\Phi_{pin,t} &= I_{0,t}(d_{pin}) \cdot F_{pin}(d_{pin}, \mathrm{NA}) && (5.21)\\
I_{0,r}(d_{pin}) &= I_{0,t}(d_{pin}) \cdot R_{r/t}(\lambda) && (5.22)\\
&= \frac{\Phi_{pin,t}}{F_{pin}(d_{pin}, \mathrm{NA})} \cdot R_{r/t}(\lambda) && (5.23)\\
& && (5.24)
\end{aligned}$$

With the known $I_{0,r}$ the total flux $\Phi_{total,r}$ out of the fibre towards the SiPM at the reflected port can be calculated:

$$\begin{aligned}
\Phi_{total,r} &= I_{0,r}(d_{pin}) \cdot F_{full}(d_{pin}, \mathrm{NA}) && (5.25)\\
&= \frac{\Phi_{pin,t} \cdot R_{r/t}(\lambda)}{F_{pin}(d_{pin}, \mathrm{NA})} \cdot F_{full}(d_{pin}, \mathrm{NA}) && (5.26)\\
& && (5.27)
\end{aligned}$$

With $\Phi_{total,r}$ we can calculate the $I_{0,r}(d_{SiPM})$ at the distance of the SiPM :

$$\begin{aligned}
I_{0,r}(d_{sipm}) &= \frac{\Phi_{total,r}}{F_{full}(d_{sipm}, \mathrm{NA})} && (5.28)\\
&= \frac{\Phi_{pin,t} \cdot R_{r/t}(\lambda)}{F_{pin}(d_{pin}, \mathrm{NA})} \cdot \frac{F_{full}(d_{pin}, \mathrm{NA})}{F_{full}(d_{sipm}, \mathrm{NA})} && (5.29)\\
&= \frac{\Phi_{pin,t} \cdot R_{r/t}(\lambda)}{F_{pin}(d_{pin}, \mathrm{NA})} \cdot \frac{d_{pin}^2}{d_{sipm}^2} && (5.30)\\
& && (5.31)
\end{aligned}$$

Finally, we can calculate the flux in the SiPM:

$$\begin{aligned}
\Phi_{sipm}(d_{sipm}, d_{pin}, \mathrm{NA}, a) &= F_{sipm}(d_{sipm}, \mathrm{NA}, a) \cdot I_{0,r}(d_{sipm}) && (5.32)\\
&= \frac{\mathrm{erf}\left(\frac{a \cdot b^2 \cdot \sqrt{1-NA^2}}{2 \cdot d_{sipm} \cdot NA}\right)^2 \cdot \Phi_{pin,t} \cdot R_{r/t}(\lambda)}{1 - \exp\left(\frac{-b^4 \cdot (1-\mathrm{NA}^2) \cdot R_{pin}^2}{d_{pin}^2 \cdot \mathrm{NA}^2}\right)} && (5.33)\\
&= c_{geom} \cdot \Phi_{pin,t} \cdot R_{r/t}(\lambda) && (5.34)\\
& && (5.35)
\end{aligned}$$

where c_{geom} is:

$$c_{geom} = \frac{\operatorname{erf}\left(\frac{a \cdot b^2 \cdot \sqrt{1-NA^2}}{2 \cdot d_{sipm} \cdot NA}\right)^2}{1 - \exp\left(\frac{-b^4 \cdot (1-\mathrm{NA}^2) \cdot R_{pin}^2}{d_{pin}^2 \cdot \mathrm{NA}^2}\right)} \tag{5.36}$$

The numerical aperture NA of the used fibre material FG400AEA [41] is stated to be $= 0.22 \pm 0.002$ [57]. The distance from the fibre end to the PiN photodiode d_{pin} was calculated from the measured distance fibre end to PiN photodiode casing and the given distance from the casing to the sensitive surface and resulted in a value $d_{pin} = 59.75 \pm 0.05\,\mathrm{mm}$. The distance $d_{sipmback}$ was directly measured to be $59.75 \pm 0.05\,\mathrm{mm}$. The distance d_{bts} from the backside of the SiPM to the sensitive surface was taken from the technical drawings in the data sheets. The distance d_{sipm} required for the calculation is $d_{sipmback} - d_{bts}$. With the determined values for the test set-up this leads to a single number for c_{geom} for different SiPMs, some values are shown in Table 5.2. If the distance d_{bts} is given directly in the datasheet, the given values for distance and tolerance are taken for the table. If it is not state directly, the distance d_{bts} is calculated from other given distances and the tolerance given in the table is the sum of all tolerances of the distances required for the calculation.

size (a) / mm	type	d_{bts} / mm	tolerance / mm	c_{geom}
1	SMD	0.55	0.25	0.02015 ± 0.00038
1	ceramic	1.00	0.20	0.02046 ± 0.00035
1.3	SMD	0.55	0.25	0.03386 ± 0.00057
1.3	ceramic	1.00	0.20	0.03438 ± 0.00064
3	SMD	1.15	0.25	0.1730 ± 0.0030
3	ceramic	1.55	0.40	0.1752 ± 0.0039
6	SMD	1.15	0.30	0.5590 ± 0.0072
6	ceramic	1.20	0.30	0.5597 ± 0.0072

Table 5.2.: Values for c_{geom} for different Hamamatsu SiPMs. The errors are calculated by combining the given tolerances/measurement uncertainties to achieve the minimum and maximum values. The largest deviation from the nominal values is stated as the error.

5.2.5. Reference light detector

The reference detector is a calibrated Newport 818 PiN photodiode [58]. The PiN photodiode is used without the accompanying OD3 filter. With the NIST[13] traceable

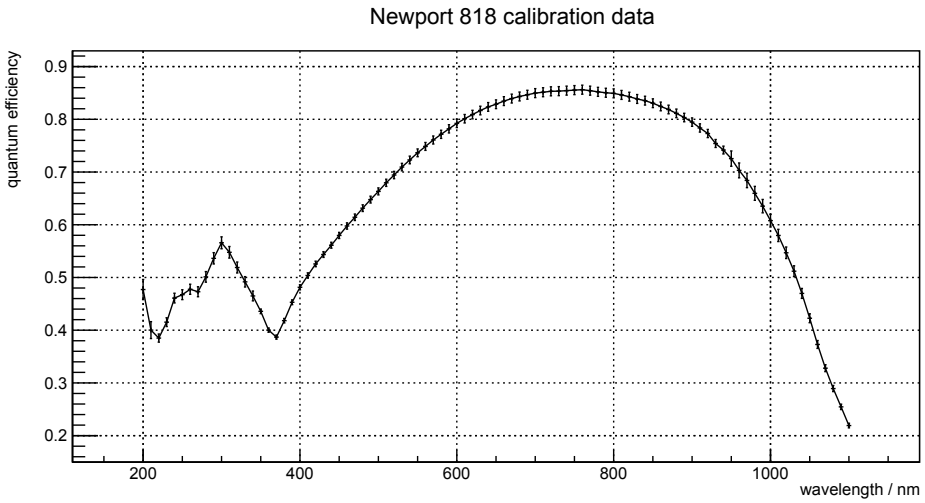

Figure 5.17.: Calibration data used for the calculation of the photon flux on the PiN photodiode Newport 818 without the OD3 attenuator from the currrent measurement. In the plot the quantum efficiency versus the wavelength is shown.

calibration data shown in Figure 5.17, the measured photocurrent I_{photo}, and the measured dark current I_{dark}, the number of photons ($\dot{n}_\gamma$) on the active area of the PiN photodiode per second or per pulse for pulsing frequency f can be calculated:

$$\dot{n}_\gamma(I_{photo}, I_{dark}, \lambda) \quad / \quad (1/\mathrm{s}) \quad = \quad \frac{I_{photo} - I_{dark}}{QE(\lambda)} \cdot \frac{1}{e} \tag{5.37}$$

$$\dot{n}_\gamma(I_{photo}, I_{dark}, \lambda, f) \quad / \quad (1/\mathrm{pulse}) \quad = \quad \frac{I_{photo} - I_{dark}}{QE(\lambda)} \cdot \frac{1}{f} \cdot \frac{1}{e} \tag{5.38}$$

$$\Phi_{pin,t} \quad = \quad \dot{n}_\gamma, \tag{5.39}$$

where e is the elementary charge. The value of $\dot{n}_\gamma$ is used for the flux on the PiN photodiode ($\Phi_{pin,t}$) in the calculations in Section 5.2.4.

5.2.6. Light flux characterisation

The light flux from the multi-purpose light source has been characterised before using it in measurements. With the obtained data the function for requesting a certain light flux works much faster, as the upper and lower limits are known. And from the curves a good starting point for tuning can be found. The characterisation is done for DC

[13] National Institute of Standards and Technology

and pulsed LED modules. Furthermore an external pulse mode[14] for the DC-LED modules is characterised. The resulting plots are similar to the one shown in Figure 5.18. The plots for all LED modules can be found in the appendix A.4.

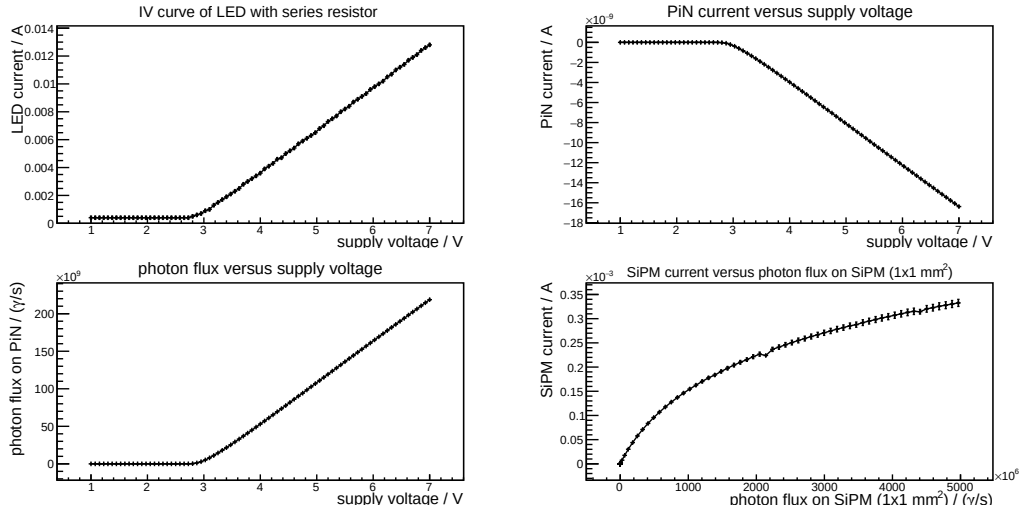

Figure 5.18.: Characterisation measurement results for LED 2 in DC mode. The shown data is raw data. No filtering of outliers has been applied.

5.3. Powering and signal processing

In the following sections the signal processing, shielding, and the powering are described.

5.3.1. SiPM amplifier

There are two ways of connecting the SiPM to the oscilloscope. The first option is to use a passive coupling capacitor. This results in a gain of 1.0. The second option is to use an transimpedance amplifier. This yields a gain of ~ 15. Both options are available for the test set-up and require only minimal manual efforts (two screws), for switching the printed circuit boards. The SiPM HV supply and the signal cable have plug connectors for tool-less exchange.

[14] This requires a manual change of a cable, swapping the DC source for a pulsed source with much lower voltages than the internal HV pulser

5.3.2. Power supply for SiPM

The voltage can be set with an absolute accuracy[15] of 65 mV. This absolute accuracy equates to a variation of the breakdown voltage due to a temperature change of $\sim 1\,\mathrm{K}$ for an older SiPM model (e.g. Hamamatsu S10362 series). The repeatability and stability during the measurements is around $\pm 1\,\mathrm{mV}$. This value corresponds to a temperature change of $\sim 0.015\,\mathrm{K}$, which is less than the achieved temperature stability. Hence the sourcemeter is not the limiting stability factor in the test set-up.

5.3.3. Electromagnetic shielding

The electromagnetic shielding was installed and tested in two ways to demonstrate its effect. The test was done with a Spectrum Analyzer R&S FSH4 model 24 [59] and an antenna placed inside the cage. The spectrum from 100 kHz to 3.6 GHz was recorded inside and outside of the shielding. The recorded spectra are shown in Figure 5.19. Furthermore, two finer binned spectra were recorded up to 500 MHz, shown in Figure 5.20. From the spectra it is clearly visible, that most of the noise is blocked by the shielding. This measurement only shows the effect of the stainless steel mesh cage.
The second method demonstrates the effect of the shielding with the cage on the real baseline signal. To this end, two measurements are taken, one with and one without shielding. The difference in the Fast Fourier Transform (FFT) and the baseline width is clearly visible in the oscilloscope screen shots shown in Figures 5.21 and 5.22.
The noise sources are for example: analog radio ($< 110\,\mathrm{MHz}$), digital terrestrial radio (T-DAB: $175 - 230\,\mathrm{MHz}$), digital terrestrial television (DVB-T: 514 MHz, 602 MHz, and 706 MHz), mobile net carrier (GSM 900 'D-Netz' $870 - 960\,\mathrm{MHz}$, GSM 1800 'E-Netz' $1710 - 1880\,\mathrm{MHz}$, and UMTS $2110 - 2200\,\mathrm{MHz}$) and the ISM band (WLAN, Blue tooth, etc. $2400 - 2500\,\mathrm{MHz}$).

[15] Keithley 2614B : 200 V range : 0,02% of range +50 mV.

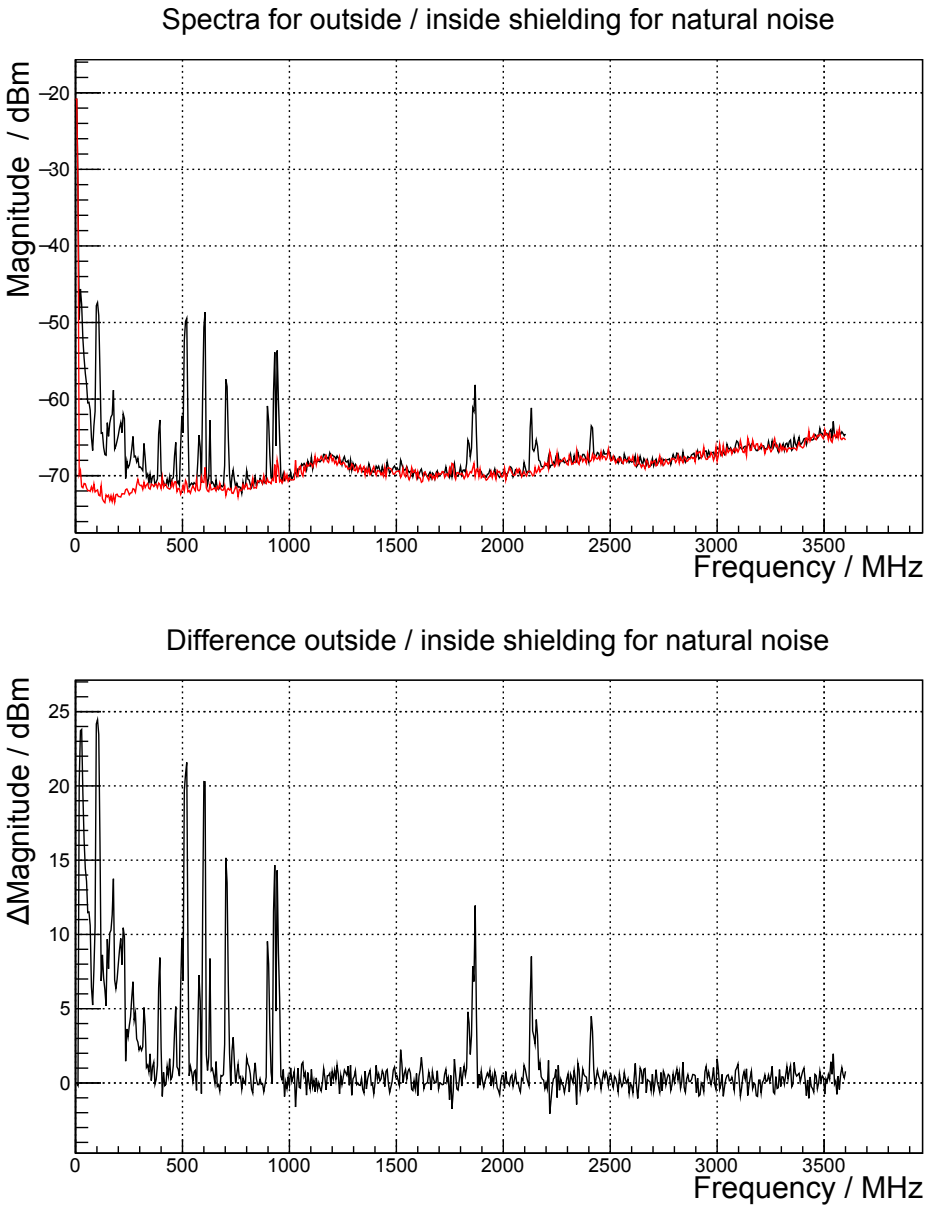

Figure 5.19.: In the upper plot the absolute spectra inside (red) and outside (black) of the shielding are shown. In the lower plot the difference (outside minus inside) is shown. The frequency range goes up to 3600 MHz.

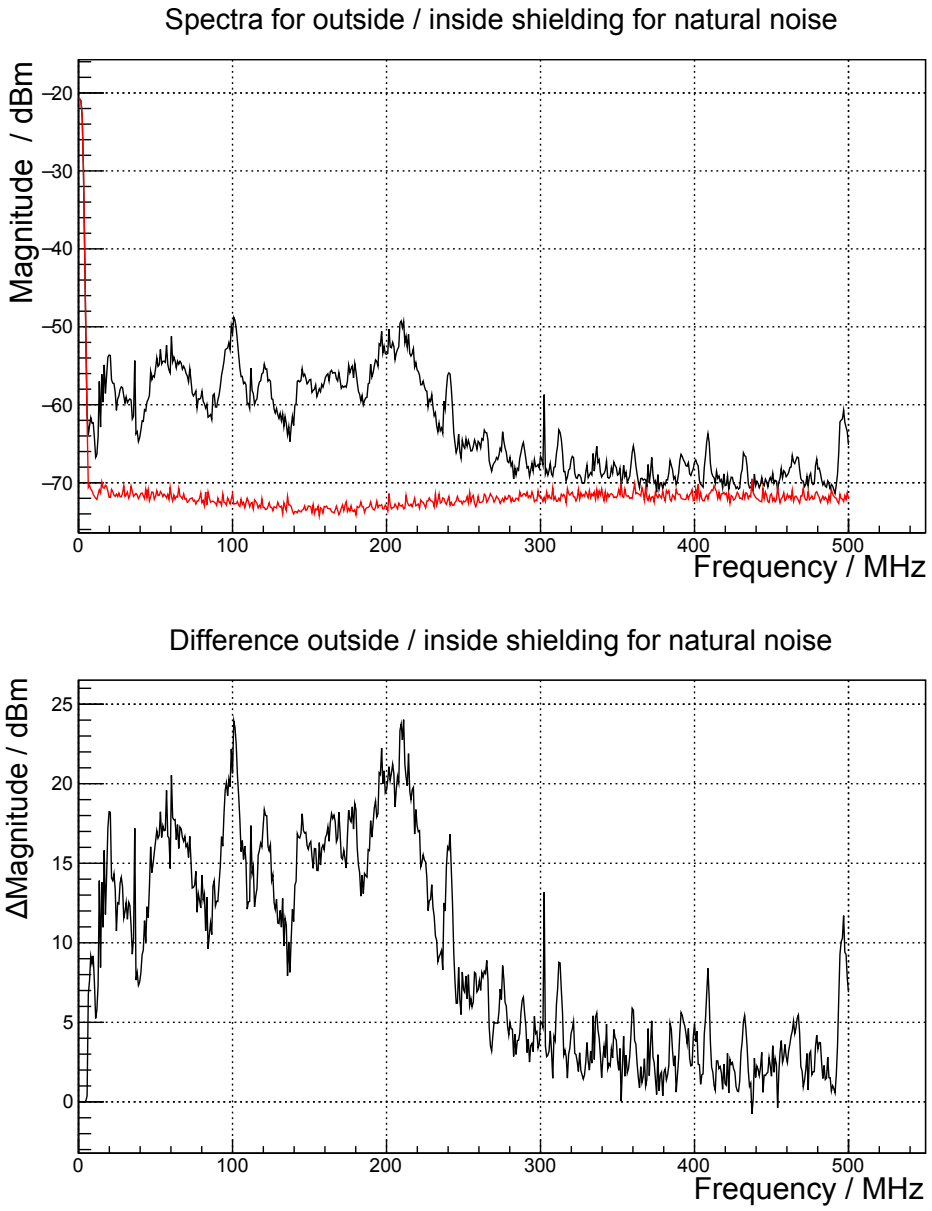

Figure 5.20.: In the upper plot the absolute spectra inside (red) and outside (black) of the shielding are shown. In the lower plot the difference (outside minus inside) is shown. The frequency range goes up to 500 MHz.

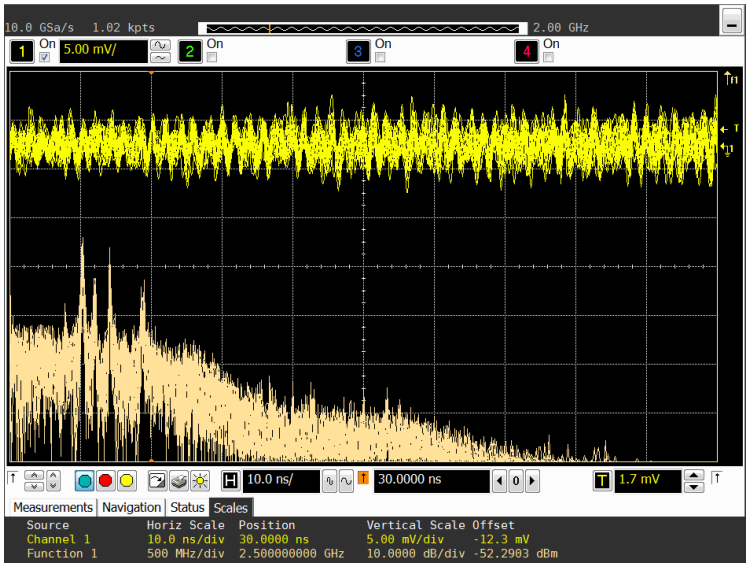

Figure 5.21.: Oscilloscope screen shot without shielding. The baseline (upper part, yellow lines) width is around 10 mV and some huge peaks are visible in the FFT (lower part, lighter yellow lines). One division correspond to 500 MHz (horizontal axis) and 10 dB (vertical axis) in the FFT data. For the base line data one division corresponds to 10 ns (horizontal axis) and 5 mV (vertical axis). Thus the highest peak is the 514 MHz DVB-T signal. Followed by the two other DVB-T signals at 602 MHz and 706 MHz. The last clearly visible peak is around 900 MHz which is the mobil net carrier GSM 900.

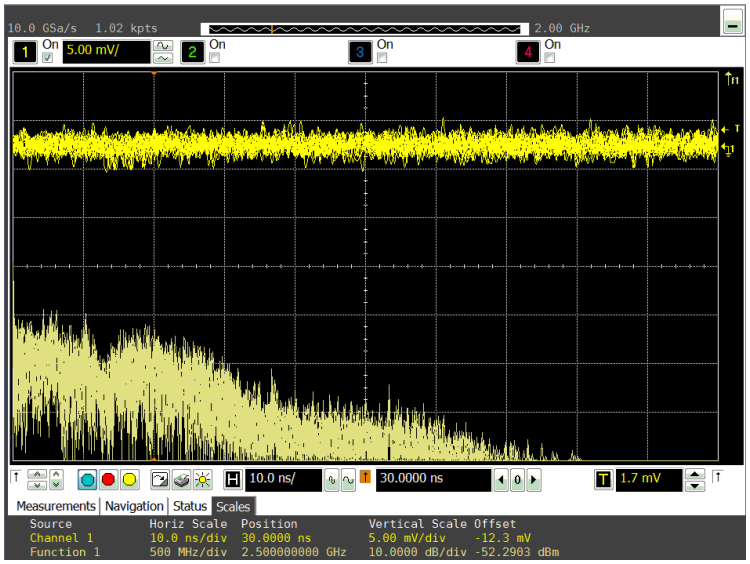

Figure 5.22.: Oscilloscope screen shot with shielding. The shielding reduces the baseline width below 5 mV and the FFT is smoother with no large peaks.The scales are the same as in the previous plot.

5.4. Remarks on operation

The test set-up offers a temperature stabilised environment for long-term, precise measurements of SiPM properties. The light source is useful for many types of measurements because it offers light fluxes with different wavelengths and a large dynamic range. The electrical operational conditions are very stable and external noise is effectively kept out of the measurements. All this provides a reliable basis for automatised characterisation measurements of SiPMs.

6. Signal Analysis

In this chapter, the implemented algorithms used to extract the signal from the recorded raw data and to convert them to usable processed data are described. The processed data serve as input to the measurements described in Chapter 7.
All shown data in the examples in this Chapter were recorded with this SiPM: Hamamatsu MPPC S10362-11-100C (serial number 2588). The parameters stated on the package are $V_{op} = 70,19\,\mathrm{V}$, gain $M = 2.4 \cdot 10^6$, and dark count rate (0.5 p.e threshold) 459 kHz at an SiPM temperature of 25 °C.

6.1. Long trace analysis

The long trace analysis is used to gain information on the time behaviour of the SiPM, the time between pulses, which can not be obtained in triggered short trace mode, since the times can be much larger than the captured window in short traces. Furthermore some properties can be determined from long traces as shown in Chapter 7. To be able to do this, the methods to extract the required data from the long traces are described in this Chapter, in particular the point in time of a signal, the signal height, the signal charge, and the possible additional signal on the trailing edge are of interest.
To obtain the times between pulses the signal is corrected for the baseline offset and cleaned from noise by averaging. Then the traces are searched for many different threshold crossings to obtain a 'trigger-rate threshold scan' from which the one p.e. signal height is extracted. This one p.e. threshold is then used to identify possible SiPM pulses in the trace. The time values of these pulses are stored in a list and used to evaluate every found pulse. The evaluation includes the peak height and charge determination and a search for afterpulses on the trailing edge of the pulse.
The default measurement consists of $41 \cdot 10^6$ points with a time step of 1 ns. This leads to a view on 41 ms out of the life of an SiPM per trace. To accumulate more statistics multiple traces (blocks) can be recorded within a single measurement. The incoming raw data for one long trace consists of the preamble and a list of $4.1 \cdot 10^7$ 16-bit integers. The preamble contains at least 21 data fields. The most important

fields are the numbers for the y-axis, the offset (*YOrigin*), and the value of the least significant bit (*YIncrement*). With these two numbers the 16-bit integers can be converted into the measured voltages. The x-axis offset and time step allow for the reconstruction of the time point for each y-value.

6.1.1. Signal processing

In the following sections the steps taken to prepare the data for analysis are described.

6.1.1.1. Baseline correction

To ensure that the baseline is at 0 V, the complete long trace voltage values are filled into a histogram, as shown in Figure 6.1. A Gaussian function is fitted around the maximum, the data to the right which contain signal are not included. The obtained mean is used to shift the whole trace in such a way that the baseline is at 0 V. The width of Gaussian function (σ) from the fit is used as a baseline noise level. The baseline correction may fail, when the trace contains too much signal. This may happen if the temperature is too high, the overvoltage is too high or there is too much light flux. In these cases the whole trace analysis will fail, too, since the signals are no longer distinguishable. Besides a current measurement no further analysis is useful in this case.

6.1.1.2. Sliding average

After reading the raw data from the input file, a moving average with a windows width of 20 ns is calculated for the whole trace. The effect of the moving average is shown in Figures 6.2 and 6.3 for a 0.5 p.e. and a 1.5 p.e. trigger threshold, respectively.

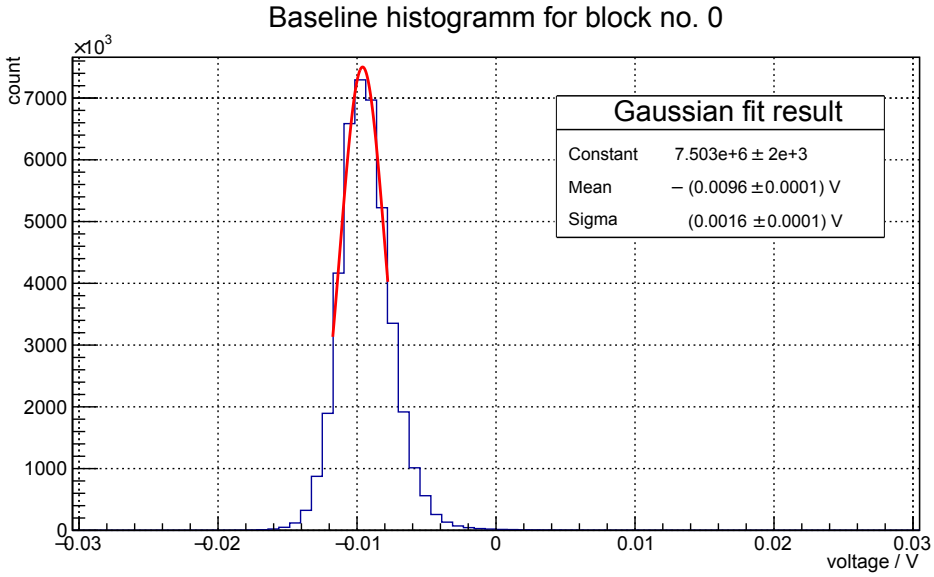

Figure 6.1.: Baseline histogram created from one block. The fitted Gaussian indicates that a global shift of 9.6 mV is required to move the average baseline to 0 V. The fit range is limited to the sharp peak because the right tail contains signal, which should not be considered when shifting the baseline.

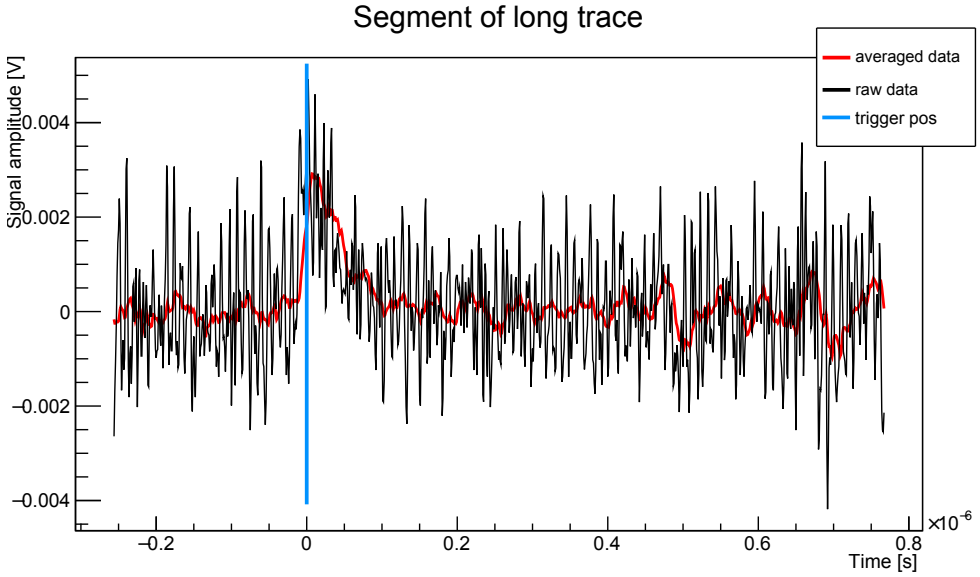

Figure 6.2.: Filter effect of sliding average on 0.5 p.e. triggered signal. The averaging facilitates the detection of peaks. In case of rise time studies, the raw trace data can be used.

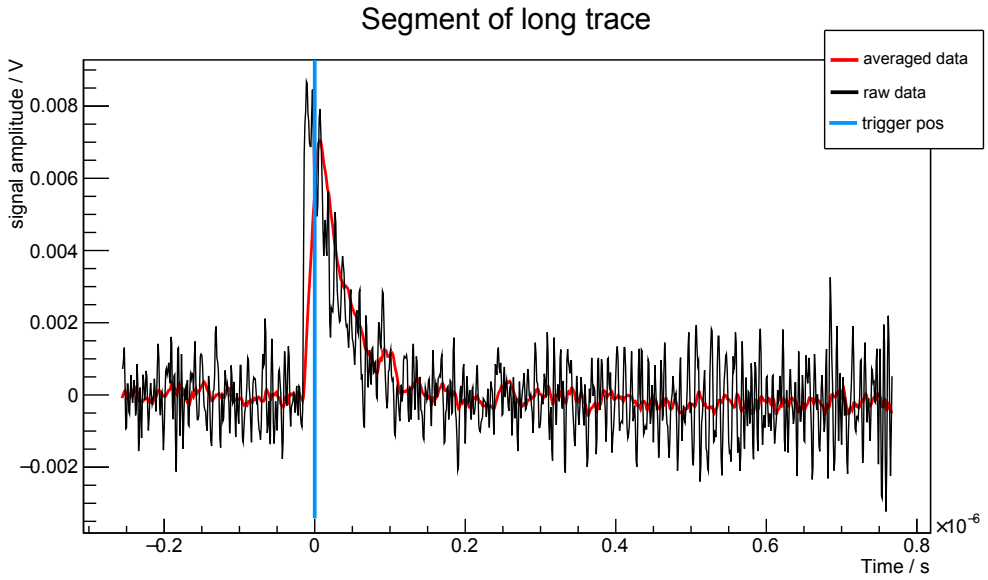

Figure 6.3.: Filter effect of sliding average on 1.5 p.e. triggered signal. The averaging facilitates the detection of peaks. In case of rise time studies, the raw trace data can be used.

6.1.1.3. Optional FFT filtering

An optional Fast Fourier Transform (FFT) filtering can be applied. This is done by calculating the FFT spectrum, setting the amplitude of the filtered frequencies to 0 and doing an inverse FFT to obtain the filtered signal. Doing this for a full trace does not work due to excessive amount of computing time. The computation time for one full trace is larger than 1000 min for a single core, no full traces FFT filtering was ever finished. Doing this for shorter segments, for example around a found trigger, is much better. For the current test set-up a filter cut-off at FFT bin 25 (frequencies < 122 MHz are kept) leads to clean results (Figure 6.4). The bin number is given, as the software works on the bins. The resulting cut frequency may not always be an integer. A lower cut value flattens the rising edge (Figure C.1). A higher cut value reduces the filter effect (Figure C.3). The FFT bin width is given defined by the number of used data points n and the time step Δt between the points:

$$f_{bin\,width} = \frac{2}{n \cdot \Delta t} \tag{6.1}$$

The resulting cut off frequency for bin b is than calculated by:

$$f_{cut\,off} = f_{bin\,width} \cdot b. \tag{6.2}$$

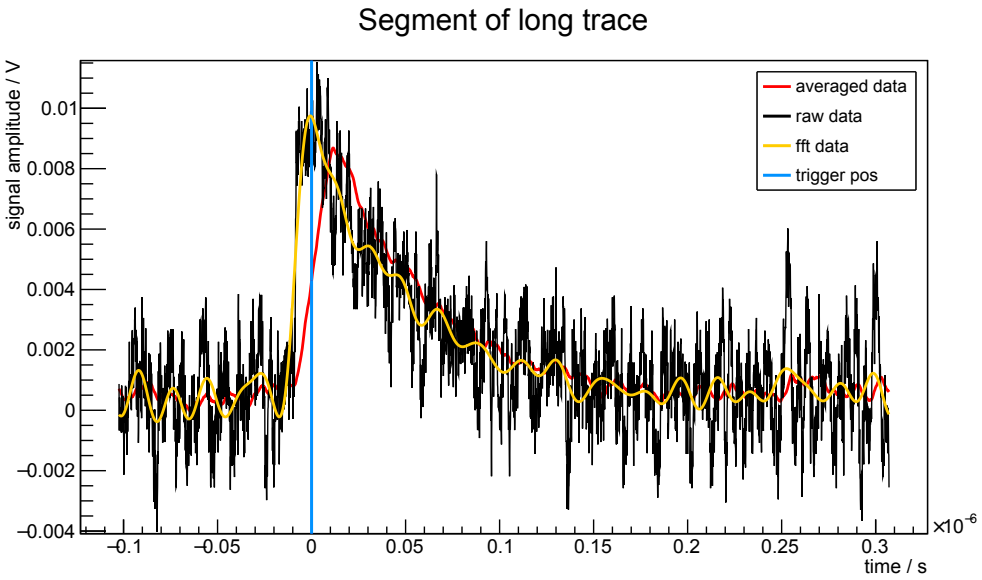

Figure 6.4.: FFT filtered short trace segment with a 1.5 p.e. trigger threshold. FFT filtered data is shown in orange. Here with a cut-off at FFT bin 25 (frequencies $f < 122\,\mathrm{MHz}$ are kept).The data contains 4096 points with a time step of $\Delta t = 100\,\mathrm{ps}$.

6.1.2. Threshold scan

The threshold scan simulates a trigger threshold scan, where the trigger frequency is measured with the oscilloscope for different trigger thresholds. For this the threshold is increased from the starting threshold (twice the baseline width) in smallest possible steps (*YIncrement*), and the number of triggers are counted. The scan is stopped, when no trigger is found for a threshold. This yields a step plot like the upper one shown in Figure 6.5. The steps originate from the discrete p.e. signals. This step size and thus the 1 p.e. signal is to be determined. The relative change of the resulting graph is calculated. For a given point i it is calculated as follows:

$$rel_{change}[i] = \frac{1}{4} \cdot \left(\sum_{n=1}^{4} N[i-n] - \sum_{n=1}^{4} N[i+n] \right) \cdot \frac{1}{N[i]}, \tag{6.3}$$

with $N[i]$ being the trigger count for step i in the measurement. The first and last four points are not calculated due to the averaging. In this relative change the extrema are located and the differences between the local extrema are calculated and averaged. This average is used as the 1 p.e. signal height. In the lower part of Figure 6.5 the relative change and the fits of parabolas to the first six extrema are shown. The

fit range is determined by the crossings of data (threshold change) and mean. The parabola have been found to be a robust solution for determination of the position of the extrema.

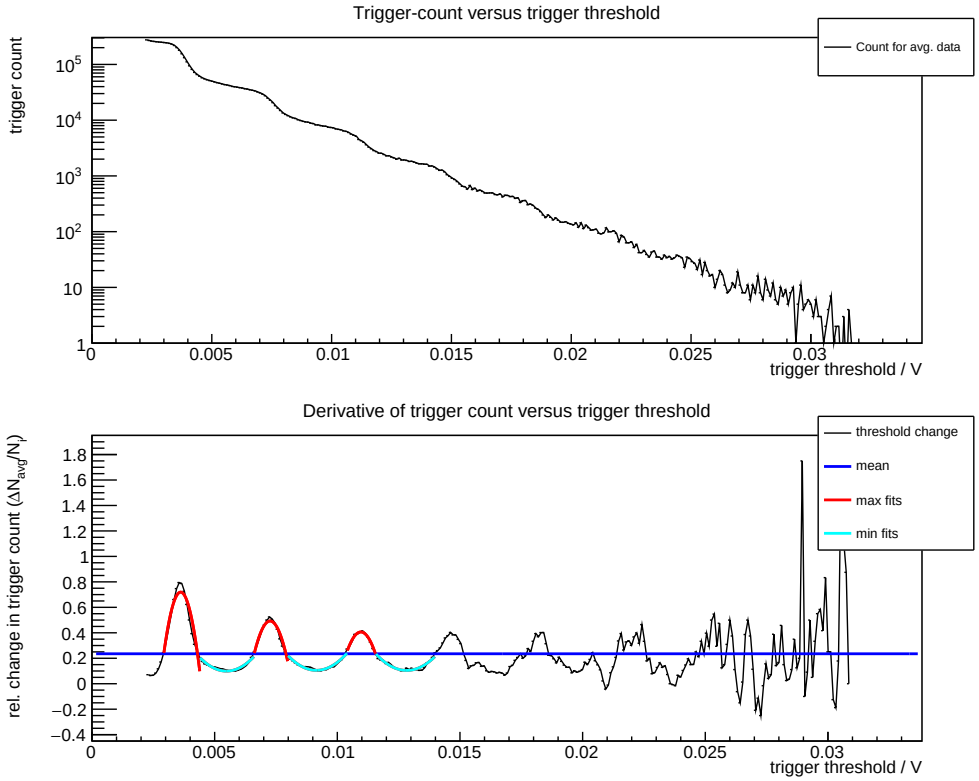

Figure 6.5.: In the upper part of the figure the accumulated trigger counts for a certain threshold are shown for ten traces/blocks. The steps are due to the discreteness of the SiPM signal for lower photon counts. To better identify these steps and thus the 1 p.e. step (in this case the signal heigth), the numerical relative change of the trigger count is calculated. This is shown in the lower part. The mean value used to find the intersections with the data that are used as the fit range for each extremum is given in blue. Fits of parabolas to maxima are shown in red and to minima in cyan. The distance between the maxima (or the minima) is the 1 p.e. peak height.

6.1.3. Peak finder

The peak finder searches for peaks which cross the given threshold. Using the previously determined 1 p.e. signal height value with a factor of 0.5 or 1.5 this peak finder will find all possible SiPM signals, as shown with the blue lines in Figure 6.6. A factor

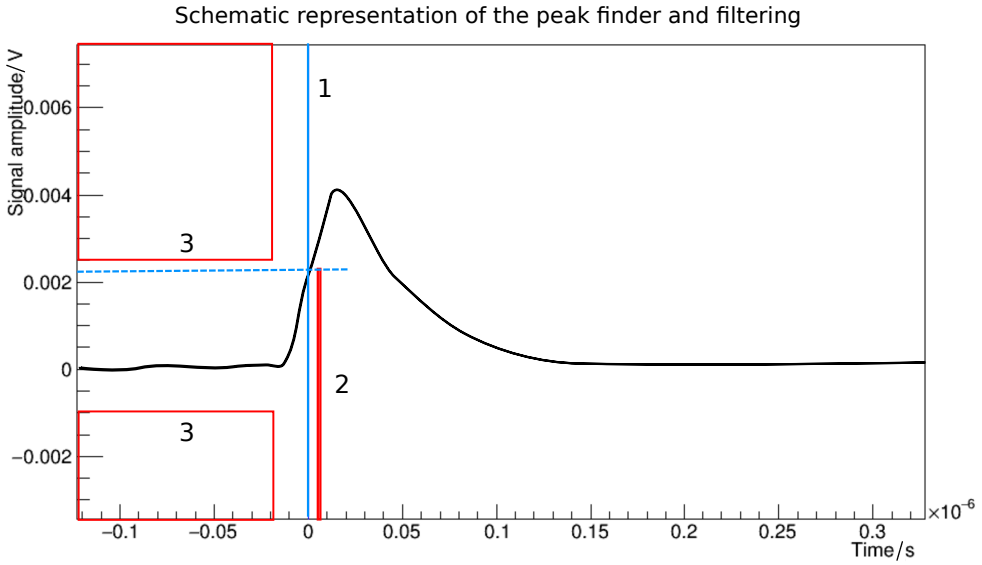

Figure 6.6.: Schematic representation of the peak finder. In the first step the data (black curve) are scanned for a crossing of the trigger threshold (blue horizontal dashed line). The position found is marked with the blue vertical line (1). Then a single data point is checked for an early edge (2), the data point a few ns after the crossing may not be lower than the trigger threshold, rejecting most of the oscillations. As the last step the time in front of the possible peak is scanned for data being out of the accepted level range (3). Red areas and boxes are forbidden zones for the signal.

of 0.5 will find all signals starting at 1 p.e. peaks. A factor of 1.5 will skip the 1 p.e. peaks and the found signals will be at least 2 p.e. peaks. Each found peak is checked for oscillations from noise signals[16], this is done by testing a single data point a few ns after the possible trigger to be not below the trigger threshold (2). In the case that an oscillation is detected, the peak is not added to the resulting trigger list. If there is no oscillation the silence criteria is checked. To ensure the found triggers correspond to clean pulses, which are not induced by afterpulsing, which can occur even $O(100)$ ns later, the data before the trigger candidate are checked to be below the 0.5 p.e. threshold plus baseline noise level and above the -0.25 p.e. threshold (3). The larger this window is, the less afterpulses are added to the clean trigger list. To speed up things only every fifth data point in the silence windows is tested. If it is outside of the allowed range, the trigger is not added to the trigger list. In short, if any data point is inside the red areas, then the candidate is rejected. Adding the

[16]There is an unidentified noise source, disturbing the AC power line. The mesh shield does not protect against this.

trace segments around all found triggered and clean pulses to a 2D-histogram (time relative to the trigger, and amplitude at that point) yields a virtual afterglow/heat map picture, as shown in Figure 6.7, where the frequency of each combination is represented by the colour-coded z-axis. This resembles the afterglow function of an oscilloscope. In general these heat map plots allow for easy visual checks by the user, that everything worked fine.

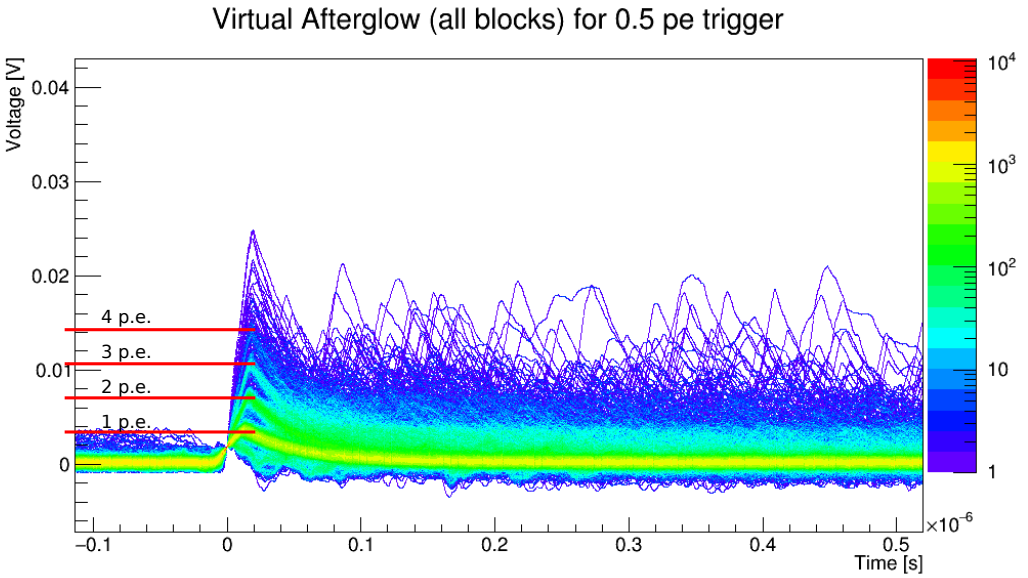

Figure 6.7.: Virtual afterglow picture for 10 blocks/traces from a single measurement. The separation between the different p.e. steps is clearly visible and marked with horizontal red lines.

6.1.4. Peak height determination

For each found clean pulse the peak height is determined. This is done by setting the starting pulse level to 0 V because the baseline is shifted to 0 V and searching for the maximum level inside the pulse duration, as depicted in Figure 6.8. Filling the determined pulse heights into a histogram results in multiple peaks, as shown in Figure 6.9. The halved distance between the peaks can be used as a 0.5 p.e. oscilloscope trigger threshold for short trace measurements. Besides the peak height, the starting point where the data crosses the baseline level of 0 V for the last time before the trigger is determined and saved. Due to the shifted baseline (average level 0 V) and the noise level on the baseline this a robust and quick method.

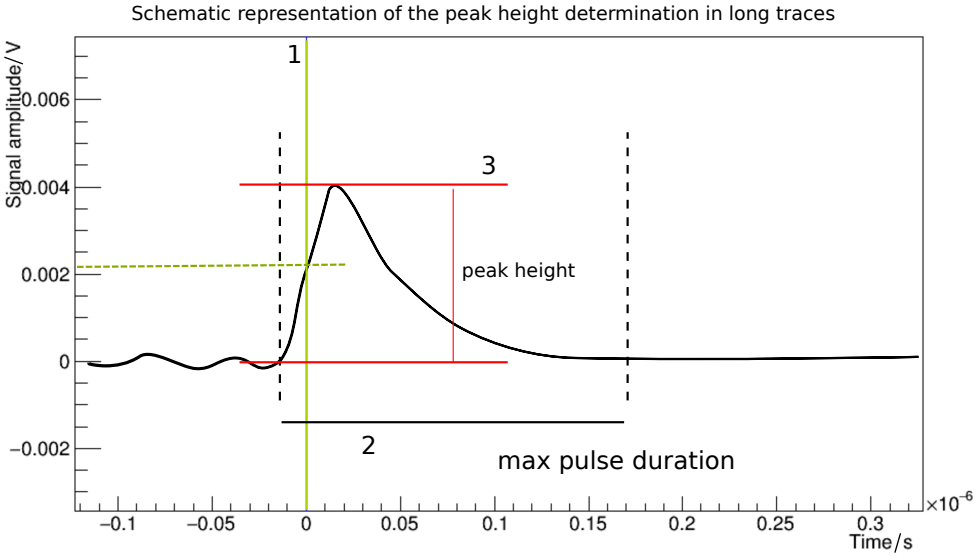

Figure 6.8.: Schematic representation of the peak height determination. Inside the pulse duration the maximum is determined and used as the peak height.

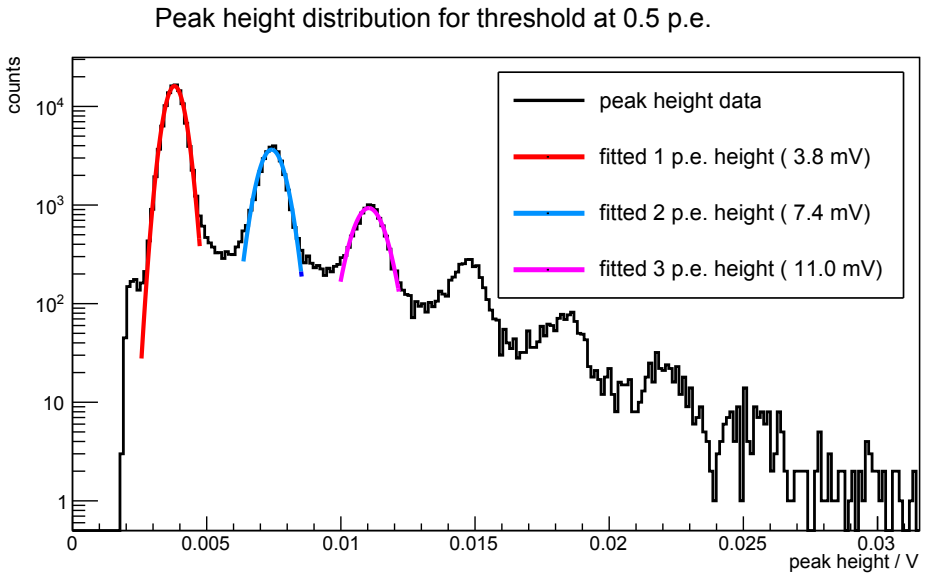

Figure 6.9.: Peak height histogram with Gaussian fits to the peaks. The halved difference between the peaks can be used as the 0.5 trigger threshold for short trace measurements.

6.1.5. Afterpulse finder and height determination

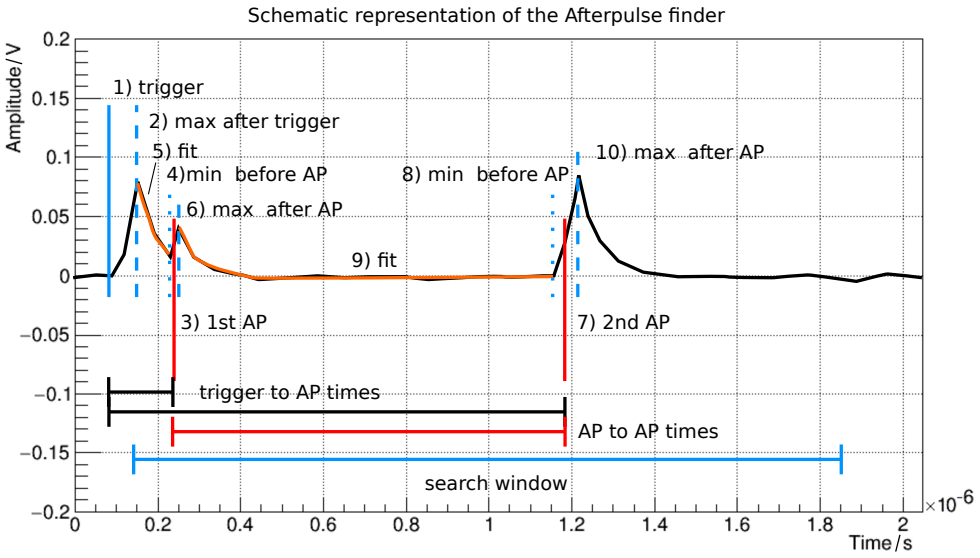

Figure 6.10.: Schematic representation of the afterpulse detection algorithm.

Each peak in the list of found peaks is searched for afterpulses. Figure 6.10 illustrates the following description of the algorithm. The blue solid line (1) marks the peak position (trigger from list of found peaks). The first step is to find the maximum after the trigger (2). From there the falling edge is searched for an increase larger than 0.3 times the one p.e. threshold in a certain time. If such an increase is found, marked with the left red solid line (3), the minimum before this point is determined (4). To determine the starting level of the first afterpulse an exponential function is fitted, shown in orange (5), from the maximum after the trigger to the minimum before the afterpulse and evaluated at the minimum position. The value obtained from the evaluation is the starting level. The maximum after the afterpulse (6) minus the starting level is the afterpulse height. For each afterpulse maximum (6) a new search loop is initiated: start from maximum (6), search for increase (7), find minimum (8) before newly found afterpulse, make fit from maximum to minimum (9), find maximum after (10), determine afterpulse height and start over from the last determined maximum position. Before taking a found increase as an afterpulse it is checked for its absolute maximum to be greater than 0.5 times the one p.e. threshold to reject baseline noise, and it is checked for an early edge in the same way as for to the normal peak filtering. The search is stopped early, before reaching the end of the search window, when the search position is the next peak in the list of found peaks. For each afterpulse the following data is stored: afterpulse height,

time, and the slope from the exponential fit. The search window and the minimum increase are passed to the function. Normally a time window of 1000 ns after the maximum after trigger (1) is searched and the default minimum increase is 0.3 times the one p.e. threshold. This threshold offers a compromise between noise rejection and detecting small and thus early afterpulses. One has to keep in mind, that one can not distinguish between normal pulses and afterpulses at larger time differences, since the pulse height is fully recovered. This ambiguity does not disturb the later analysis shown in Section 7.2.5.

6.1.6. Charge determination

For each triggered clean pulse (no afterpulse) the charge is calculated for three different integration times. The comparison between the three integration times is shown in Figure 6.12. The charge determination is done by summing the voltage values and

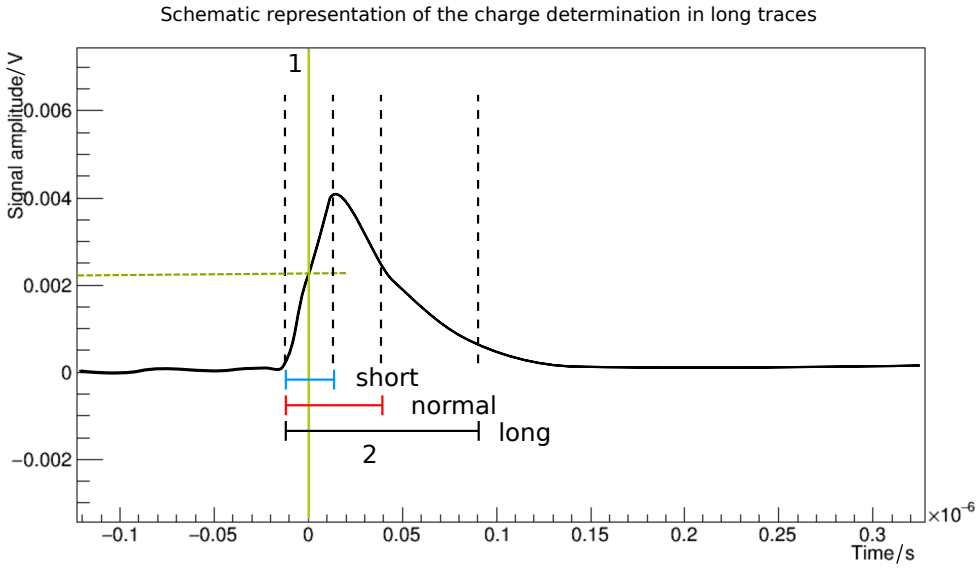

Figure 6.11.: Schematic representation of the charge determination. The charge determination starts at the previously determined starting point of the peak and then a summation is performed over three different integration times.

calculating the charge as follows:

$$Q_i = \frac{V_i}{R \cdot M_{gain}} \Delta t \tag{6.4}$$

$$Q = \sum_{i=start}^{stop} Q_i = \frac{1}{R \cdot M_{gain}} \cdot \Delta_t \cdot (stop - start) \cdot \sum_{i=start}^{stop} V_i, \tag{6.5}$$

where V_i is the measured voltage, *start* and *stop* are the starting and stopping time bin numbers (dimensionless) for the integral, Δ_t is the time bin width, R is the input impedance of the oscilloscope (50 Ω) and M_{gain} is the gain of the pre-amplifier. If only a coupling capacitor is used without any amplifier, the factor M_{gain} becomes 1. The start of the integral is set to the starting point of the peak. The normal integration time (default 50 ns) is passed to the function, while the short ($0.5 \cdot$ normal) and long time ($2 \cdot$ normal) are calculated. This is done to give the user feedback, if a shorter or longer time could improve the resulting finger spectrum. Filling many charge measurements into a histogram should result in a finger spectrum similar to the ones shown in 6.13 and 6.14. From the coarse (wide bins) histogram the possible peaks are identified and then fitted with a Gaussian. The resulting fit parameters are then used to fit the fine (narrow bins) finger spectrum.

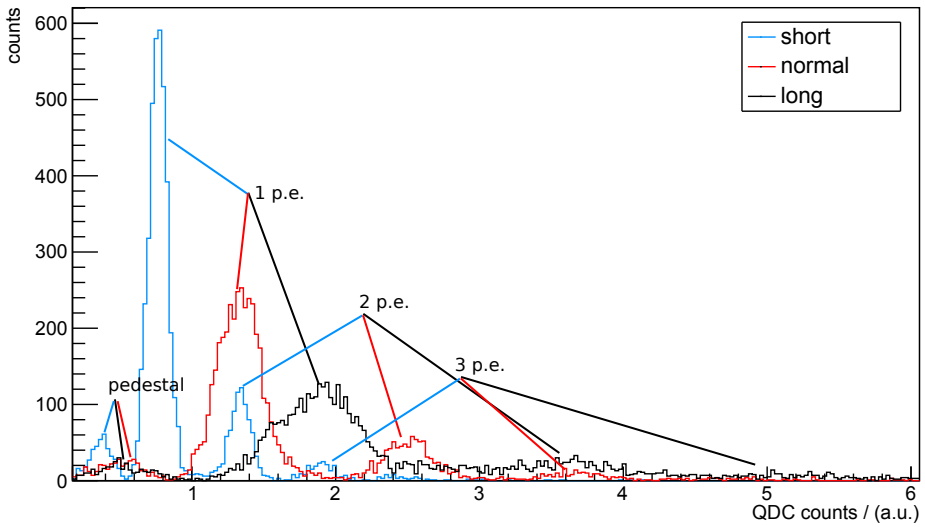

Figure 6.12.: Fine (narrow bin) histogram for the charge for 25 ns (short), 50 ns (normal), and 100 ns(long) integration times.

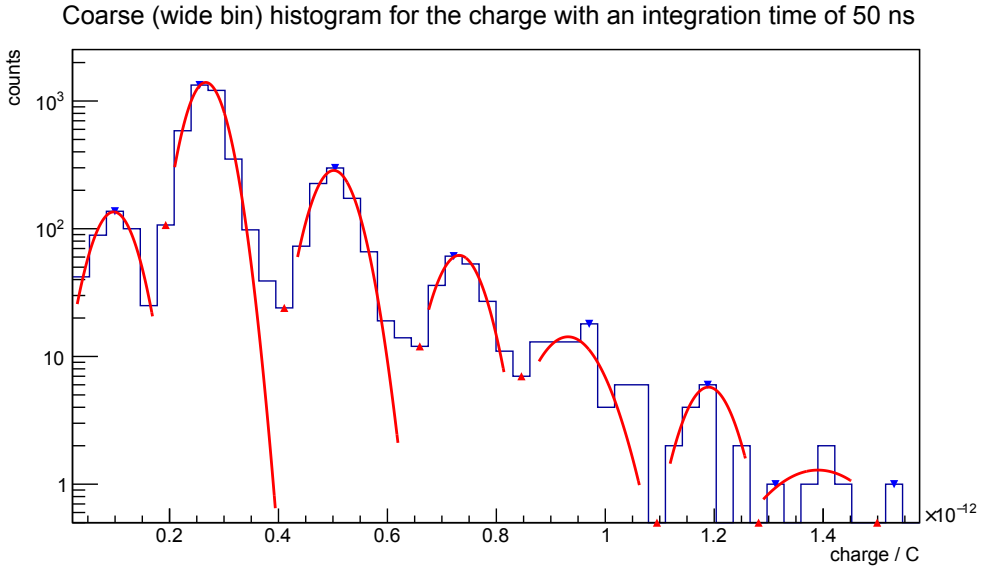

Figure 6.13.: Coarse (wide bin) histogram for the charge for a 50 ns integration time. It is used to find the fitting positions with a simple min/max finder. The results of the fits of Gaussian function to the data between the minima are used in the next step.

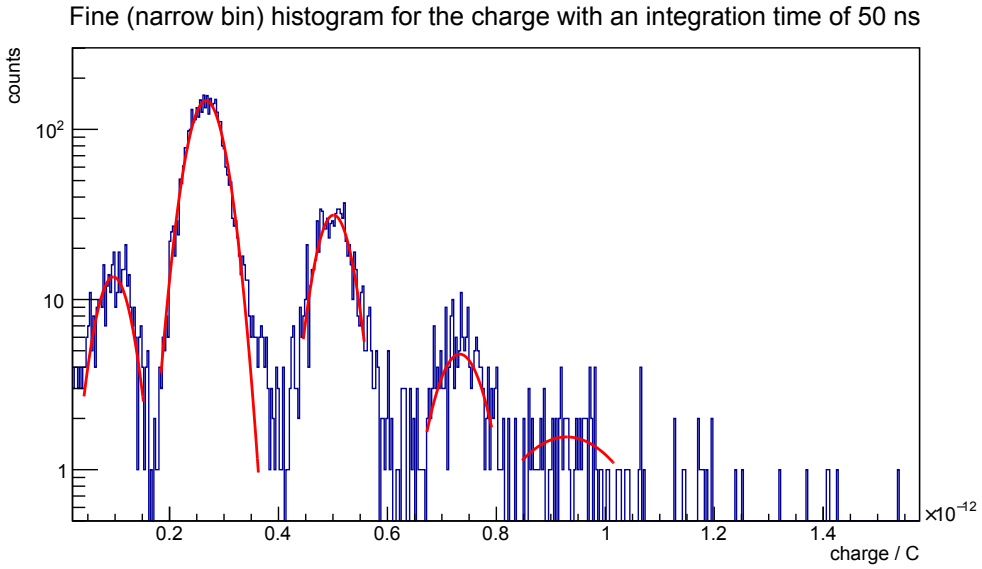

Figure 6.14.: Fine (narrow bin) histogram for the charge with fits to the single peaks for 50 ns integration time. The initial parameter for the fits of Gaussian functions to the data are obtained from the fits to the data in the coarse histogram.

6.2. Short trace analysis

The segmented memory function of the oscilloscope allows for a fast acquisition of triggered short traces. These have the great advantage, that they contain the desired signal.
The incoming raw data consists of the preamble and a list of up to 8192 segments of trace data. A single trace data segment consists of usually 1024 or 2048 integers with a default time step of 1 ns. The information required to convert the raw data to the measured values is stored in the preamble. In addition to the information that was used for the long trace, the segment count and trace segment length are now also required. In the long trace they are not required because it is only one segment with all raw data.

6.2.1. SoftQDC

The SoftQDC is used to measure the charge like a hardware charge to digital converter (QDC). With default settings the trigger occurs in the middle of the short

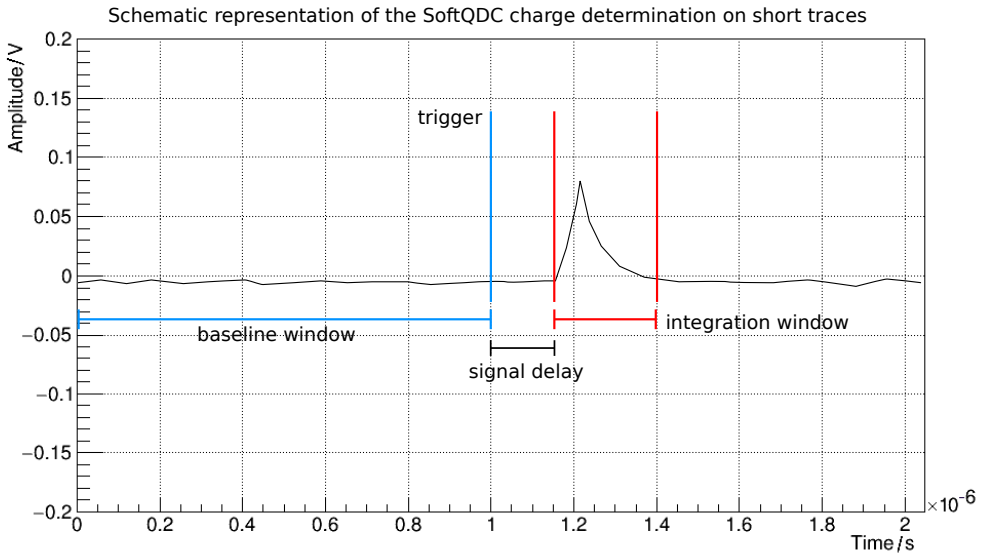

Figure 6.15.: Schematic representation of the charge determination with SoftQDC. The dedicated external trigger occurred in the middle of the trace. Left of the trigger are the data for the determination of the baseline level. After the signal delay the integration windows for the signal charge determination begins.

trace as shown in Figure 6.15. Due to the difference in signal run time, generated

electrical trigger to oscilloscope and generated electrical trigger to the pulser, followed by light creation and finally light arrival on SiPM, the SiPM signal is delayed by some time and thus appears after the trigger of the trace. For each short trace the charge is determined according to Equation 6.7. This includes a correction for a possible baseline shift by determining the average baseline level in the first half of the short trace and subtracting the average from each value that is summed up:

$$Q_i = \frac{V_i - V_{\text{avg.baseline}}}{R \cdot M_{gain}} \Delta t \tag{6.6}$$

$$Q = \sum_{i=start}^{stop} Q_i = \frac{\Delta_t \cdot (stop - start)}{R \cdot M_{gain}} \cdot \sum_{i=start}^{stop} (V_i - V_{\text{avg.baseline}}), \tag{6.7}$$

where V_i is the measured voltage, $V_{\text{avg.baseline}}$ the average baseline level, *start* and *stop* are the start and stop time bin for the integral, Δ_t is the time bin width, R is the input impedance of the oscilloscope ($50\,\Omega$) and M_{gain} is the gain of the pre-amplifier. The factor M_{gain} becomes one, if only a coupling capacitor without any amplifier is used.

The resulting charge values are filled into a histogram. Depending on the light flux level this can result in spectra with: clearly separated peaks with a pedestal for low light flux (Figure 6.16), separated peaks and very small pedestal for medium light fluxes (Figure 6.17), or one large merged peak for high light fluxes (Figure 6.18).

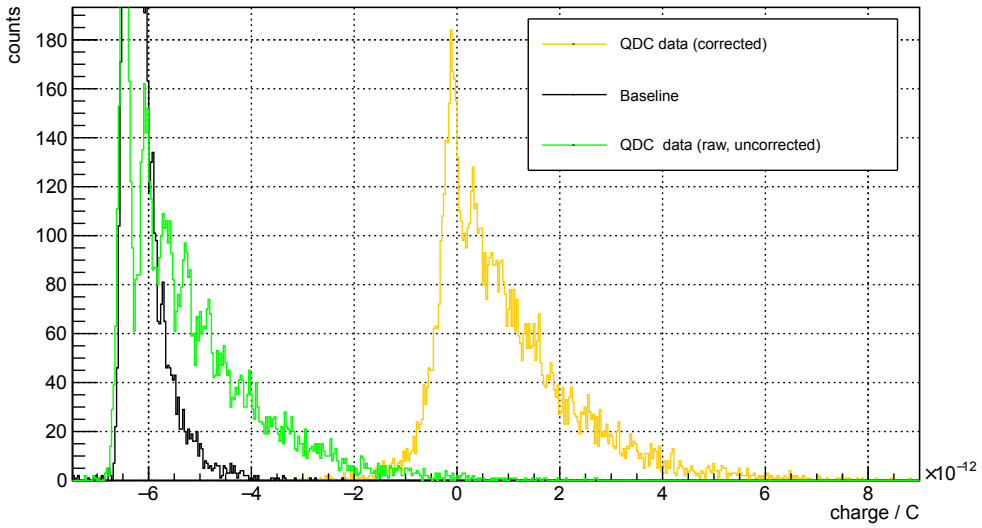

Figure 6.16.: SoftQDC spectrum for low (O(1)) photon count per event. The large pedestal and several p.e. peaks are visible. The pedestal is peak at 0 C for the corrected data. Right to it is the 1 p.e. peak at around $0.5 \cdot 10^{-12}$ C. In the uncorrected data (shown in green) the pedestal is around $-6.5 \cdot 10^{-12}$ C. Right to it is at around $-6.0 \cdot 10^{-12}$ C the 1 p.e. peak. Since the baseline has a large shoulder on the right side, even two small peaks are visible, the corrected signal is not only shifted as desired but also smeared. In the data shown here the uncorrected data shows a better separation than the corrected. If the baseline is a smooth peak, the corrected signal would show equal or even better separation.

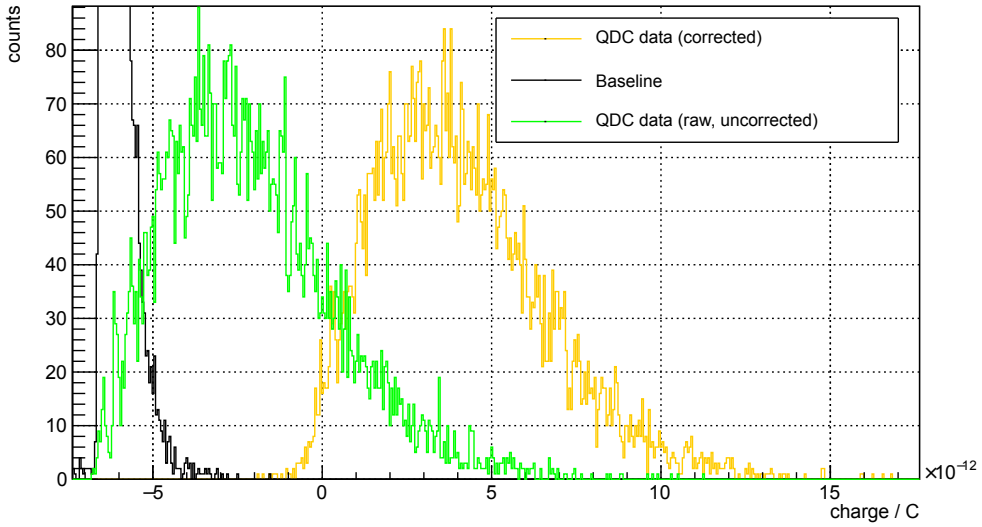

Figure 6.17.: SoftQDC spectrum for a little higher photon count (~ 20 incident). The small pedestal peaks, at 0 C (corrected) and $-6.5 \cdot 10^{-12}$ C (raw), and several p.e. peaks right to the pedestals are visible. In this spectrum ~ 8 p.e. are recorded in average.

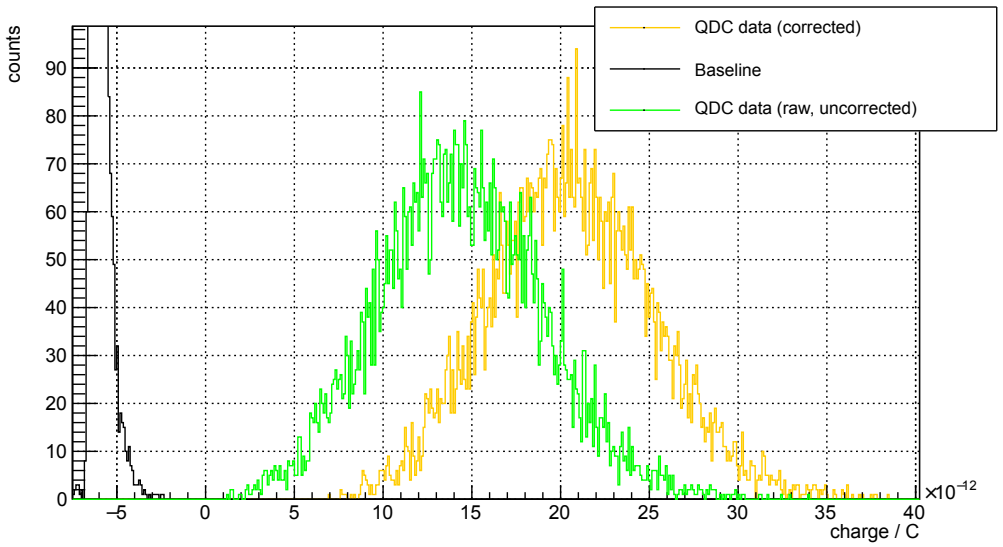

Figure 6.18.: SoftQDC spectrum for high photon count ($\sim$ 110 incident). The pedestal is not existent, as every captured trace contains signal far away from the baseline height. No entry for the corrected signal is near 0 C. Single p.e. peaks are no longer visible, instead there is a large peak around the average determined charge. In this spectrum ~ 40 p.e. are recorded in average.

6.3. Sourcemeter measurements

The sourcemeter (described in Chapter 3.8.2) is used to measure the currents and voltages of the SiPM and the reference detector which are required for all analyses. These measurements are used to ensure the correct operational parameters for the SiPM, determine the light flux on the reference detector and thus on the SiPM, and gain access to the I-V characteristics of the SiPM.
The default measurement settings are an integration time of one power line cycle (50 Hz) and internal averaging (filtering) over 50 internal analog-to-digital conversions. Each measurement point is the average of ten (default setting) such filtered values. For these ten values a mean and a standard deviation are calculated. Both channels of the sourcemeter, connected to the SiPM and the reference detector, are converted in parallel. The time difference of the starting point between the two channels is equivalent to the time required to send the measurement command (< 20 bytes). To cancel out any potential systematic offset and correct for the dark current of the PiN photodiode and SiPM a dark measurement is done with the same settings and subtracted from the light measurement, if applicable.
The measurements for the SiPM are used as recorded, while the reference detector data is used to calculate the light fluxes.

6.3.1. Light flux determination

In this section the light flux calculations from data for the different light path options are described. A precise measurement of the light flux is required for p.d.e. and dynamic range measurements.

6.3.1.1. Light flux on reference detector

With the measured PiN photodiode current, the calibration data, and the measured wavelength of the incident light, the light flux on the PiN photodiode can be determined with the formulae given in Section 5.2.5. For a typical measurement of 10 points the error for larger light fluxes (200 photons on PiN which corresponds to 5 photons on SiPM with 1 mm $\times$ 1 mm active area) is around 0.5 %. For lower light fluxes ($\sim$ 30 photons on PiN which corresponds to < 1 photon on SiPM with 1 mm $\times$ 1 mm active area) the noise effects and the fluctuations of the sourcemeter have a much larger impact and the resulting error is around 3 %. These errors do not include the systematic error from the calibration.

6.3.1.2. Light flux on SiPM

The average light flux on the SiPM is calculated with Equation 5.35. The statistical error on the average light flux is calculated by the propagation of the statistical error of the reference current measurement. For the direct light path the (now systematic) error of the measured ratio $R_{r/t}$ (Table 5.1) for each LED is negligible (Table 5.1). When the light path via the monochromator is used, the systematic error of the measured ratio $R_{r/t}(\lambda)$ can be the major contribution to the total systematic error (Figure 5.15). The second source for systematic error is the calibration of the PiN photodiode, which can be up to 4%. The calibration errors also defines the absolute precision limits that can be achieved by this set-up.
The statistical error is around 1 % for single photon pulses (1-5 photons on the SiPM) with a repetition rate 1 MHz. The high repetition rate is needed to be able to measure the reference detector current with sufficient precision. For higher photon counts per pulse (around 100 photons on SiPM) the statistical errors goes down to 0.1% at the same repetition rate. For the DC operation the statistical errors are similar to the ones in pulsed operation mode, around 1 % for fluxes around $5 \cdot 10^6$ photon per second on the SiPM, dropping down 0.1% for fluxes larger than $100 \cdot 10^6$ photons per second on the SiPM.

7. Measuring Methods

In this chapter the measuring methods used for the reference detectors and the SiPM properties are described and shown in some examples. All shown data in the examples in this Chapter were recorded with this SiPM : Hamamatsu MPPC S10362-11-100C (serial number 2588). The parameters stated on the package are $V_{op} = 70,19\,\mathrm{V}$, gain $M = 2.4 \cdot 10^6$, and dark count rate (0.5 p.e threshold) 459 kHz at an SiPM temperature of 25 °C.

7.1. Reference detectors

7.1.1. PiN photodiode measurements / photon flux determination

Whenever the photon flux needs to be measured, the following procedure is used with the sourcemeter: take a dark measurement of the PiN current (SiPM current is measured in parallel automatically) with LEDs turned off if meaningful[17], then take a measurement with the light flux to be measured and last take an additional dark measurement (again, only if meaningful). Each of these three measurements consists of typically ten (default setting) measured data points with an integration time of one power line cycle and internal averaging over 50 measurements. After the average (corrected for the dark current if possible) and error calculations described in Section 6.3 this measurement yields a single number for the average photon flux on the SiPM which is then used for further calculations.

7.1.2. Spectrometer measurements

The spectrometer can be used to determine the wavelength of the currently used photons. The spectra are captured automatically in many of the implemented measurements. Furthermore software was developed by the author of this thesis that allows for a real-time check, if the light flux is in the correct order of magnitude,

[17] Not meaningful during long term LED output measurements as it would interrupt the LED heating process.

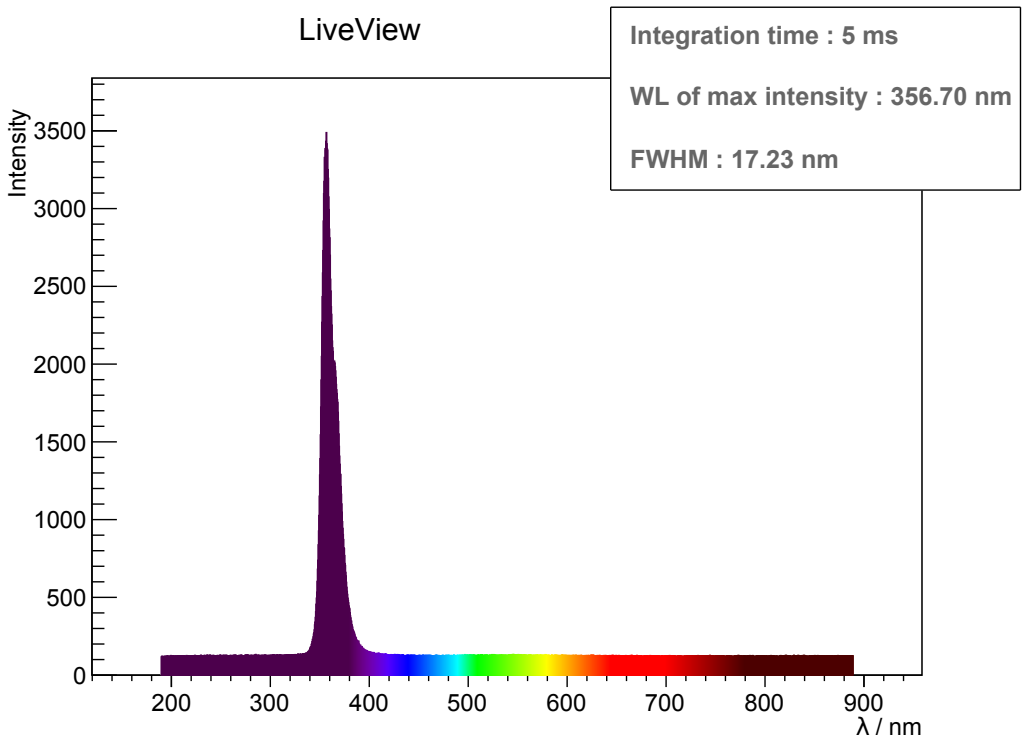

Figure 7.1.: Screen shot of spectrometer LiveView while monitoring LED 4 via direct light path. Shown are the current spectrometer data, the determined peak wavelength and width, and the chosen integration time.

while the user is adjusting or changing components of the test set-up. This software offers a real time display (LiveView) of the current spectrometer data, including real-time analysis of peak wavelength and peak width (FWHM). A screen shot of the software in action is shown in Figure 7.1. Different options can be passed to the software at start, e.g. setting fixed or automatic integration time, choosing different averaging modes, set the background subtraction level, and enable plot creation and data export.

7.2. SiPM measurements

In this section some of the possible SiPM measurements are described.

7.2.1. Polarity and quenching resistor value

The first measurement of a newly installed SiPM is a quick polarity check to protect the SiPM from possible damage. In case the SiPM was plugged in the wrong way a measurement with low voltage will run into the implemented current limit of 1 mA. The error condition is displayed in the terminal output on the controlling computer and the user is asked to reinsert the SiPM in the correct orientation. The measurement of the forward current can also be done on purpose as shown in Figure 7.2 to obtain the quenching resistance value. This is possible because the GAPD cells are supplied with forward bias and thus the depletion is reduced and the pn-junctions become conductive. Hence a simple linear fit obtains the resistance value. From the measured resistance (R) the single quenching resistor (R_Q) can be determined by assuming that the resistors from all cells are used in parallel as shown in Figure 2.15. The results shown here match to the values stated in [60]. This leads to the following equation:

$$R_Q \quad = \quad R \cdot n_{cell}, \tag{7.1}$$

where n_{cell} is the number of cells in the SiPM. The measured temperature dependency of the resistance is shown in Figure 7.3.

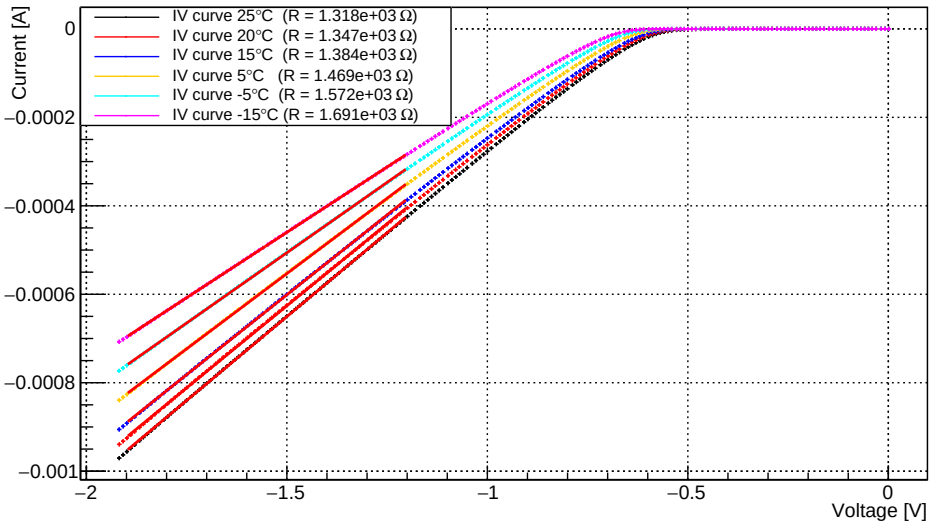

Figure 7.2.: Forward I-V measurement at different temperatures with fits for the total forward resistance R.

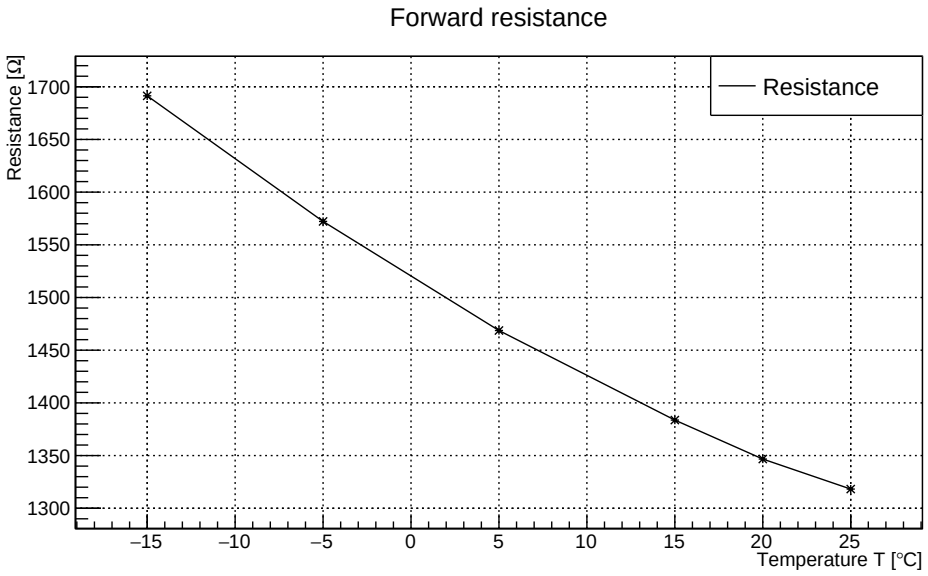

Figure 7.3.: SiPM forward resistance versus temperature.

7.2.2. I-V characteristics

The next measurement performed on any new SiPM is a simple current versus voltage curve with no light source (see Figure 7.4). This measurement starts at the low voltage (0 V) and may go up to 75 V[18], the currently hard coded safety limit. If SiPMs with higher required voltages are tested the measurement software requires a few simple changes and a recompilation. The hardware could deliver and withstand up to 100 V. Increasing the voltage above the hardware limit requires the exchange of the used SiPM HV supply voltage filtering components. The measurement is stopped if the measured current reaches 1 mA. If this limit is reached at voltages of a few volts, a warning is raised, as the SiPM is probably polarity-reversed. The voltage at which the current limit is reached is used as the upper limit for the next measurements at the current temperature.

[18] Currently the highest used supply voltage for SiPM measurements with this test set-up.

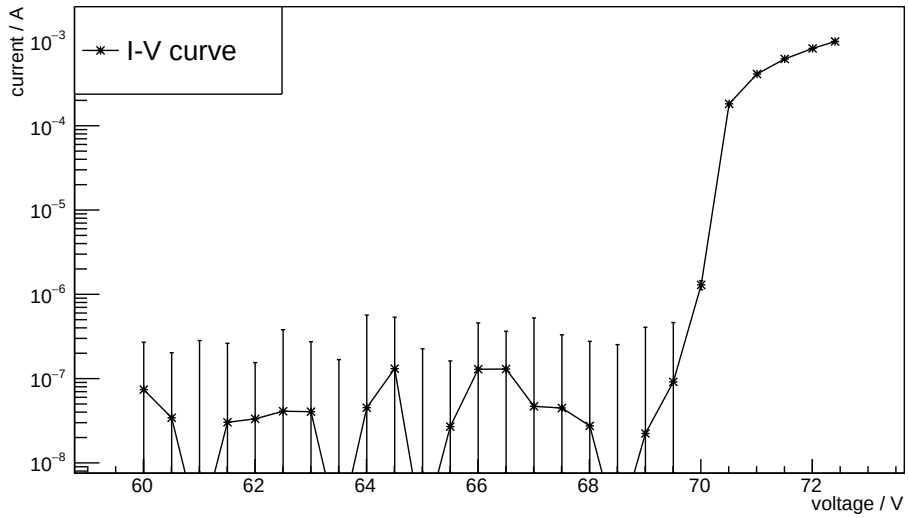

Figure 7.4.: Simple and quick IV scan without light for first voltage limit. It is stopped when the current limit of 1 mA is reached. The currents voltages smaller than 69 V are induced by the connected pre-amplifier. Stabilised SiPM temperature during this measurement was 10 °C

.

7.2.3. I-V characteristics with high light flux

Doing a similar measurement with a continuous high light flux illuminating the SiPM, one can extract more information from the I-V scan, namely the breakdown voltage of the SiPM. The first scan in this measurement starts at the upper voltage limit determined with normal dark I-V measurement described in Section 7.2.2. The first scan spans a range of 7 V in steps of 250 mV downwards from the upper voltage limit. From the measured I-V data a relative change per volt c_{rel} (analytical):

$$c_{rel} = \frac{dI}{dV} \cdot \frac{1}{I} \tag{7.2}$$

is calculated in three ways (numerical) from the n discrete data points of voltage V and current I:

$$c_{rel+}[n] = \frac{I[n+1]-I[n]}{V[n+1]-V[n]} \cdot \frac{1}{I[n]} \tag{7.3}$$

$$c_{relavg}[n] = \frac{I[n+1]-I[n-1]}{V[n+1]-V[n-1]} \cdot \frac{1}{I[n]} \tag{7.4}$$

$$c_{rel-}[n] = \frac{I[n]-I[n-1]}{V[n]-V[n-1]} \cdot \frac{1}{I[n]} \tag{7.5}$$

The calculation of c_{rel+} (c_{rel-}) lacks the last (first) point, and c_{relavg} lacks both. The resulting curve is given in Figure 7.5 and one can see the two large peak for c_{rel+} and c_{rel-}, while c_{relavg} is much lower. These large peaks are scanned and their positions are averaged and used as the central voltage of the final I-V scan. This last scan only uses the small window of $\pm 1\,\mathrm{V}$ and steps of $25\,\mathrm{mV}$ around the determined central voltage. The relative changes c_{rel+} and c_{rel-} are computed and the peak positions are determined and fitted again. The peak positions correspond to the breakdown voltage of the SiPM. Using the two ways of calculating c_{rel} an uncertainty can be estimated. The quantity c_{relavg} is not used for the final result as it had in many cases a large error on its fitted peak position and was often shifted.

An additional peak somewhat left of the current peak can be found, if the current measurement is done with only a directly connected SiPM and no further components. The additional components increase the leakage current and hence the minimal flowing current.

The result of the fine scan shown in Figure 7.6 is a breakdown voltage of $V_{br} = (69.295 \pm 0.017)\,\mathrm{V}$. Doing this measurement at different temperatures allows for the determination of the temperature dependency of the breakdown voltage as shown in Figure 7.7. The error of the single measurement of V_{br} is obtained from the average of the two different calculations of c_{rel} and thus having two peak positions. A cross-check of this error estimate was done by repeating the measurement at a constant SiPM temperature for a long time ($\sim 23\,\mathrm{h}$). The measurement shows some variation over time as can be seen in Figure 7.8, but stays within the given error of $\pm 20\,\mathrm{mV}$ of the single measurement points. There seems to be a correlation between varying ambient (and hence also the sourcemeter) temperature and the determined breakdown voltage (V_{br}) of the temperature-stabilised SiPM. During tests of this method the influence of the light flux and the used wavelength was tested. The wavelength was found to have no influence on the result. The light flux has influence on the peak height and width but not on the peak position, but lower fluxes lead to smaller and wider peaks. The used flux of $3.7 \cdot 10^7$ photons per seconds at a wavelength around $460\,\mathrm{nm}$ was sufficient for a precise peak position determination.

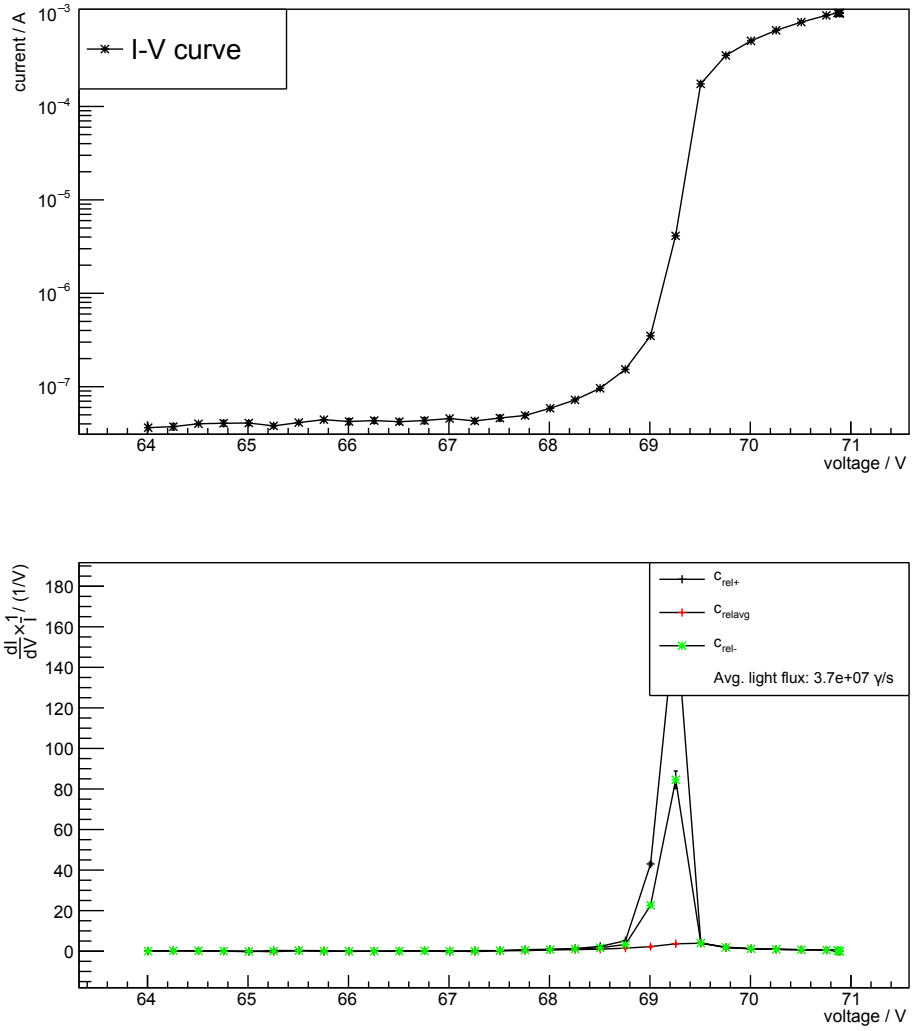

Figure 7.5.: Coarse scan for V_{br} at a stabilised SiPM temperature of $-5\,°C$. In the upper half the measured I-V curve is shown. The lower part shows the $dI/(dV \cdot I)$ data.

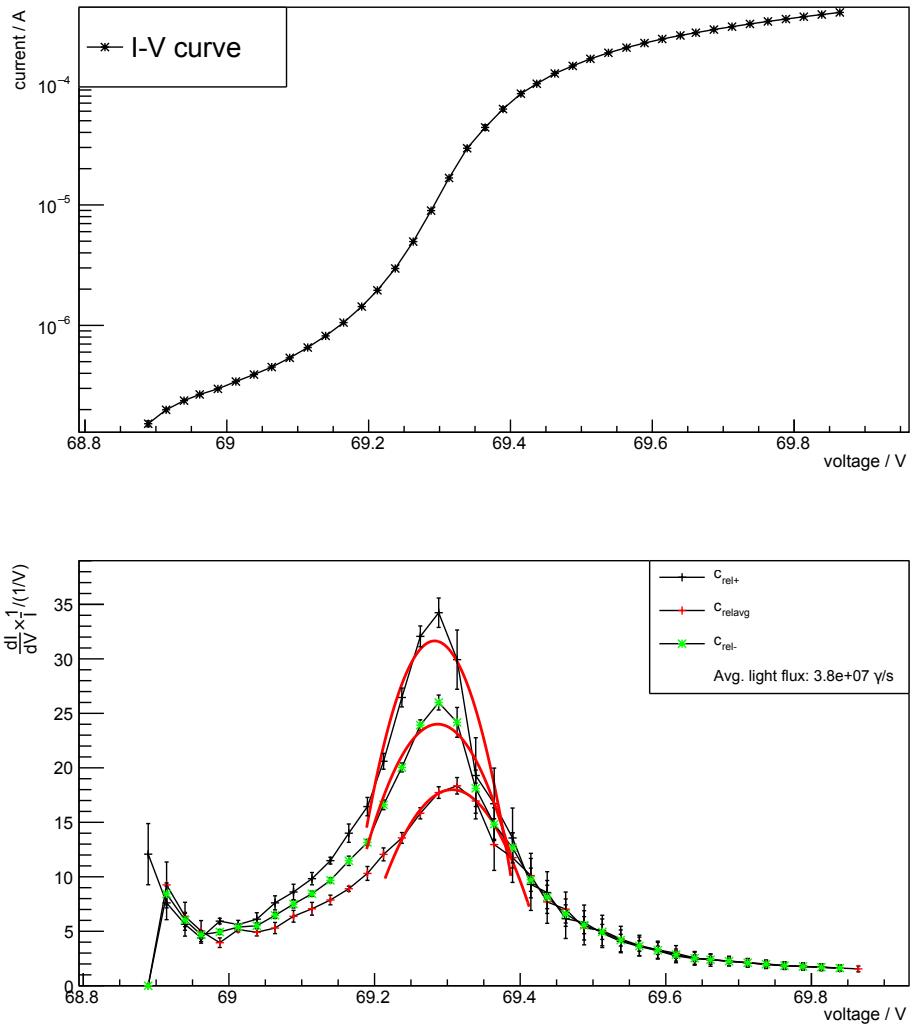

Figure 7.6.: Fine scan for breakdown voltage (V_{br}) at a stabilised SiPM temperature of $-5\,°C$. In the upper plot the measured I-V curve is shown. The lower plot shows the fine $dI/(dV \cdot I)$ data with fits to the peaks (red lines).

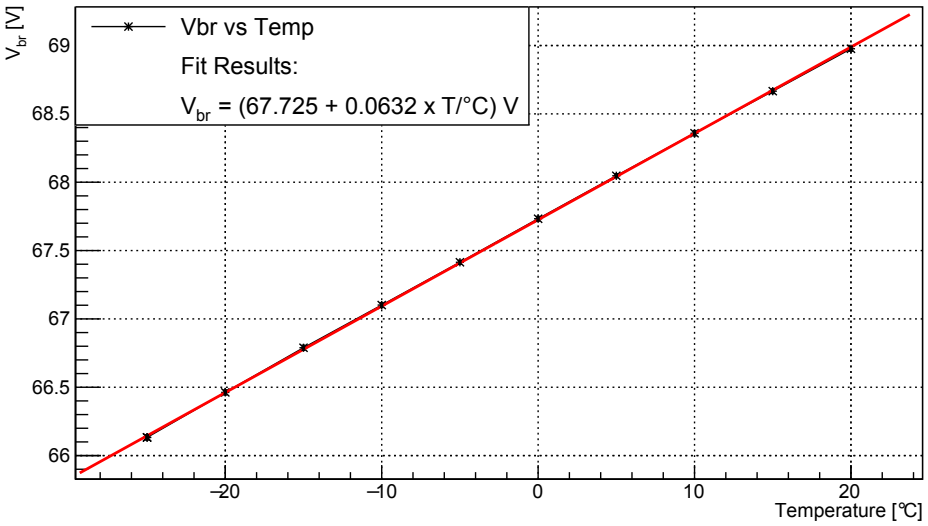

Figure 7.7.: Temperature dependency of breakdown voltage (V_{br}).

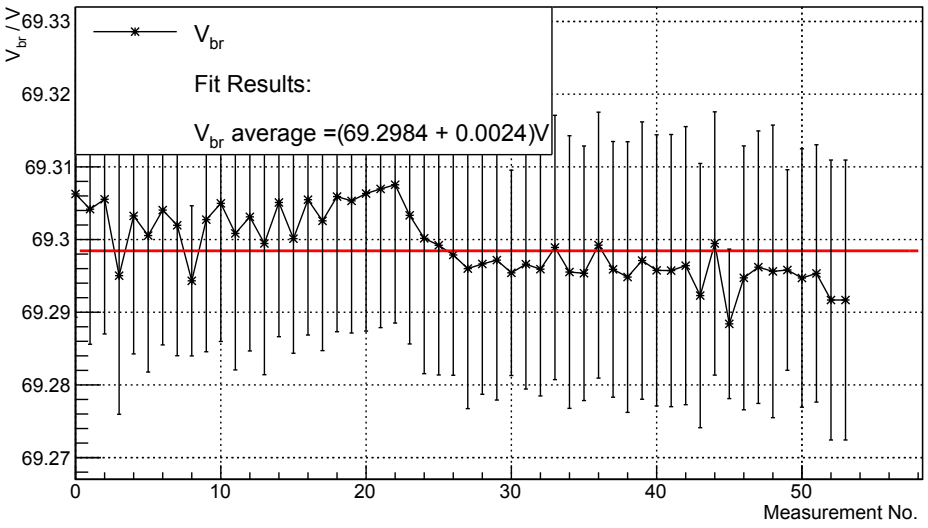

Figure 7.8.: Variation of breakdown voltage (V_{br}) over time at a temperature of 25 °C.

7.2.4. Thermal noise

The thermal noise rate (dark count rate) can be determined from long SiPM traces recorded in the dark. The peak finder described in Section 6.1.3 is used to identify the single peaks. If the measurement is taken in the dark, all these clean (filtered) events should be mostly thermal noise events, but a contamination with afterpulses is possible. The contamination is investigated in Section 7.2.5. The time differences between the single events are filled into a histogram. This histogram has a clear turn on at the time difference required in the filtering. Due to the optimised filter approach described in Section 6.1.3, some entries are in the time bins below the turn on, but these do not affect the following analysis. An exponential fit to the high time tail ($> 4\,\mu$s) yields the thermal noise rate.

$$f(\Delta t) \quad = \quad \exp(a + b \cdot \Delta t) \tag{7.6}$$

where a is the *Constant* and b is the *Slope*. An example distribution and the exponential fit are shown in Figure 7.9, the obtained χ^2/ndf is 0.91. The thermal noise rate/dark count rate (parameter b times -1) for the shown example is $(350 \pm 2)\,$kHz at a temperature of $15\,^{\circ}$C. It should be noted that each filtered peak lowers the thermal noise rate, as a missed peak leads to the combination of two times into one time.

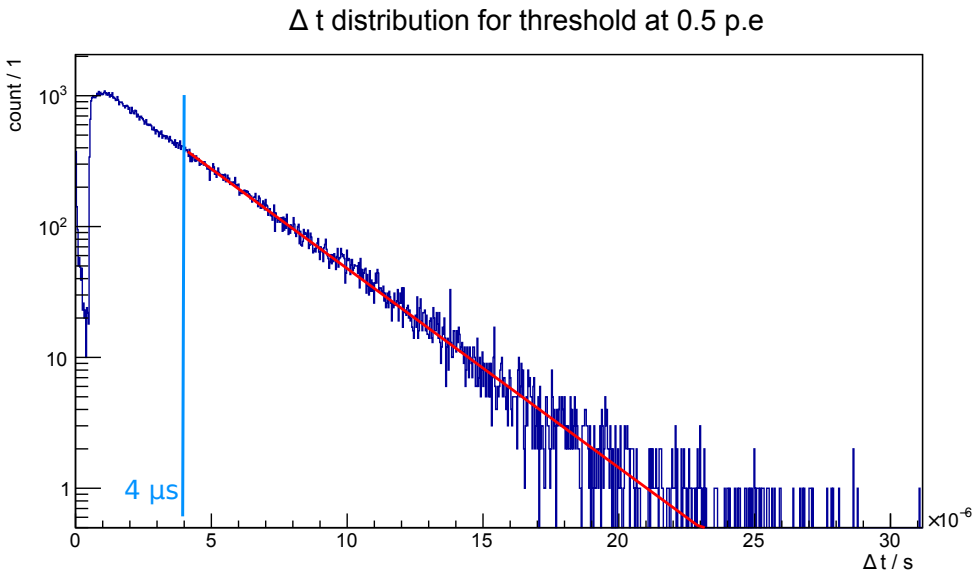

Figure 7.9.: Thermal noise plot displayed with y-axis in log-scale for a temperature of 15 °C. The data used for this are time differences from the found clean triggers. The exponential fit range starts at 4 μs and ends with the last filled bin.

7.2.5. Afterpulses

A similar approach to the one shown for the thermal noise in Section 7.2.4 can be used to determine the afterpulsing properties. Figure 7.10 shows the now used three consecutive, more and more constrained fits to extract the short and long afterpulse time constants, too. This analysis can also be run with a 0.5 p.e. triggered short trace. The best available one p.e. threshold is derived from the peak height spectrum. Doing the measurement with low light flux (e.g. single-photon pulses) instead of no flux, the real and unbiased[19] time constants for the long and short component of the afterpulsing can be determined. The result of the first fit has no longer the meaning of the thermal noise, as it is largely increased by the light flux to suppress the effects of the thermal noise bias. To prevent further bias one could use only single-photon signals as initial event triggers, since higher signals contain multiple firing cells and thus have a higher chance of creating afterpulses. However, this does not protect against crosstalk in an afterpulse. The filtering criteria have large impact on the fit results to the Δt distribution as shown in the Table 7.1. The same plot as shown in Figure 7.10 can be found in Figures C.7 to C.10 for the

[19] Normally there are a few noisy cells which account for most of the dark noise. If photon flux is present the firing cells are random.

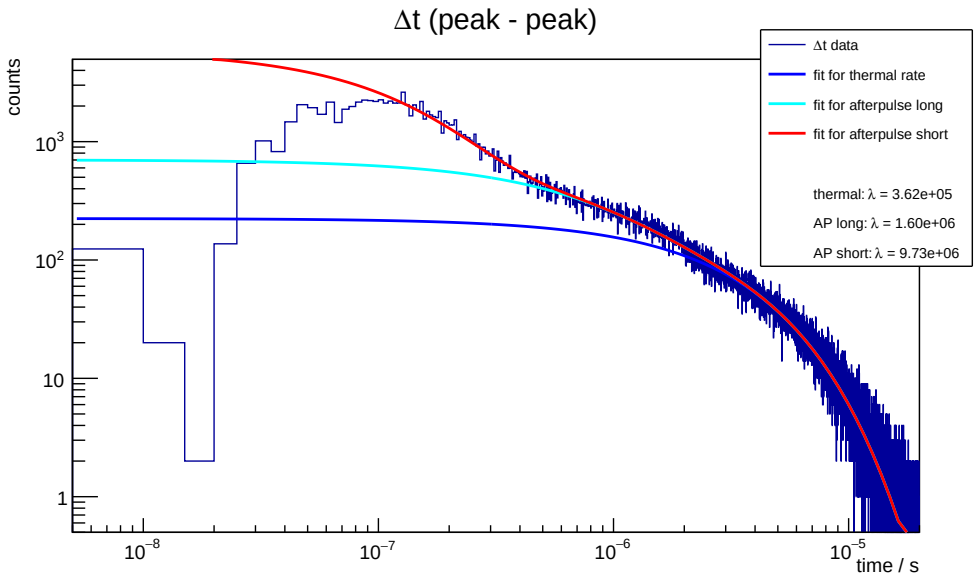

Figure 7.10.: Distribution of peak to peak times from the afterpulse search with three fits. The first fit is a simple exponential function, shown in blue. It covers the high time range and thus the thermal noise component. The next fit is a sum of two exponential functions for the long component of the afterpulses, it is shown in cyan. One of the exponential functions is constrained with the results from the first fit. The last fit is a sum of three exponential functions taking care also of the short component of the afterpulses, shown in red. Two of the functions are constrained with the result from the second fit. The filtering parameter in this plot are any p.e. and 500 ns silence time.

different filtering parameters. For the same filtering settings (500 ns, any p.e.) the thermal time constants are similiar for the distributions shown in Figure 7.9 and 7.10 although one contains many afterpulse events and the other mostly clean signal.
The data obtained from the afterpulse analysis can also be displayed as a 2D plot, as shown in Figure 7.11. A measurement described and performed [61] for the same type of SiPM obtained a single time constant of 217.5 ± 5.9 ns, corresponding to a rate of $4.6 \cdot 10^6$. This value lays in the range of the values obtained by the different filtering parameters.

	1 p.e. 50 ns	1 p.e. 500 ns	any p.e. 50 ns	any p.e. 500 ns
thermal	$3.45 \cdot 10^5$	$2.28 \cdot 10^5$	$4.80 \cdot 10^5$	$3.62 \cdot 10^5$
AP long	$1.85 \cdot 10^6$	$1.63 \cdot 10^6$	$2.21 \cdot 10^6$	$1.60 \cdot 10^6$
AP short	$1.20 \cdot 10^7$	$7.52 \cdot 10^6$	$1.05 \cdot 10^7$	$9.73 \cdot 10^6$

Table 7.1.: Fit results for the three parameter for different filtering parameters (1 p.e. or any p.e.; silence time 50 ns or 500 ns) at a temperature of 15 °C and an overvoltages of 1.2 V. The unit of the fitted parameter is 1/s.

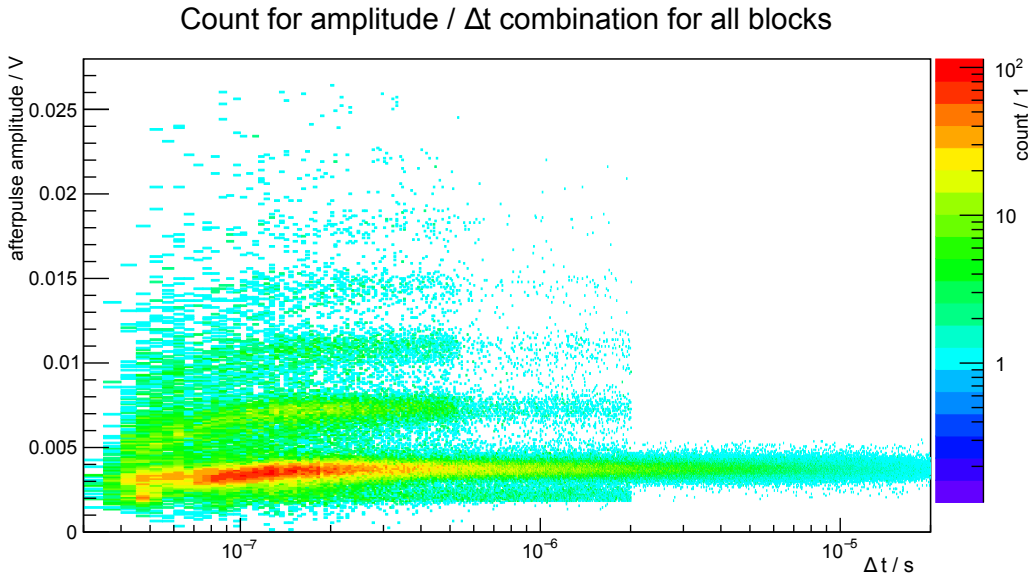

Figure 7.11.: Count versus afterpulse amplitude and Δt evaluated for 1 p.e. peaks (initial trigger). Crosstalk occurring in an afterpulse signal has not been removed. The corresponding plot with all triggers is shown in Figure C.11.

7.2.6. Optical crosstalk

Long traces of SiPM signals recorded with low light flux can be used to determine the optical crosstalk. For each event in the data the charge is calculated by the algorithm described in Section 6.1.6. The charge value is filled into a histogram. As shown in Figure 7.12 some peaks can be fitted with a Gaussian function. If the event selection is fully efficient no pedestal peak is visible. If the event selection (peak filtering) does not work efficiently due to non-rejected noise events, some events will be in the pedestal. The contamination is typically below 1 %.

The optical crosstalk probability can be calculated by using two integrals: the first is that from the end of the pedestal or, alternatively, from the nominal zero position,

if no pedestal is present, to the middle between first and second p.e. peaks and the second is that from the middle between first and second p.e. peaks to infinity:

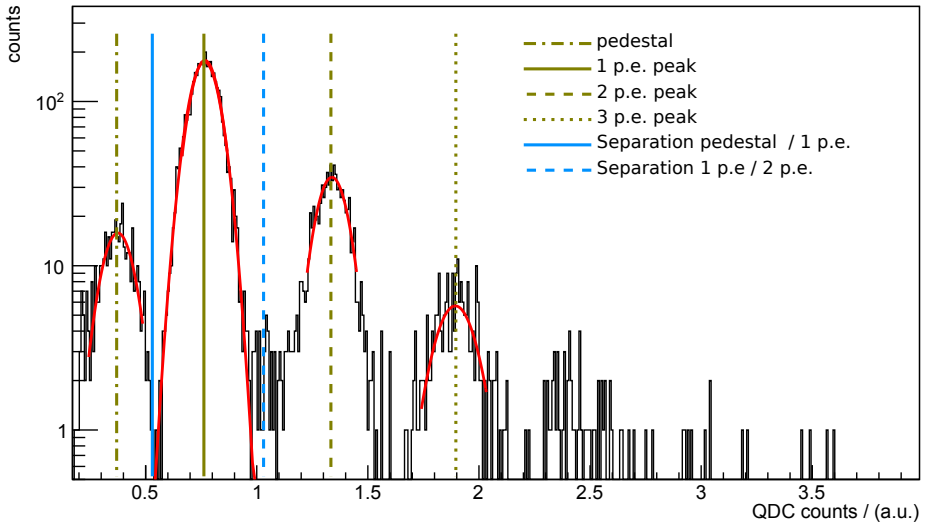

Figure 7.12.: QDC Histogram with the markers used for optical crosstalk and gain determination. The blue solid line marks the separation of the pedestal on the left and the one p.e. peak/signal region on the right. The black dashed line marks the separation between 1 p.e. and 2 p.e. signal. The olive dash-dotted line marks the pedestal peak, the solid, dashed and dotted olive lines mark $1, 2, 3$ p.e. peaks, respectively.

$$N_{1\mathrm{pe}} = \sum_{0.5p.e.}^{1.5p.e.} \#entries \tag{7.7}$$

$$N_{>1\mathrm{pe}} = \sum_{1.5p.e.}^{\mathrm{inf}} \#entries \tag{7.8}$$

$$P_{ct} = \frac{N_{>1pe}}{N_{1pe} + N_{>1pe}}. \tag{7.9}$$

This analysis can also be run with a 0.5 p.e. triggered short trace. The best available p.e. threshold is from the peak height spectrum.

7.2.7. Gain

The average gain of an SiPM can be determined from a QDC spectrum where the 1 p.e. and 2 p.e. peak positions can be determined. The difference of the peak posi-

tions, a charge value, is now corrected for the gain from the pre-amplifier (see Section 5.3.1). Dividing this charge value by the elementary charge e gives the gain of the SiPM. One has to keep in mind that for a correct gain measurement the full SiPM signal must be integrated for the QDC histogram. The histogram shown in Figure 7.12 is optimized for peak separation and thus not useful for the gain determination.

7.2.8. Photon detection efficiency

In this section the relative and absolute p.d.e. measurements are described.

7.2.8.1. Relative p.d.e.

The relative p.d.e. (photon detection efficiency) is the ratio of the p.d.e. at a certain wavelength and the p.d.e. at the wavelength chosen for normalisation. Normally this is a point out of the same measurement. In this case the relative p.d.e. is 1 at the normalisation point. If a comparison across different measurements is need, a freely chosen normalisation can be used for all of them. This inter measurement comparison is only useful, if the overvoltage is kept at the same value, as the SiPM current depends on the gain and the gain depends on the overvoltage. This allows for example for a comparison of the relative p.d.e. at different temperature for the same overvoltage.
For the relative p.d.e. the currents of the reference detector and the SiPM are recorded for different wavelengths (including the dark current measurement and the correction for it). The current of the reference detector is used to calculate the light flux on the SiPM at each measured wavelength. Then the ratio between the SiPM current and light flux on the SiPM is calculated and normalised:

$$\Phi_{sipm}(\lambda) = \Phi_{pin}(I_{pin}, \lambda) \cdot c_{geom} \cdot R_{r/t}(\lambda) \tag{7.10}$$

$$rel.\,p.d.e.(\lambda) = \frac{I_{sipm}(\lambda)}{\Phi_{sipm}(\lambda)} \cdot \frac{1}{c_{normalise}} \quad \text{with} \tag{7.11}$$

$$c_{normalise} = \frac{I_{sipm}(500\,\text{nm})}{\Phi_{sipm}(500\,\text{nm})} \quad \text{or} \tag{7.12}$$

$$c_{normalise} = 0.1 \cdot 10^{-12} A \cdot s/\gamma. \tag{7.13}$$

The key to this measurement is to tune the light flux, where the SiPM signal current is sufficiently large compared to the dark current but the SiPM is still in the linear regime of the dynamic range which is described in Chapter 7.2.9. Hence the photon flux times the recovery time of a cell should be much smaller than the number of

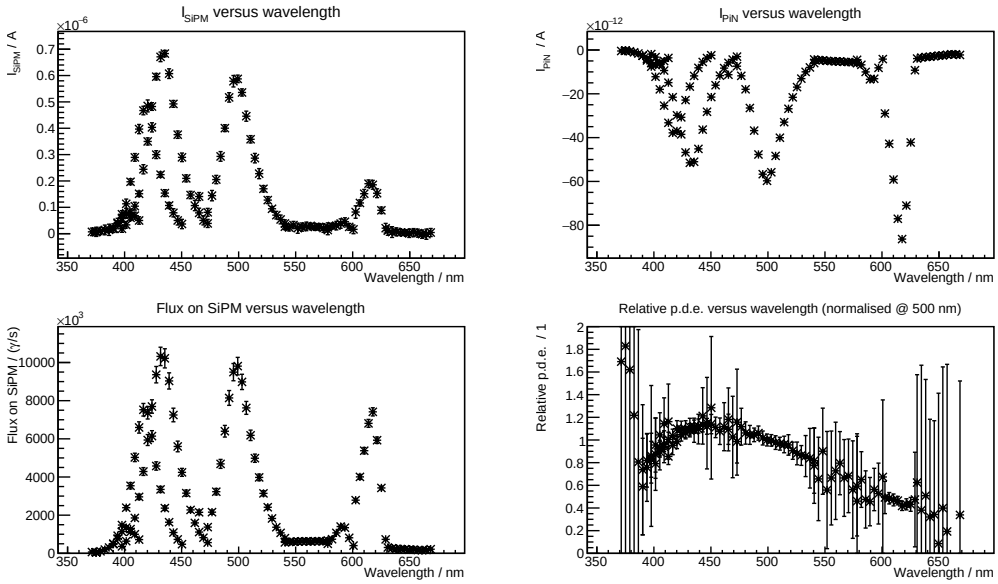

Figure 7.13.: Relative p.d.e. measurement at 25 °C and an overvoltage of 1.0 V (recommended by manufacturer), normalised at 500 nm.

cells of the SiPM. The four used variables and their errors are shown in Figure 7.13. The errors becomes large, where only lowest fluxes are available.

7.2.8.2. Absolute p.d.e.

The absolute p.d.e. is the main property of an SiPM, that defines the optical performance.It is the probability that an single incident photon creates an one p.e. or larger signal. In most cases the highest possible absolute p.d.e. is desired, as reducing the incoming light by a filter is always possible (easily by filter foil in front of SiPM) to stay in the dynamic range of the SiPM. While increasing the number of photons on the SiPM is often a complex process of optimising the whole set-up. Thus when testing SiPMs the absolute p.d.e. must be measured. To measure the absolute p.d.e. two short trace measurements are recorded with known (measured) pulsed low (single photon) light flux, one with low light flux and one in the dark. From these two measurements four numbers are determined and used for the calculation of the absolute p.d.e. with the help of the underlying Poisson statistics.
To give an impression of the signal recorded in the low light flux measurement, it is shown as a virtual afterglow/heatmap overlaying all short signal traces in Figure 7.14. The signal region integrated by the analysis software SoftQDC is marked in blue and starts 75 ns after the trigger, which occurs in the middle of the shown traces and is marked in black. The integration windows ends 175 ns after the trigger. The analysis software tool SoftQDC, as presented in Section 6.2.1, is used to create

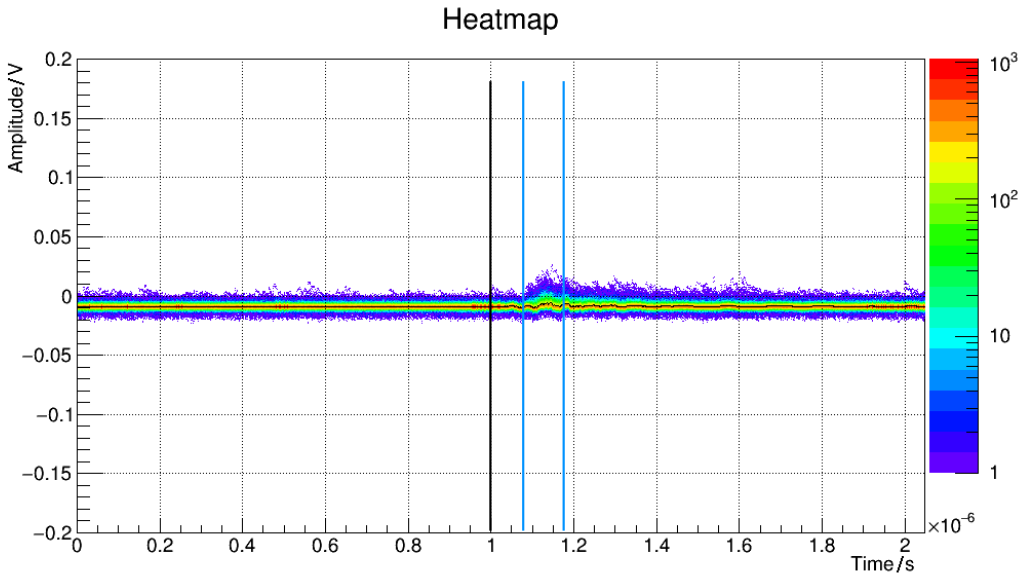

Figure 7.14.: Heat map for the absolute p.d.e. measurement at low light flux. The used signal region, marked with blue lines, is from +75 ns to +175 ns after the trigger, which occurs at the middle of the traces (1000 ns) and is marked with a black line.

finger spectra for both measurements similar to the ones shown in Figures 7.15 and 7.16. The shown examples were measured at −5 °C and 503 nm. The red lines are

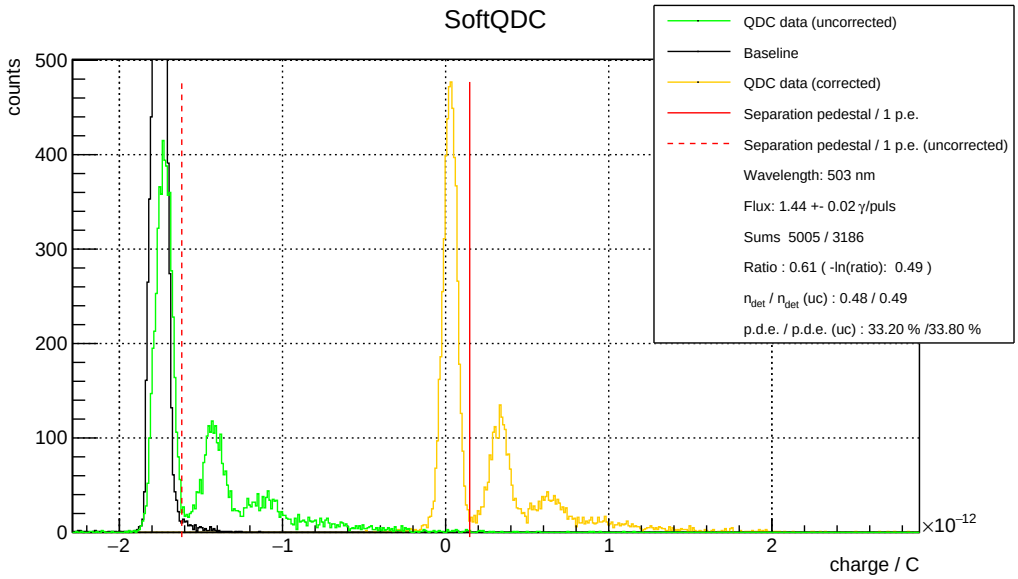

Figure 7.15.: Finger spectrum for absolute p.d.e. measurement (low light flux) for 8191 short traces for a overvoltage of 1.2 V. This plot is taken directly from the output of the analysis software.

determined in the low light flux measurement and represent the position where the pedestal and signal peaks are separated for analysis in both measurements. The yellow curve is the corrected QDC data resulting from correcting each trigger for its baseline shift. The baseline shift is drawn in black and the raw uncorrected QDC data in green.

For higher overvoltages the baseline tends to get noisier. Examples for the noisy QDC spectrum and the corresponding heat map are shown in Figure 7.17 and 7.18 and a simple shift correction does not always improve the results. The correction with the baseline is still required in cases the pedestal is not in the measured spectrum. Hence the p.d.e. is calculated from the uncorrected QDC data, too. It is marked with 'uc' in the legend. The sum over the pedestal peak and the sum over the signal are

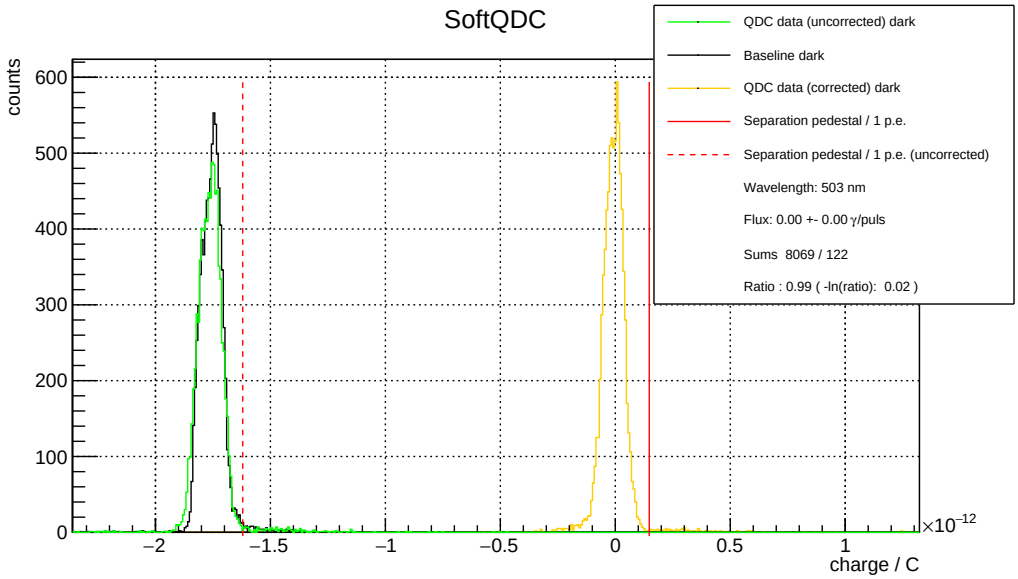

Figure 7.16.: Finger spectrum for absolute p.d.e. measurement (dark) for 8192 short traces for a overvoltage of 1.2 V. This plot is taken directly from the output of the analysis software, due to automatised plot creation the zero position is not at the same position as for the low light flux measurement.

calculated for the low light flux measurement (Figure 7.15):

$$N_{ped} = \sum_{-\infty}^{0.5p.e.} \#entries\,(\text{lowlightflux}) = 5005 \tag{7.14}$$

$$N_{signal} = \sum_{0.5p.e.}^{\infty} \#entries\,(\text{lowlightflux}) = 3186 \tag{7.15}$$

$$N_{tot} = N_{ped} + N_{signal} = 8191 \tag{7.16}$$

and for the dark measurement (Figure 7.16):

$$N_{ped,dark} = \sum_{-\infty}^{0.5p.e.} \#entries\,(\text{dark}) = 8069 \tag{7.17}$$

$$N_{signal,dark} = \sum_{0.5p.e.}^{\infty} \#entries\,(\text{dark}) = 122 \tag{7.18}$$

$$N_{tot,dark} = N_{ped,dark} + N_{signal,dark} = 8191. \tag{7.19}$$

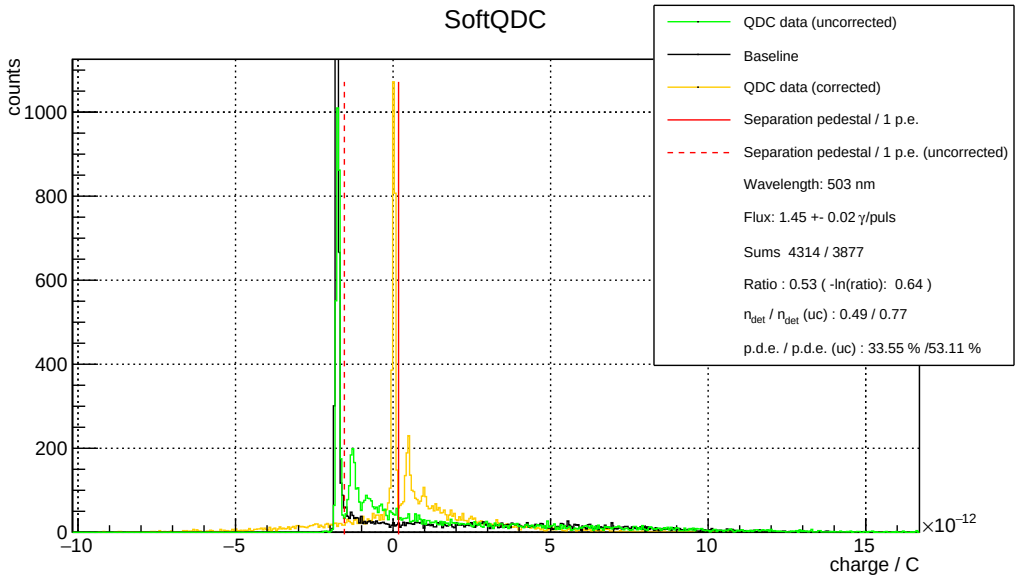

Figure 7.17.: SoftQDC spectrum for absolute p.d.e. measurement at low light flux and too high overvoltage (1.9 V). Temperature and wavelength are the same as in the measurement shown in Figure 7.15. The baseline data shows a sharp peak and right next to it a very wide spread resulting in a very broad corrected data distribution.

The underlying Poisson statistics is defined as:

$$P_\lambda(n) \quad = \quad \frac{\lambda^n e^{-\lambda}}{n!} \tag{7.20}$$

with n as the number of detected photons and λ the average number of detected photons. Since n is disturbed by noise (crosstalk and afterpulses) only the value of $n = 0$ is interesting for the analysis since it does not include any noise. This simplifies the expression to:

$$P_\lambda(0) \quad = \quad e^{-\lambda} \tag{7.21}$$

This expression can be used to determine the average number of detected photons λ that are expected when the left part is known. The probability of detecting 0 photons can be determined from numbers extracted from the QDC spectra and corrected for the noise events:

$$P_\lambda(0) \quad = \quad \frac{N_{ped}}{N_{tot}} \cdot \frac{N_{tot,dark}}{N_{ped,dark}} \tag{7.22}$$

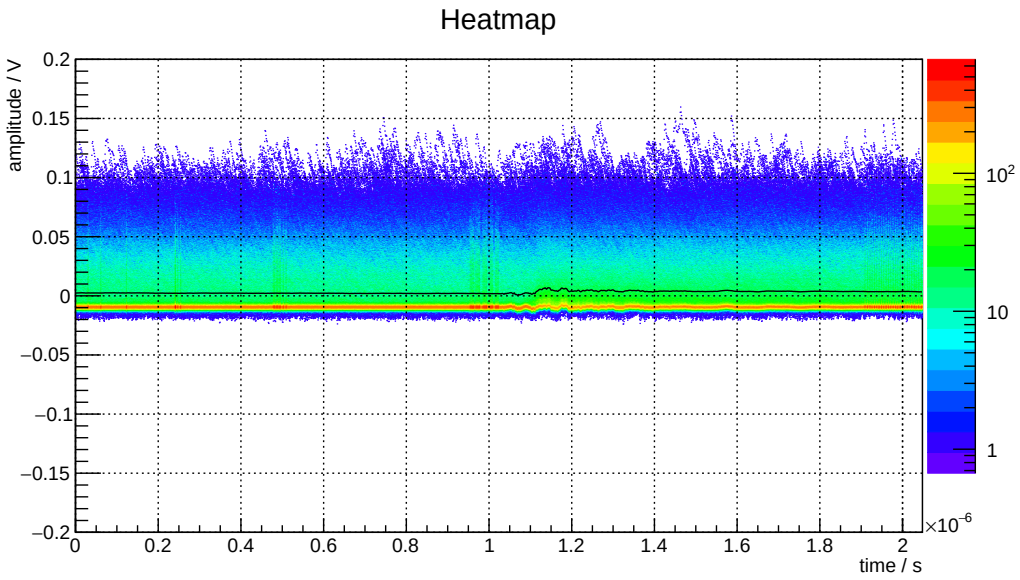

Figure 7.18.: Heat map for the absolute p.d.e. measurement at low light flux and too high overvoltage. The chosen signal region is from 75 ns to 175 ns after the trigger at 1000 ns. The signal region does not differ from the surrounding noise signals.

Combining Equations 7.21 and 7.22 leads to:

$$e^{-\lambda} = \frac{N_{ped}}{N_{tot}} \cdot \frac{N_{tot,dark}}{N_{ped,dark}} \tag{7.23}$$

$$\lambda = -\ln\left(\frac{N_{ped}}{N_{tot}}\right) + \ln\left(\frac{N_{ped,dark}}{N_{tot,dark}}\right) \tag{7.24}$$

$$\lambda = 0.48\,\gamma\,\text{per pulse} \tag{7.25}$$

Using the measured light flux ($n_{\gamma\,per\,pulse} = 1.44 \pm 0.02$ photons per pulse), one can now calculate the absolute p.d.e.:

$$p.d.e. = \frac{\lambda}{n_{\gamma\,per\,pulse}} = \frac{0.48}{1.44} = 33.2\% \tag{7.26}$$

The uncertainties are determined from the statistical error of the light flux measurement ($n_{\gamma\,per\,pulse}$) and the result of a variation of the position of the red line, thus varying the four determined numbers. For the example this shift of the separation between pedestal and signal results in the two values of 34.13% and 32.97% for a shift of two bins. For the given example the relative statistical error for the measured light flux is around 0.015. The systematic uncertainty (1 %) from the calibration of the reference detector are not included here. The final value with out the systematic

from the reference calibration is $(33.20^{+0.93}_{-0.23} \pm 0.50)\%$ at a temperature of $-5°C$ and an overvoltage of 1.2 V for a wavelength of 503 nm. There is no value for this exact operating point given by the manufacture, but the result is very reasonable as the extrapolation of the manufacturer given curves matches well.
Measuring the absolute p.d.e. for various operating conditions yields plots like Figure 7.19. This plot proves that the absolute p.d.e. is independent of the temperature for the tested range from $-25\,°C$ to $25\,°C$ for not to high overvoltages (less than 1.8 V). The recommended overvoltage for the used SiPM is 1.0 V.

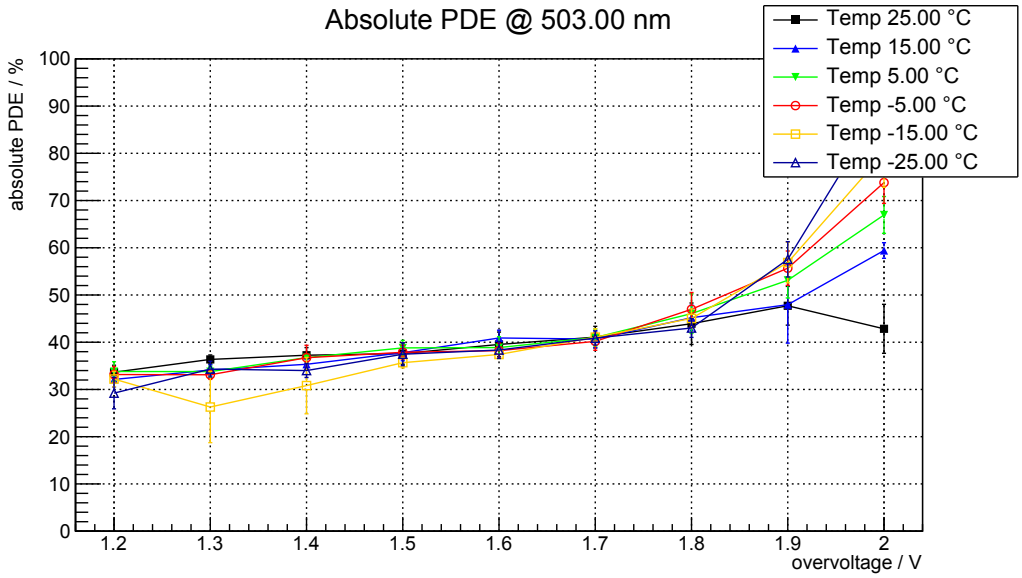

Figure 7.19.: Absolute p.d.e. versus overvoltage for 503 nm for different temperatures from the uncorrected QDC data. For the high overvoltages the limits of the Poisson method can be seen, as the noise contribution is getting so large at 25 °C, that the rise in p.d.e. is not visible any more (black curve) and a spread between the p.d.e. for different temperatures is observed. The given uncertainties are the statistical error of the light flux measurement ($n_{\gamma\, per\, pulse}$) and the result of a variation of the position of the red line, thus varying the four integrals used for calculation.

7.2.9. Dynamic range measurement

The deviation from the linear response is due to the limited dynamic range of the SiPM, since it has only a limited number of cells with a finite recharge time. While all cells are recharging, no new full height signals are generated. For measuring the dynamic range, the incident photons on SiPM and the response of the SiPM are

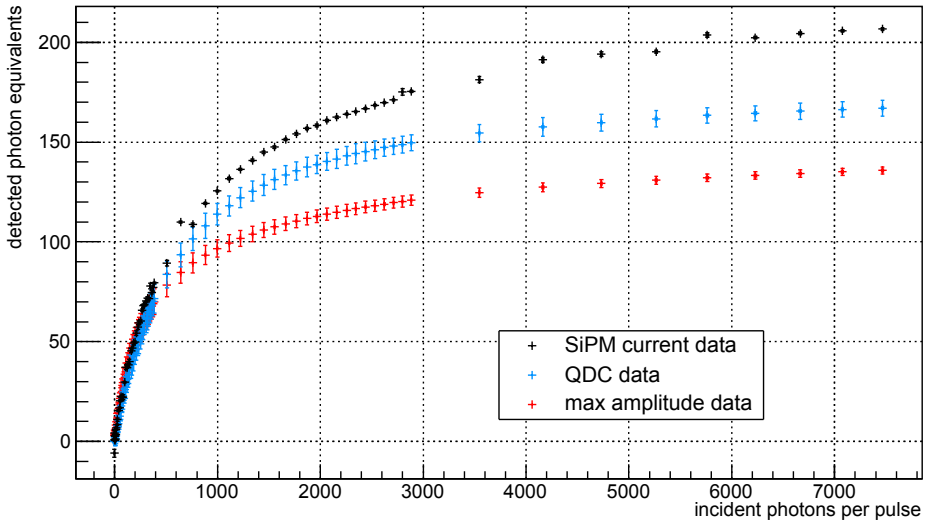

Figure 7.20.: Dynamic range measurement with three different methods for determination. The current data (black) is the highest, because it is influenced most by the afterglow of the LED. The QDC data (blue) is a little less influenced by this phenomena. The maximum amplitude has the cleanest signal, as it is not influenced by the extended light flux.

measured. The SiPM active area is completely illuminated. For each measurement point the incident photon number is increased by raising the voltage of the HV pulser. The resulting curves are shown in the Figure 7.20. In this figure three different results for the same dynamic range measurement are shown. Shown are the result from the current (black), the SoftQDC (blue), and the maximal amplitude (red). There are some differences in these three results. The amplitude method has the flattest tail, as it measures only the initial rise in the SiPM response. The SoftQDC method is more influenced by the timely extended photon flux which is longer at higher pulser voltages (see Figure 7.21 and 7.22) and thus have a steeper rising tail than the maximum amplitude method. The gain for the pulses triggered by the later arriving photons is lower than in the Geiger mode but still high enough to generate significant amounts of charge that contribute to the SiPM current and the SoftQDC signal. Since the integration windows is limited the tail flattens out. The current result keeps rising, too, as the current measurement can be seen as a QDC measurement with infinite integration time.

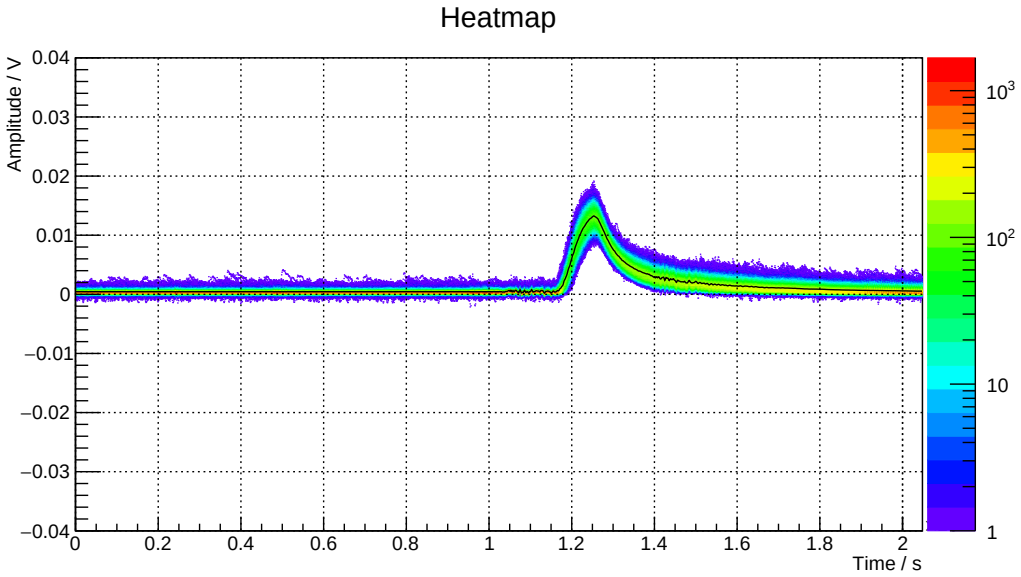

Figure 7.21.: Dynamic range heat map for a HV pulse voltage, where the afterglow of the LED is not yet a problem.

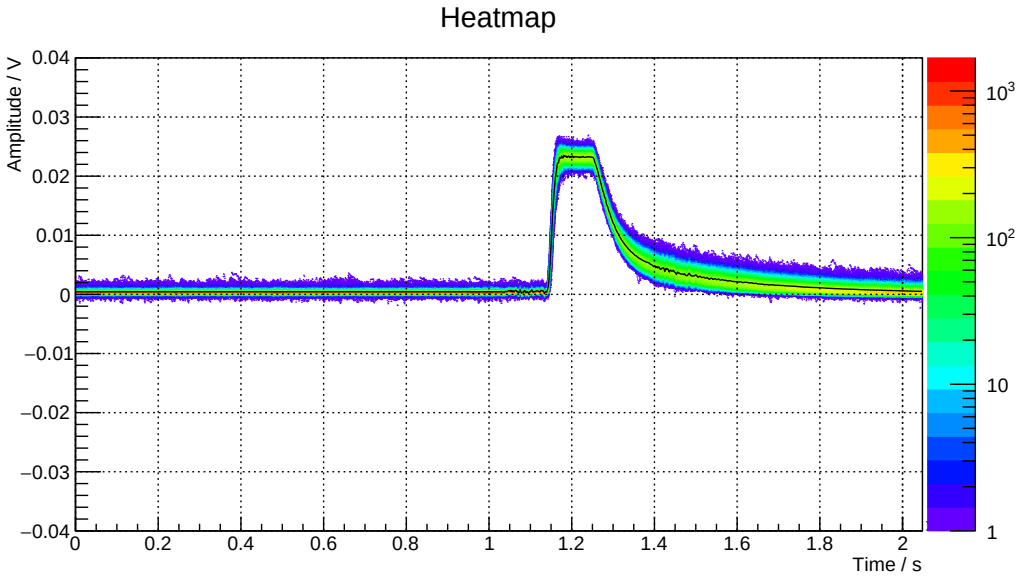

Figure 7.22.: Dynamic range heat map for a HV pulse voltage, where the afterglow of the LED is a problem as is leads to a flat plateau. It was checked, that this is no saturation effect of any electronics beside the SiPM.

8. Summary and Conclusion

In the context of this doctoral thesis a test set-up which offers a 4D parameter space for characterisation of SiPM properties was designed, built and tested. The 4D parameter space is defined by the 4 parameters that can be controlled by the test set-up: the temperature, the overvoltage, the wavelength, and intensity of the incident photons. The realisation of the concept was achieved with commercial and custom-made hardware. The development of the custom-made hardware was done in the course of this doctoral thesis, some ideas and concepts were tested in Bachelor and Master theses beforehand. The required custom hardware was built by the mechanics workshop of the Physics Institute III A. Ideas for the electronics were developed by the author of this doctoral thesis and then realised with the help of the electronics workshop of the Physics Institute III A. The firmware for the custom-made hardware was developed and tested. After the functional tests for each part had been carried out, all components were integrated into the test set-up. The final complete test set-up was characterised down to the smallest details with respect to e.g. temperature performance, wavelength and light flux in different operational modes, and noise and electromagnetic shielding. All this work resulted in a fully working test set-up for SiPM characterisation in the temperature range from $-30\,^{\circ}\mathrm{C}$ to $60\,^{\circ}\mathrm{C}$ with photons from 300 nm to 650 nm and intensities from single photons up to continuous light flux.

Software for the recording of the raw data from the oscilloscope, the sourcemeter, spectrometer, and the other monitored hardware components was developed and tested. The developed signal analysis tool chain is able to prepare the data in such a way, that many measurements of different parameters can be performed. These tools include the long trace analysis (threshold scan, peak finder, afterpulse search, and charge determination), the short trace analysis (SoftQDC), I-V-scan, and light flux determination. Furthermore the error calculation from the raw data is implemented. Based upon these prepared data many measurements have been implemented, e.g breakdown voltage $V_{br}(T)$, noise characterisation (thermal, afterpulse, and crosstalk) as a function of overvoltage and temperature as well as relative and absolute p.d.e. as a function of temperature, overvoltage and wavelength and dynamic range mea-

surements. Each measurement point in the parameter space will require roughly 20 s. The light creation and distribution system has been improved in the UV regime so that it can be used even for dynamic range measurements at 315 nm. The high-speed, low-noise, high-precision oscilloscope used for the data acquisition allows for nearly any data analysis the user can imagine, but it requires more computing power than the traditional dedicated hardware measurements.

9. Outlook

The test set-up is fully usable and capable of performing the presented measurements. The test set-up offers a simple interface to SiPM characterisation measurements, even for users that do not have great experience in the field of hardware or programming. While dark measurements without a trigger take some time and require the taking of full traces, the trigger mode, either self- or externally triggered, delivers high statistics within a short time. The ability to measure the absolute p.d.e. at freely chosen narrow wavelength ranges is useful and could be a replacement for the normally used scaling of a relative p.d.e. measurement to very few absolute p.d.e. measurements. The relative p.d.e. measurement could be improved by a few more LEDs closing the gaps in the spectrum usable after the monochromator. The dynamic range measurements could be further improved by finding a way to suppress the afterglow of the LEDs, since the electrical pulse is much shorter than the resulting photon pulse. Further improvement of the light distribution towards a more stable and more reliable system could be achieved by the replacement of the beam splitters with a multi-spliced fibre. A multi-spliced fibre with 32 inputs and four or more outputs could be installed in such a way that each input fibre is placed in an optimal location in front of each of the LEDs. Another useful upgrade could be the installation of a supercontinuum light [62] source which could cover a large spectral range from deep UV [63] to IR without significant gaps.

Bibliography

[1] R. Hawkes et al. 'Silicon photomultiplier performance tests in magnetic resonance pulsed fields'. In: *Nuclear Science Symposium Conference Record, 2007. NSS '07. IEEE* 5 (Oct. 2007), pp. 3400–3403. ISSN: 1095-7863. DOI: 10.1109/NSSMIC.2007.4436860 (cit. on p. 1).

[2] CMS Collaboration. *Technical proposal for the upgrade of the CMS detector through 2020*. Tech. rep. CERN-LHCC-2011-006. LHCC-P-004. Geneva: CERN, 2011. URL: http://cds.cern.ch/record/1355706 (cit. on p. 1).

[3] *LHCb : Technical Proposal*. Tech. Proposal. Geneva: CERN, 1998. URL: https://cds.cern.ch/record/622031 (cit. on p. 1).

[4] K. Abe et al. 'The {T2K} experiment'. In: *Nuclear Instruments and Methods in Physics Research Section A: Accelerators, Spectrometers, Detectors and Associated Equipment* 659.1 (2011), pp. 106 –135. ISSN: 0168-9002. DOI: http://dx.doi.org/10.1016/j.nima.2011.06.067. URL: http://www.sciencedirect.com/science/article/pii/S0168900211011910 (cit. on p. 1).

[5] H. Abramowicz et al. 'The International Linear Collider Technical Design Report - Volume 4: Detectors'. In: (2013). arXiv: 1306.6329 (cit. on p. 1).

[6] 'The Pierre Auger Project Design Report'. In: (1996) (cit. on p. 1).

[7] F. Halzen and S. Klein. 'Invited Review Article: IceCube: An instrument for neutrino astronomy'. In: *Review of Scientific Instruments* 81.8, 081101 (2010). DOI: http://dx.doi.org/10.1063/1.3480478. URL: http://scitation.aip.org/content/aip/journal/rsi/81/8/10.1063/1.3480478 (cit. on p. 1).

[8] H.Anderhub et al. 'Design and Operation of FACT - The First G-APD Cherenkov Telescope'. In: *JINST* 8 (2013), P06008. DOI: 10.1088/1748-0221/8/06/P06008. arXiv: 1304.1710 [astro-ph.IM] (cit. on p. 1).

[9] M. Actis and et al. 'Design concepts for the Cherenkov Telescope Array CTA: an advanced facility for ground-based high-energy gamma-ray astronomy'. In: *Experimental Astronomy* 32 (Dec. 2011), pp. 193–316. DOI: 10.1007/s10686-011-9247-0. arXiv: 1008.3703 (cit. on p. 1).

[10] E. Aprile et al. 'The XENON dark matter search experiment'. In: *New Astronomy Reviews* 49.2–6 (2005). Sources and Detection of Dark Matter and Dark Energy in the Universe 6th UCLA Symposium on Sources and Detection of Dark Matter and Dark Energy in the Universe, pp. 289 –295. ISSN: 1387-6473. DOI: http://dx.doi.org/10.1016/j.newar.2005.01.035. URL: http://www.sciencedirect.com/science/article/pii/S1387647305000473 (cit. on p. 1).

[11] B. Lutz and the CMS collaboration. 'Upgrade of the CMS Hadron Outer Calorimeter with SiPM sensors'. In: *Journal of Physics: Conference Series* 404.1 (2012), p. 012018. URL: http://stacks.iop.org/1742-6596/404/i=1/a=012018 (cit. on p. 1).

[12] C. Joram et al. *LHCb Scintillating Fibre Tracker Engineering Design Review Report: Fibres, Mats and Modules*. Tech. rep. LHCb-PUB-2015-008. CERN-LHCb-PUB-2015-008. Geneva: CERN, Mar. 2015. URL: https://cds.cern.ch/record/20048117 (cit. on p. 1).

[13] T. Buanes et al. 'The CALICE hadron scintillator tile calorimeter prototype'. In: *Nuclear Instruments and Methods in Physics Research Section A: Accelerators, Spectrometers, Detectors and Associated Equipment* 623.1 (2010). 1st International Conference on Technology and Instrumentation in Particle Physics, pp. 342–344. ISSN: 0168-9002. DOI: http://dx.doi.org/10.1016/j.nima.2010.02.242. URL: http://www.sciencedirect.com/science/article/pii/S0168900210005279 (cit. on p. 1).

[14] Y. Kudenko et al. 'The near neutrino detector for the {T2K} experiment'. In: *Nuclear Instruments and Methods in Physics Research Section A: Accelerators, Spectrometers, Detectors and Associated Equipment* 598.1 (2009). Instrumentation for Collding Beam PhysicsProceedings of the 10th International Conference on Instrumentation for Colliding Beam Physics, pp. 289 –295. ISSN: 0168-9002. DOI: http://dx.doi.org/10.1016/j.nima.2008.08.029. URL: http://www.sciencedirect.com/science/article/pii/S0168900208012473 (cit. on p. 2).

[15] A. Biland et al. 'Calibration and performance of the photon sensor response of FACT - the first G-APD Cherenkov telescope'. In: *Journal of Instrumentation* 9.10 (2014), P10012. URL: http://stacks.iop.org/1748-0221/9/i=10/a=P10012 (cit. on p. 2).

[16] G. Ambrosi et al. 'INFN Camera demonstrator for the Cherenkov Telescope Array'. In: *ArXiv e-prints* (Sept. 2015). arXiv: 1509.01979 [astro-ph.IM] (cit. on p. 2).

[17] M. Lauscher et al. 'FAMOUS: a prototype silicon-photomultiplier telescope for the fluorescence detection of ultra-high-energy cosmic rays'. In: *Proc. SPIE* 8460 (2012), 84601N–84601N–15. DOI: 10.1117/12.929229. URL: http://dx.doi.org/10.1117/12.929229 (cit. on p. 2).

[18] E. Aprile et al. 'Detection of liquid xenon scintillation light with a silicon photomultiplier'. In: *Nuclear Instruments and Methods in Physics Research Section A: Accelerators, Spectrometers, Detectors and Associated Equipment* 556.1 (2006), pp. 215 –218. ISSN: 0168-9002. DOI: http://dx.doi.org/10.1016/j.nima.2005.09.046. URL: http://www.sciencedirect.com/science/article/pii/S0168900205018954 (cit. on p. 2).

[19] S. Vandenberghe and P. K. Marsden. 'PET-MRI: a review of challenges and solutions in the development of integrated multimodality imaging'. In: *Physics in Medicine and Biology* 60.4 (2015), R115. URL: http://stacks.iop.org/0031-9155/60/i=4/a=R115 (cit. on p. 2).

[20] K. A. Tadday. 'Scintillation Light Detection and Application of Silicon Photomultipliers in Imaging Calorimetry and Positron Emission Tomography'. In: *PhD Thesis* (2011). URL: http://www.ub.uni-heidelberg.de/archiv/12959 (cit. on p. 2).

[21] D. Mazin et al. 'Towards SiPM camera for current and future generations of Cherenkov telescopes'. In: *Proceedings, 33rd International Cosmic Ray Conference (ICRC2013): Rio de Janeiro, Brazil, July 2-9, 2013*. 2014, p. 1078. arXiv: 1410.5070 [astro-ph.IM]. URL: http://inspirehep.net/record/1322885/files/arXiv:1410.5070.pdf (cit. on p. 2).

[22] A.Vacheret et al. 'Characterization and Simulation of the Response of Multi Pixel Photon Counters to Low Light Levels'. In: *Nucl. Instrum. Meth.* A656.1 (2011), pp. 69–83. DOI: 10.1016/j.nima.2011.07.022 (cit. on p. 2).

[23] Y. Musienko. 'Advances in multipixel Geiger-mode avalanche photodiodes (silicon photomultipliers)'. In: *Nuclear Instruments and Methods in Physics Research Section A: Accelerators, Spectrometers, Detectors and Associated Equipment* 598 (2009), pp. 213–216. DOI: http://dx.doi.org/10.1016/j.nima.2008.08.031 (cit. on p. 3).

[24] S.M. Sze and Kwok K. Ng. *Physics of Semiconductors*. Wiley-Interscience, 2007 (cit. on pp. 5, 7, 8, 10, 12–16).

[25] Laser Components GmbH. *Avalanche Photodioden Das ist die perfekte Lawine.* www.lasercomponents.com/de/fileadmin/user_upload/home/Datasheets/lc/applikationsreport/avalanche-photodioden.pdf. 2012 (cit. on p. 20).

[26] F. Sun et al. 'Silicon Photomultiplier with High Photon Detection Efficiency'. In: *International Journal of Information and Electronics Engineering* 2.6 (2012), pp. 872 –875. ISSN: 2010-3719. DOI: 10.7763/IJIEE.2012.V2.229. URL: http://www.ijiee.org/papers/229-L0012.pdf (cit. on p. 25).

[27] J. Kindt and H. W. van Zeijl. 'Modelling and fabrication of Geiger mode avalanche photodiodes'. In: *IEEE Trans. Nucl. Sci.* 45 (3 1998), pp. 715 –519. DOI: 10.1109/23.682621 (cit. on p. 26).

[28] A. Lacaita et al. 'On the bremsstrahlung origin of hot-carrier-induced photons in silicon devices'. In: *IEEE Trans. Electron. Dev.* 40 (3 1993), pp. 577 –582. DOI: 10.1109/16.199363 (cit. on p. 26).

[29] AdvanSiD. *AdvanSiD SiPM.* http://advansid.com/products/single-sipms. 2016 (cit. on p. 27).

[30] Excelitas Technologies Corp. *Excelitas SiPMs.* http://www.excelitas.com/pages/product/SiPM-Chips-Packages.aspx. 2016 (cit. on p. 27).

[31] Hamamatsu Photonics K.K. *Hamamatsu MPPC.* http://www.hamamatsu.com/us/en/product/category/3100/4004/4113/index.html. 2016 (cit. on p. 27).

[32] SensL. *AdvanSiD SiPM.* http://advansid.com/products/single-sipms. 2016 (cit. on p. 27).

[33] Hamamatsu Photonics K.K. *Hamamatsu MPPC datasheet S12571.* http://www.hamamatsu.com/resources/pdf/ssd/s12571-010_etc_kapd1044e.pdf. 2016 (cit. on p. 27).

[34] Hamamatsu Photonics K.K. *Hamamatsu MPPC datasheet S13360.* http://www.hamamatsu.com/resources/pdf/ssd/s13360_series_kapd1052e.pdf. 2016 (cit. on p. 27).

[35] KETEK GmbH. *SiPM World Record for Photon Detection Efficiency.* http://www.ketek.net/news/product-and-company-news/news-details/?cHash=f88abc7fd039deafde8e82030e6f0cd3&tx_ttnews[day]=26&tx_ttnews[month]=04&tx_ttnews[tt_news]=54&tx_ttnews[year]=2013. 2013 (cit. on p. 27).

[36] Hamamatsu Photonics K.K. *Hamamatsu MPPC datasheet S12572*. http://www.hamamatsu.com/resources/pdf/ssd/s12572-010_etc_kapd1045e.pdf. 2016 (cit. on p. 27).

[37] T. Enzweiler. 'Development of a Multipurpose Light Source for SiPM Characterization'. MA thesis. Physikalisches Institut IIIA der RWTH Aachen, 2013 (cit. on pp. 30, 49).

[38] M. Lins. 'Construction and testing of a tunable light source for characterisation of Silicon Photomultipliers'. MA thesis. Physikalisches Institut IIIA der RWTH Aachen, 2010 (cit. on p. 32).

[39] B. Glauss. 'Optical Test Stand and SiPM characterisation studies'. MA thesis. Physikalisches Institut IIIA der RWTH Aachen, 2012 (cit. on p. 32).

[40] Thorlabs. *GR13-0605 - Ruled Reflective Diffraction Grating*. https://www.thorlabs.de/thorproduct.cfm?partnumber=GR13-0605. 2016 (cit. on p. 32).

[41] Thorlabs. *FG400AEA UV Solarization-Resistant, Step-Index Multimode Fiber*. https://www.thorlabs.de/thorcat/TTN/FG400AEA-SpecSheet.pdf. 2016 (cit. on pp. 32, 33, 63).

[42] Thorlabs. *MTS Series Motorized Translation Stages User Guide*. http://www.thorlabs.de/thorcat/19500/MTS50_M-Z8-Manual.pdf. 2016 (cit. on p. 32).

[43] Thorlabs. *TDC001 DC Servo Motor Driver User Guide*. http://www.thorlabs.de/thorcat/15700/TDC001-APTManual.pdf. 2016 (cit. on p. 32).

[44] Thorlabs. *BPD254S-FS - Polka Dot Beamsplitter*. https://www.thorlabs.de/thorproduct.cfm?partnumber=BPD254S-FS. 2016 (cit. on p. 33).

[45] Thorlabs. *F220SMA-A - 543 nm, SMA905 Fiber Collimation Pkg*. https://www.thorlabs.de/thorproduct.cfm?partnumber=F220SMA-A. 2016 (cit. on p. 33).

[46] Rhode & Schwarz GmbH. *Programmable Power Supplies 188 W | 384 W HMP Series*. https://cdn.rohde-schwarz.com/pws/dl_downloads/dl_common_library/dl_brochures_and_datasheets/pdf_1/HAMEG_BR_HMP_SP_EN.pdf. 2013 (cit. on p. 34).

[47] Keysight. *Infiniium 9000 H-Series High-Definition Oscilloscopes*. http://literature.cdn.keysight.com/litweb/pdf/5991-1520EN.pdf?id=2279691. 2016 (cit. on p. 36).

[48] Keithley. *Source Measure Units (SMU) Instruments*. https://www.keithley.de/data?asset=57466. 2016 (cit. on p. 37).

[49] Tektronix. *AFG3000 Arbitrary/Function Generator*. http://www.tek.com/datasheet/afg3000c-arbitrary-function-generator-datasheet. 2016 (cit. on p. 38).

[50] Thorlabs. *Thorlabs APT Controllers Host-Controller Communications Protocol*. http://www.thorlabs.de/Software/MotionControl\APT_Communications_Protocol_Rev_18.pdf. 2016 (cit. on p. 39).

[51] Ocean Optics. *USB 650 Red Tide Fiber Optic Spectrometer Installation and Operation Manual*. http://oceanoptics.com//wp-content/uploads/USB-650-Red-Tide-Installation-and-Operation-Instructions.pdf. 2016 (cit. on p. 39).

[52] Atmel Corporation. *ATmega640/1280/1281/2560/2561 Complete*. http://www.atmel.com/Images/Atmel-2549-8-bit-AVR-Microcontroller-ATmega640-1280-1281-2560-2561_datasheet.pdf. 2016 (cit. on p. 40).

[53] Texas Instruments Incorporated. *MSP430G2x53, MSP430G2x13 Mixed Signal Microcontroller (Rev. J)*. http://www.ti.com/lit/gpn/msp430g2553. 2016 (cit. on p. 40).

[54] Atmel Corporation. *ATmega48A/PA/88A/PA/168A/PA/328/P Complete*. http://www.atmel.com/images/Atmel-8271-8-bit-AVR-Microcontroller-ATmega48A-48PA-88A-88PA-168A-168PA-328-328P_datasheet_Complete.pdf. 2016 (cit. on p. 41).

[55] M. H. Weik. *Fiber Optics Standard Dictionary*. Springer-Science + Business Media, 1997 (cit. on pp. 59, 60).

[56] D. Wilson. 'Angular Dependence of the Relative Photon Detection Efficiency of Silicon Photomultipliers'. MA thesis. Physikalisches Institut IIIA der RWTH Aachen, 2012 (cit. on p. 59).

[57] G. Nolde, Thorlabs Technical Support. personal communication, e-mail from 21.1.2016 (cit. on p. 63).

[58] Newport Corporation. *818 Series Calibrated Photodiode Sensors*. http://assets.newport.com/webDocuments-EN/images/39052.pdf. 2016 (cit. on p. 63).

[59] Rohde & Schwarz. *Rohde & Schwarz R&S FSH4/R&S FSH8/R&S FSH13/R&S FSH20 Spectrum Analyzer*. http://www.rohde-schwarz.de/file_20074/fsh. 2016 (cit. on p. 66).

[60] N. Dinu et al. 'Temperature and bias voltage dependence of the MPPC detectors'. In: *IEEE Nuclear Science Symposuim Medical Imaging Conference* (Oct. 2010), pp. 215–219. DOI: http://dx.doi.org/10.1109/NSSMIC.2010.5873750 (cit. on p. 93).

[61] M. Caccia et al. *A simple and robust method to study after-pulses in Silicon Photomultipliers*. http://www.caen.it/servlet/checkCaenDocumentFile?Id=10187. 2016 (cit. on p. 102).

[62] NKT Photonics A/S. *SuperK EXTREME supercontinuum lasers*. http://www.nktphotonics.com/product/superk-extreme-supercontinuum-lasers/. 2016 (cit. on p. 117).

[63] NKT Photonics A/S. *SuperK EXTEND-UV supercontinuum extension unit*. http://www.nktphotonics.com/product/superk-extend-uv-supercontinuum-extension-unit/. 2016 (cit. on p. 117).

A. Appendix: Characterisation

A.1. SiPM temperature stability plots

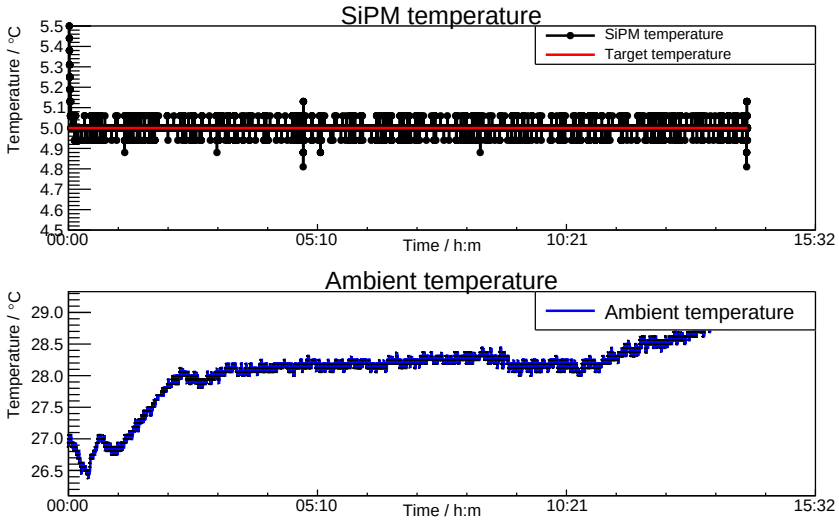

Figure A.1.: SiPM temperature stability at $5\,°C$ over 14 h. The absolute variation after stabilisation is smaller than $0.07\,°C$.

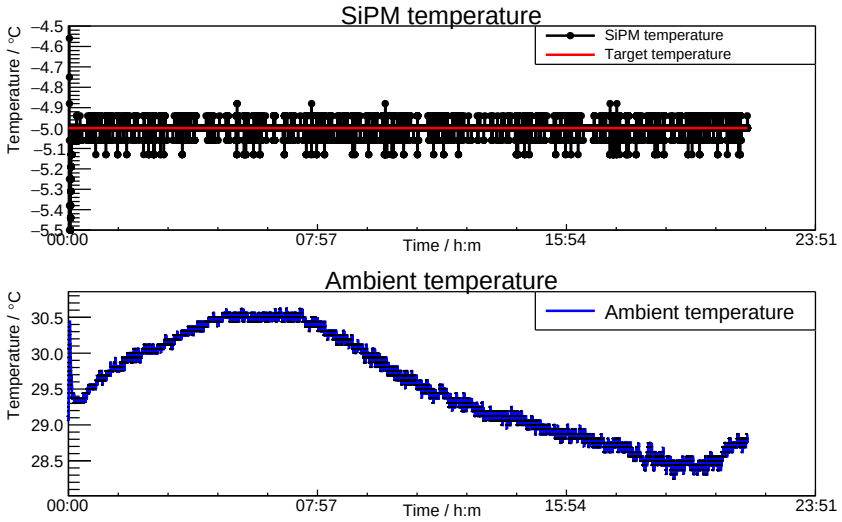

Figure A.2.: SiPM temperature stability at $-5\,°C$ over 21 h. The absolute variation after stabilisation is smaller than $0.07\,°C$.

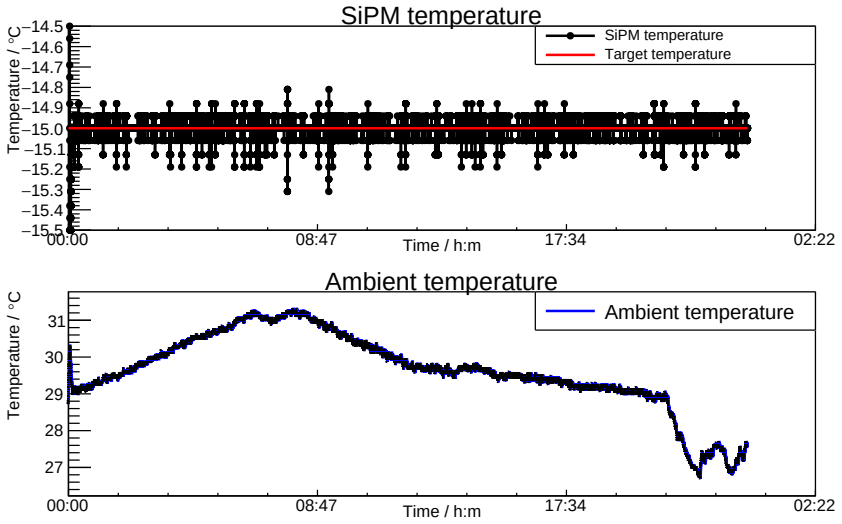

Figure A.3.: SiPM temperature stability at $-15\,°C$ over 24 h. The absolute variation after stabilisation is smaller than $0.13\,°C$.

A.2. Monochromator

The FHWM data (upper part of Figures A.4 and A.5) is spiky because it relies on the bins from the CCD in the spectrometer. The σ data (lower part of Figures A.4 and A.5) is smooth but the peak in the recorded spectrum is not a always a perfect Gaussian which can results in bad fits.

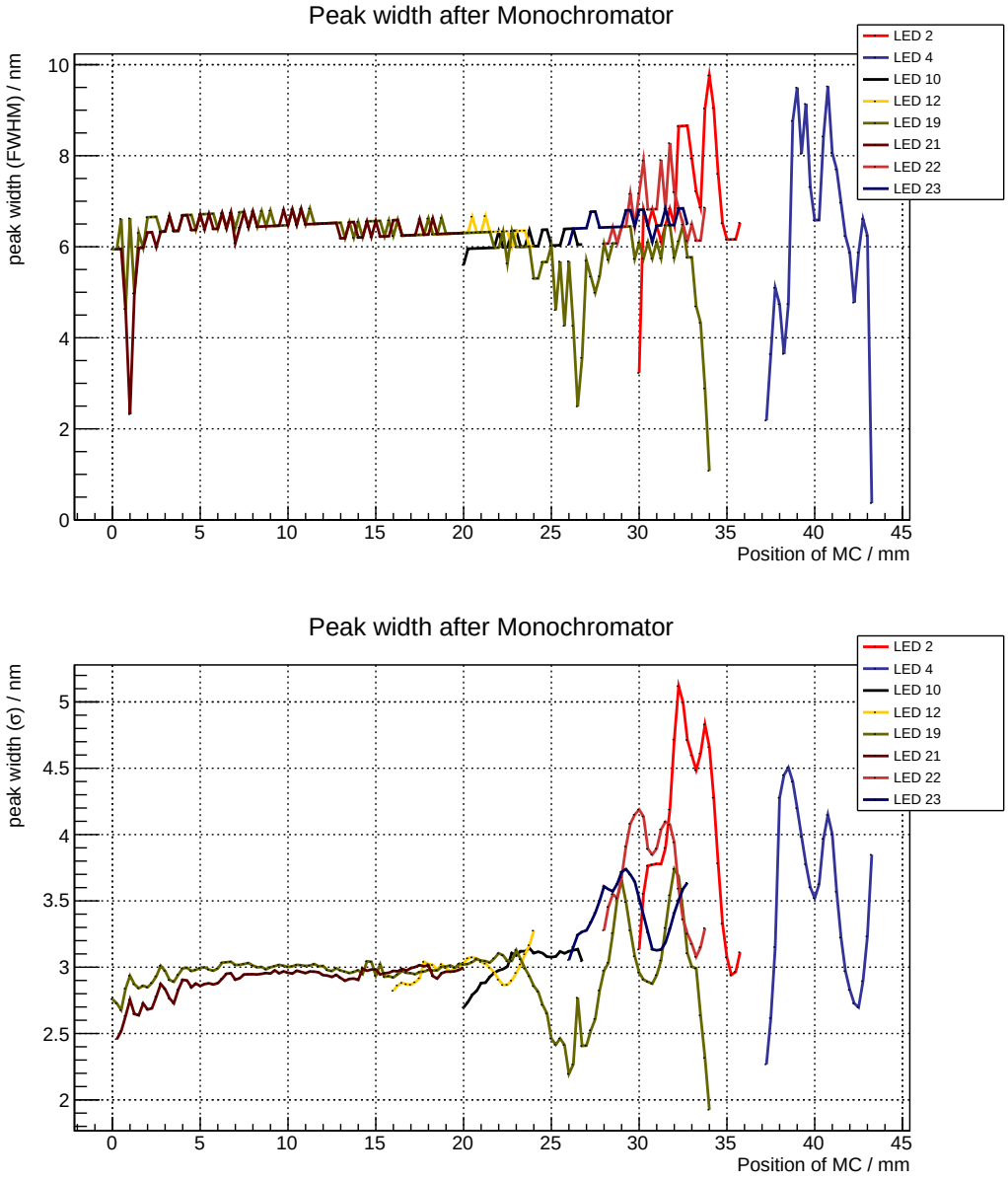

Figure A.4.: Monochromator FWHM and σ of Gaussian fitted versus position

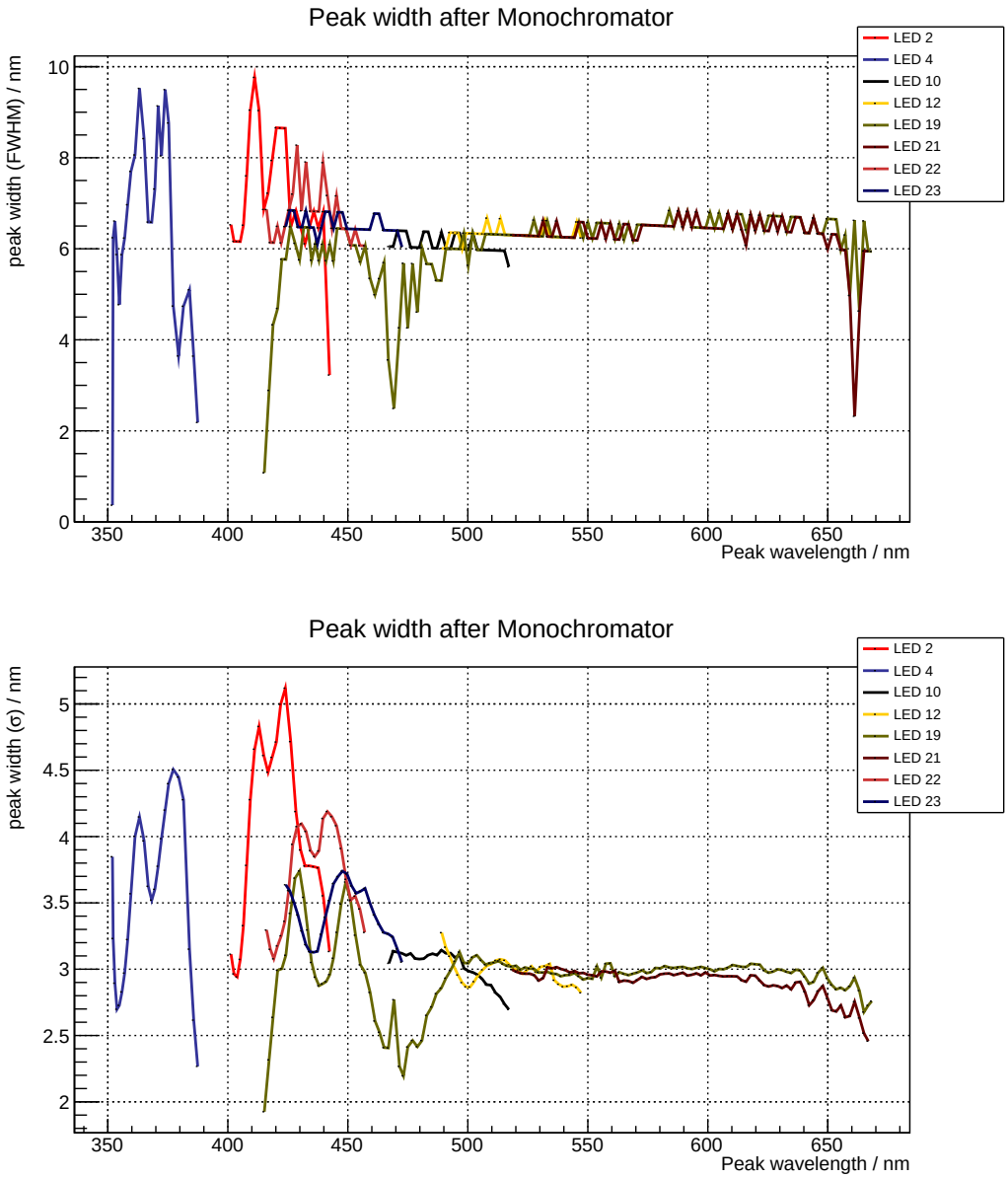

Figure A.5.: Monochromator FWHM and σ of Gaussian fitted versus wavelength

A.3. Beamsplitter characterisation measurements

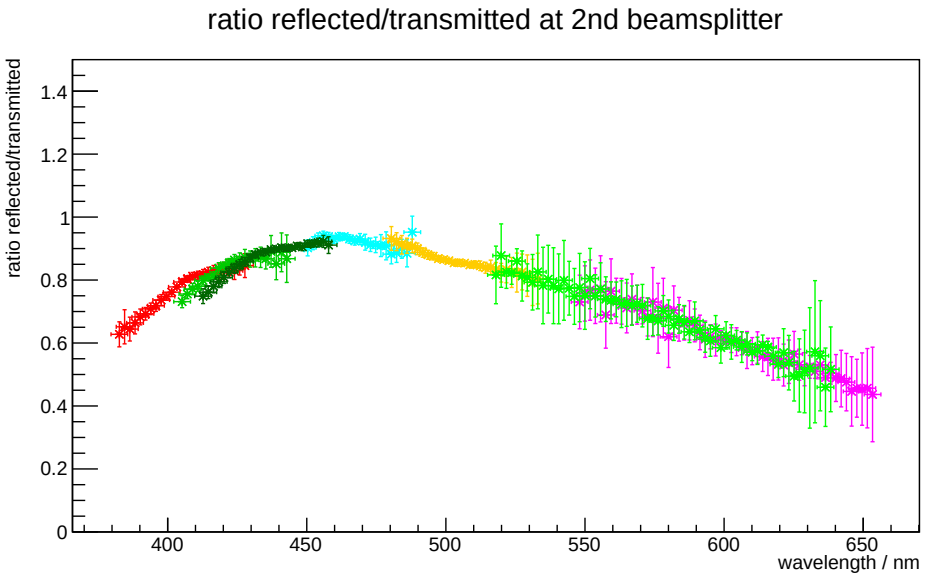

Figure A.6.: Beam splitter ratio $R_{r/t}$ using the combination of the 7 single measurements to one curve versus the wavelength.

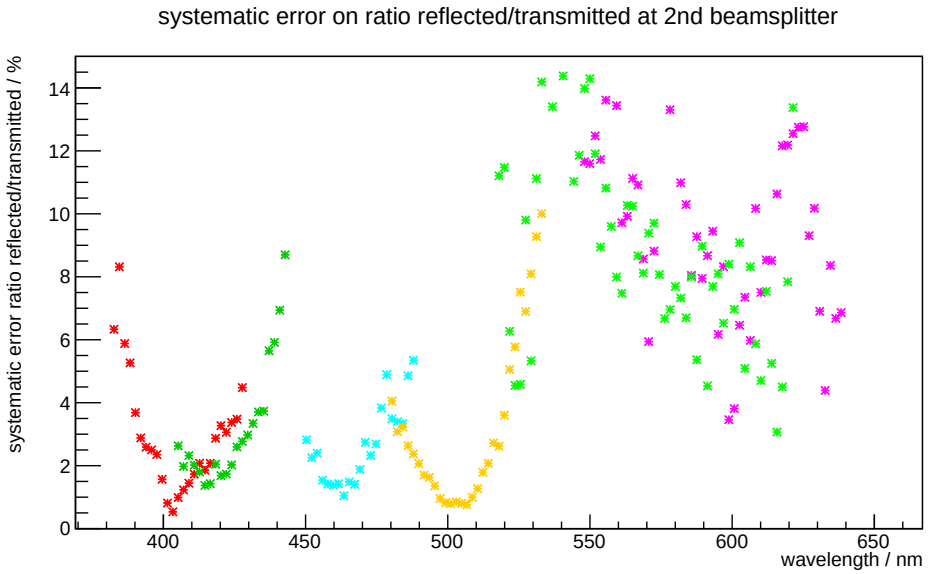

Figure A.7.: Systematic error of the ratio $R_{r/t}$ versus the wavelength.

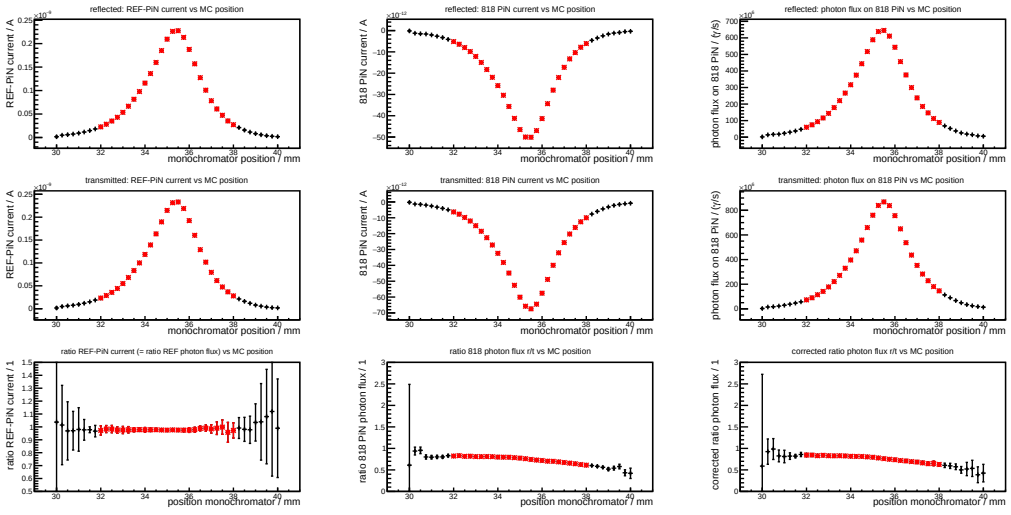

Figure A.8.: Beam splitter measurements for LED 02.

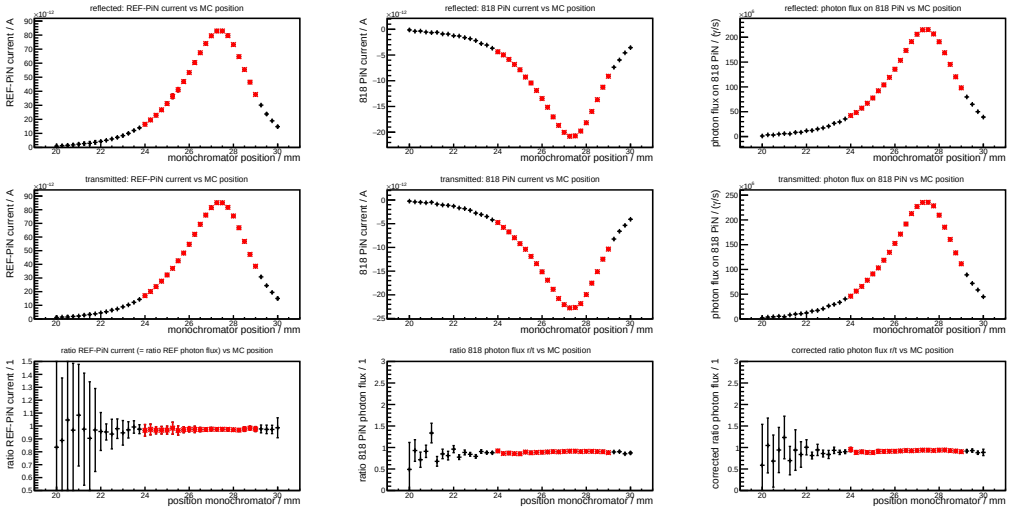

Figure A.9.: Beam splitter measurements for LED 10.

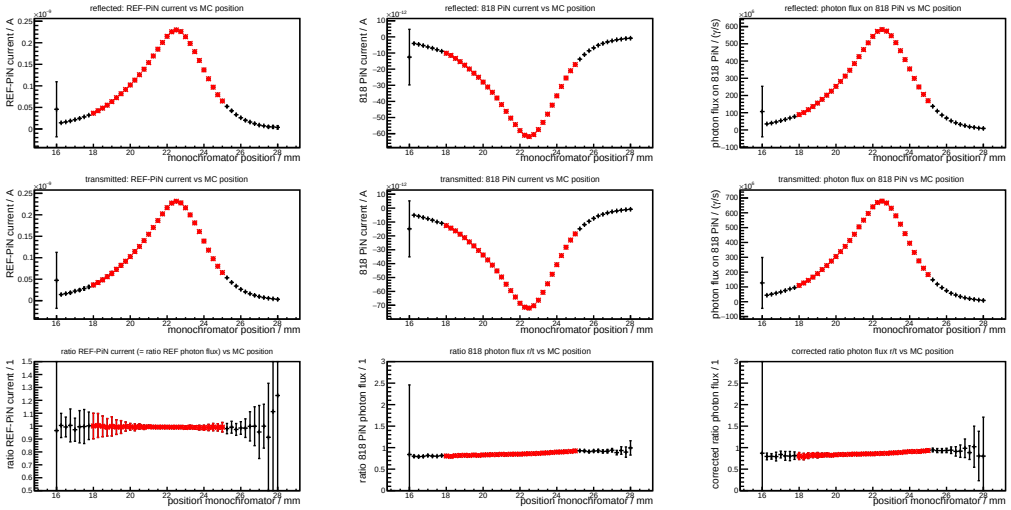

Figure A.10.: Beam splitter measurements for LED 12.

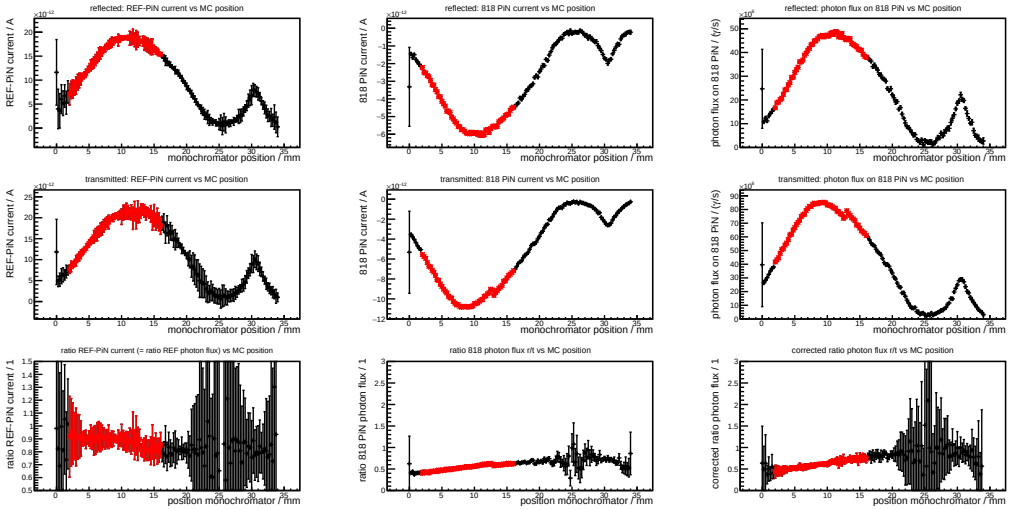

Figure A.11.: Beam splitter measurements for LED 19.

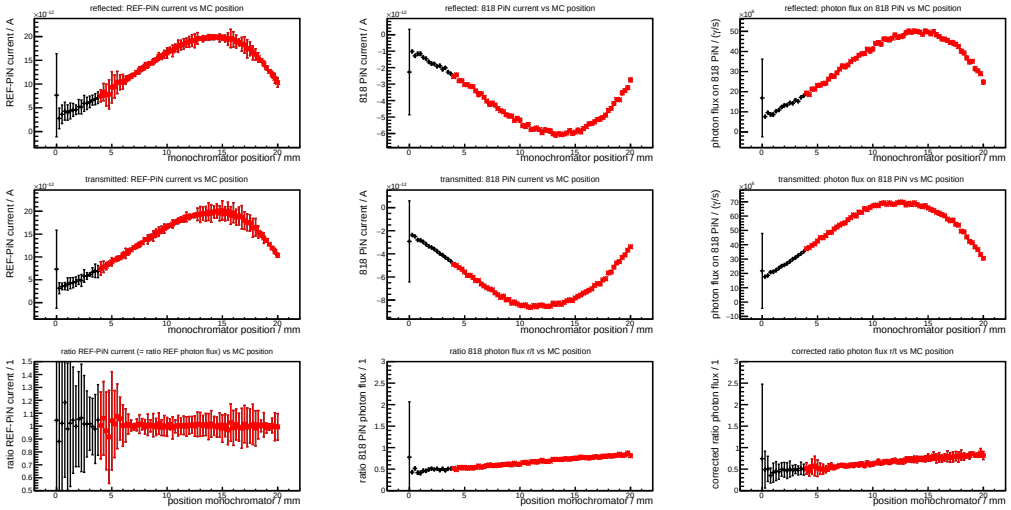

Figure A.12.: Beam splitter measurements for LED 21.

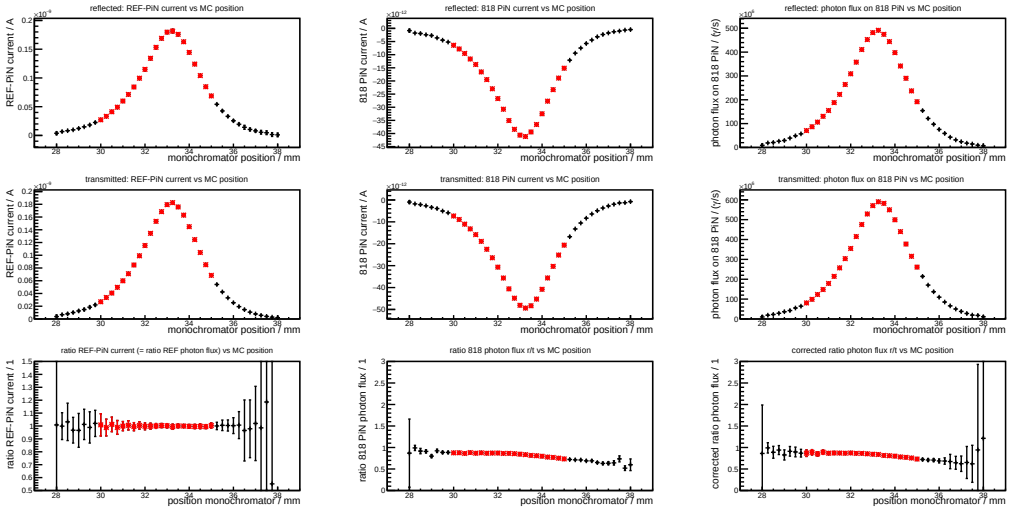

Figure A.13.: Beam splitter measurements for LED 22.

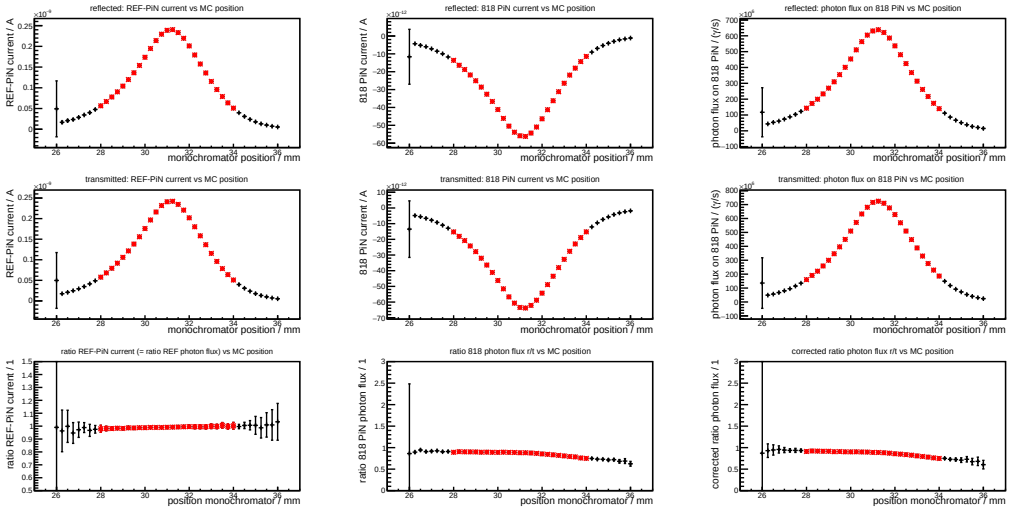

Figure A.14.: Beam splitter measurements for LED 23.

A.4. MPLS light flux characterisation plots

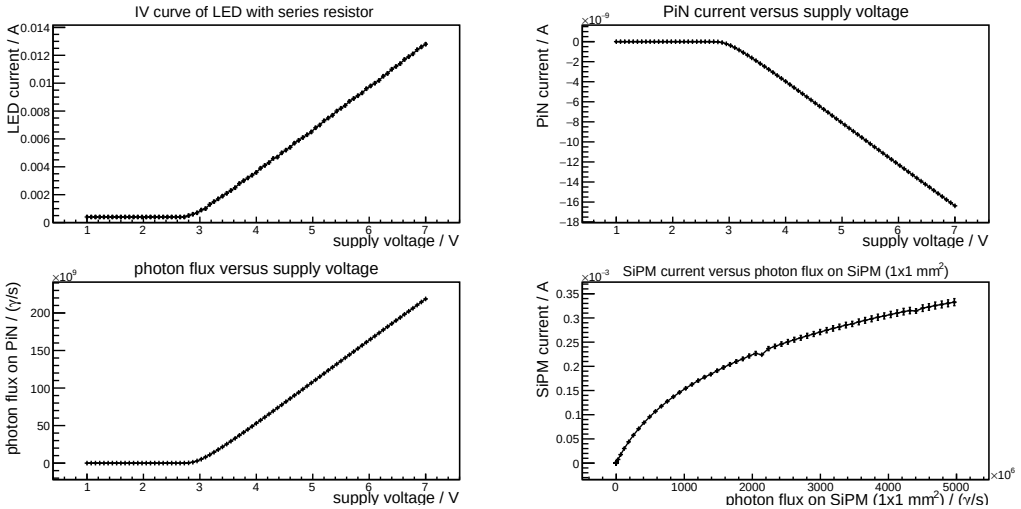

Figure A.15.: Characterisation measurement for LED 2 in DC mode

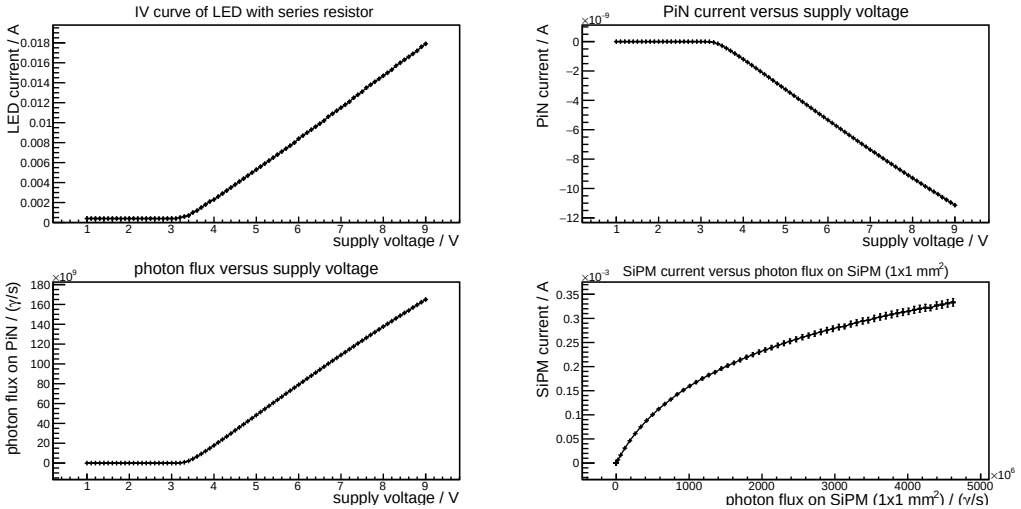

Figure A.16.: Characterisation measurement for LED 4 in DC mode

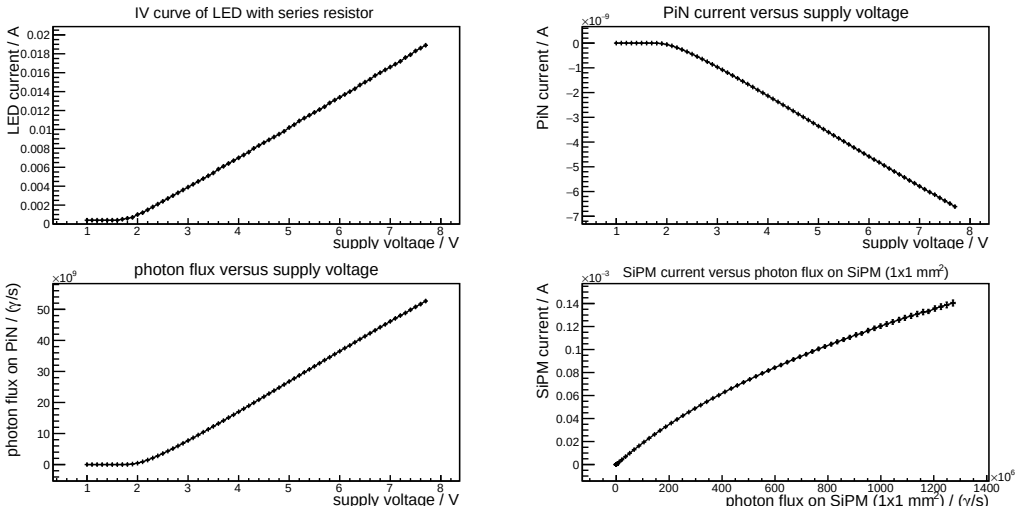

Figure A.17.: Characterisation measurement for LED 6 in DC mode

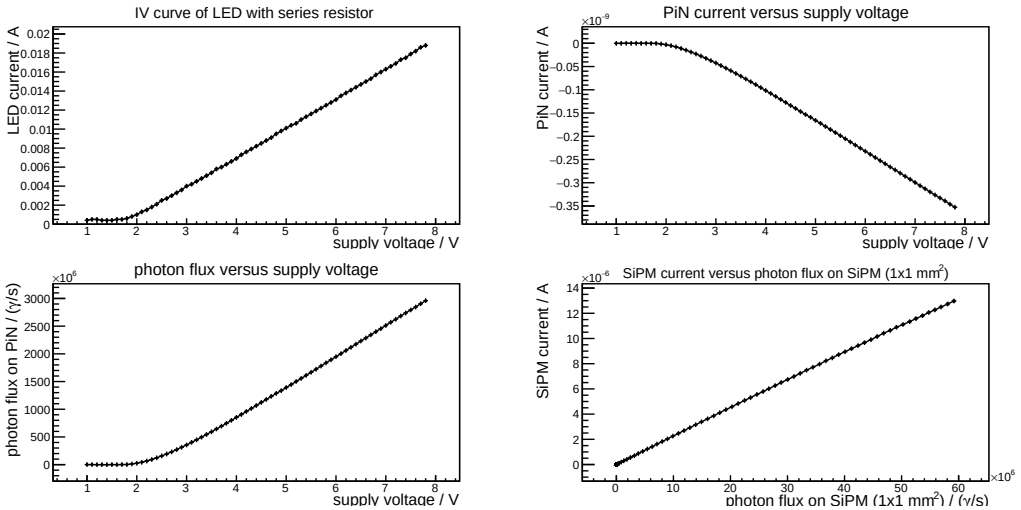

Figure A.18.: Characterisation measurement for LED 8 in DC mode

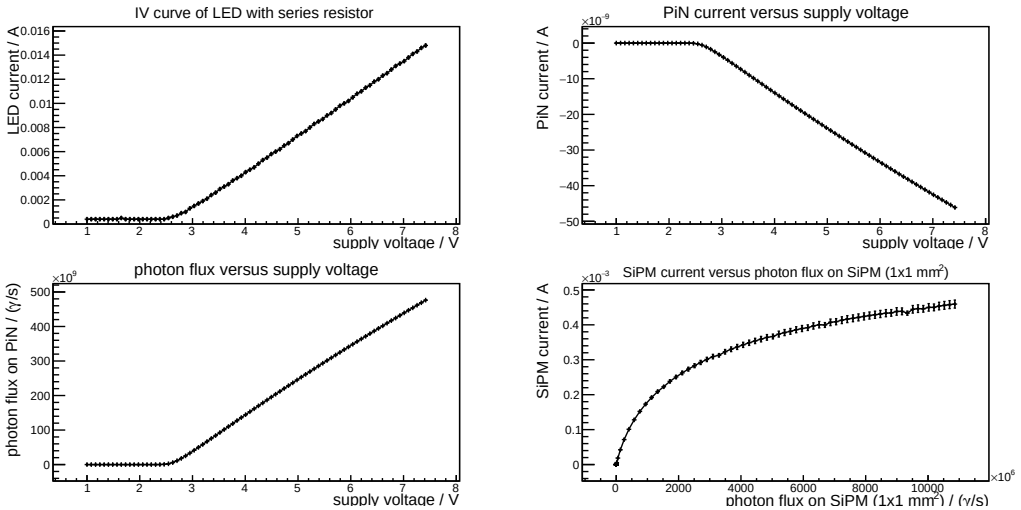

Figure A.19.: Characterisation measurement for LED 10 in DC mode

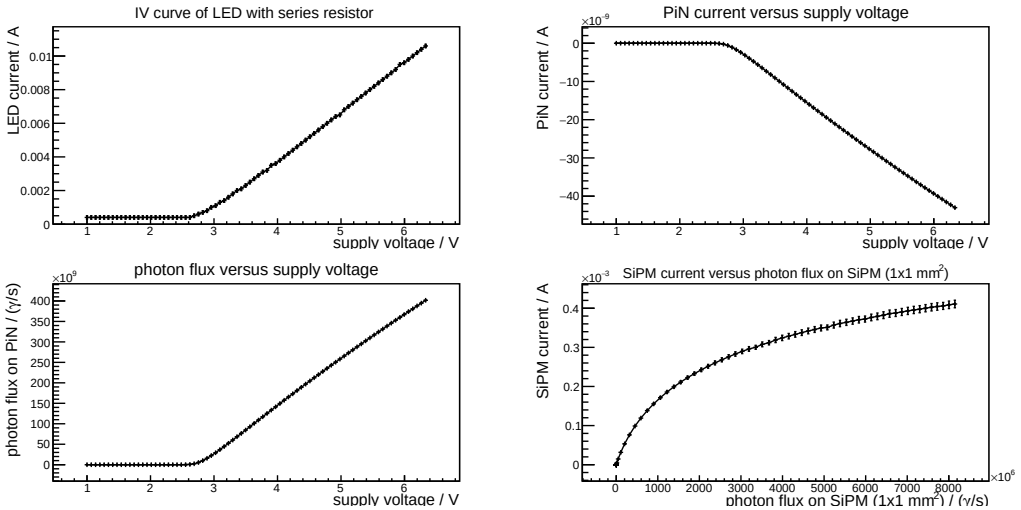

Figure A.20.: Characterisation measurement for LED 12 in DC mode

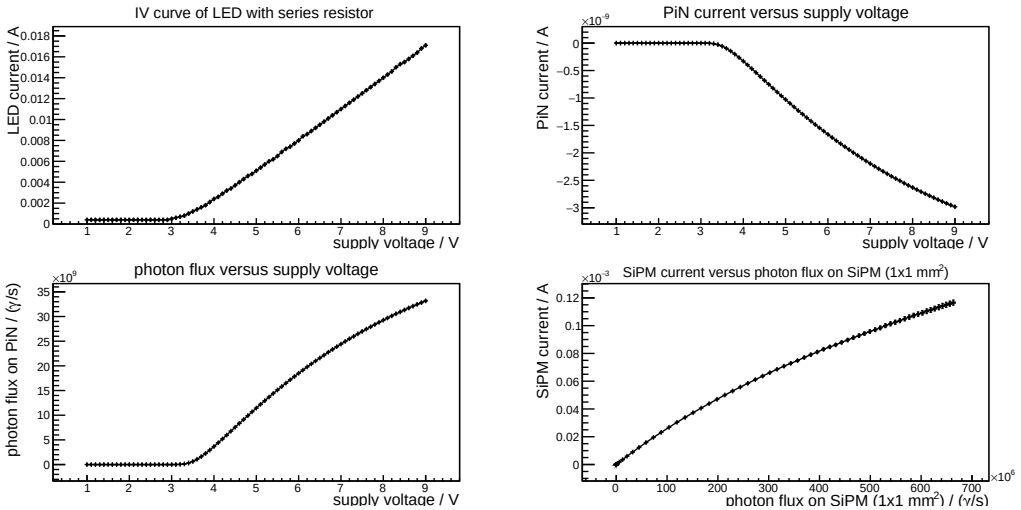

Figure A.21.: Characterisation measurement for LED 13 in DC mode

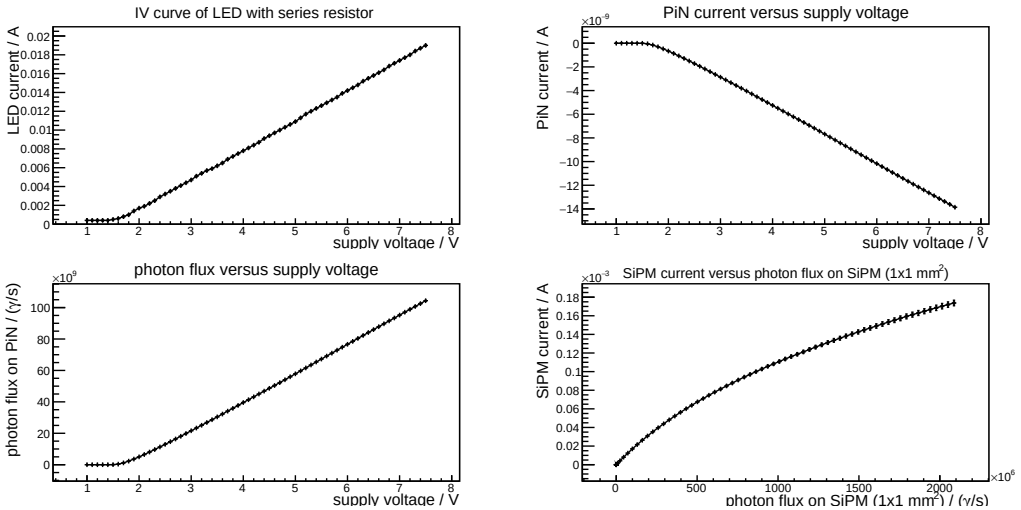

Figure A.22.: Characterisation measurement for LED 14 in DC mode

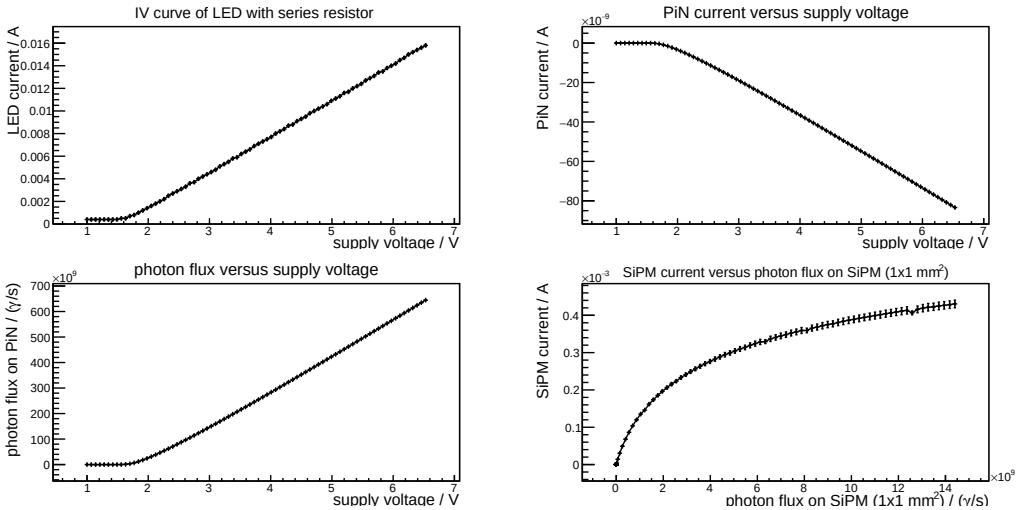

Figure A.23.: Characterisation measurement for LED 18 in DC mode

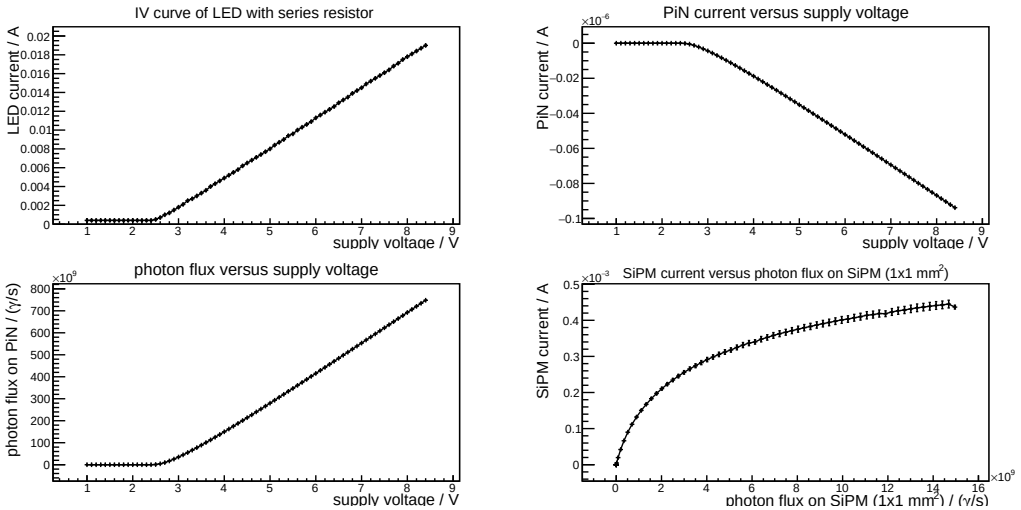

Figure A.24.: Characterisation measurement for LED 19 in DC mode

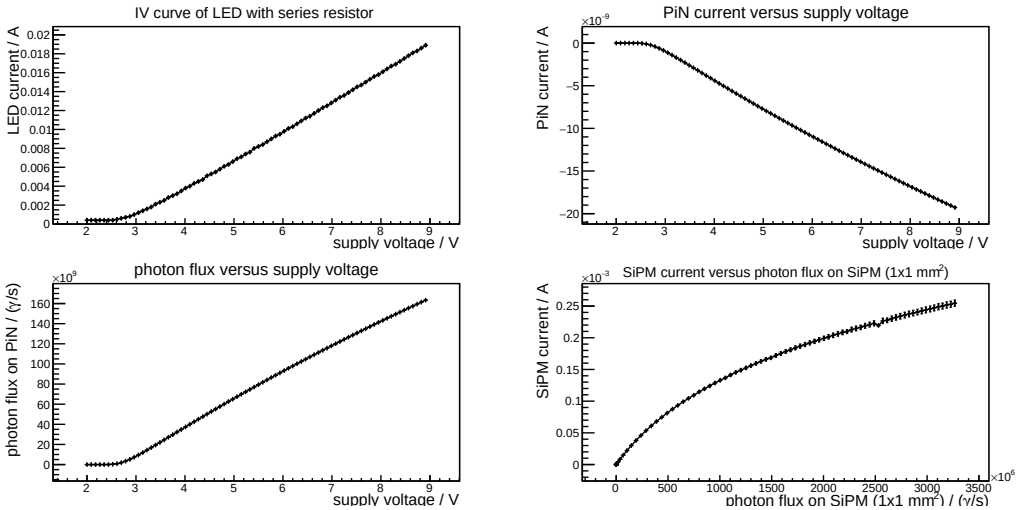

Figure A.25.: Characterisation measurement for LED 20 in DC mode

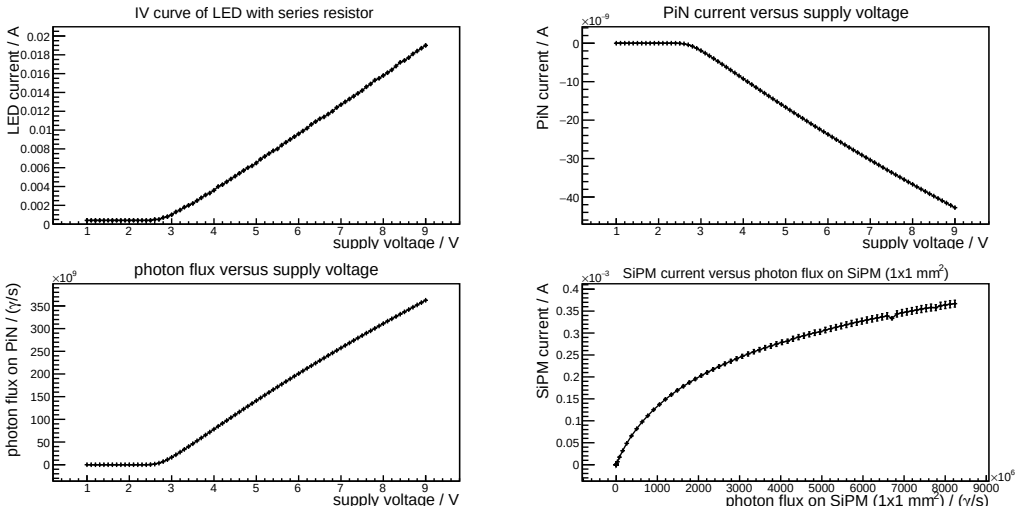

Figure A.26.: Characterisation measurement for LED 21 in DC mode

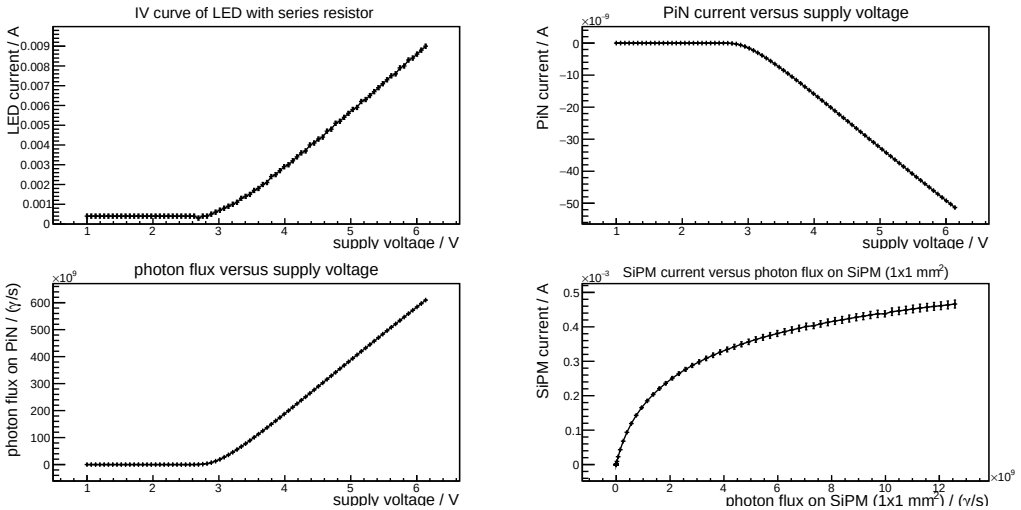

Figure A.27.: Characterisation measurement for LED 22 in DC mode

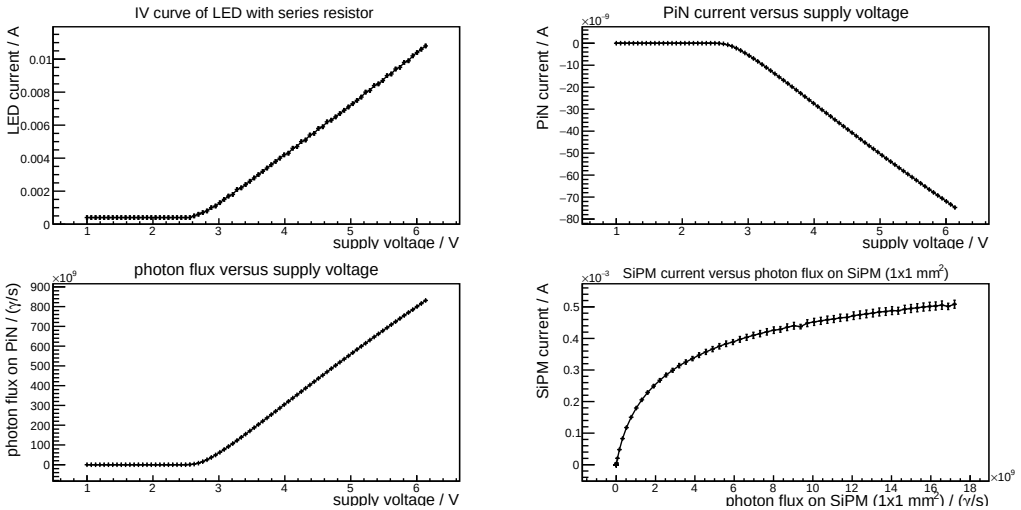

Figure A.28.: Characterisation measurement for LED 23 in DC mode

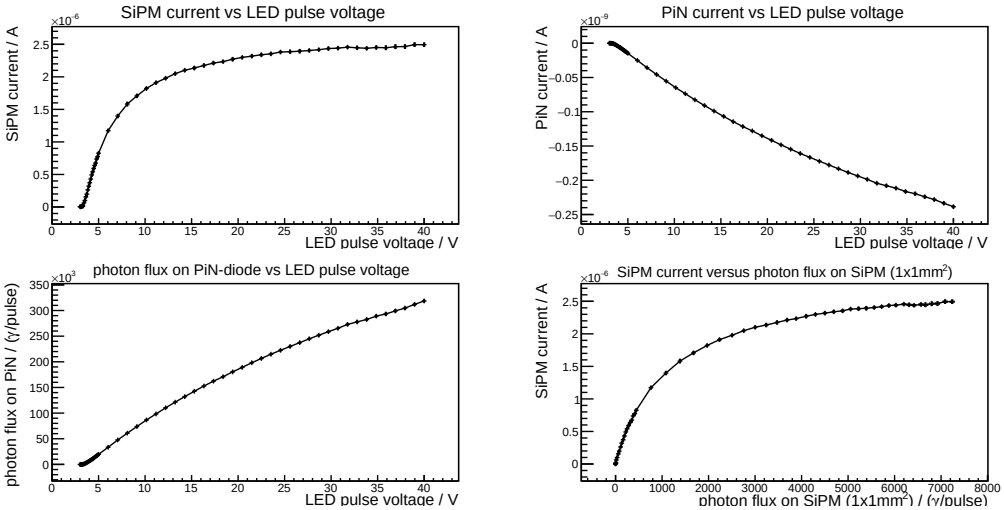

Figure A.29.: Characterisation measurement for LED 1 in pulsed mode

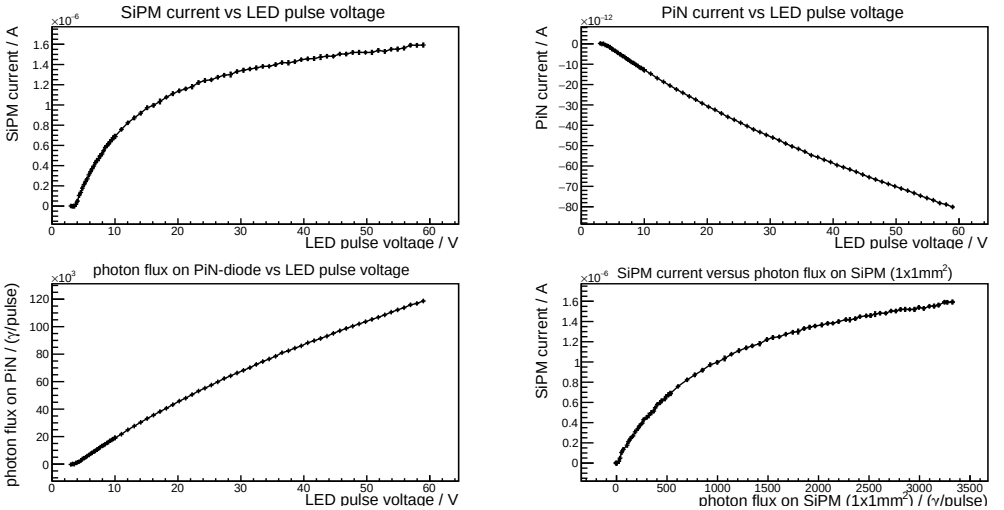

Figure A.30.: Characterisation measurement for LED 3 in pulsed mode

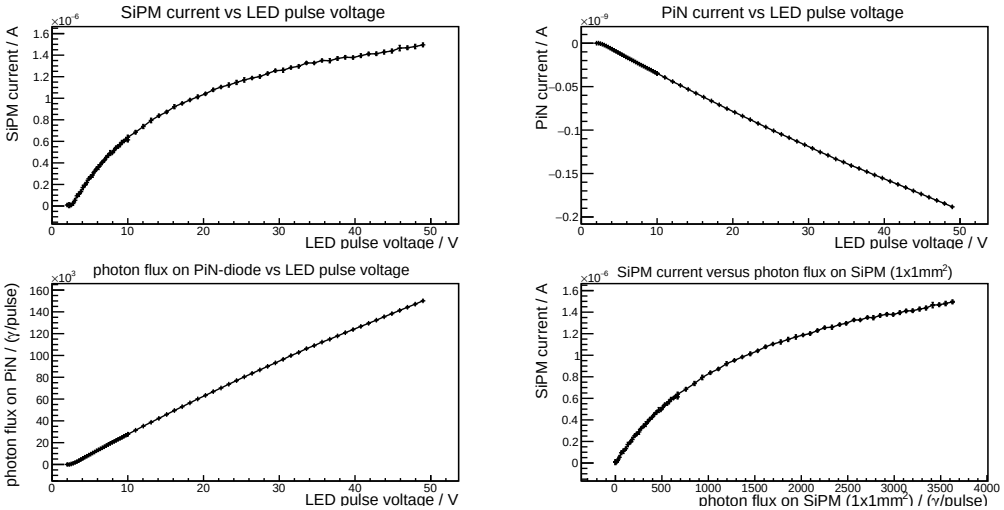

Figure A.31.: Characterisation measurement for LED 5 in pulsed mode

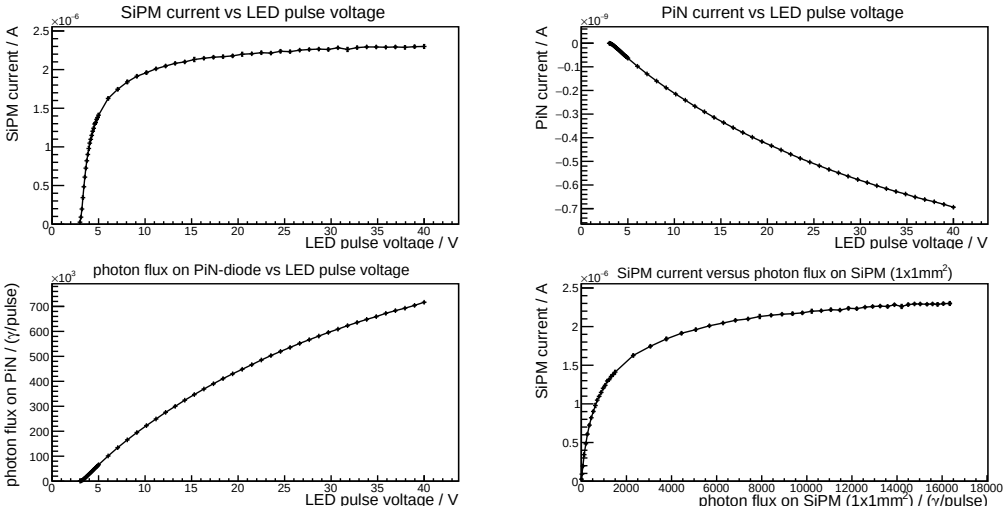

Figure A.32.: Characterisation measurement for LED 9 in pulsed mode

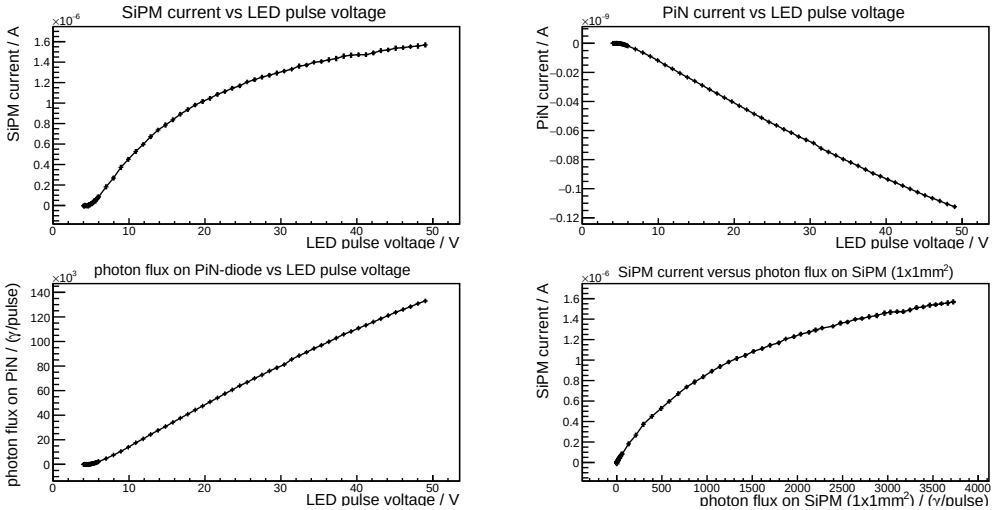

Figure A.33.: Characterisation measurement for LED 11 in pulsed mode

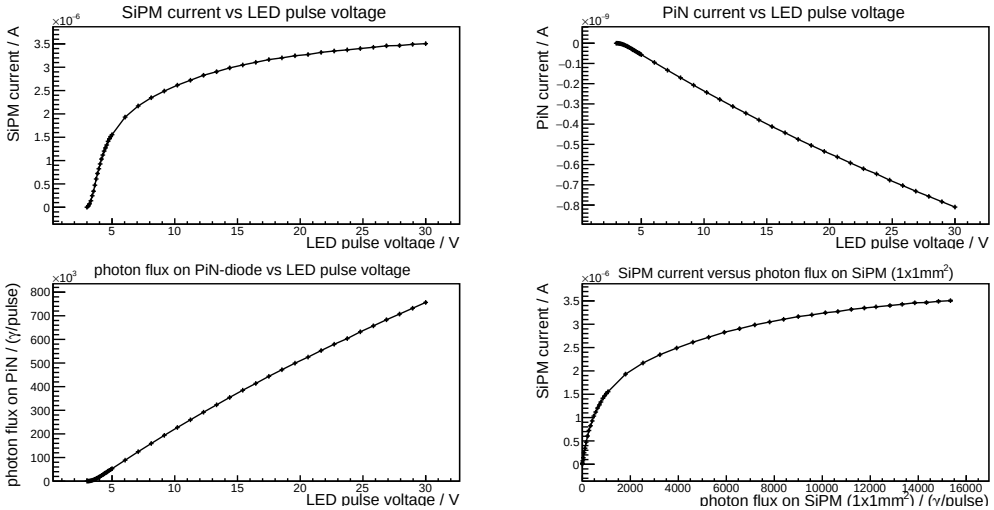

Figure A.34.: Characterisation measurement for LED 15 in pulsed mode

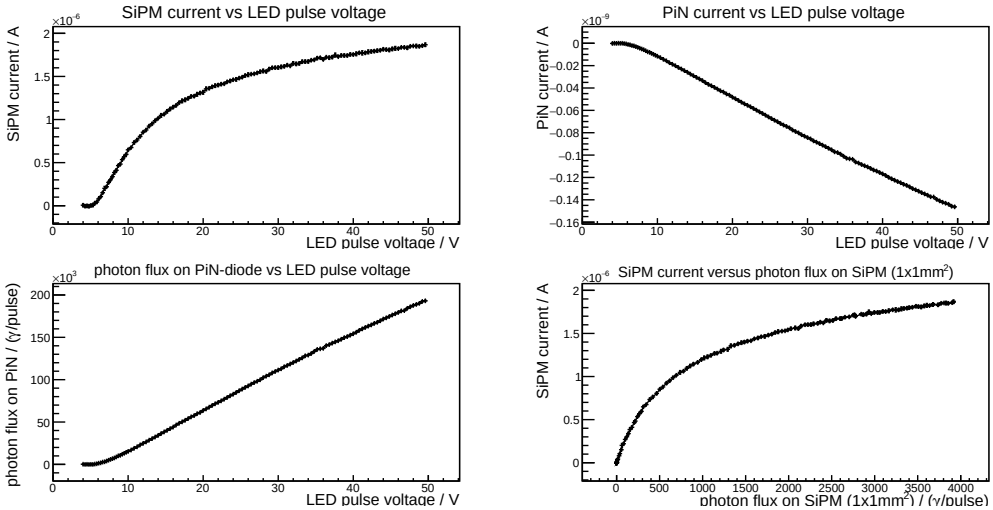

Figure A.35.: Characterisation measurement for LED 16 in pulsed mode

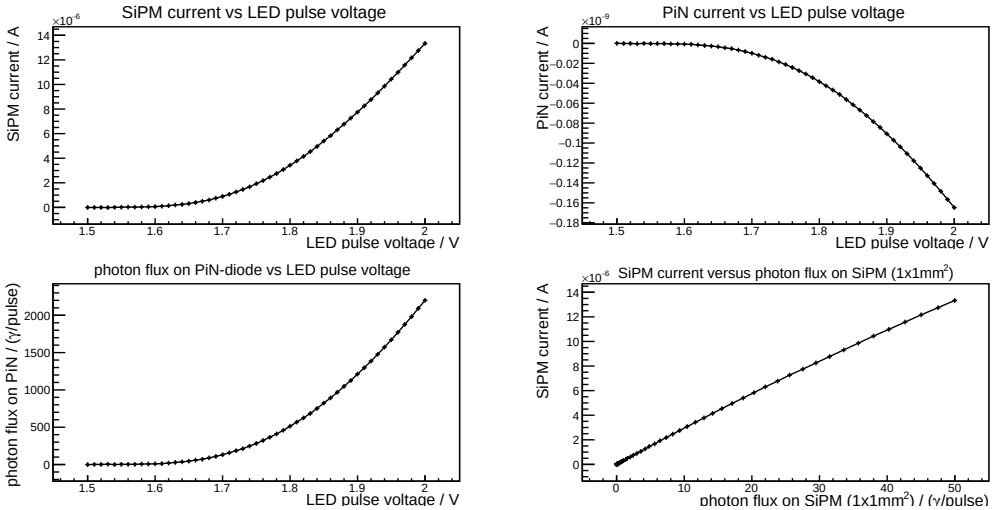

Figure A.36.: Characterisation measurement for DC LED 2 in external pulsed mode

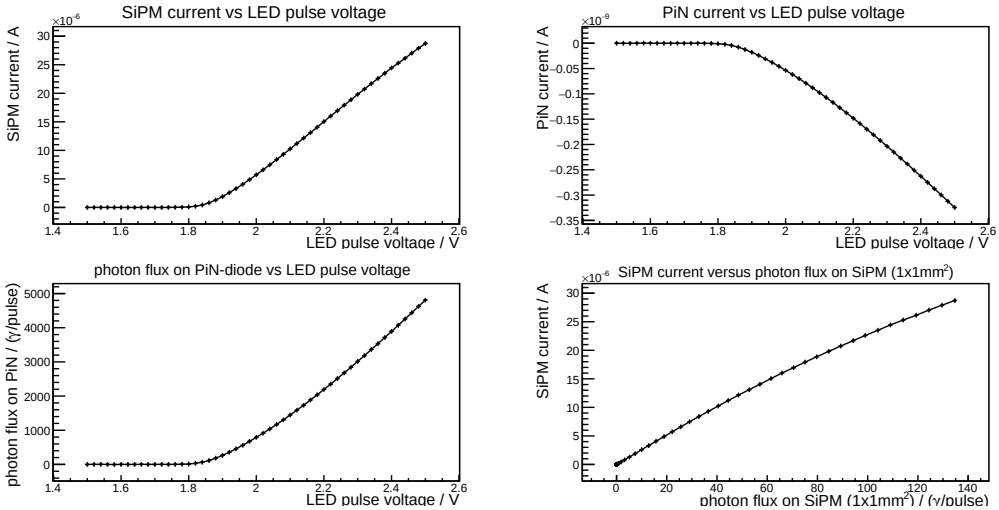

Figure A.37.: Characterisation measurement for DC LED 4 in external pulsed mode

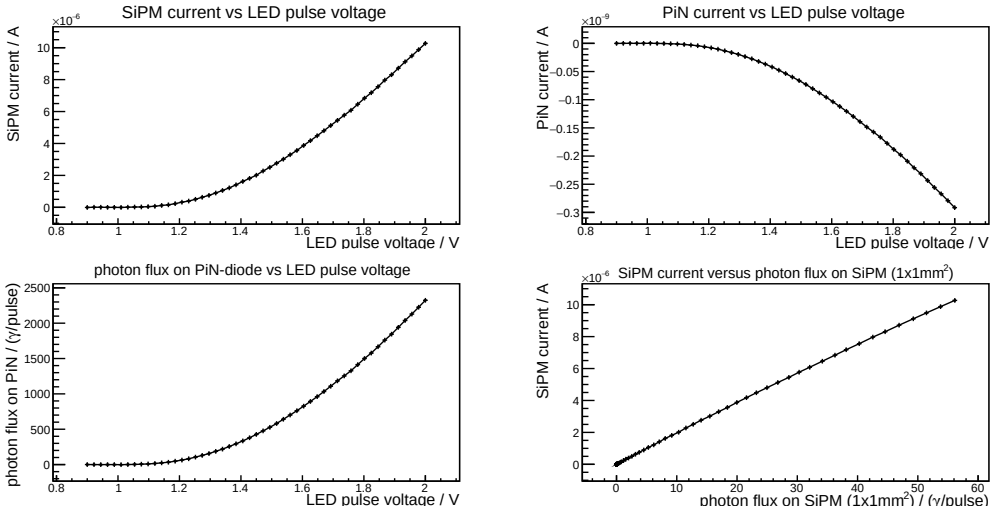

Figure A.38.: Characterisation measurement for DC LED 6 in external pulsed mode

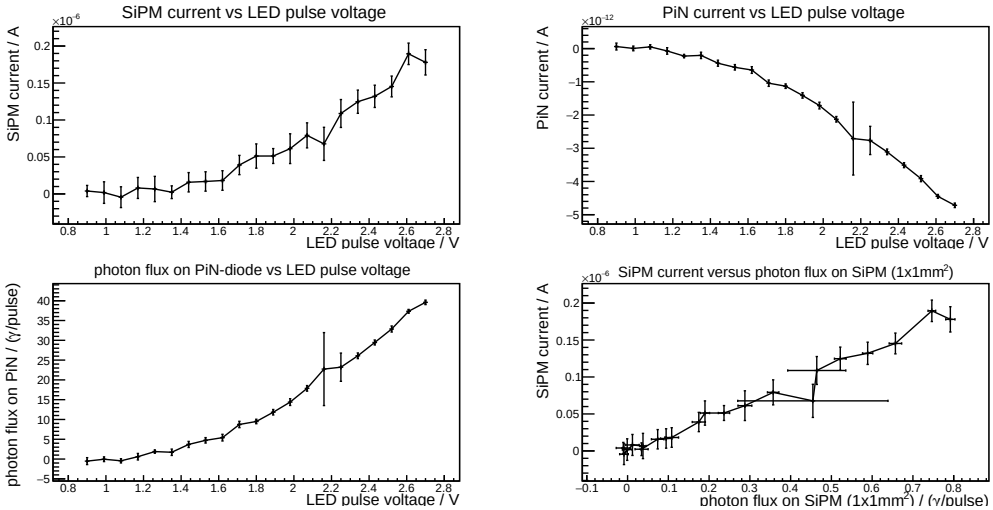

Figure A.39.: Characterisation measurement for DC LED 8 in external pulsed mode

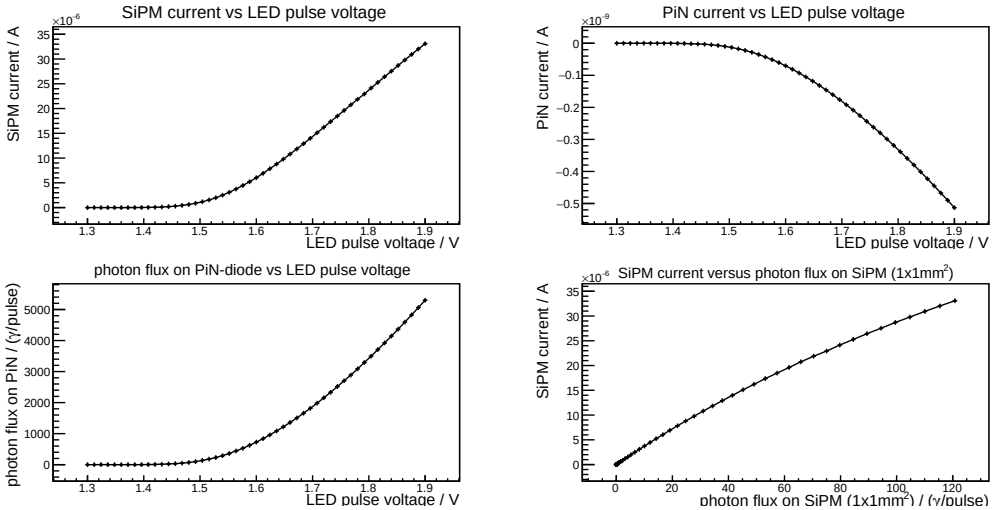

Figure A.40.: Characterisation measurement for DC LED 10 in external pulsed mode

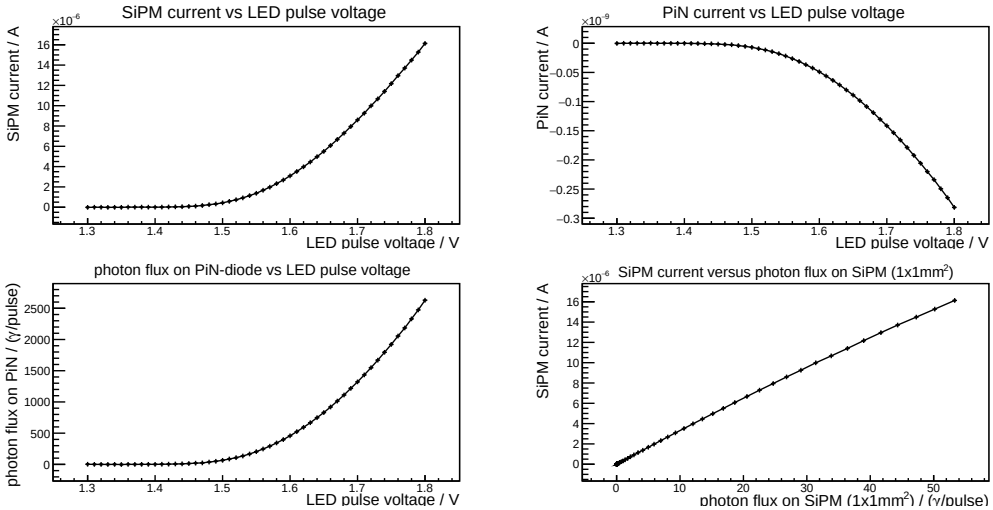

Figure A.41.: Characterisation measurement for DC LED 12 in external pulsed mode

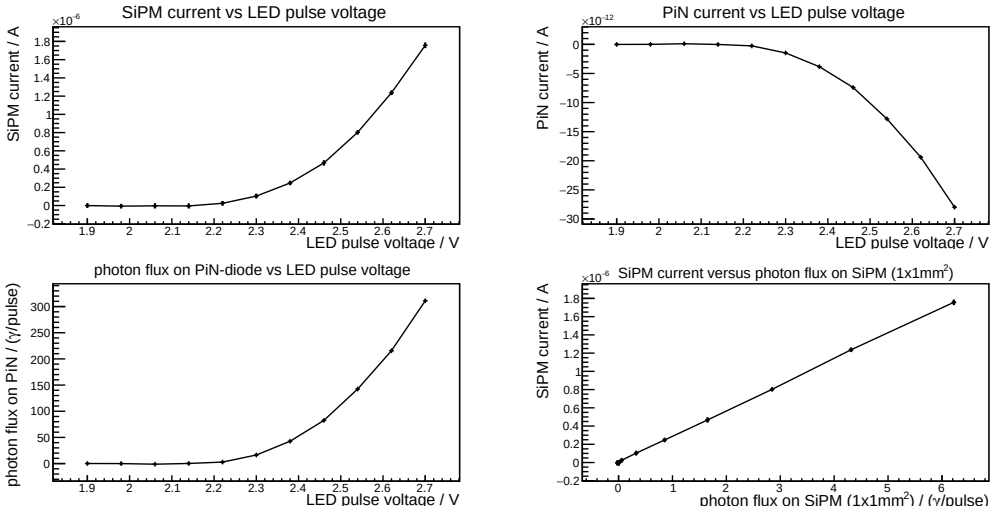

Figure A.42.: Characterisation measurement for DC LED 13 in external pulsed mode

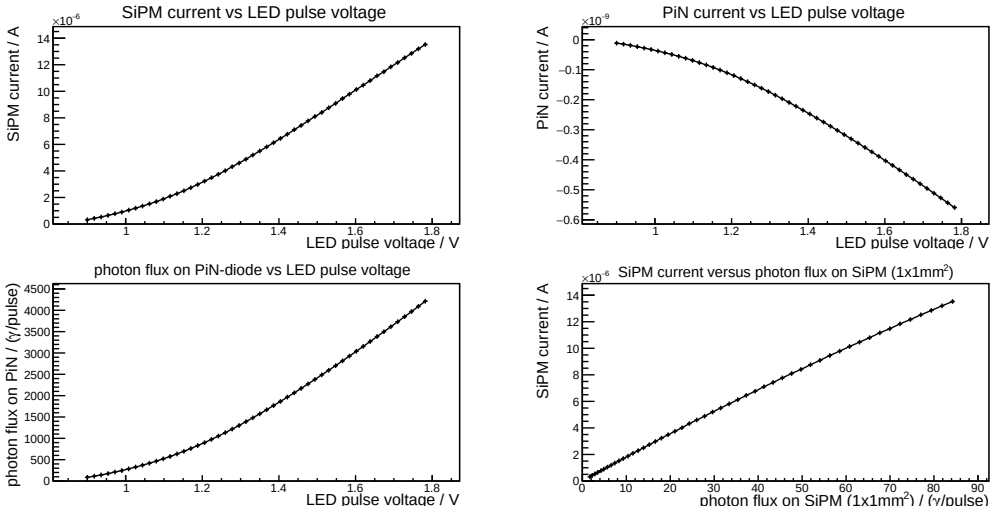

Figure A.43.: Characterisation measurement for DC LED 14 in external pulsed mode

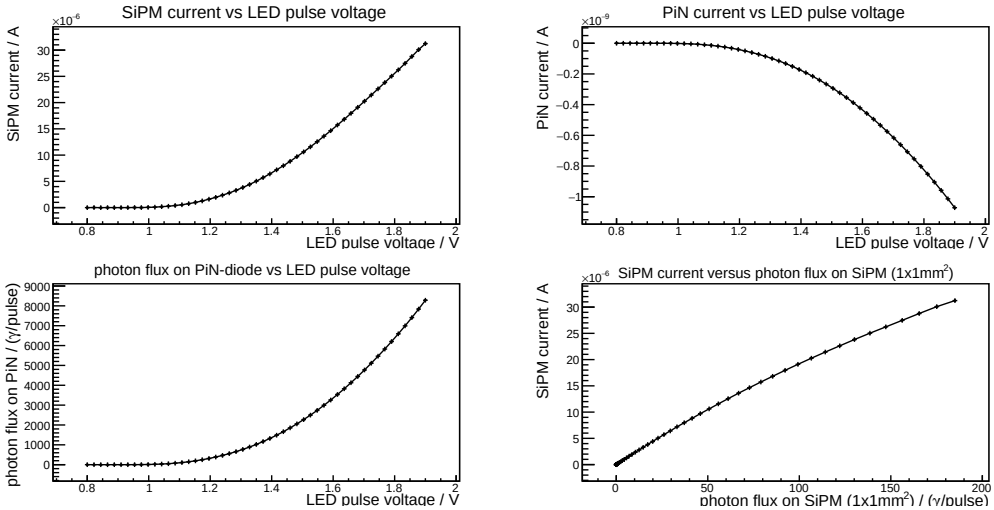

Figure A.44.: Characterisation measurement for DC LED 18 in external pulsed mode

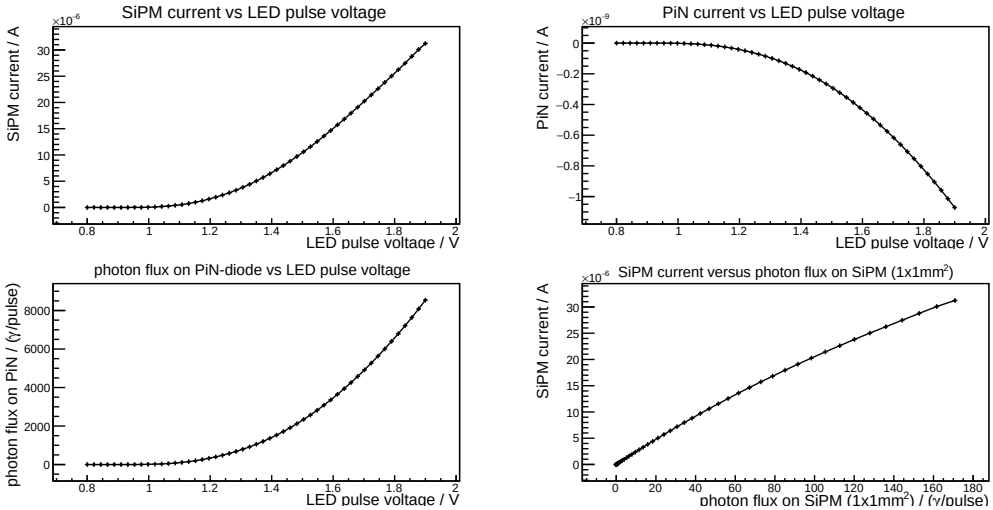

Figure A.45.: Characterisation measurement for DC LED 19 in external pulsed mode

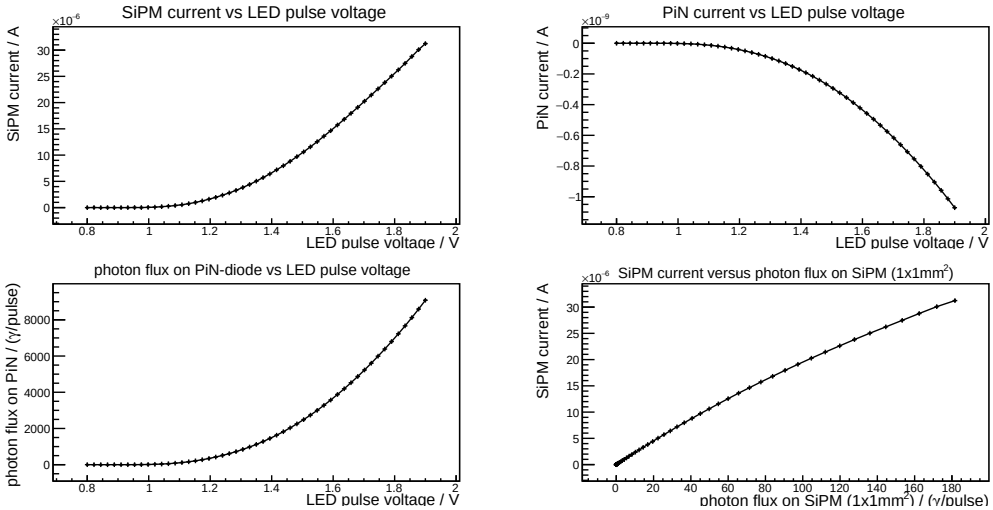

Figure A.46.: Characterisation measurement for DC LED 20 in external pulsed mode

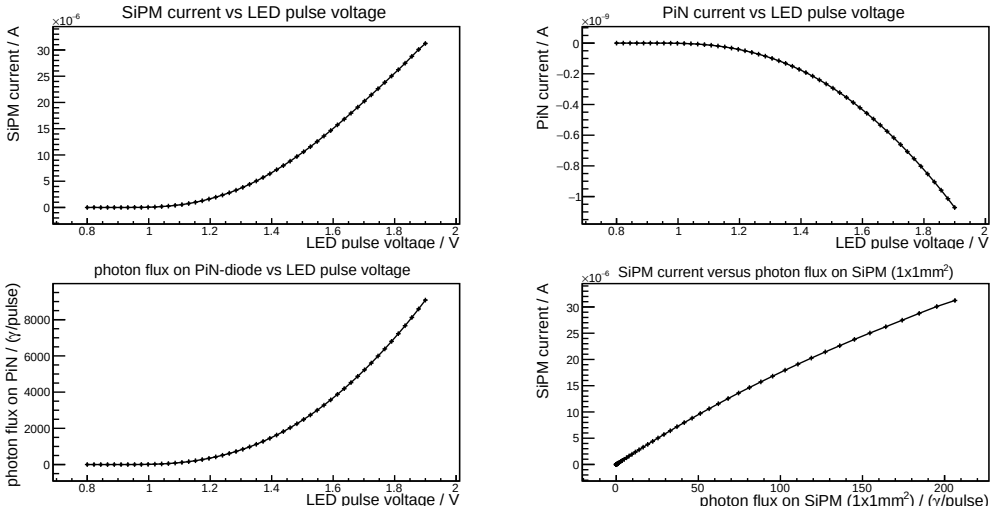

Figure A.47.: Characterisation measurement for DC LED 21 in external pulsed mode

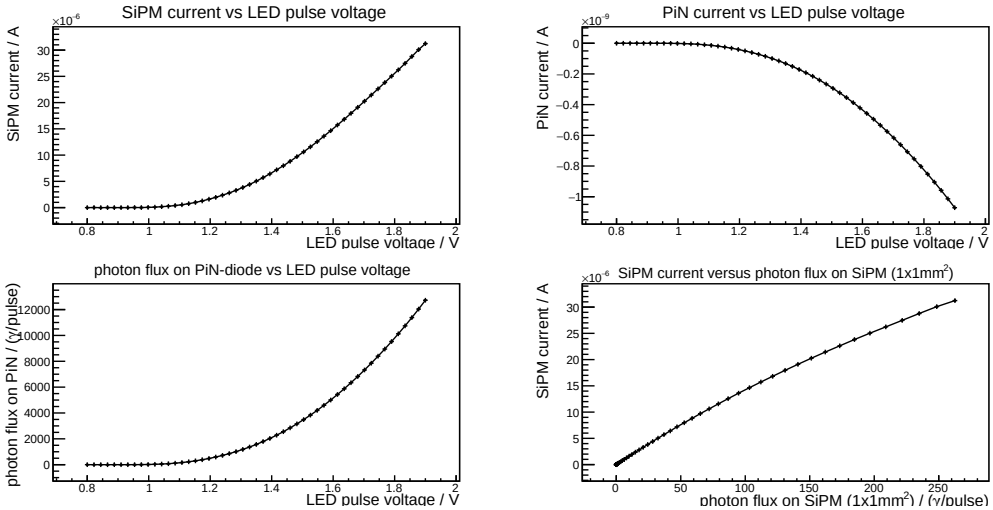

Figure A.48.: Characterisation measurement for DC LED 22 in external pulsed mode

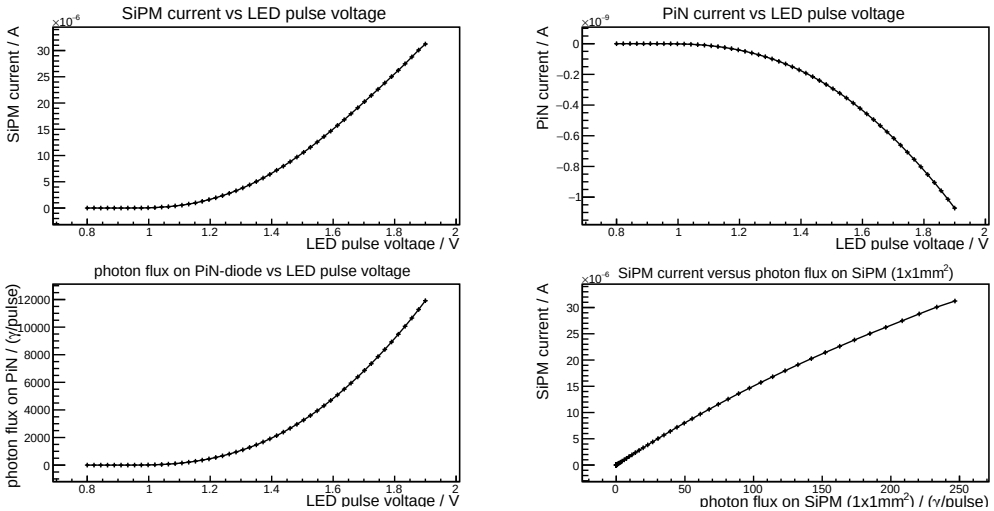

Figure A.49.: Characterisation measurement for DC LED 23 in external pulsed mode

B. Appendix: Effective isolation resistance of coaxial and triaxial cables

The isolation resistance of a coaxial cable is given by the integral over thin shells of the isolation material from the core diameter r_0 to the inner diameter of the shielding r_1 with a electrical resistivity $\rho[\Omega \cdot \mathrm{m}]$[20]:

$$dR = \frac{\rho}{2\pi r L} dr \tag{B.1}$$

$$R = \int_{r_0}^{r_1} \frac{\rho}{2\pi r L} dr = \frac{\rho}{2\pi L} \int_{r_0}^{r_1} \frac{dr}{r} \tag{B.2}$$

$$R = \frac{\rho}{2\pi L} \ln(\frac{r_1}{r_0}) \tag{B.3}$$

Longer cables have a lower isolation resistance and thus a higher leakage current, which disturbs the low current measurements since the cables have a finite length. With the used sourcemeter this effect can not be measured for the used coaxial cable (type RG316) with Teflon dielectric. To prevent this disturbance one can use triaxial cable. This has an additional guard layer between the core and the shielding as shown in the schematic B.1. The guard is supplied with the same potential as the core with regard to the shielding. This results in potential difference of 0 around the core and ensures a zero leakage current between core and shield. The leakage current between shielding and guard is not accounted for in the measurement.

[20] Polyethylene has a ρ from $1 \cdot 10^{15} \Omega \cdot \mathrm{m}$ to $1 \cdot 10^{18} \Omega \cdot \mathrm{m}$, Teflon (PTFE) from $1 \cdot 10^{23} \Omega \cdot \mathrm{m}$ to $1 \cdot 10^{25} \Omega \cdot \mathrm{m}$

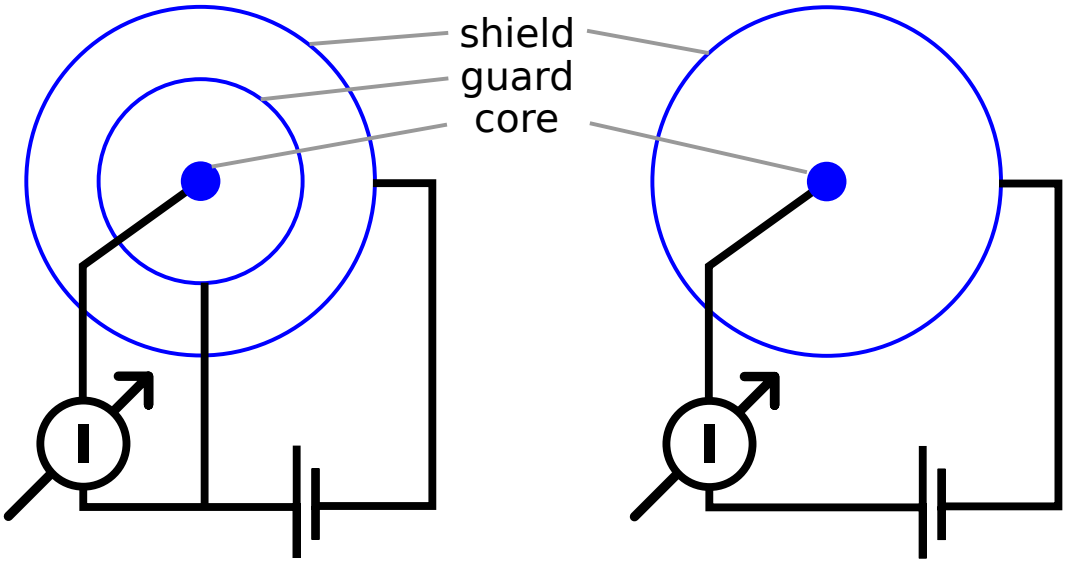

Figure B.1.: Schematic of triaxial cable on the left and coaxial cable on the right.

C. Appendix: Signal analysis

C.1. FFT filtering examples

The cut off bin can be converted to the frequency by:

$$f_{bin\,width} = \frac{2}{n \cdot \Delta t} \tag{C.1}$$

$$f_{cut\,off} = f_{bin\,width} \cdot bin \tag{C.2}$$

with Δt the time step in acquisition, n the number of points used for the FFT. The plots shown in Figures C.1 to C.3 have $\Delta t = 100\,\text{ps}$ an $n = 4096$, resulting in $f_{binwidth} \approx 4.88\,\text{MHz}$.

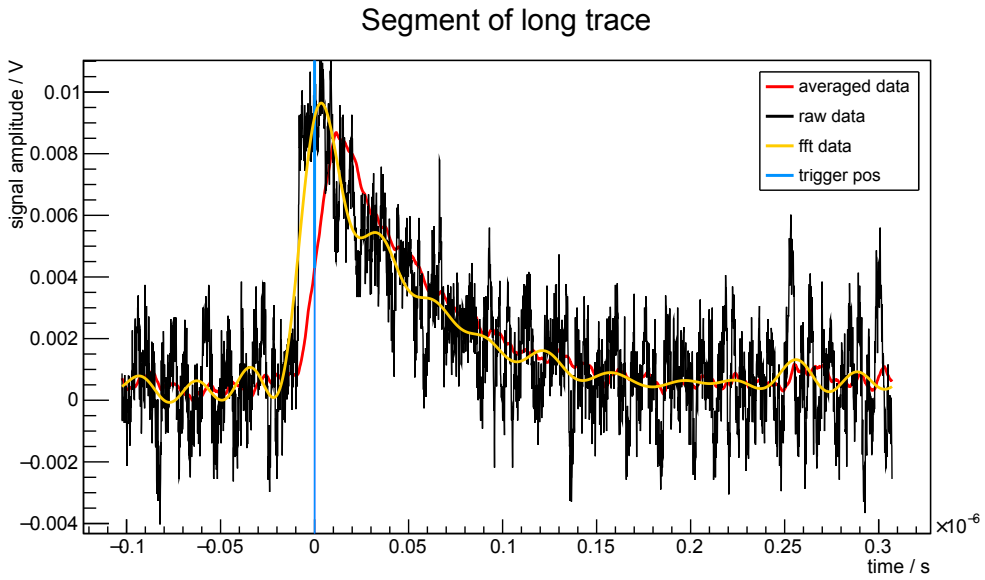

Figure C.1.: FFT filtered short trace segment. FFT filtered data is shown in orange. Here with a cut off at FFT bin 15 (73 MHz). The rising edges is flattened.

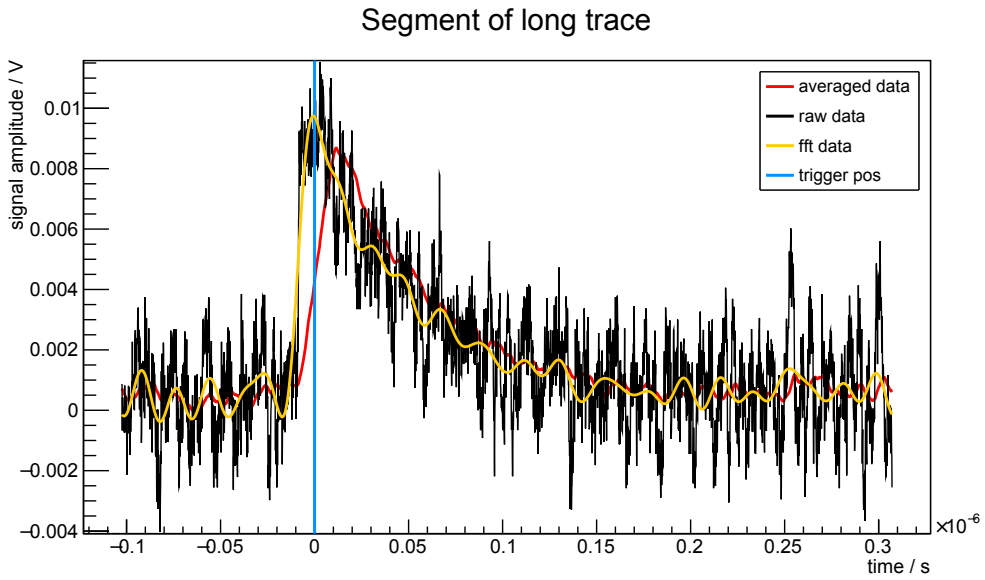

Figure C.2.: FFT filtered short trace segment. FFT filtered data is shown in orange. Here with a cut off at FFT bin 25 (122 MHz).

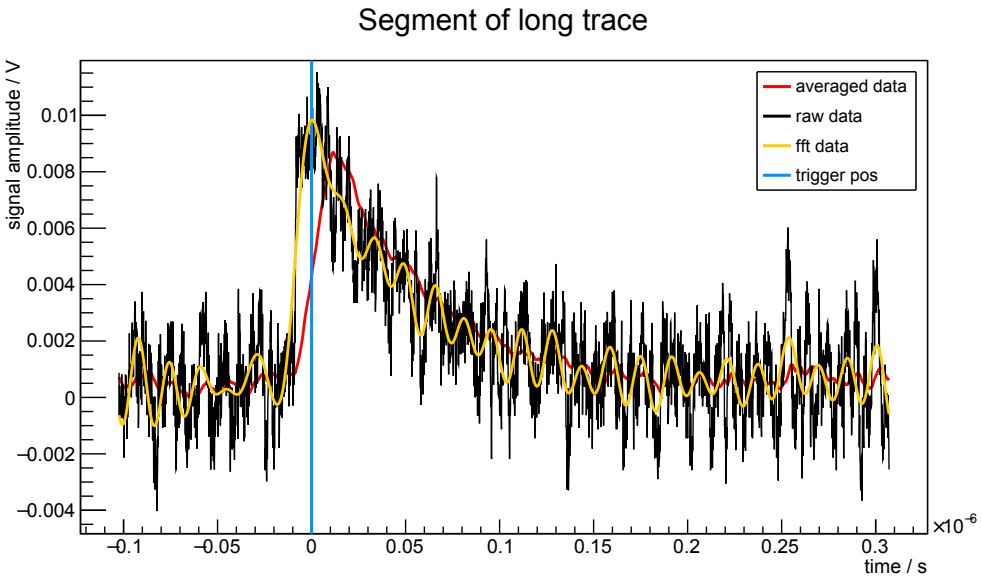

Figure C.3.: FFT filtered short trace segment. FFT filtered data is shown in orange. Here with a cut off at FFT bin 30 (146 MHz). The (noise) filtering effect is reduced.

The following three plots (Figures C.4 to C.6) show the FFT filtering for data with $\Delta t = 1\,\text{ns}$ and $n = 1024$, resulting in $f_{binwidth} \approx 1.95\,\text{MHz}$.

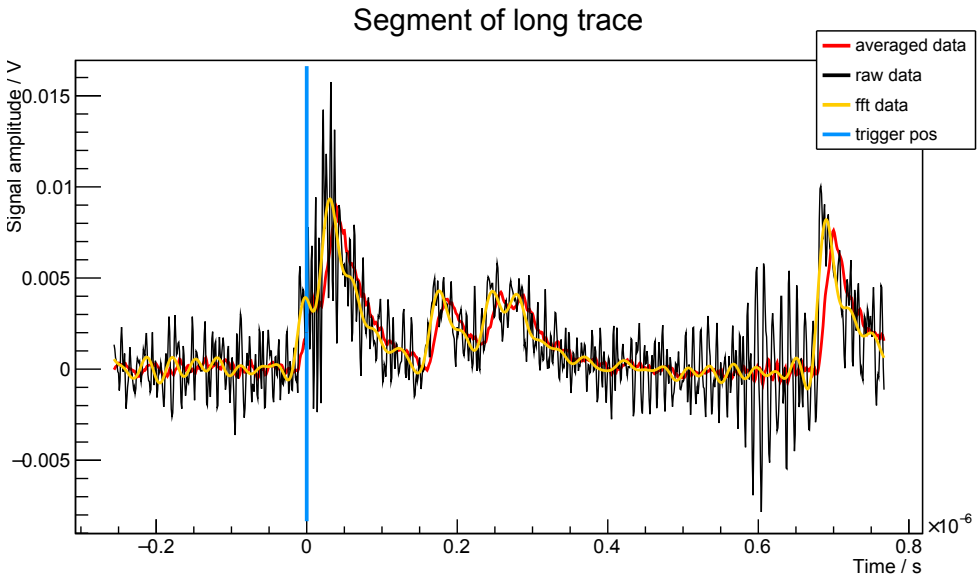

Figure C.4.: FFT filtered short trace segment. FFT filtered data is shown in orange. Here with a cut-off at FFT bin 37 (73 MHz).

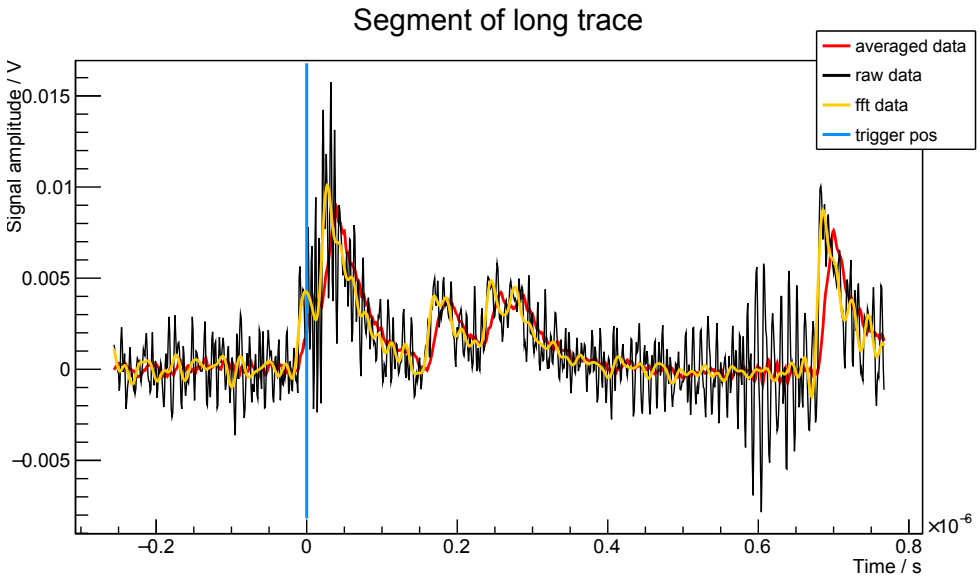

Figure C.5.: FFT filtered short trace segment. FFT filtered data is shown in orange. Here with a cut-off at FFT bin 62 (122 MHz).

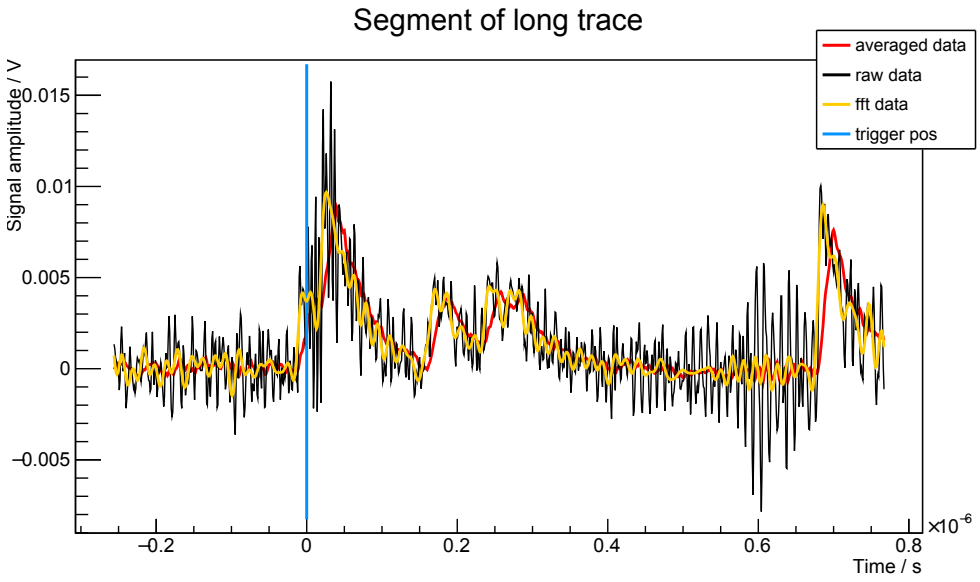

Figure C.6.: FFT filtered short trace segment. FFT filtered data is shown in orange. Here with a cut-off at FFT bin 76 (150 MHz).

C.2. Time distributions for peak to peak

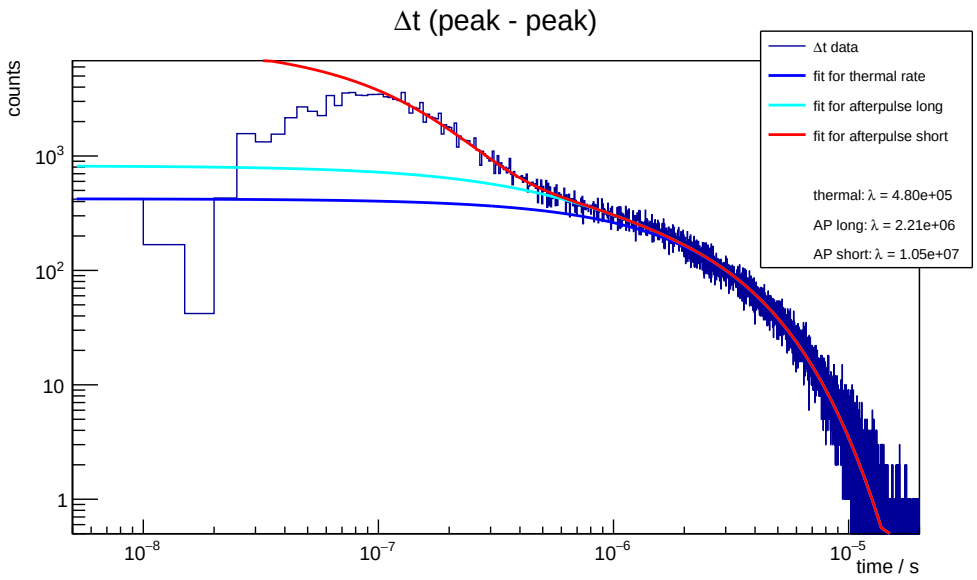

Figure C.7.: The silence window in the filtering is 50 ns and all found peaks are searched for afterpulses.

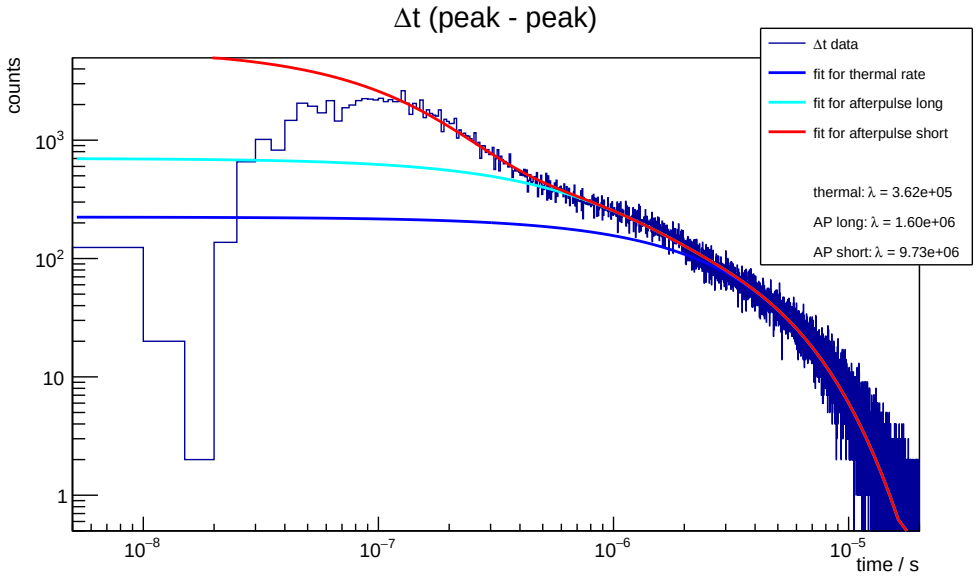

Figure C.8.: The silence window in the filtering is 500 ns and all found peaks are searched for afterpulses.

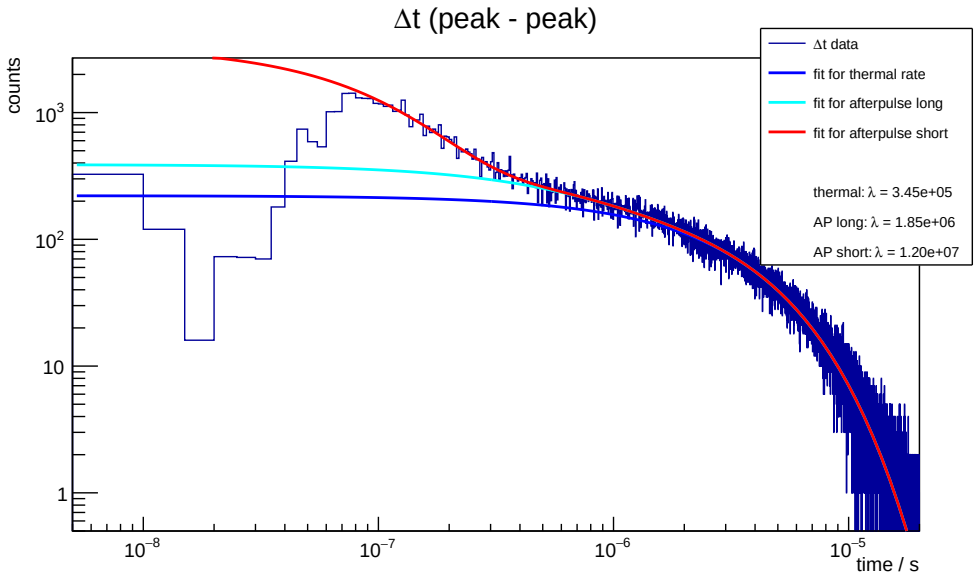

Figure C.9.: The silence window in the filtering is 50 ns and only 1 p.e. peaks are searched for afterpulses.

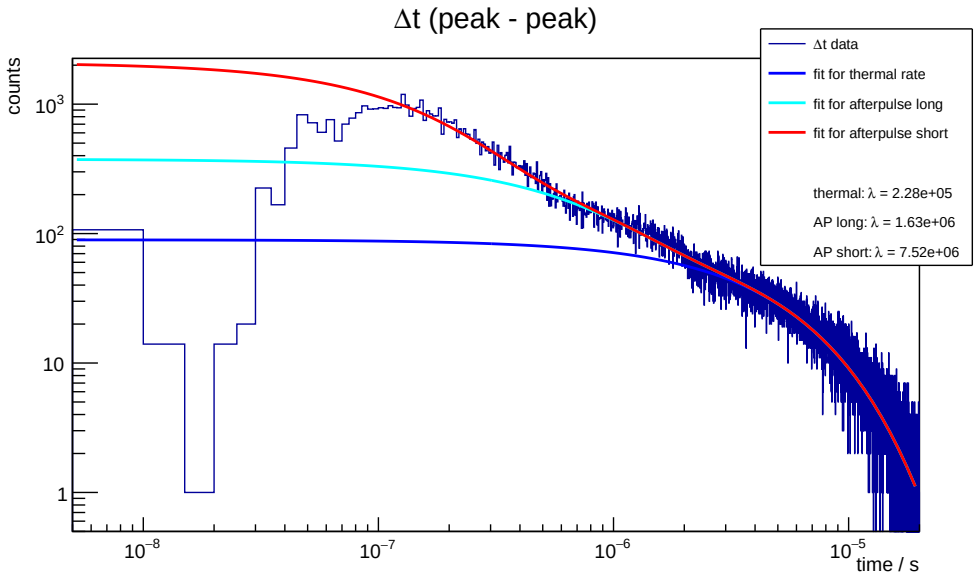

Figure C.10.: The silence window in the filtering is 500 ns and only 1 p.e. peaks are searched for afterpulses.

C.3. Count distributions for peak to peak times and amplitude

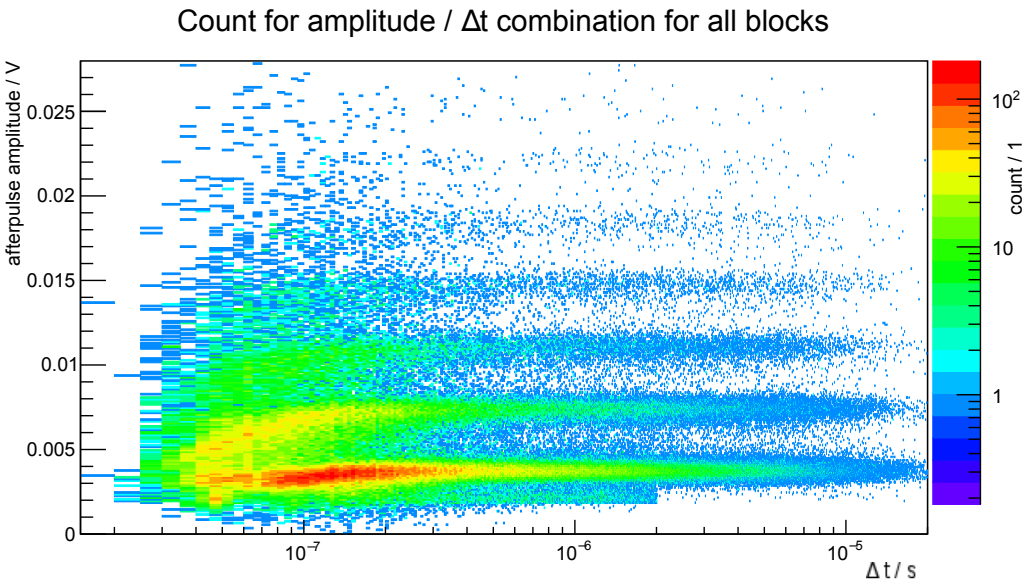

Figure C.11.: Afterpluse count versus amplitude and Δt with all peaks evaluated.

Danksagung

Diese Arbeit habe ich allein geschrieben, doch für den erfolgreichen Abschluss eben dieser bin ich einigen Menschen zum Dank verpflichtet. An erste Stelle möchte ich meinem Doktorvater Professor Hebbeker danken, der mir diese sehr interessante Arbeit ermöglicht hat. Ganz besonderer Dank gebührt Markus Merschmeyer, dessen Tür mir jederzeit für Diskussionen offen stand. Für die technische Realisierung meiner Ideen möchte ich mich bei den Mitarbeitern der mechanischen Werkstatt und der elektronischen Werkstatt bedanken. Meinen Kollegen danke ich für die angenehme Atmosphäre und ihr offenes Feedback. Meinen Testlesern Katharina, Markus und Daniel danke ich für ihre zahlreichen Anmerkungen und Verbesserungsvorschlägen. Besonderer Dank gilt meiner Familie und meiner Freundin Katharina, die mich immer unterstützt und motiviert haben. Dafür bin ich euch auf ewig dankbar.

Euer Carsten